GEORGIA DOT RESEARCH PROJECT 17-09

FINAL REPORT

PHASE II – INVESTIGATION OF RECYCLED TIRE CHIPS AND FIBER REINFORCEMENT FOR USE IN GDOT CONCRETE USED TO CONSTRUCT BARRIER WALLS AND OTHER APPLICATIONS

OFFICE OF PERFORMANCE-BASED MANAGEMENT AND RESEARCH

600 WEST PEACHTREE STREET NW
ATLANTA, GA 30308

TECHNICAL REPORT DOCUMENTATION PAGE

1. Report No.: FHWA-GA-20-1709	2. Government Accession No.: N/A	3. Recipient's Catalog No.: N/A
4. Title and Subtitle: Phase II – Investigation of Recycled Tire Chips and Fiber Reinforcement for Use in GDOT Concrete Used to Construct Barrier Walls and Other Applications		5. Report Date: November 2020 6. Performing Organization Code: N/A
7. Author(s): Stephan A. Durham, Ph.D., P.E. https://orcid.org/0000-0002-6177-3491; Mi G. Chorzepa, Ph.D., P.E. https://orcid.org/0000-0001-7259-3165; Alex Blankenship; Grace Darling; Victor Lopez; and Tofail Ahmed		8. Performing Organization Report No.: 17-09
9. Performing Organization Name and Address: University of Georgia College of Engineering Driftmier Engineering Center Athens, GA 30602 Phone: (706) 542-9480 Email: sdurham@uga.edu		10. Work Unit No.: N/A 11. Contract or Grant No.: PI#0015711
12. Sponsoring Agency Name and Address: Georgia Department of Transportation Office of Performance-based Management and Research 600 West Peachtree Street NW Atlanta, GA 30308		13. Type of Report and Period Covered: Final Report August 2017 – November 2020 14. Sponsoring Agency Code: N/A
15. Supplementary Notes: Prepared in cooperation with the U.S. Department of Transportation, Federal Highway Administration.		
16. Abstract: Concrete median barriers (CMBs) are installed to decrease the overall severity of traffic accidents by producing higher vehicle decelerations. In 2016, an update to the AASHTO *Manual for Assessing Safety Hardware* (*MASH*) saw a 58.00 percent increase in impact severity of test level 4 (TL-4) impact conditions when compared to the *NCHRP Report 350* testing criteria. This study investigates the use of fiber-reinforced rubberized CMBs in dissipating the impact energy to improve driver safety involved in crashed vehicles. This study was completed in three major investigations: (1) fiber-reinforced rubberized concrete mixtures evaluation, (2) finite element model (FEM) and laboratory-scale barrier wall testing and simulations, and (3) steel fiber–reinforced concrete (SFRC) mixture design and testing. The fiber-reinforced rubberized concrete mixture investigation examined the energy dissipation capacity of fiber-reinforced rubberized concrete mixtures subjected to impact forces. Results from this testing confirmed that fiber-reinforced rubberized concrete demonstrated significantly improved energy dissipation capacity and impact resilience, particularly with 1.00 percent steel fiber addition and 20.00 percent tire chips. An FEM was developed in order to perform a vehicle crash simulation of a single-slope CMB as a viable alternative to a full-scale crash test. Full-scale CMB prototypes incorporating shear keys were tested by applying TL-4 quasi-dynamic impact conditions. An additional investigation was performed to evaluate the influence of steel fiber volume and geometry on fresh and hardened concrete properties as well as the influence on the flexural and shear capacities of scaled laboratory beams. Lastly, machine learning methods were used to construct SFRC compressive and flexural strength prediction models.		
17. Keywords: Single-Slope Barrier, Rubberized Concrete, Fiber Reinforced Concrete, Energy Dissipation Capacity, Dynamic Impact, Steel Fibers, Concrete Median Barrier, *MASH* Testing	18. Distribution Statement: No Restriction	

19. Security Classification (of this report): Unclassified	20. Security Classification (of this page): Unclassified	21. No. of Pages: 211	22. Price: Free

Form DOT 1700.7 (8-72) Reproduction of completed page authorized

GDOT Research Project 17-09

Final Report

PHASE II – INVESTIGATION OF RECYCLED TIRE CHIPS AND FIBER REINFORCEMENT FOR USE IN GDOT CONCRETE USED TO CONSTRUCT BARRIER WALLS AND OTHER APPLICATIONS

By

Stephan A. Durham, Ph.D., P.E.
Professor

Mi G. Chorzepa, Ph.D., P.E.
Associate Professor

Alex Blankenship
Graduate Research Assistant

Grace Darling
Graduate Research Assistant

Victor Lopez
Graduate Research Assistant

Tofail Ahmed
Graduate Research Assistant

University of Georgia Research Foundation, Inc.

Contract with
Georgia Department of Transportation

In cooperation with
U.S. Department of Transportation Federal Highway Administration

November 2020

SI* (MODERN METRIC) CONVERSION FACTORS

APPROXIMATE CONVERSIONS TO SI UNITS

Symbol	When You Know	Multiply By	To Find	Symbol
		LENGTH		
in	inches	25.4	millimeters	mm
ft	feet	0.305	meters	m
yd	yards	0.914	meters	m
mi	miles	1.61	kilometers	km
		AREA		
in^2	square inches	645.2	square millimeters	mm^2
ft^2	square feet	0.093	square meters	m^2
yd^2	square yard	0.836	square meters	m^2
ac	acres	0.405	hectares	ha
mi^2	square miles	2.59	square kilometers	km^2
		VOLUME		
fl oz	fluid ounces	29.57	milliliters	mL
gal	gallons	3.785	liters	L
ft^3	cubic feet	0.028	cubic meters	m^3
yd^3	cubic yards	0.765	cubic meters	m^3
		NOTE: volumes greater than 1000 L shall be shown in m^3		
		MASS		
oz	ounces	28.35	grams	g
lb	pounds	0.454	kilograms	kg
T	short tons (2000 lb)	0.907	megagrams (or "metric ton")	Mg (or "t")
		TEMPERATURE (exact degrees)		
°F	Fahrenheit	5 (F-32)/9 or (F-32)/1.8	Celsius	°C
		ILLUMINATION		
fc	foot-candles	10.76	lux	lx
fl	foot-Lamberts	3.426	$candela/m^2$	cd/m^2
		FORCE and PRESSURE or STRESS		
lbf	poundforce	4.45	newtons	N
lbf/in^2	poundforce per square inch	6.89	kilopascals	kPa

APPROXIMATE CONVERSIONS FROM SI UNITS

Symbol	When You Know	Multiply By	To Find	Symbol
		LENGTH		
mm	millimeters	0.039	inches	in
m	meters	3.28	feet	ft
m	meters	1.09	yards	yd
km	kilometers	0.621	miles	mi
		AREA		
mm^2	square millimeters	0.0016	square inches	in^2
m^2	square meters	10.764	square feet	ft^2
m^2	square meters	1.195	square yards	yd^2
ha	hectares	2.47	acres	ac
km^2	square kilometers	0.386	square miles	mi^2
		VOLUME		
mL	milliliters	0.034	fluid ounces	fl oz
L	liters	0.264	gallons	gal
m^3	cubic meters	35.314	cubic feet	ft^3
m^3	cubic meters	1.307	cubic yards	yd^3
		MASS		
g	grams	0.035	ounces	oz
kg	kilograms	2.202	pounds	lb
Mg (or "t")	megagrams (or "metric ton")	1.103	short tons (2000 lb)	T
		TEMPERATURE (exact degrees)		
°C	Celsius	1.8C+32	Fahrenheit	°F
		ILLUMINATION		
lx	lux	0.0929	foot-candles	fc
cd/m^2	$candela/m^2$	0.2919	foot-Lamberts	fl
		FORCE and PRESSURE or STRESS		
N	newtons	0.225	poundforce	lbf
kPa	kilopascals	0.145	poundforce per square inch	lbf/in^2

* SI is the symbol for the International System of Units. Appropriate rounding should be made to comply with Section 4 of ASTM E380. (Revised March 2003)

TABLE OF CONTENTS

LIST OF FIGURES

LIST OF TABLES

EXECUTIVE SUMMARY

Concrete median barriers (CMBs) are installed to decrease the overall severity of traffic accidents by producing higher vehicle decelerations. In 2016, an update to the AASHTO *Manual for Assessing Safety Hardware* (*MASH*) saw a 58.00 percent increase in impact severity of test level 4 (TL-4) impact conditions when compared to the *NCHRP Report 350* testing criteria. This study investigates the use of fiber-reinforced rubberized CMBs in dissipating the impact energy to improve driver safety involved in crashed vehicles. This study was completed in three major investigations: (1) fiber-reinforced rubberized concrete mixtures evaluation, (2) finite element model and laboratory-scale barrier wall testing and simulations, and (3) steel fiber–reinforced concrete (SFRC) mixture design and testing.

The aim of the fiber-reinforced rubberized concrete mixture investigation was to maximize the energy dissipation capacity of fiber-reinforced rubberized concrete mixtures subjected to impact forces for the purpose of improving the impact resilience of GDOT CMBs and other applications. Small-scale testing of mixtures to optimize compressive strength, modulus of rupture, and impact resilience using a fixed percentage of tire chip replacement of the coarse aggregate and varying volume fractions of steel, polypropylene, and polyvinyl alcohol fibers was performed to inform a larger scale static and impact beam investigation. Results from this testing confirmed that fiber-reinforced rubberized concrete demonstrated significantly improved energy dissipation capacity and impact resilience, particularly with 1.00 percent steel fiber addition and 20.00 percent tire chip replacement when compared to a control mixture without fibers and rubber tire chips.

A finite element model was developed in order to perform a vehicle crash simulation of a single-slope CMB as a viable alternative to a full-scale crash test. In a parameter study, two material models were evaluated to study the effect of associated material parameters on beam response during impact and validate the beam analysis results against available drop-weight impact test data. The analysis scheme established from the study was successfully implemented to characterize increased impact resilience in concrete barriers made of the rubber and steel fiber modified concrete mixture. Crash test simulations were performed with a pickup truck as well as a heavy commercial truck. Results show that the change in the material parameters related to failure and post-failure behavior, particularly in the Riedel–Hiermaier–Thoma material model, has significant effect on the peak impact force reduction. Energy dissipation mechanisms and implications of modeling fiber-reinforced concrete barriers by studying post-failure mechanism are discussed. A laboratory-scale CMB study was also carried out. Two full-scale barrier prototypes with shear keys were constructed and tested under TL-4 quasi-dynamic impact conditions in a laboratory setting. Compared to the GDOT-specified barrier, the fiber-reinforced rubberized concrete mixture, a design with 20.00 percent replacement of the coarse aggregate by volume with recycled rubber tire chips and a 1.00 percent steel fiber addition, was evaluated based on its performance in toughness, energy absorption capacity, and plastic response.

Lastly, the study included a three-part experimental and analytical investigation of the mechanical performance enhancement potentials of SFRC. The fresh and hardened properties of SFRC mixtures containing varying fiber geometries and concentrations was studied. Based on results of these mixtures, large-scale static beam testing of select SFRC mixtures was created to examine the additional shear and flexural capacity provided by steel fibers. Machine learning methods were used to construct SFRC compressive and flexural strength prediction models. The

prediction models allow for the evaluation of SFRC as a potential design solution for GDOT applications by estimating compressive strength, modulus of rupture, and cost.

CHAPTER 1. INTRODUCTION

OVERVIEW

Safety features along roadways are designed to restrain vehicles from entering opposing lanes of traffic. According to the American Association of State Highway and Transportation Officials (AASHTO) *Roadside Design Guide*, median barriers are only required when the median width is 30.0 to 50.0 ft (9.1 to 15.2 m) (Zou et al. 2014). In situations where narrow medians are present, the probability of crossover accidents increases and results in more multiple vehicle collisions. Some states have begun to install roadside barriers, typically flexible cable barriers due to costs, to reduce the possibility of accidents. Concrete median barriers (CMBs) are installed to decrease the overall severity of traffic accidents by producing higher vehicle decelerations and to prevent any lateral deflection. Due to these rigid systems having a higher stiffness than other barrier systems, such as guardrails and cable barriers, impacts with CMBs have a tendency to be more severe. A way to mitigate this outcome is to develop engineered cementitious composites that not only possess adequate compressive and flexural strength, but also exhibit substantial ductility and energy dissipation capacity. The incorporation of recycled tire chips by Durham et al. (2017) in Georgia Department of Transportation's (GDOT) Research Project 15-14 demonstrated promise for improving energy dissipation capacity as well as decreasing the overall severity to the concrete due to impact and provided basis for further investigation in this research study. The inclusion of fiber reinforcement in concrete mixtures has been found to improve the flexural capacity and toughness of the concrete. In order to test the ability for fiber-reinforced rubberized concrete mixtures to perform acceptably for use in CMBs, full-scale testing, as well as collision simulation models, must be performed in accordance to the *Manual for Assessing Safety*

Hardware (*MASH*) and National Cooperative Highway Research Program (NCHRP) *Report 350* test levels.

Demand for the use of engineered cementitious composites that aid in the impact resilience of reinforced concrete structures has been increasing. Standard concrete mixtures do not exhibit the necessary properties to effectively dissipate energy caused by intense dynamic loading. As a result, several recent studies have been conducted to observe the impact response of reinforced concrete structures (Masud 2015, Li et al. 2005, Fujikake et al. 2009, Saatci and Vecchio 2009). These studies have shown that standard concrete members are susceptible to localized failure responses when subjected to impact loads, resulting in target fracture and section loss instead of exhibiting significant deformation. Specifically, this issue has been observed several times in high-speed highway-related accidents. Over the last few decades, research has been conducted that incorporates supplementary fiber reinforcement within concrete mixtures (Masud 2015, Noaman et al. 2017, Afroughsabet and Ozbakkaloglu 2015). Fibers such as steel, polypropylene (PP), and polyvinyl alcohol (PVA) have all proven to improve ductility under static and dynamic loading (Masud 2015). These fibers come in various geometries and, depending on the application, are used to bridge both macrocracks and microcracks.

This report examines the inclusion of recycled tire chips as a coarse aggregate replacement and supplementary fiber reinforcement with the aim of enhancing the impact performance of CMBs. To accomplish the research study objectives, a multi-phase investigation approach was undertaken. An initial phase consisted of testing small-scale mixtures to determine an optimized fiber type and quantity for use in concrete for CMB applications. This phase included testing for fresh concrete properties, compressive strength, modulus of rupture (MOR), and drop-hammer impact resilience. In addition, scaled laboratory beams consisting of fiber-reinforced rubberized

mixtures and fiber-reinforced–only concrete mixtures were produced and subjected to flexural beam testing as well as impact. A second phase consisted of the design, construction, and testing of two single-slope barriers, one being the control and the other being the optimized fiber-reinforced rubberized mixture derived from the earlier phase. The results from this experimental testing were then used to validate a finite element model (FEM) developed under this investigation. The FEM was then used to further analyze full-scale crash simulations to understand the three-dimensional (3D) impact response and energy absorption capacity of rubberized concrete barrier walls. A final investigation was completed in order to provide additional information on the use of steel fiber–reinforced concrete (SFRC) for GDOT applications. Within this study phase, the influence of steel fiber volume and geometry on fresh and hardened concrete properties, as well as impact on the flexural and shear capacities of scaled laboratory beams, were studied. Lastly, machine learning methods were used to construct SFRC compressive and flexural strength prediction models.

STUDY OBJECTIVES

The primary objective of this research was to assess the performance of scaled concrete median barriers, incorporating recycled tire chips and fiber reinforcement, under dynamic impact loading test conditions. Utilizing an optimized fiber-reinforced rubberized concrete mixture developed through the research investigation, and the recent implementation of *MASH* for cast-in-place concrete barriers by GDOT, two 8.0 ft (2.4 m) long single-slope barriers were constructed and evaluated under *MASH* test level 4 (TL-4). In addition, a finite element model was created in order to further analyze. Although much research has been performed on concrete members that study fiber and recycled rubber aggregates individually, little research has been conducted on the effects of combining these constituents in scaled concrete structures subjected to impact forces.

The strength enhancements provided by SFRC can potentially provide enough capacity to eliminate a portion of the steel reinforcing bars and even reduce the concrete thickness. While several studies have examined the response of unreinforced SFRC beams to static loading, i.e., Choi et al. (2007), Kwak et al. (2002), and Yakoub (2011), limited research has been conducted on SFRC beams containing conventional shear reinforcement at different ratios.

The major objectives of this study are:

1. Develop an optimized hybrid concrete mixture that incorporates fiber reinforcement and recycled tire rubber aggregates for use in concrete safety barriers and other applications.
2. Assess the performance of scaled concrete median barriers, incorporating recycled tire chips and fiber reinforcement, under dynamic impact loading test conditions using experimental and analytical approaches.
3. Subject two scaled concrete barrier walls—a control specimen and one incorporating the optimized fiber-reinforced rubberized concrete mixture—to dynamic impact testing to gauge the members' performance in toughness, energy absorption capacity, and plastic response.
4. Develop a more complete understanding of the structural benefit and material saving potential presented by SFRC mixtures.

Through this study, additional understanding regarding the structural adequacy and potential use on highways for rubberized concrete median barriers is developed and compared to existing portland-cement concrete barriers. Ultimately, this study presents results such as transverse impact responses and energy absorption of rubberized concrete barriers, the development of a

finite element model for running full-scale crash simulations, and an exploration of the benefits served by the utilization of SFRC mixtures.

CHAPTER 2. LITERATURE REVIEW

OVERVIEW

This literature review examines the effects of fiber reinforcement for use in concrete applications and past studies of concrete barrier wall testing procedures and designs. The review notes the evolving trends that researchers of past studies have investigated to improve testing methodologies, barrier design requirements, and evaluation guidelines to produce sustainable high-strength CMBs. Within this literary review, a better understanding of how the inclusion of steel fibers affects the mechanical properties of concrete, as well as traditional barrier designs and structural validation methods.

FIBER-REINFORCED CONCRETE

Since the beginning of the modern development of fiber reinforcement, thousands of technical papers have been published and multiple guidelines and standards have been developed for fiber-reinforced cements and composites. The inclusion of fiber reinforcement within concrete has been shown to increase compressive and splitting tensile strengths, modulus of rupture, and toughness of the composite material (Song and Hwang 2004). The fiber material type, geometry, orientation, and concentration within the concrete matrix has a direct impact on the shear strength and ductility of the concrete (Zollo 1997). FRC design was developed based on the fracture mechanics concept, in which the fibers served to reinforce the matrix and bridge cracks. One role of the fibers within the concrete matrix is to mitigate crack propagation. Figure 1 illustrates how fibers effectively mitigate crack growth, and absorb energy while holding the composite together in the event of cracking.

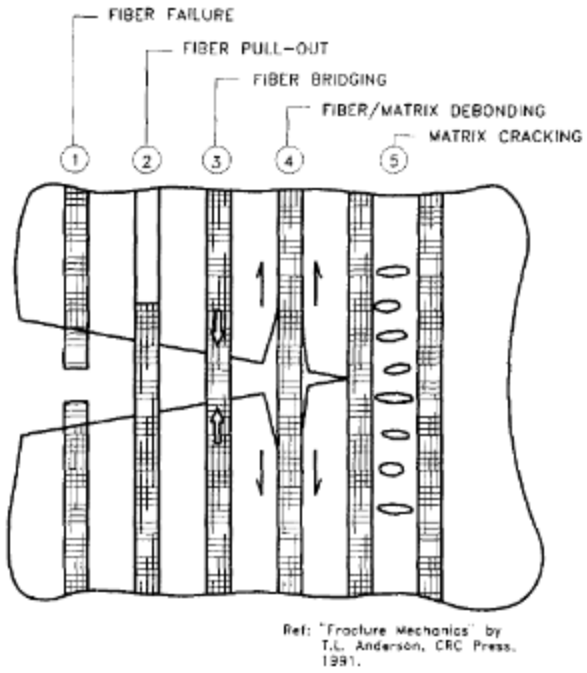

Figure 1. Image. Energy-absorbing fiber/matric mechanisms (Zollo 1997).

Fiber Reinforcement Types

There are many fiber types developed to reinforce concrete. Materials used for fibers include steel, polypropylene, carbon, and glass, among others. Fiber types may be organized into four main categories: metallic, glass, synthetic, and natural fibers. Steel fibers are the most widely used fiber type to reinforce concrete mixtures due to their high stiffness and malleability, which allows them to be manipulated and deformed into distinct shapes without effecting the high stiffness values (Dopko 2018). A number of fiber deformation designs have been incorporated into concrete and studied. Deformation of the fibers aids with mechanical anchorage into the composite and has a direct influence on fiber pull-out resistance. Types of fiber deformations include hooked-end, twisted, bent, crimped, and other anchorage methods. The effectiveness of the fiber is related to its bond strength, which is dependent on the strength of the concrete matrix.

This idea is similar to the development length concept with traditional steel reinforcement bars in concrete beams.

The geometry of the fiber also influences its effectiveness within the composite matrix. Several researchers have studied the geometries of the fibers, mainly the anchorage and aspect ratio, to determine the optimum fiber geometry. Yoo et al. (2017) studied fiber geometries and aspect ratios at different volume fractions, comparing straight, hooked-end, and twisted fibers of varying lengths. Within that study, the researchers concluded that while straight fibers produced higher strength results, a larger number of fibers was required to achieve this strength in comparison to hooked-end fibers. Mixtures containing hooked-end fibers possessed higher MOR values and toughness indexes with low fiber volumes in comparison to mixtures containing straight fibers at an equal fiber concentration. The hooked end of the fibers provide additional anchorage within the composite material, which helps to enhance the pull-out strength of the fibers, directly increasing the tensile strength of the composite.

In recent years, the end anchorage of these hooked-end fibers has been studied and improved upon. As shown in figure 2, three-dimensional, four-dimensional (4D), and five-dimensional (5D) configurations are being used in industry. Information regarding the benefits of these fibers is presented in the following section. The fiber pull-out strength, i.e., the axial load required to pull the fiber out of the hardened concrete matrix, is dependent on the fiber geometry and its interaction with the concrete matrix. Abdallah (2017) compared the pull-out behavior of the 3D, 4D, and 5D end anchorages by measuring the force necessary to dislodge the fiber, concluding that the 5D configuration possessed the greatest pull-out strength of the three. Water-to-binder (w/b) ratios of 0.11, 0.15, and 0.20, as well as varying embedment length including 0.4 inch (10 mm), 0.8 inch (20 mm), and 1.2 inch (30 mm) were investigated. Abdallah found that for

series with 3D, 4D, and 5D steel fibers with a w/b ratio of 0.20, the peak load was increased by 48.68, 30.94, and 43.95 percent, respectively, in comparison to straight fibers (Abdallah 2017). Additionally, the longer the embedment length, the greater the pull-out resistance due to the greater surface area of fiber in contact with the binder matrix. By analyzing the pull-out results shown in figure 3, a redistribution of the load occurs as the fiber begins to slip out of the matrix, which is similar to load–deflection observations.

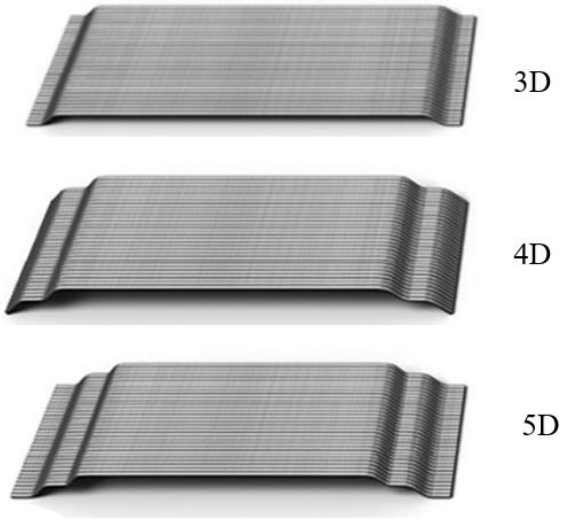

Figure 2. Images. Examples of steel fiber end anchorage (Bekaert Corp. 2020).

Concrete Specifications

The governing specification for FRC in North America is ASTM C1116/C1116M-15 *Standard Specification for Fiber-Reinforced Concrete*, which covers all forms of FRC. For steel fibers in particular, specifications are further dictated by ASTM A820/A820M-16 *Standard Specification for Steel Fibers for Fiber-Reinforced Concrete*. According to ASTM A820, there are five general types of steel fibers: cold-drawn wire (type I), cut sheet (type II), melt-extracted (type III), mill cut (type IV), and modified cold-drawn wire (type V).

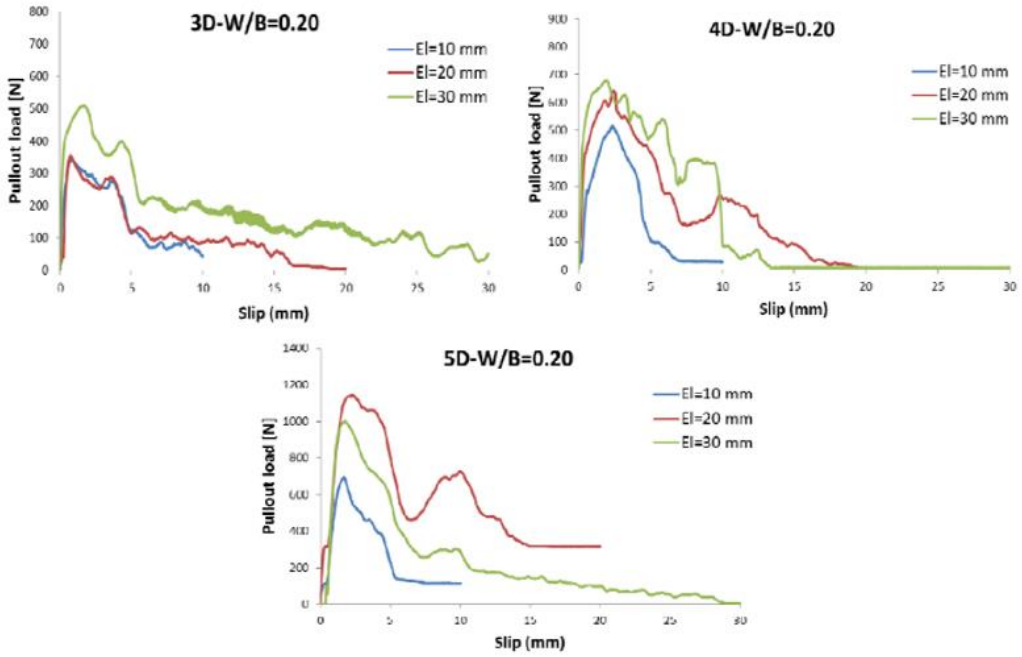

Figure 3. Graphs. Steel fiber pullout load results (Abdallah 2017).

Mixture Design

The American Concrete Institute (ACI) 544.4R-18 *Guide to Design with Fiber-Reinforced Concrete* (ACI 2018) provides design guidelines for FRC, which are discussed within this section. Within these guidelines, concrete residual strength is considered as the main parameter, which is determined from standard three-point bending beam tests. The ultimate limit state (ULS) and serviceability limit state (SLS) are observed for strength requirements, crack width limits, and deflection limits. The SLS design level is considered for smaller deflections for which crack widths range from 0.016 to 0.04 inch (0.4 to 1.0 mm). ULS is considered for larger deflections in which crack widths range from 0.08 to 0.14 inch (2.0 to 3.5 mm).

Flexural Design

The stress block concept used within traditional reinforced concrete design can also be used in the design of FRC. ACI provides expressions for calculating the flexural strength of SFRC. Three-point loading flexural tests performed following ASTM C1609/C1609M-19 is used to obtain design parameters. The needed design parameters are f_{600}^{D}, f_{150}^{D}, and $f_{e,3}$, which are FRC flexural residual strength at L/600, at L/150, and equivalent FRC flexural residual strength at L/150, respectively, reported in psi (MPa). The equivalent FRC flexural residual strength is a measurement of the toughness of an FRC beam, and is used in place of f_{150}^{D} during the design of continually supported beams, such as slabs-on-grade. The ultimate tensile strength of the cracked FRC section may be calculated using equation 1. The nominal bending moment of the FRC section may be calculated using equation 2.

$$f_{ut-FRC} = 0.37 f_{150}^{D} \tag{1}$$

$$M_{n-FRC} = f_{150}^{D}\, x\, \frac{bh^2}{6} \tag{2}$$

Where b = section width; h = section height

Flexure-Hybrid Reinforcement

Hybrid reinforcement refers to the use of steel fibers as a reinforcing material in conjunction with traditional rebar reinforcement. Design of hybrid-reinforced members is performed simply by summing the moment capacities obtained from the traditional reinforcement bars and fiber reinforcement, as shown in equation 3. This type of design allows the tensile load to be carried by the hybrid action of the reinforcing rebar and fibers. The moment capacity then becomes a function of the rebar and fibers working together.

$$M_{n-HFRC} = M_{n-RC} + M_{n-FRC} \quad (3)$$

An expression developed by Campione and Letizia Mangiavillano (2008) takes into account the residual strength of SFRC and depth of the tensile zone, as shown as equation 4.

$$M_n = [\rho f_y(1 - 0.5\frac{0.80c}{d} + f_r(\frac{h-e}{d})(\frac{h}{d} - \frac{h-e}{2d} - 0.5\frac{0.80c}{d}]b_w d^2 \quad (4)$$

Where $e = \frac{\frac{f_{ctf}}{E_{ct}} + \varepsilon_{o85}}{\varepsilon_{o85}}$; ρ = reinforcement ratio of longitudinal bars; f_y = yielding stress; c = cover; d = depth of section; h – e = depth of the tensile zone; b_w = section base

Shear Design

Many researchers have proposed expressions for predicting the ultimate shear capacity of SFRC beams without stirrups, i.e., Lee, Han et al. (2017); Kwak et al. (2002); and Yakoub (2011). Recently Torres and Lantsoght (2019) performed a comparison of available proposed equations for calculating the shear capacity of SFRC. From this comparison it was observed that the equations proposed by Kwak et al. (2002) predict the ultimate shear capacity with the greatest accuracy with an average tested/predicted value of 1.209, standard deviation of 0.421, and coefficient of variation of 34.8 (Torres and Lantsoght 2019). Equation 5 is the expression for predicting the ultimate shear capacity and the predicted inclined cracking load, f_{sp} , both proposed by Kwak et al. (2002).

$$V_u = [3.7ef_{sp}^{\frac{2}{3}}\left(\rho\frac{d}{a}\right)^{\frac{1}{3}} + 0.8v_b]b_w d \quad (5)$$

Where e = 1 when $\frac{a}{d} > 3.4$; $e = 3.4\frac{a}{d}$ when $\frac{a}{d} \leq 3.4$; with $f_{sp} = \frac{f_{cuf}}{20-\sqrt{F}} + 0.7 + \sqrt{F}$

MECHANICAL PROPERTIES

The performance of a fiber-reinforced composite material is governed by the fiber tensile strength, elastic modulus, ultimate strain, chemical compatibility with the mixture, fiber dimensions, and bond properties (Dopko 2018). Since the development of FRC, numerous studies have been conducted on how these factors affect the performance of FRC. Within this literature review, various studies are referenced to develop an understanding of the effects of fiber reinforcement on the mechanical properties of concrete. Table 1 summarizes the referenced research papers, fiber types studied, and overall focus of each paper.

Effects of Fiber Reinforcement on Concrete Properties

Fresh Properties

Addition of fibers to the concrete matrix has been shown to have detrimental effects on fresh concrete properties. These negative effects include decreased workability and increased unit weight. The effect of fibers on air content is unclear due to limited studies.

The addition of steel fibers into concrete mixtures lowers the slump, and, thus, the workability of the mixture. The workability of the mixture is reduced due to surface area of fibers diminishing the cement paste available for the free movement of aggregates and fibers (Deluce and Vecchio 2013). Acikgenc et al. (2013) found that the workability of FRC is linearly related to the fiber aspect ratio and volume. As the fiber aspect ratio or volume increased, the slump decreased (Acikgenc et al. 2013). Once the fiber volume content reached 1.5 percent, the slump was rendered zero and considered a poorly workable mixture.

Table 1. Summary of fiber-reinforced concrete studies referenced.

Author(s) (year)	Fiber Type(s)	Research Scope
Abdallah (2017)	Steel	Effects of hooked-end anchorages on bond–slip characteristics
Acikgenc et al. (2013)	Steel	Effects of fiber length and diameter on fresh and hardened properties
Al-Ameeri (2013)	Steel	Mechanical properties of self-compacting SFRC
Alavi Nia et al. (2012)	Steel, polypropylene	Impact resistance of FRC
Amirkhanian and Roesler (2019)	Steel, synthetic	Overview of FRC bridge decks
Balaguru and Ramakrishnan (1988)	Steel	Properties of FRC: workability, behavior under long-term loading, and air-void characteristics
Banthia and Sappakittipakorn (2007)	Steel	Toughness enhancement through fiber hybridization
Baun (1992)	Steel	SFRC bridge deck overlays – Ohio DOT
Bhutta et al. (2018)	Steel, polypropylene	Influence of inclination angle (0° and 45°) on the interfacial bond–slip behavior of macro fibers
Bordelon (2007)	Steel, synthetic	Fracture behavior of concrete materials for rigid pavement systems
Choi et al. (2007)	Steel	Shear strength of SFRC beams without stirrups
Deluce and Vecchio (2013)	Steel	Cracking behavior of SFRC containing conventional steel reinforcement
Dopko (2018)	Synthetic, carbon	Tailoring composite properties with discrete fibers
Guerini et al. (2018)	Steel, synthetic	Influence of fibers on slump, air content, and hardened properties
Guler et al. (2019)	Steel, synthetic, hybrid	Strength prediction models
Lee, Han et al. (2017)	Steel	Shear capacity of SFRC beams
Lee et al. (2018)	Steel	Effect of steel fibers on fracture parameters
Lee et al. (2019)	Steel	Effect of hooked-end steel fiber geometry and volume fraction on flexural behavior of bridge decks
Naaman (2003)	Steel	Technical background on development and design of steel fibers for use in composites
Natajara et al. (1999)	Steel	Statistical variations in impact resistance from drop-weight tests of SFRC

Table 1. (Continued).

Song and Hwang (2004)	Steel	Mechanical properties of SFRC
Soulioti et al. (2011)	Steel	Effects of fiber geometry and volume fraction on flexural behavior of SFRC
Tate (2019)	Steel	Use of rubber aggregates and recycled steel fiber for impact resistant concrete
Torres and Lantsoght (2019)	Steel	Influence of fiber content on shear capacity of SFRC beams
Wafa and Ashour (1992)	Steel	Influence of fiber contents on compressive strength, modulus of rupture, toughness, and splitting tensile strength
Yazıcı et al. (2007)	Steel	Influence of aspect ratio and volume fraction on mechanical properties
Yoo et al. (2017)	Steel	Effects of fiber shape, aspect ratio, and volume fraction on flexural behavior of ultra-high performance fiber-reinforced concrete

Unit weight is increased with the inclusion of steel fibers, as the steel fibers possess a density that is much higher than any of the other materials commonly used within the concrete matrix (Dopko 2018). Steel fibers are the heaviest of the fibers commonly used within concrete.

The effect the inclusion of steel fibers has on the air content of concrete is unclear due to limited studies reporting air content results. Balaguru and Ramakrishnan (1988) found that the addition of steel fibers decreased the air content by a small fraction, with the specific surface area of air bubbles being smaller than that of normal concrete. However, in a recent study comparing steel and macrosynthetic fibers on concrete properties, Guerini et al. (2018) found that steel fibers cause a marginally small increase in air content without having any noticeable effect on the compressive strength. Lastly, Al-Ameeri (2013) noted an increase in entrapped air with the inclusion of steel fibers in self-consolidating concrete, stating that the increased air content may have lowered the compressive strength slightly, but the effect was negligible.

Compressive Strength

Researchers have attempted to construct analytical models to predict the compressive strength behavior of SFRC (Song and Hwang 2004, Dopko 2018). These studies have concluded that the addition of steel fibers increases the compressive strength up to a certain percentage based on the fiber geometry. Song and Hwang (2004) found that the compressive strength of high-strength concrete (HSC) was improved with the addition of steel fibers up to 1.50 percent, dropping slightly at 2.00 percent. Despite the drop in compressive strength, a 2.00 percent fiber volume yielded an increase in compressive strength of 12.90 percent in comparison to the control. Equation 6, the prediction equation, was able to accurately predict the compressive strength of the SFRC with an error less than 1.00 percent.

$$f'_{cf}\,(\text{MPA}) = 85\,(\text{MPa}) + 15.12V_f - 4.71V_f^{\,2} \tag{6}$$

Where f'_{cf} = compressive strength; V_f = fiber volume

In another study, which observed the effect steel fibers have on self-consolidating concrete (SCC), Al-Ameeri (2013) found that steel fibers increased the compressive strength by 10.55 and 29.45 percent for 0.50 and 0.75 percent fiber content by total volume, respectively. The compressive strength lowered for fiber volumes greater than 0.75 percent, while still being 20.00 percent higher than the control mixture (Al-Ameeri 2013). The increase in compressive strength was attributed to the steel fibers' ability to enhance crack controlling by decreasing the amount of crack propagations. Ultimately, a more ductile failure mode was experienced when compared to traditional concrete. As the concrete begins to crack and break apart during the compressive test, fibers bridge the crack formation and hold the specimen together, resulting in a more ductile failure.

Lastly, Guler et al. (2019) analyzed many proposed strength-prediction equations, showing that each one predicted that compressive strength increased with the addition of steel fibers, and increased with increasing fiber volume fraction or reinforcement index. Guler's study found that the expressions proposed by Abadel et al. (2016), Guler et al. (2019), and Padmarajaiah (1992) predicted the compressive strength of the SFRC mixtures within 4.00, 1.00, and 2.00 percent of the observed value, respectively. However, other researchers have found that the addition of hooked-end fibers does not have an effect on the concrete's compressive strength. Lee et al. (2019) studied the effects of the aforementioned 3D, 4D, and 5D fiber end anchorages and volume fractions on bridge deck concrete. Their study tested fiber volume fractions of 0.37, 0.60, and 1.00 percent with each anchorage geometry. Results indicated a negligible effect on the compressive strength. Lee et al. (2019) concluded that the fibers lead to both positive and negative effects on the compressive strength, resulting in no significant influence.

Flexural Strength

The modulus of rupture is a measurement of the load at which a beam fails by flexure, or the ultimate bending strength at which rupture occurs. MOR is an incredibly important property for concrete as it indicates the bending capabilities of concrete before cracking. The MOR concept is based on the elastic beam theory, in which the maximum normal stress in the beam is calculated from the ultimate bending moment, M_u, with the assumption that the beam will behave elastically. This is calculated by equation 7, in which f_r is the MOR, b is the beam width, and d is the beam depth.

$$f_r = \frac{6M_u}{bd^2} \tag{7}$$

Song and Hwang (2004) reported that for mixtures with 0.50, 1.00, 1.50, and 2.00 percent steel fibers by volume, the MOR was increased by 28.10, 57.80, 92.20, and 126.60 percent, respectively, compared to the control mixture. Song and Hwang (2004) measured the MOR of their high-strength concrete mixture to be 928 psi (6.4 MPa), which equates to 0.69 $\sqrt{f'_c}$, in which f'_c is equal to 12,328 psi (85.0 MPa). These measurements were compared to the ACI 318-01 MOR equation of 0.63 $\sqrt{f'_c}$ for HSC in MPa, which is slightly lower than the value measured by Song and Hwang. Yazıcı et al. (2007) examined the effect that aspect ratio and volume fractions of steel fibers have on mechanical properties, and reported that SFRC had a 3.00 to 80.00 percent increase in flexural strength when compared to the control mixture, depending on the fiber geometry. In a study conducted by Guler et al. (2019), the highest increase of flexural strength for SFRC was 53.70 percent in comparison to the control for a 0.75 percent fiber by volume mixture. From this information it is concluded that the addition of steel fibers to the concrete matrix will increase the flexural capacity of the concrete.

The study conducted by Guler et al. (2019) cited an increase in flexural strength with the addition of steel fibers as reported by a variety of researchers. Guler's study compared various proposed flexural strength prediction expressions, reporting that the expressions proposed by Abadel et al. (2016), Padmarajaiah (1992), and Guler accurately predicted the flexural strength of SFRC mixtures within 11.00, 3.00, and 19.00 percent, respectively, of the observed values.

Shear Strength

The addition of steel fibers to concrete increases the shear strength by transferring tensile stresses across crack surfaces, reducing the intensity of diagonal tensile cracking, and increasing the effective stiffness after cracking occurs (Choi et al. 2007). Kwak et al. (2002) studied the

influence of fiber volume fraction and *a/d* ratio (where *a* is the shear span and *d* is the effective depth) on strength and ductility of FRC beams without stirrups. They reported that the addition of fibers increased the ultimate shear strength by 122.00 to 180.00 percent in comparison to beams without fibers (Kwak et al. 2002). From their study, it was indicated that the failure mode of SFRC beams without stirrups shifted from a shear failure to a flexural failure with a 0.75 percent fiber volume percentage. Similar results were found by Marar et al. (2016), who investigated the influence of fiber volume and aspect ratio on shear strength, reporting a 111.00 to 148.00 percent increase in shear strength with the addition of fibers.

Torres and Lantsoght (2019) investigated SFRC beams of various fiber volume percentages with no stirrups, reporting that a steel fiber volume percentage of 1.20 percent could be used to replace ACI 318-14 minimum stirrup requirements. Comparable results were reported by Choi et al. (2007), suggesting that a 0.75 percent fiber volume percentage could be used to replace ACI 318-14 minimum stirrup requirements in SFRC beams.

Toughness

Toughness is considered the amount of energy absorbed during loading of a concrete member and is determined by calculating the area under a load–deflection curve. It is one of the most important characteristics of FRC. For a typical reinforced concrete beam, the load–deflection curve has a steep increase until the initial cracking of the concrete occurs and the tensile steel begins to hold the load until rupture, at which ultimate failure occurs. However, with FRC, loading continues past the failure of tensile steel as fibers work to bridge cracks and effectively redistribute the load as deflection continues to increase. Within the study conducted by Acikgenc et al. (2013) it was concluded that the aspect ratio has the greatest effect on the toughness

enhancement of SFRC. Further, mixtures containing fibers with the largest aspect ratio resulted in the highest toughness.

Song and Hwang (2004) observed similar results by developing toughness indexes to compare the increase in toughness. The toughness indexes were calculated by dividing the measured flexural toughness at a specified deflection by the first crack deflection of the nonfiber-reinforced concrete. Control mixtures possessed a toughness index of 1.0, while fiber volume fractions of 0.50, 1.00, 1.50, and 2.00 percent possessed indexes of 3.0, 3.3, 4.2, and 6.5, respectively. Similar results were reported by Naaman (2003). Figure 4 compares the stress elongation behavior of conventional FRC to high-performance FRC (HPFRC) subjected to tensile loading (Naaman 2003).

Soulioti et al. (2011) examined the effects that hooked-end fibers and waved fibers have on flexural behavior of concrete, concluding that hooked-end fibers have a greater increase in the flexural capacity than waved fibers. Based on these findings, it is concluded that the addition of fiber reinforcement to concrete mixtures increases the member toughness, and prolongs member life during periods of high deflection.

Energy Absorption and Impact Resistance

Concrete brittleness is increased as compressive strength increases. The use of fibers in high-strength concrete mixtures for impact resistance has been performed by construction, nuclear, and military applications for several years to combat this increase in brittleness. The impact resistance of concrete is the ability of the material to withstand a high-velocity projectile impact, which may occur from wind gusts, earthquakes, vehicle impacts, and others. As concluded in the previous section, researchers have found that the addition of steel fibers greatly increases the

energy absorption capabilities, or toughness, of concrete. However, there is little research published on the impact resistance of SFRC due to the complexity of quantitatively investigating dynamic events and measuring the SFRC response. Energy wave propagation occurs throughout the composite material during a dynamic impact, causing difficulty in measuring an accurate response.

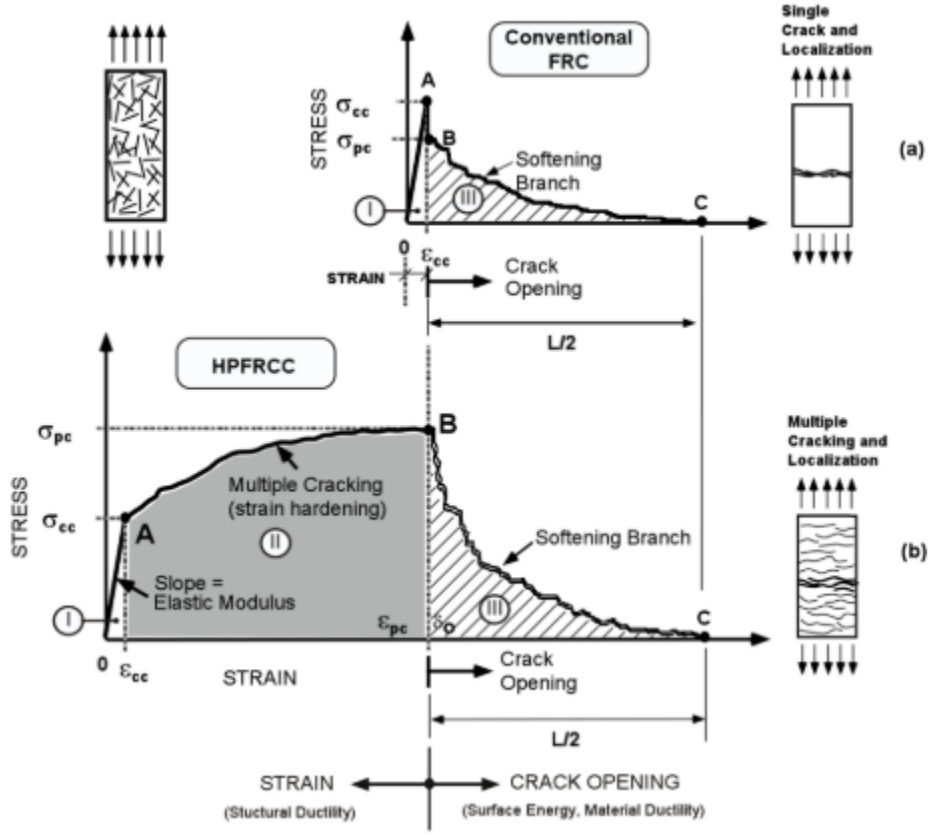

Figure 4. Graph. Typical stress elongation response of fiber-reinforced concrete (Naaman 2003).

One method of measuring impact resistance of concrete is by a drop-weight test proposed by the ACI 544.4R-18 *Guide to Design with Fiber-Reinforced Concrete* (ACI 2018). The concentrations and orientations of fibers within concrete, placement methods, flow of the fresh

concrete, and the degree of compaction all influence the impact resistance of the composite (Nataraja et al. 1999). Nataraja et al. (1999) studied the statistical variations of the drop-weight impact test, concluding that the observed coefficients of variation for SFRC are 57.00 percent for first-crack resistance and 46.00 percent for ultimate resistance. Due to the high variance in the impact test results, a goodness-of-fit test indicated poor fitness of impact-resistance test results to a normal distribution at a 95.00 percent level of confidence for both SFRC and plain concrete (Nataraja et al. 1999). Despite the low statistical confidence, it was evident that the steel fibers contributed to the impact resistance of the concrete with more observed impacts before failure. Similar results were found in a study by Alavi Nia et al. (2012) in which concrete mixtures included steel and polypropylene fibers. Hooked-end steel fibers with an aspect ratio of 80 were used at 0.50 and 1.00 percent volume fractions and produced better performance than polypropylene due to greater length, tensile strength, and advanced end anchorage (Alavi Nia et al. 2012).

BARRIER WALL DESIGN

Concrete median barriers are installed to decrease the overall severity of traffic accidents by producing higher vehicle decelerations and to prevent any lateral deflection. However, due to these rigid systems having a higher stiffness than other barrier systems (e.g., guardrails and cable barriers), impacts with CMBs have a tendency to be more severe (Zou et al. 2014). Under typical crash conditions, traffic barriers operate to prevent vehicles from entering opposite lanes and causing traffic accidents, as shown in figure 5.

Figure 5. Photos. Typical single-unit truck impact response with single-slope barrier (Sheikh et al. 2012).

Although CMBs cannot guarantee safe redirecting of the vehicle post-impact, barriers function to decrease the potential for excessive vehicular deceleration or excessive vehicle redirection by allowing the vehicle to penetrate the safety barrier or stopping the vehicle in a controlled manner. How a vehicle responds to the impact from the CMBs is dependent on multiple factors: impact characteristics, geometry of barrier, reinforcement within barrier, and location of the walls.

Wall Geometry

Testing procedures, whether full-scale testing or laboratory, determine the concrete barrier dimensions. Common concrete barriers include (1) the safety shape, further classified as the New Jersey and F-shape; and (2) the single slope. Another variable that determines the design of the barrier is the angle of the impact, whether it is a shallow or higher angle hit. The design of a barrier wall is only one property that determines its overall performance. The total safety measures and the performance of the barrier walls depend on drivers' operation of their vehicles. The implementation of a cast-in-place barrier wall design is dependent on location and traffic conditions. Table 2 summarizes concrete barrier types, dimensions, and reinforcement used in testing conditions. As shown, the majority of the literature reviewed focused mainly on New Jersey and F-shape barriers.

Table 2. Summary concrete barrier dimensions.

Author(s) (year)	Barrier Shape	Top Width (in.)	Base Width (in.)	Total Height (in.)	No. Bars
Hirsch et al. (1972)	New Jersey	8.0	27.0	32.0	8 – #5
Itoh et al. (2007)	F-Shape	9.8	26.8	43.3	—
Beason et al. (1989)	Single Slope	8.0	24.0	42.0	—
Bligh et al. (2004)	Vertical[1]	9.5	9.5	27.0	—
Atahan and Sevim (2008)	New Jersey	9.8	17.7	39.4	—
McDevitt (2000)	F-Shape + New Jersey	12.0	32.3	42.0	—
	Single Slope	8.0	24.0	42.0	—
Bligh et al. (2004)	F-Shape	9.3	23.7	32.0	8 – #5 (#5 Stirrups)
Jewell et al. (1997)	Single-Slope	6.0	24.0	56.0	11 – #5
	Single Slope	6.0	27.2	56.0	11 – #5
	Single Slope[1]	—	—	32.0	—
Elchalakani (2015)	New Jersey	13.8	28.8	34.7	12 – #5
Polivka et al. (2006a)	New Jersey	6.0	15.0	32.0	8 – #4 (#5 Stirrups)
Mak et al. (1994)	Single Slope[1]	9.5	15.6	32.0	8 – #4 (#5 Stirrups)
Williams et al. (2011)	Single Slope[1]	7.5	13.0	36.0	—
Rowhani et al. (1993)	New Jersey	6.0	24.0	32.0	4 – #4 (#5 Stirrups)
Rosenbaugh et al. (2007)	Vertical[1]	20.0	24.1	42.0	11 – #4 (#5 Stirrups)
Sheikh et al. (2008)	Single Slope	—	—	42.0	—
Sheikh et al. (2012)	Single Slope	—	—	39.0	—
	Single Slope	—	—	38.0	—
	Single Slope	—	—	37.0	—
	Single Slope	—	—	36.0	—
	New Jersey	—	—	32.0	—
Hammonds and Troutbeck (2012)	Single Slope	7.5	13.0	36.0	0.4in bars #3 stirrups
	F-Shape	—	25.0	32.0	—
Namy et al. (2015)	—[1]	8.9	16.1	34.6	8 – #5 (#5 Stirrups)
	—[1]	7.5	14.8	34.6	3 – #5 (#5 Stirrups)
El-Salakawy et al. (2001)	—[1]	8.9	16.1	34.6	8 – #5 (#5 Stirrups)
	—[1]	8.9	17.1	45.0	14 – #5 (#5 Stirrups)
Bullard et al. (2010)	New Jersey[1]	6.0	15.0	32.0	8 – #4 (#5 Stirrups)
Ulker et al. (2008)	F-Shape	6.0	24.0	32.0	—

Table 2. (Continued).

Lee, Zi et al. (2017)	—	6.0	23.0	50.0	—
Bielenberg et al. (2014)	F-Shape	8.0	22.5	32.0	3 – #5, 2 - #4 (#4 Stirrups)
Dobrovolny et al. (2015)	F-Shape	9.5	24.0	32.0	8 – #4 (#4 Stirrups)
Stolle et al. (2014)	Single Slope	12.5	24.0	36.0	—
	Single Slope	10.5	24.0	42.0	—
	Single Slope	6.0	24.0	56.0	—
Sheikh et al. (2009)	Single Slope	8.0	24.0	42.0	10 – #5 (#4 Stirrups)
Sheikh et al. (2008)	F-Shape	9.5	24.0	32.0	8 – #5 (#5 Stirrups)
Mongiardini et al. (2013)	New Jersey[1]	9.0	18.0	32.0	#4 and #6
	Vertical[1]	9.0	16.0	32.0	10 – #4 through #6
Wielbelhaus et al. (2010)	F-Shape	8.1	22.5	32.0	Varies
	Single Slope	8.0	21.5	42.0	Varies

Note: [1] Barriers tested with slabs; — = No data

Single Slope

Although the majority of CMBs in North America are considered a New Jersey barrier, many states have been transitioning to a single-sloped barrier design in an effort to reduce costs. As a response to the constant maintenance of roadways, researchers at the Texas State Department of Highways and Public Transportation in the 1980s developed a single-slope barrier wall that would not be affected by the resurfacing of the pavement adjacent to the longitudinal barrier. Due to the constant slope of the CMB, the performance of the single-slope barrier would not be affected by the thickness of the overlay—unlike the safety shape barriers—allowing for significant savings in maintenance (Beason et al. 1989).

Variations to the face design of the single-slope barrier are: (1) a constant slope and (2) a vertical slope, as shown in Figure 6 (a) and (b), respectively. Generic dimensions of the single-slope barrier include a base width of 24.0 inches (610 mm), total height of 42.0 inches (1,067 mm), and a top width that tends to range between 8.0 and 10.5 inches (203 and 267 mm), depending on

installation location and the slope design. The angle, with respect to the vertical axis, can range between 9.1 and 10.8 degrees, with each design affecting the vehicle's stability post-impact, whereas the vertical CMB design is built to a height of 42.0 inches (1,067 mm) to incorporate an integral glare screen (Federal Highway Administration 2013).

Typically used as a side barrier in bridges, the single-slope design can be used as median barriers or barriers directly in front of rigid objects that are near the traveled way. Vertical CMBs have been known to offer the best post-impact vehicle trajectory and structural adequacy. The vertical design minimizes vehicle roll, pitch, and yaw angles, whereas a sloped front face barrier design minimizes lift forces during impact, providing stability to the vehicle. Overall, the single-slope CMBs are the largest in height, providing a built-in glare screen, as well as prohibiting a vehicle from climbing over the barrier (Namy 2015).

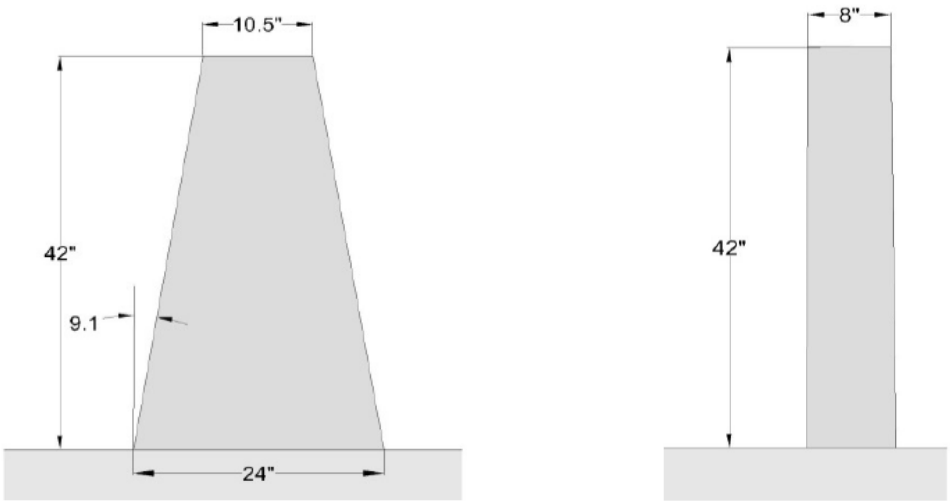

Figure 6. Images. Single-slope barrier shape profile: (a) constant slope, (b) vertical slope (Federal Highway Administration 2013).

Testing the performance of single-slope CMBs has been completed in a variety of methods: as a full-scale crash test as a median barrier, as crash tests as a bridge rail, and through computer simulations. Beason et al. (1989) at the Texas State Department of Highways and Public Transportation developed the single-slope CMB shape to be used interchangeably with the New Jersey barrier and in an effort to successfully redirect and stabilize vehicles. The CMB designed was approximately 30 percent taller than the New Jersey safety barrier, as shown in figure 7. At a height of 42.0 inches (1,067 mm) and a base width of 24.0 inches (610 mm) producing a 10.8-degree slope, the barrier was designed to have a center of gravity at a distance of 18.0 inches (457 mm) from the base, similar to that of typical vehicles. Sheikh et al. (2009) studied single-slope barriers embedded 10.0 inches (254 mm) into the ground located on a 1.5H:1V slope. The section of the barrier exposed during the full-scale crash testing tapered from a 24.0 inch (610 mm) base width to an 8.0 inch (203 mm) top width. In conclusion, the 42.0 inch (1,067 mm) tall barrier performed acceptably according to the requirements of *MASH* and was preferred over other barrier types.

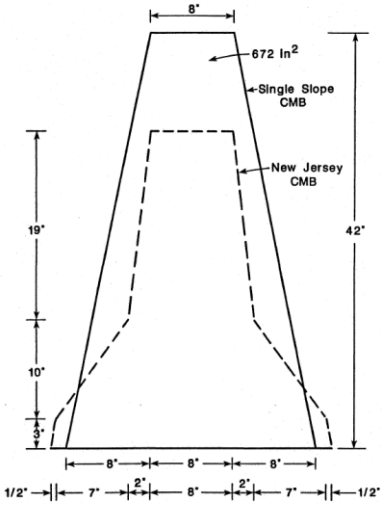

Figure 7. Image. Single-slope and New Jersey CMB comparison (Beason et al. 1989).

The majority of single-slope barriers are implemented as bridge rails and tested with a moment slab. Mak et al. (1994) developed a single-slope concrete bridge rail test installation to evaluate the impact performance in accordance to the guidelines of *NCHRP Report 350* and the 1989 *AASHTO Guide Specifications*. A 32.0 inch (813 mm) tall single-slope barrier with a slope of 10.8 degrees, a base width of 15.6 inches (396 mm), and a top width of 9.5 inches (241 mm) underwent three full-scale crash tests. Mak et al. (1994) observed that higher angles of impact produced a greater possibility of vehicular instability due to much higher roll angle. Higher angles of impact also showed a slightly higher climb on the barrier during impact. Jewell et al. (1997) examined vehicular crash tests on slip-formed Texas profile and Type 60G concrete barriers, with integral glare screens, complying with the guidelines of *NCHRP Report 350*. The difference between the 56.0 inch (1,422 mm) tall barriers is that the bottom width of the Texas barrier is 3.0 inches (76 mm) wider than the 24.0 inch (610 mm) base Type 60G barrier, producing a lower slope. The study concluded that the 56.0 inch (1,422 mm) tall barriers could be successfully slip-formed over pavement. Williams et al. (2011) evaluated the performance of a single-slope traffic rail on a pan-formed deck during a full-scale crash test. The single-slope traffic rail was 36.0 inches (914 mm) tall with a constant slope of 11.0 degrees that was struck by a pickup truck and able to contain and redirect the vehicle without allowing the vehicle to penetrate, underride, or override the barrier.

A recent advancement in analyzing barrier walls is through computer simulation modeling. Stolle et al. (2014) utilizing simulation models to conduct a zone of intrusion analysis on 9.1-degree single-slope CMBs with differing total heights. The results from the simulations showed that shorter barriers permitted the impact vehicles to experience larger roll angles. Sheikh et al. (2012) performed a finite element analysis to study *MASH* TL-4 impact conditions

on rigid single-slope barriers of various heights, from a 42.0 inch (1,067 mm) height to 36.0 inch (914 mm) height. The 42.0 inch (1,067 mm) tall barrier resulted in the greatest vehicular stability and the ability to withstand larger lateral impact loads. A full-scale crash test of a 36.0 inch (914 mm) tall barrier that had a width of 13.0 inches (330 mm) at its base and 7.5 inches (191 mm) at the top was conducted to study the performance of the barrier under *MASH* Test 4-21 impact conditions. The results exposed the outdated *NCHRP Report 350* TL-4 criteria on minimum rail height and design impact load through an increased impact severity of 56 percent produced by *MASH* Test 4-21.

Rosenbenbaugh et al. (2007) developed a vertical faced CMB to undergo TL-5 conditions. The 42.0 inch (1,067 mm) tall CMB was impacted by a tractor-trailer weighing over 79.0 kips (351.4 kN) and traveling at a speed of 52.7 mph (85.0 km/h). The barrier was able to provide satisfactory vehicle stability while exhibiting minimal damage to itself considering *NCHRP Report 350* performance criteria. Bligh et al. (2004) conducted a full-scale static test on a vertical concrete barrier located on top of a mechanically stabilized earth wall. The barrier was 27.0 inches (686 mm) tall with a total width of 9.5 inches (241 mm), and was attached to a 54.0 inch (1,372 mm) moment slab. A static test was performed to verify the amount of force required to initiate movement in the barrier system. Two dynamic tests were performed to determine the maximum force at failure that the barrier system could endure. Overturning of the vertical barriers was presented in the results before any sliding occurred. Bligh et al. (2004) later went on to analyze different heights of mechanically stabilized earth (MSE) walls and different barrier designs showing minimum damage and displacement of the barrier system and MSE wall.

Materials

Concrete median barriers are constructed using normal weight portland-cement concrete. GDOT requires the compressive strength of the concrete mixture to meet Class AA concrete of 3,500 psi (24.1 MPa) for new installments of CMBs, while preexisting concrete barriers have a compressive strength of 3,000 psi (20.7 MPa) for Class A concrete. Table 3 summarizes the concrete mixture specification for GDOT. As for reinforcement, the steel must be of Grade 60. However, the reinforcement design will differ between barrier wall designs and the constructor of the CMB. As shown in table 2, typical rebar size used for longitudinal reinforcement are No. 4 and No. 5 rebar, diameters of 0.5 and 0.6 inch (13 and 16 mm), respectively. The average rebar used for shear reinforcement is the No. 5 rebar. Spacing of the stirrups varies between CMB designs.

Table 3. GDOT concrete mixture specification (GDOT 2006).

Class of Concrete	Coarse Aggregate Size No.	Min. Cement Factor (lb/yd^3)	Max. Water/ Cement Ratio	Slump Acceptance Limits		Entrain Air Acceptance Limits (%)		Min. Compressive Strength at 28 days (psi)
				Lower	Upper	Lower	Upper	
AA	56, 57, 67	635	0.445	2	4	3.5	7.0	3,500
A	56, 57, 67	611	0.490	2	4	2.5	6.0	3,000

Notes: Conversion: 1 lb./yd^3 = 0.59 kg/m^3; 1 psi = 6.9 kPa

Due to the rigidity of CMBs, the barriers can withstand large deceleration forces from vehicles during high-impact collisions. These forces can cause severe damages to the vehicles, injury to occupants, damages to the barriers, and possibly an overturned vehicle. Introducing tire chips within CMBs was based on the idea to increase the absorbency of the concrete, resulting in less severe collisions. Only a few studies have evaluated rubberized concrete as a possible substitute for the use of rigid CMBs.

Elchalakani (2015) analyzed high-strength sustainable roadside barriers by replacing fine aggregates with recycled crumb rubber. To achieve high strength, Elchalakani added silica fume to the mixture and observed a reduction in 28-day shrinkage by 50 percent and an increase in hardened concrete properties. The rubberized concrete outperformed the plain concrete specimens in the cube drop tests, indicating a possible good crash performance in rubberized concrete barriers. Atahan and Sevim (2008) conducted a study focused on the use of shredded waste tire chips in concrete barrier walls by conducting static and dynamic tests. The compressive strength of six concrete mixtures with tire chip percentages, increasing from 0 to 100 percent, decreased with the addition of rubber tire chips. Dynamic tests consisted of impacting rubberized CMBs to measure the energy absorption and acceleration with an increase of rubber tire chips within a concrete mixture. Compared to the control mixture, which had 0.00 percent tire chips, the energy absorbed after the impact increased as the acceleration of the vehicle decreased linearly with the increase of shredded tire chips (Atahan and Sevim 2008).

Further research has been conducted to develop more sustainable CMBs that can perform to the standards of *MASH* and *NCHRP Report 350*. Dhakal et al. (2013) developed a fly ash–based geopolymer CMB as an alternative to using portland cement. Fly ash is a byproduct of coal combustion with pozzolan-like properties, which when used within concrete can increase strength and durability. A finite element analysis, which was later validated through full-scale testing, was conducted on a New Jersey barrier for which material properties were determined through laboratory testing. The barrier performed with compliance equivalent to a TL-2 barrier.

As a possible resolution to expensive bridge repairs due to early-age cracking that increases the risk of corrosion, Namy et al. (2015) performed experimental testing and numerical modeling on high-performance steel fiber–reinforced concrete bridge barriers. Fabricated precast barriers

allow for early-age barrier movement, reducing the potential for cracking. While the addition of steel fibers is often used to limit the size of the crack openings, a 10.00 percent reduction in the barrier cross-sectional surface area, as well as a 60.00 percent reduction in steel reinforcement was observed due to the addition of steel fibers. The barriers tested under static loading conditions all exceeded the static design criteria specified by bridge design codes of the Canadian Standards Association (CSA).

BARRIER WALL CODES

The following section reviews the prominent standards and codes used in vehicular tests to evaluate the impact performance of permanent and temporary CMBs. Longitudinal barriers undergo full-scale testing of six crash-test levels for evaluating multiple impact conditions, outlined in table 4, following the recommended guidelines of *AASHTO MASH 2016* and *NCHRP Report 350*. Vehicle type, test speed, and crash angle are the main components tested within each test level. Primary safety performance factors, such as structural adequacy, occupant risk, and post-impact behavior of the vehicle, are examined separately (see table 5).

NCHRP Report 350

The NCHRP, conducted by the Transportation Research Board, developed a set of guidelines for full-scale vehicle crash testing for highway safety features based on the existing procedures published in Highway Research Correlation Services Circular 482 (Highway Research Board Committee on Guardrails and Guide Posts 1962). The procedures included details on vehicle mass, impact speed, and approach angle, but left a number of questions unaddressed. *NCHRP Report 350* was the first set of guidelines to include test levels to create uniformity in crash testing procedures.

Table 4. Summary test matrix for longitudinal barriers (AASHTO MASH 2016 and Ross et al. 1993).

Codes	Impact Conditions						
NCHRP Report 350	Test Vehicle (kg)	700C	820C	2000P	8000S	36000V	36000T
	Crash Angle, θ (deg)	20	20	25	15	15	15
	Test Level	Test Speed (mph)					
	1	31	31	31	—	—	—
	2	44	44	44	—	—	—
	3	62	62	62	—	—	—
	4	62	62	62	50	—	—
	5	62	62	62	—	50	—
	6	62	62	62	—	—	50
AASHTO MASH 2016	Test Vehicle (kg)	1100C	2270P	10000S	36000V	36000T	
	Crash Angle, θ (deg)	25	25	15	15	15	
	Test Level	Test Speed (mph)					
	1	31	31	—	—	—	
	2	44	44	—	—	—	
	3	62	62	—	—	—	
	4	62	62	56	—	—	
	5	62	62	—	50	—	
	6	62	62	—	—	50	

Note: — = No data

NCHRP Report 350 has separate test designations for the type of barrier section, with sections classified as either a length of need (LON) or a transition section. A LON of a longitudinal barrier wall or guardrail is the sum of the length needed upstream to protect the area of concern, the length parallel to the area of concern, and the length of downstream barrier, whereas the transition barrier section occurs when transitioning to another barrier wall design (Ross et al. 1993). TL-4 through TL-6 are valid for only longitudinal barrier evaluations, specifically cast-in-place barriers. Precast, or temporary, concrete barriers are categorized with TL-1 through TL-3.

Table 5. Summary safety testing guidelines for CMBs (AASHTO MASH 2016 and and Ross et al. 1993).

<table>
<tr><th>Evaluation Factors</th><th colspan="2">Evaluation Criteria[2]</th><th>Applicable Testing Standards</th></tr>
<tr><td>Structural Adequacy</td><td>A.</td><td>Test article should contain and redirect the vehicle; the vehicle should not penetrate, underride, or override the installation although controlled lateral deflection of the test article is acceptable.</td><td>NCHRP 350, MASH 2016</td></tr>
<tr><td rowspan="4">Occupant Risk</td><td>D.</td><td>Detached elements, fragments, or other debris from the test article should not penetrate or show potential for penetrating the occupant compartment, or present an undue hazard to other traffic, pedestrians, or personnel in a work zone. Deformations of, or intrusions into, the occupant compartment that could cause serious injuries should not be permitted.</td><td>NCHRP 350, MASH 2016</td></tr>
<tr><td>F.</td><td>The vehicle should remain upright during and after collision although moderate roll, pitching, and yawing are acceptable.</td><td>NCHRP 350, MASH 2016</td></tr>
<tr><td>G.</td><td>It is preferable, although not essential, that the vehicle remain upright during and after collision.</td><td></td></tr>
<tr><td>H.</td><td>Occupant impact velocities should satisfy the following:
<table><tr><th colspan="3">Occupant Impact Velocity Limits (m/s)</th></tr><tr><th>Component</th><th>Preferred</th><th>Maximum</th></tr><tr><td>Longitudinal and Lateral</td><td>9</td><td>12</td></tr><tr><td>Longitudinal</td><td>3</td><td>5</td></tr></table></td><td>NCHRP 350, MASH 2016</td></tr>
<tr><td>I.</td><td>Occupant ridedown accelerations should satisfy the following:
<table><tr><th colspan="3">Occupant Ridedown Acceleration Limits (g’s)</th></tr><tr><th>Component</th><th>Preferred</th><th>Maximum</th></tr><tr><td>Longitudinal and Lateral</td><td>15</td><td>20</td></tr></table></td><td>NCHRP 350, MASH 2016</td></tr>
<tr><td rowspan="3">Vehicle Trajectory</td><td>K.</td><td>After collision, it is preferable that the vehicle’s trajectory not intrude into adjacent traffic lanes.</td><td>NCHRP 350</td></tr>
<tr><td>L.</td><td>The occupant impact velocity in the longitudinal direction should not exceed 12 m/s and the occupant ridedown acceleration in the longitudinal direction should not exceed 20 g’s.</td><td>NCHRP 350</td></tr>
<tr><td>M.</td><td>The exit angle from the test article preferably should be less than 60.00 percent of test impact angle, measured at time of vehicle loss of contact with test device.</td><td>NCHRP 350</td></tr>
</table>

Thus, temporary barriers are designed for impact conditions of TL-1 through TL-3. TL-1 evaluates impact conditions of local roadways with low annual average daily traffic (AADT) and low speed zones. TL-2 barriers are qualified to be installed on local roadways and most work-

zone areas. Most longitudinal concrete barriers along high-speed highways are rated at TL-3. TL-4 through TL-6 encounter impact conditions that occur in heavy vehicle traffic and along tractor-trailer routes. Each test level corresponds to specific testing vehicles that have increased in size and weight due to modern styles of cars, noted in the *AASHTO MASH 2016* test matrix. A passenger car (C) and pickup truck (P) are analyzed in TL-1 through TL-3 at different testing speeds. Single-unit trucks (S), tractor van trailers (V), and tractor tank trailers (T) are used in testing TL-4 through TL-6, respectively.

AASHTO Manual for Assessing Safety Hardware

AASHTO recently updated, as of 2016, the *MASH* guidelines for full-scale crash testing permanent and temporary highway safety features such as CMBs and the recommended evaluation criteria. *MASH* was developed to consider the "worst practical conditions" and "state-of-the-possible" scenarios by selecting test parameters that specify the most critical conditions (*AASHTO MASH 2016*).

MASH utilizes a "worst practical conditions" philosophy by combining parameters such as the weight of a small test vehicle that represents approximately the second percentile with the impact speed and crash angle that represents approximately the 93rd percentile of real-world crashes to produce an extreme impact condition. If a CMB can withstand severe impact conditions such as the one described, then the CMB would be suitable for all impact conditions in between. In addition, cost effective guidelines are instated to ensure practical test parameters.

MASH (AASHTO 2016) maintained the six test levels, defined by the impact conditions and type of test vehicle that the *NCHRP Report 350* specified. CMBs designed and tested for one of the lower three levels would be used on urban streets. CMBs designed and tested for one of the

higher three levels would be used on freeways. TL-4 through TL-6 are designed and tested to perform in scenarios with heavy trucks. The CMBs designed based on *MASH* impact performance criteria will produce higher vehicle decelerations and prevent any lateral deflection.

Influence of Codes in Full-Scale Crash Testing

NCHRP Report 350 (Ross et al. 1993) has maintained its status as the recognized guidelines followed for vehicle crash testing. In 2009, the original *MASH* was developed, but was flawed due to inaccurate test levels. In 2016, an updated version of *MASH* was released to include an increase in the mass of the test vehicles, corresponding to the new model of vehicles being produced, and to correct the mistakes of the old version of *MASH*. Compared to *NCHRP Report 350* (Ross et al. 1993), *MASH* (AASHTO 2016) includes modifications made for the single-unit truck test for TL-4 and the impact conditions of the small vehicle. The impact severity of the TL-4 test increased, due to the change in specified vehicle weight from 17,600 lb (7,983 kg) to 22,000 lb (9,979 kg), and speed from 50.0 mph (80.0 km/h) to 56.0 mph (90.0 km/h). An error within the *NCHRP Report 350* caused the TL-3 test to have a higher impact energy than the TL-4 test. As for the small vehicle, the weight increased from 1,800 to 2,420 lb (816 to 1,098 kg) and the impact angle increased from 20.0 to 25.0 degrees.

Impact severity (IS) is determined by the vehicular mass (kg), impact speed (km/h), and impact angle (degree), as in equation 8.

$$IS = \frac{1}{2} M (V \sin \theta)^2 \text{ (kJ)} \quad (8)$$

The variables can be adjusted within reason to achieve the desired impact severity. However, impact severity is highly affected by the impact angle. Testing with a greater impact severity

than designed could possibly result in an unacceptable performance according to *NCHRP Report 350* and *AASHTO MASH 2016*.

When conducting full-scale testing, primary safety performance factors set forth by *MASH* (2009, 2016) and *NCHRP Reports 230* and *350* (1980, 1993), such as structural adequacy, occupant risk, and post-impact behavior of vehicle, are examined to determine potential safety risks due to the outcome of the vehicular crash into a CMB. *Structural adequacy* refers to the performance of the safety structure during impact, whether the vehicle is redirected, stopped in a controlled manner, or allowed to penetrate the safety barrier. *Occupant injury risk* during impact is largely determinant of the design of the occupant compartment within the vehicle. Occupant risk criteria in terms of full-scale testing refers to the potential of detached elements, fragments, or other debris from the test article penetrating the occupant compartment or presenting a potential hazard to other traffic. A third evaluation factor, *vehicle trajectory*, evaluates the potential of the vehicle's post-impact trajectory to cause a subsequent vehicular accident. A summary of the safety testing guidelines for CMBs for the *NCHRP Report 350* and *AASHTO MASH 2016* is listed in table 4.

Due to a general global acceptance of the *NCHRP Report 350* testing standards, some experimental research involving highway safety features is rated based on its test level definitions. The United States evaluates bridge rails, concrete barriers attached to a bridge deck or moment slab, and CMBs using the TL system, whereas, the Canadian Standards Association (CAN/CSA-S6) evaluates the safety performance of bridge rails based on performance levels (PLs) and CMBs on TLs. The Federal Highway Administration documented the equivalency between performance levels and test levels due to intermittent use of the two systems, shown in table 6.

Table 6. Performance level and test level equivalency (Alberta Infrastructure and Transportation Roadside Design Guide 2007).

Performance Level (PL)	Test Level (TL)
PL-1	TL-2
PL-2	TL-4
PL-3	TL-5

Performance levels were originally introduced within the AASHTO 1989 *Guide Specifications for Bridge Railings*. The 2000 edition of the *Canadian Highway Bridge Design Code* accepted the PL system and has since been updated for the 2006 edition (Alberta Infrastructure and Transportation *Roadside Design Guide* 2007). As mentioned previously, *NCHRP Report 350* was published in 1993 and established six crash test guidelines that replaced the PL system used in the United States (Ross et al. 1993).

EXPERIMENTAL TESTING

Designing and developing new CMBs is a complicated process that requires multiple testing measures, ultimately ending with a full-scale crash test, to validate a satisfactory impact performance. Prior to full-scale testing, other analytical assessments are conducted due to the high costs associated with full-scale testing. These initial testing techniques include principles of mechanics, static tests, dynamic tests, and computer simulation models.

Table 7 summarizes the field testing, laboratory testing, and model analysis conducted in the past on different concrete barrier shapes. As shown, the majority of the tests involved full-scale testing due to the lack of laboratory equipment that could simulate field tests. Recent years have seen an increase in computer modeling simulations; however, these tests still require validation through full-scale testing.

Table 7. Summary of barrier.

Author(s) (year)	Test Method	Barrier Shape	Test Level	Dynamic Testing			Static Testing		Occupant Ridedown	
				Initial Speed (mph)	Weight of Vehicle (lb)	Impact Angle (°)	Force at Failure (kip-force)	Avg. Dynamic Displacement (in.)	Avg. Longitudinal Deceleration (g's)	Avg. Transverse Deceleration (g's)
Hirsch et al., (1972)	Field	New Jersey	—	62.4	4,000	25.0	—	—	3.2	4.4
	Field	New Jersey	—	55.7	4,230	25.0	—	—	1.8	2.8
	Field	New Jersey	—	60.9	4,210	7.0	—	—	0.5	1.8
	Field	New Jersey	—	60.7	4,210	15.0	—	—	1.4	3.0
Itoh et al. (2007)	Field	F-shape	—	62.1	44,092	17.0	—	—	—	—
Beason et al. (1989)	Field	Single Slope	—	60.3	4,500	15.2	—	7.0	−2.5	−7.7
	Field	Single Slope	—	60.7	4,500	19.9	—	—	−2.3	−9.2
	Field	Single Slope	—	63.1	1,800	26.5	—	—	−4.2	−10.7
	Field	Single Slope	—	62.0	4,500	15.1		6.0	−3.2	−6.2
Bligh et al. (2004)	Lab	Vertical[1]	TL-3	—	—	90.0	9.0		—	—
	Lab	Vertical[1]	TL-3	13	5,000	90.0	42.5	3.8	—	—
	Lab	Vertical[1]	TL-3	18	5,000	90.0	54.1	5.9	—	—
Atahan and Sevim (2008)	Field	New Jersey	—	12.4	1,102	90.0	—	—	—	—
Bligh et al. (2004)	Field	F-Shape	TL-3	62.3	4,531	25.7	—	19.0	−3.7	10
Jewell et al. (1997)	Field	Single Slope	TL-3	57.7	1,863	19.5	—	—	−2.1	16.7
	Field	Single Slope	TL-3	60.7	4,409	25.2	—	—	−6.7	2.3
	Field	Single Slope	TL-3	57.0	1,906	19.8	—	—	−2.6	11.3
	Field	Single Slope	TL-3	44.4	4,409	53.0	—	—	—	—
	Field	Type 70[1]	TL-3	64.7	22,028	20.0	—	—	−2.9	−16
Polivka et al. (2006) (a)	Field	New Jersey	TL-3	60.8	2,579	26.1	—	—	5.49	8.08
Polivka et al. (2006) (b)	Field	New Jersey	TL-4	56.5	22,045	16.2	—	—	−22.39	−8.84
Mak et al. (1994)	Field	Single Slope	—	60.4	4,409	25.5	—	—	−6.1	−12.6
	Field	Single Slope	—	51.0	18,000	10.0	—	—	−1.3	−2.6
	Field	Single Slope	—	51.3	18,000	17.9	—	—	−2.7	−10.2
Williams et al. (2011)	Field	Single Slope	TL-3	63.8	5,036	24.8	—	—	−5.3	−11.7
Rowhani et al. (1993)	Field	New Jersey	—	55.3	5,400	20	—	0.39	—	—
	Field	New Jersey	—	56.2	4,500	25	—	0.21	—	—
Rosenbaugh et al. (2007)	Field	Vertical	TL-5	52.7	79,705	15.4	—	—	—	—
Sheikh et al. (2012)	Model	Single Slope	TL-4	56.0	22,050	15.0	—	—	—	—
	Model	New Jersey	TL-4	56.0	22,050	15.0	—	—	—	—
	Field	Single Slope	TL-4	57.2	22,150	16.1	—	—	13.7	9

Table 7. (Continued).

Hammonds and Troutbeck (2012)	Field	F-shape	TL-3	62.1	2,425	20.0	—	—	—	—
	Field	F-shape	TL-3	62.1	4,078	20.0	—	—	—	—
	Field	F-shape	TL-3	62.1	5,511	20.0	—	—	—	—
	Field	F-shape	TL-4	49.7	17,636	20.0	—	—	—	—
Grzebieta et al. 2002	Field	—	TL-3	50.0	—	45.0	—	3.9	—	—
	Field	—	TL-3	69.6	—	20.0	—	3.9	—	—
	Field	—	TL-3	68.4	—	20.0	—	3.9	—	—
Namy et al. (2015)	Lab	—[1]	TL-4	—	—	25.0	69.7	—	—	—
	Lab	—[1]	TL-4	—	—	25.0	97.8	—	—	—
Tropynina (2012)	Lab	—	PL-3	—	—	90.0	37.1	—	—	—
	Lab	—	PL-3	—	—	90.0	42.6	—	—	—
	Lab	—	PL-3	—	—	90.0	133.3	—	—	—
	Lab	—	PL-3	—	—	90.0	136.5	—	—	—
	Lab	—	PL-3	—	—	90.0	139.6	—	—	—
El-Salakawy et al. (2001)	Lab	—	PL-2	—	6,503	—	170.4	—	—	—
	Lab	—	PL-2	—	6,503	—	155.1	—	—	—
	Lab	—	PL-2	—	6,503	—	164.3	—	—	—
	Lab	—	PL-2	—	6,503	—	96.2	—	—	—
	Lab	—	PL-3	—	6,503	—	161.0	—	—	—
	Lab	—	PL-3	—	6,503	—	114.9	—	—	—
	Lab	—	PL-3	—	6,503	—	167.3	—	—	—
	Lab	—	PL-3	—	6,503	—	145.9	—	—	—
Bullard et al. (2010)	Field	New Jersey[1]	—	57.4	22,090	14.4	—	—	−4.3	7.7
	Field	New Jersey[1]	—	62.6	5,049	25.2	—	—	−5.6	−9.6
Ulker et al. (2008)	Model	F-Shape	—	62.4	4,499	25.0	—	—	—	—
Lee, Zi et al. (2017)	Model	—	—	—	50,000	—	315.9	—	—	—
	Field	—	SB6	53.4	28,000	15.0	—	—	—	—
Bielenberg et al. (2014)	Field	F-Shape	TL-3	63.6	4,998	24.9	—	43.0	4.6	7.6
	Field	F-Shape	TL-3	64.8	4,978	25.4	—	40.7	4.9	7.8
Dobrovolny et al. (2015)	Field	F-Shape	TL-3	62.2	5,056	24.8	—	17.8	4.1	12.7
	Field	F-Shape	TL-3	63.5	5,064	25.0	—	34.2	11.6	14.9
Sheikh et al. (2009)	Field	Single Slope	TL-3	63.1	4,953	24.2	—	5.6	−2.4	−11.3
Sheikh et al. (2008)	Field	F-Shape	TL-3	62.9	4,621	24.7	—		−5.5	8.5
	Field	F-Shape	TL-3	62.6	4,586	26.9	—	13.8	−8.3	9.0
Mongiardini et al. (2013)	Field	New Jersey[1]	TL-3	62.3	4,470	26.0	—			
	Field	Vertical[1]	TL-3	61.1	5,179	25.8	—	4.4	6.5	−6.3
Wiebelhaus et al. (2010)	Field	F-Shape + Single Slope	TL-3	62.5	5,175	24.7	—	2.6	−4.7	6.8
	Field	F-Shape + Single Slope	TL-3	62.2	5,160	26.2	—	44.3	−18.7	13.3
Kim et al. (2010)	Lab	New Jersey[1]	TL-3	21.8	5,000	90.0	73.4	—	—	—
	Lab	Vertical[1]	TL-3	20.3	5,000	90.0	66.1	—	—	—
	Lab	Vertical[1]	TL-3	20.1	5,000	90.0	70.2	—	—	—
	Lab	Vertical[1]	TL-3	20.1	5,000	90.0	64.4	—	—	—
El-Salakawy and Islam (2014)	Lab	—[1]	PL-2	—	—	90.0	87.9	—	—	—
	Lab	—[1]	PL-2	—	—	90.0	83.85	—	—	—
	Lab	—[1]	PL-2	—	—	90.0	55.08	—	—	—
	Lab	—[1]	PL-2	—	—	90.0	53.28	—	—	—
Dhakal et al. (2013)	Lab	New Jersey	TL-2	—	—	90.0	41.0	—	—	—
Jeon et al. (2008)	Lab	—	TL-4	—	—	90.0	74.2	—	—	—
	Lab	—	TL-5	—	—	90.0	80.9	—	—	—

Notes: [1] Barriers tested with slabs; — = No data
Conversions: 1 mph = 1.61 km/h; 1 lb = 0.45 kg; 1 kip-force = 4.45 kN; 1 inch = 25.4 mm

Laboratory Testing

Laboratory testing considers two categories: static tests and dynamic tests. Static testing allows researchers to establish the ultimate capacity of the materials, strength connections, and load–deflection characteristics. Dynamic tests allow for the recreation of realistic crash load histories and determine the dynamic capacity of the CMB, while evaluating the structural capacity of precast CMB designs (*AASHTO MASH 2016*). Precast CMBs are utilized for testing, and are typically shorter in longitudinal length due to only transverse loading being applied. Namy et al. (2015) noted that the length of the precast barrier affects its strength, showing, with a computer simulation model, that an increased length in the barrier segments increases the ultimate strength.

Static Testing

Static tests do not allow for a dynamic understanding of the barrier's performance and are incapable of assessing occupant risk. The experimental setup is developed based upon the researcher's intuition since no ASTM standard was provided. For instance, static loading with an actuator will only affect a small area of the barrier, similar to that of a point load; the addition of a load distribution plate will transfer the load along the barrier over a controlled surface. Key factors to consider for static testing include barrier length, boundary condition, and loading surface.

Namy et al. (2015) performed experimental tests on three Pl-2 (TL-4) barrier configurations, each made with HPFRC concrete mix with 1.50 percent-vol. steel fibers. One of the test configurations included three 6.6 ft (2.0 m) long precast barriers connected with a shear key. A 13.8 by 27.6 inch (350 by 700 mm) ultra-high performance fiber-reinforced concrete (UHPFRC)

loading plate, as specified as an impact dimension in the AASHTO 1989 *Guide Specifications for Bridge Railings*, was attached to the CMB to distribute the load from the actuator. Namy et al. determined that the shear key connection increases the strength capacity and is beneficial for limiting barrier deflections during service loads.

Dhakal et al. (2013) compared the structural responses of a yield line analysis, full-scale static testing, and a finite element crack analysis of a geopolymer concrete median barrier. The impact load was distributed over a length of 36.0 inches (914 mm) with the barrier reaching an ultimate failure capacity of 41.0 kips (182.4 kN) during static testing with a predicted failure capacity of 45.9 kips (204.2 kN) through the yield line analysis. The comparison of the bending stress at the centerline between the FE model, experimental testing, and the yield line analysis were also found to be in close agreement, validating the predictions from the yield line analysis on the geopolymer CMB.

Dynamic displacement, known as the deformation of the barrier, is measured using potentiometers and allows for the structural accuracy evaluation of the CMB. Data from the potentiometer can be plotted in load versus displacement graphs. For full-scale crash tests, these graphs can analyze the amount of deformation a barrier designed for that TL could endure in similar installations. For laboratory testing, the measurement of the dynamic displacement evaluates the maximum amount of deformation the CMB experiences before failure.

Occupant ridedown acceleration is a specific evaluation criterion to determine occupant risks. The ridedown acceleration is determined based upon the vehicle's center of gravity accelerations. Measured in two directions, the longitudinal occupant ridedown is affected by whether the vehicle can easily slide along the barrier. The occupancy ridedown acceleration is

limited to a maximum of 20 g's before the testing is considered unsatisfactory due to an increase in occupancy risk.

BARRIER WALL REVIEW SUMMARY

This review of past studies of concrete barrier wall testing procedures and designs, as well as existing codes for testing, has revealed the following trends suitable for this research project:

- The F-shape safety barrier replaced the predominantly used New Jersey barrier due to the reduction in the distance from the ground to the location of the sloped face by 3.0 inches (76 mm); this reduction improved vehicle stability.
- Single-slope barriers are 30.00 percent taller than the New Jersey barrier due to a built-in glare screen.
- Single-slope barriers are preferable to reduce maintenance costs because the design and performance of the barrier is not affected by resurfacing the adjacent pavement.
- The experimental test setup is typically developed based upon the researcher's intuition due to no ASTM standard being provided.
- The majority of static load testing is conducted on concrete bridge railings using hydraulic actuators.
- Reducing the height of a barrier increases vehicle instability by increasing the roll and pitch of the vehicle's center of gravity.
- A lateral design impact load of 80.0 kips (355.9 kN) is recommended for *MASH* TL-4 single-slope CMBs with a height of 42.0 inches (1,067 mm), as determined by Sheikh (2012) and Fossier (2016).

- A shear key connection increases the strength capacity and is beneficial for limiting barrier deflections during service loads.

CHAPTER 3. FIBER-REINFORCED RUBBERIZED CONCRETE MIXTURES

FIBER-REINFORCED RUBBERIZED CONCRETE MIXTURE DESIGN

The initial phase of this research study was ultimately to develop an optimized hybrid mixture consisting of fiber reinforcement and recycled tire chips before proceeding to scaled beam testing. Twelve preliminary mixtures were batched and tested, and of these twelve, eight were to be considered as mixture pairs. Of those eight, four contained a 20.00 percent coarse aggregate replacement of tire chips, while the other four did not. These mixture pairs were used to analyze the relationship between the tire chips and fiber reinforcement. The primary constituents used for the mixtures in this study are Portland cement, virgin coarse and fine aggregates, and recycled tire chip aggregates; the fibers used included steel, polypropylene, and polyvinyl alcohol. All specimens were batched with the same w/c ratio and cement content of 0.42 and 611 lb/yd^3 (362 kg/m^3), respectively.

Materials

Cementitious Materials

In compliance with ASTM C150 *Standard Specification for Portland Cement*, a Type I/II cement was used for the purpose of this study. No other cementitious materials were observed. Table 8 lists the physical and chemical properties of the cement used in this study.

Natural Aggregates

All coarse and fine aggregates used in this study adhere to ASTM C33, GDOT Section 800 (coarse aggregate), and GDOT Section 801 (fine aggregate). The coarse aggregate was obtained from Hanson Aggregates East and were locally sourced from Athens, Georgia. The coarse

aggregate size is a graded #57 stone (NMAS 1.0 inch [25 mm]) and is categorized as granite gneiss/amphibolite. The fine aggregate was sourced from Redland Sand, Inc. located in Watkinsville, Georgia, and is categorized as an alluvial sand.

Table 8. Chemical and physical properties of Type I/II cement.

Chemical and Physical Properties		Test Results	ASTM C150 Specifications
SiO_2	(%)	19.7	—
Al_2O_3	(%)	4.7	6.0 max
Fe_2O_3	(%)	3	6.0 max
CaO	(%)	63.3	—
MgO	(%)	3.1	6.0 max
SO_3	(%)	3.2	3.0 max
CO_2	(%)	1.7	—
Limestone	(%)	4	5.0 max
$CaCO_3$ in Limestone	(%)	98	70 min
C_3S	(%)	54	—
C_2S	(%)	15	—
C_3A	(%)	7	8 max
C_4AF	(%)	9	—
$C_3S + 4.75C_3A$	(%)	89	100 max
Loss of Ignition	(%)	2.7	3.0 max
Blaine Fineness	(cm^2/g)	387	260–430
Air Content of PC Mortar	(%)	8	12 max
Specific Gravity		3.16	—

Sieve analysis was conducted on these natural aggregates in compliance with ASTM Standard C136, *Test Method for Sieve Analysis of Fine and Coarse Aggregates*, and the results are seen in figure 8 and figure 9 for the coarse and fine aggregate, respectively.

Tire Chips

The tire chips used in this study were in compliance with ASTM D6270 *Standard Practice for Use of Scrap Tires in Civil Engineering Applications.* Table 9 highlights specific terminology and defines their properties.

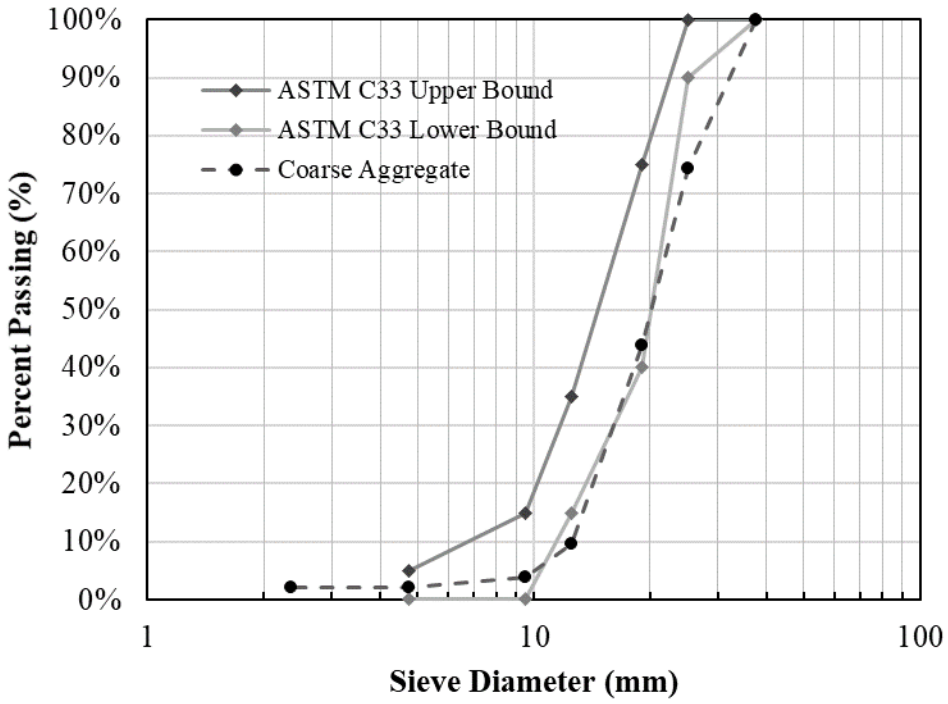

Figure 8. Graph. Sieve analysis of natural coarse aggregate in compliance with ASTM C136.

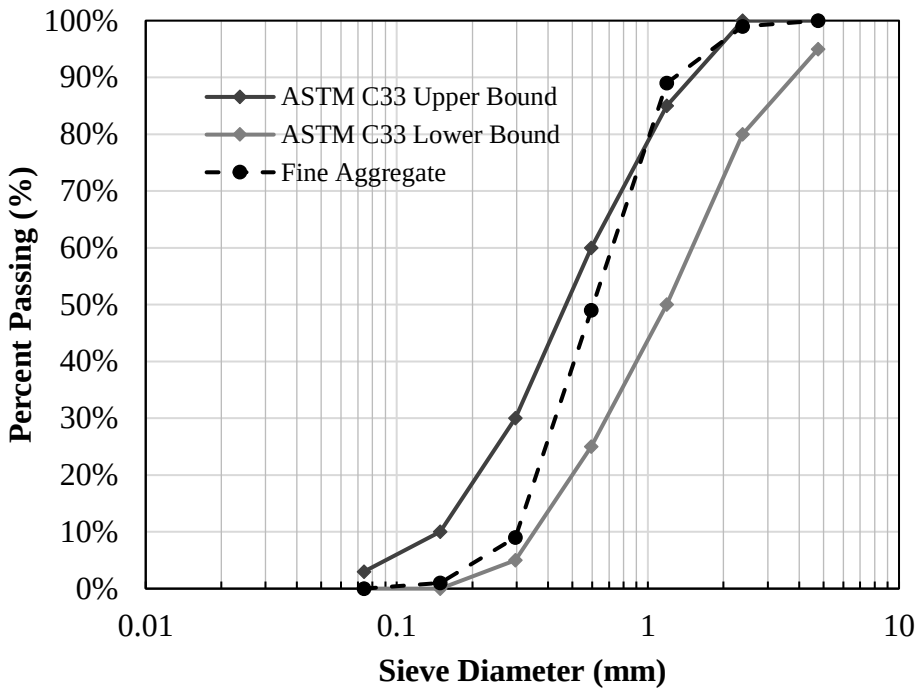

Figure 9. Graph. Sieve analysis of natural fine aggregate in compliance with ASTM C136.

Table 9. Definition of terms specific to ASTM D6270.

Material	Minimum Size, in. (mm)	Maximum Size, in. (mm)
Rough Shred	1.96 × 1.96 × 1.96 (50 × 50 × 50)	30 × 1.96 × 3.94 762 × 50 × 100
Tire-Derived Aggregate (TDA)	0.47 (12)	12 (305)
Tire Chips	0.47 (12)	1.96 (50)
Granulated Rubber	<0.017 (0.425)	0.47 (12)
Ground Rubber	<0.017 (0.425)	0.079 (2)
Powdered Rubber	—	<0.017 (0.425)

Note: — = No data

For this particular study, only tire chips 0.5 to 2.0 inches (12 to 50 mm) were used to replace a percentage of the coarse aggregate. Although the size of the tire chips can exceed that of the coarse aggregate's nominal maximum aggregate size (NMAS) of 1.0 inch (25 mm), the sieve analysis of the tire chips, which was conducted in GDOT RP15-14 (Durham et al. 2017), for the

most part remains within the upper and lower bounds set by ASTM standards. The sieve analysis of the tire chips used in this study is shown in figure 10.

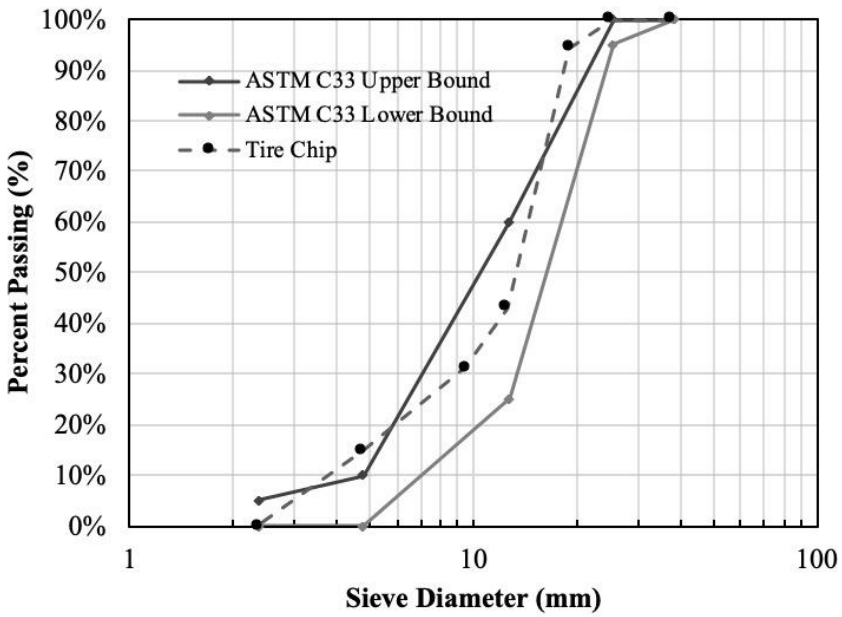

Figure 10. Graph. Sieve analysis of recycled tire chip in compliance with ASTM C136.

All rubberized mixtures in this study will contain a 20.00 percent volume fraction of the coarse aggregate. The results from Durham et al. (2017) demonstrated that for the specific mixture design used, a 20.00 percent replacement of coarse aggregate exceeded the requirements of GDOT Class A concrete, demonstrated increased toughness up to 374.00 percent compared to the control, and proved to be the most cost-effective option relative to the control (Durham et al. 2017).

Fiber Reinforcement

Three separate types of fiber were used in this study—steel, polypropylene, and polyvinyl alcohol. Due to their lengths, steel (1.3 inches) and PP (2.3 inches) fibers were used specifically

to bridge the macrocracks that develop in the concrete matrix under loading. Similarly, PVA (0.3 inch [8 mm]) fibers were used to bridge microcracks. Properties of each fiber can be seen in Table 10. The steel, PP, and PVA fibers can be seen in figure 11. A coin is placed alongside each fiber type to show relative size comparison.

Table 10. Properties of fiber reinforcement.

Properties	Steel	Polypropylene	Polyvinyl Alcohol
Geometry	Hooked ends	Straight, Fibrillated	Straight, Monofilament
Tensile Strength, ksi (MPa)	195 (1345)	83–96 (570–660)	160–203 (1100–1400)
Young's Modulus, ksi (GPa)	30,458 (210)	290 (2)	6091 (42)
Specific Gravity	7.8	0.91	1.3
Length, in. (mm)	1.25 (30)	2.25 (54)	0.313 (8)
Diameter, in. (mm)	0.022 (0.55)	0.02 (0.5)	0.001 (0.038)

Chemical Admixtures

All chemical admixtures used adhered to ASTM Standard C494, *Specification for Chemical Admixtures for Concrete.* A polycarboxylate-based high-range water-reducing (HRWRA) superplasticizer was used to increase slump, as the inclusion of tire chips has a negative impact on the workability of the mixture. The quantity of HRWRA for the mixtures in this study ranged from 7 to 15 fl oz/cwt. Quantities varied due to tire chip inclusion, type of fiber, and quantity of fiber. Viscosity modifying agent (VMA) was used as a thickener to stagnate tire chips and produce a more uniform mixture. The dosages for this study ranged from 8 fl oz/cwt and 5 to 6 fl oz/cwt for Part I and Parts II and III, respectively. To ensure the mixtures in this study adhered to GDOT Class A requirements for air content (2.50 to 6.00 percent), 1.3 fl oz/cwt was determined sufficient in keeping this mixing within the acceptable range. The dosage remained

constant for Parts I, II, and III, as there was little variance in air content regardless of tire chip or fiber inclusion.

(a) **(b)** **(c)**

Figure 11. Photos. Size comparison of fibers: (a) steel fiber, (b) PVA, (c) PP.

Design Methodology

All procedures in this study are in compliance with ASTM standards and ACI recommendations. Procedures used for batching, mixing, and curing were in compliance with ASTM C192 *Standard Practice for Making and Curing Concrete Test Specimens in the Laboratory.* Prior to mixing, all materials were weighed out in 5-gallon buckets, which were color coded for each specific material to avoid contamination, and were stored at room temperature (68–86°F [20–30°C]) for 24 hours in advance with lids on to prevent moisture loss. The moisture contents of the coarse and fine aggregates were measured shortly before the mixing process using a microwave oven, as per ASTM C566 *Standard Test Method for Total Evaporable Moisture Content of Aggregate by Drying*, ensuring the sample was well stirred and uniformly heated. After the moisture content of the aggregates was determined, the batch was re-proportioned accordingly to account for water content. Once all of the materials were prepared and shortly before mixing, the HRWRA, VMA, and air-entraining admixture (AEA) were measured and combined with the water used for mixing to disperse the admixtures uniformly.

Certain procedures were taken prior to mixing to maximize uniform distribution of fibers. The PP fibers used were initially in the form of twisted strands. To prevent clumping and provide a less varied comparison with the individual steel fibers, these strands were separated into individual strands. On the other hand, the steel fibers were submerged in the water used for mixing to saturate and weaken the adhesive bonding between the strands to ensure all fibers were separated. This preparation process was used for all parts of this study. The types of molds used and preparation of molds were in compliance with ASTM C192 *Standard Practice for Making and Curing Concrete Test Specimens in the Laboratory* and ASTM C470 *Standard Specifications for Molds for Forming Concrete Test Cylinders Vertically*.

Once all materials and molds were prepped, mixing was performed. All mixing was conducted with a 12.5 ft^3 capacity Workman *II* Multimixer. All aggregates were first placed into the rotating mixing drum, before adding the tire chips and allowing the mixer to run for 7 to 8 minutes to induce mechanical abrasion of the tire chip surface. Cement and water were then added incrementally to promote complete cement hydration while preventing clumping. Since the addition of fibers would hinder the flow of the concrete and render the slump test ineffective, once the batch was mixed, a slump test was conducted prior to adding the fibers. Once the slump test had been run, fibers were added incrementally to ensure that clumping did not occur.

Fresh Concrete Properties

Table 11 presents each fresh property test along with the appropriate ASTM and AASHTO standard used.

Table 11. Fresh concrete properties tested under ASTM standards.

Fresh Property Test	Standard	Testing Day
Slump	ASTM C143 / AASHTO T119	Batching Day
Unit Weight	ASTM C138 / AASHTO T121	Batching Day
Air Content	ASTM C231 / AASHTO T152	Batching Day
Temperature	ASTM C1064 / AASHTO T309	Batching Day

Curing Concrete Specimens

Specimens were removed from their respective molds 24 ± 8 hours after casting and set to cure for the proper amount of time prior to the testing date. For Part I mixtures, specimens were placed in curing tanks that were maintained at a constant 70°F (21°C). The curing tanks were filled with water saturated with calcium hydroxide. Static and impact beam specimens were cured in burlap and maintained in a temperature-regulated environment. Due to the size of the scaled beams, which exceeded the dimensional capacity of the curing tanks, the accompanying beam cylinders were also cured in burlap to maintain consistent curing conditions. Water was continuously added to the beams and covered in plastic to minimize evaporation. As a result, the relative humidity of the air surrounding the specimens was maintained at near 100.00 percent for the duration of the curing process. The curing methods used in this study adhered to ASTM C511, *Specification for Mixing Rooms, Moist Cabinets, Moist Rooms, and Water Storage Tanks*.

Hardened Concrete Properties

As hardened concrete properties give insight to the overall performance of concrete, the tests laid out within table 12 were conducted at the appropriate testing times.

Table 12. Hardened concrete properties tested under ASTM standards.

Hardened Concrete Tests	Standard	Testing Day
Compression	ASTM C39	1, 7, 28 Days
Modulus of Rupture (MOR)	ASTM C78	28 Days
Drop-Hammer Impact Resilience	ACI 544.2R	28 Days

Fresh Concrete Properties Results

For quality control measures, each mixture was tested for the fresh concrete properties discussed in table 11 upon batching. The goal was to meet specifications for GDOT Class A concrete. Table 13 illustrates the results from the various fresh properties tests conducted during the fiber-reinforced rubberized concrete mixture study phase. Chemical admixtures were planned accordingly for each mixture based on batch size to meet all specifications for GDOT Class A concrete. Admixture amounts varied per mixture to achieve the desired fresh concrete properties, as the addition of tire chips and fibers within the concrete mixture has a negative impact on the slump and homogeneity of the mixture.

Slump

The ACI guide (ACI 544.2R 2009) indicates that slump may not be a good indicator of workability for FRC. As a result, selected mixtures that contained tire chips were tested for slump prior to the inclusion of fibers and after the addition of tire chips. Figure 12 shows the test results for slump. Ultimately, regardless of slump, the most workable rubberized FRC mixtures were those that contained solely steel fibers as opposed to PP and PVA. This was because clumping was experienced with both PP and PVA fibers. In the worst cases, the PVA fibers would absorb moisture from the cement paste and cause the paste to segregate from the aggregates. Based on the mixture design, it was deemed that the quantity of PVA fibers would

have to be reduced, potentially to 0.20 percent of the total 1.00 percent volume fraction, in order to be practical for cast-in-place applications. For these reasons, it was determined that the most practical mixture designs to use for testing static and impact resistance of fiber-reinforced rubberized concrete beams were those containing only steel fibers and tire chips.

Table 13. Fresh concrete property results for Part I mixtures.

Mixture Description	Slump (in.)	Temperature (°F)	Unit Weight (lb/ft³)	Air Content (%)
Control	3.8	77	145.8	4.20
ST1.0-PV0.0-TC0	0.0	93	145.4	6.10
PP1.0-PV0.0-TC0	0.0	75	145.2	3.30
ST0.5-PV0.5-TC0	0.0	92	142.2	5.30
PP0.6-PV0.4-TC0	0.0	89	140.6	6.80
ST1.0-PV0.0-TC20	0.3	88	141.8	1.90
PP1.0-PV0.0-TC20	4.0	91	136.0	4.80
ST0.6-PV0.4-TC20	0.0	93	140.6	2.90
PP0.6-PV0.4-TC20	1.0	91	135.8	4.60
ST0.0-PV0.0-TC20	0.5	84	139.0	5.00
ST0.5-PV0.0-TC20	0.5	75	139.8	3.60
ST0.75-PV0.0-TC20	1.5	63	141.6	4.50

Unit Weight

Unit weights ranged from 135.8 lb/ft³ (2,175 kg/m^3) (PP0.6-PV0.4-TC20) to 145.8 8 lb/ft³ (2,335 kg/m^3) (control). Taking into account all of the mixture pairs (equivalent mixtures with and without tire chips), there was an average 3.80 percent decrease in unit weight with tire chip inclusion. The difference in unit weight between the control and the ST0.0-PV0.0-TC20 was 4.60 percent. As a result, mixtures containing tire chips can be considered lighter than standard normal weight concrete. Figure 13 illustrates the unit weight results.

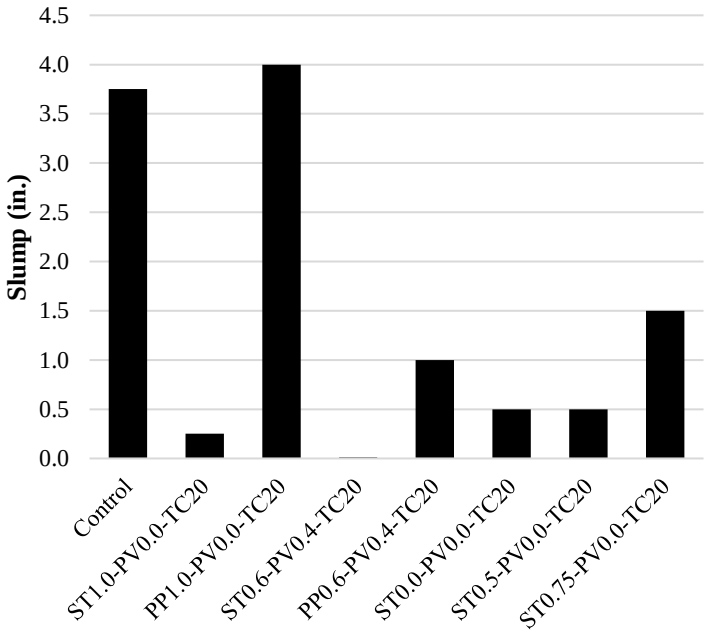

Figure 12. Graph. Slump test results for selected Part I mixtures.

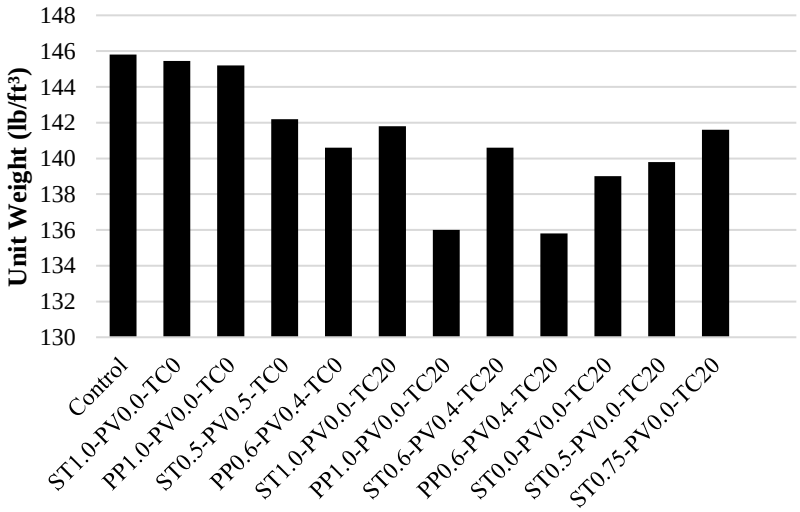

Figure 13. Graph. Unit weight results for selected Part I mixtures.

Air Content

For the purpose of this study, the target entrained air content for GDOT Class A concrete is between 2.50 and 6.00 percent. The AEA used was dosed accordingly at 1.3 fl oz/cwt, and this

dosage was maintained throughout the course of this study. As shown in figure 14, nine of the twelve mixtures were within the 2.50 to 6.00 percent range.

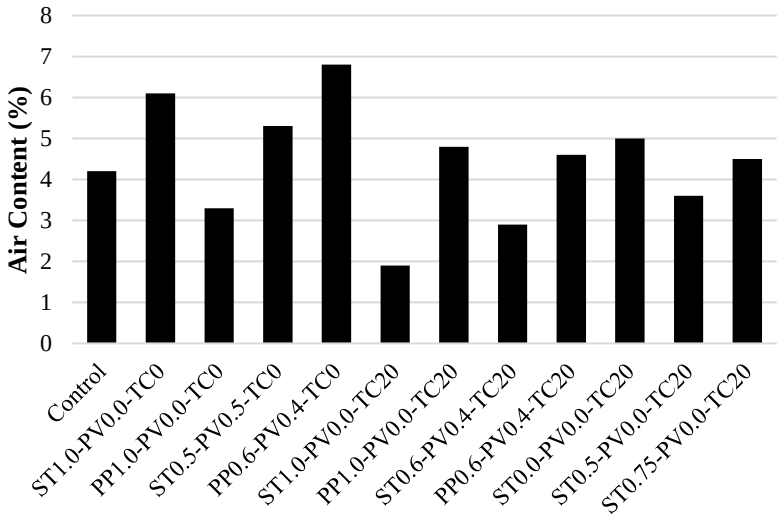

Figure 14. Graph. Air content results for selected Part I mixtures.

Concrete Temperature

Concrete batching temperatures are important for the strength and durability of concrete. Ideal ambient temperatures for batching range between 50 and 85°F (10 to 32°C) for efficient cement hydration, and temperatures exceeding 90°F (32°C) should be avoided to prevent plastic shrinkage and loss of strength (Kardos and Durham 2015).

Some mixtures batched in Part I slightly exceeded the 85°F (29°C) maximum limit. The concrete was batched outdoors during hot temperatures, then moved inside to a temperature-controlled environment for placement and property testing. Temperatures were able to stabilize to more acceptable temperatures. Figure 15 shows the temperatures of the concrete mixtures.

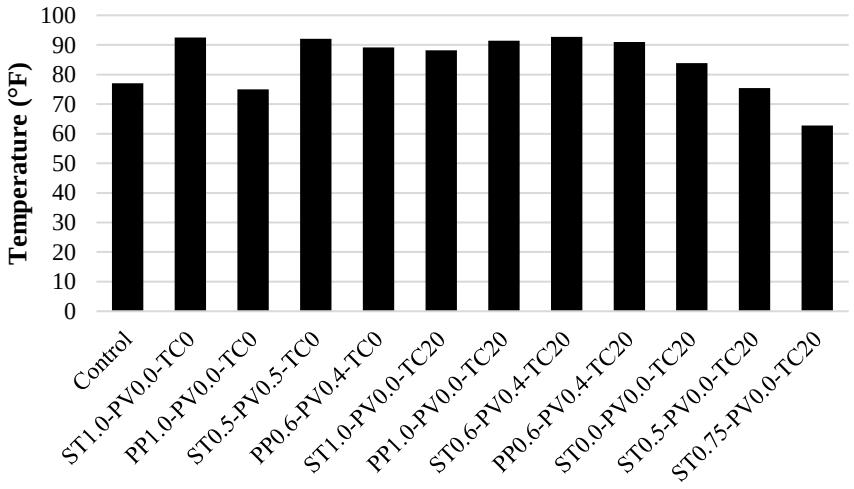

Figure 15. Graph. Temperature results for selected Part I mixtures.

Hardened Concrete Properties Results

Compressive Strength

All compression tests were performed in accordance with ASTM C39. Compressive strength minimums are as per Section 500 of the GDOT Supplemental Specification. Class AA, Class A, and Class B concrete must possess a minimum of 3,500 psi (24.1 MPa), 3,000 psi (20.7 MPa), and 2,200 psi (15.2 MPa), respectively. For the purpose of this study, the concrete used adhered to the target requirements of Class A concrete used in GDOT RP15-14 (Durham et al. 2017). Values for compressive strength at 28 days ranged from 3,002 psi (20.7 MPa) to 8,976 psi (61.9 MPa) and are represented in table 14.

Table 14. Average compressive strength of Part I mixtures.

Mixture Description	Average Compressive Strength, psi (MPa)		
	1-Day	7-Day	28-Day
Control	3755	5805	7128
ST1.0-PV0.0-TC0	4524	6870	8976
PP1.0-PV0.0-TC0	2700	4569	5843
ST0.5-PV0.5-TC0	2536	5509	7289
PP0.6-PV0.4-TC0	2159	4125	5351
ST1.0-PV0.0-TC20	1503	2736	3637
PP1.0-PV0.0-TC20	1454	2544	3002
ST0.6-PV0.4-TC20	2181	3716	3908
PP0.6-PV0.4-TC20	1723	3010	3290
ST0.5-PV0.0-TC20	1685	3159	3585
ST0.75-PV0.0-TC20	1324	2834	3759

It is apparent that the inclusion of tire chips significantly diminished the compressive strength of each mixture pair, up to 59.00 percent. Table 15 shows the overall compressive strength reduction of each mixture when tire chips were used. Despite this loss in strength, the fiber reinforcement prevented each mixture from falling below the minimum 3,000 psi (20.7 MPa).

Table 15. Reduction of compressive strength with tire chip inclusion.

Mixture Description	Compressive Strength Reduction, %
ST1.0-PV0.0-TC0 / ST1.0-PV0.0-TC20	59.0
PP1.0-PV0.0-TC0 / PP1.0-PV0.0-TC20	48.6
ST0.5-PV0.5-TC0 / ST0.6-PV0.4-TC20	46.4
PP0.6-PV0.4-TC0 / PP0.6-PV0.4-TC20	38.5

The inclusion of rubber in the mixtures caused an impedance of compressive strength development over the span of 28 days. The average compressive strength increase from 7 days to 28 days for mixtures that did not contain tire chips was 28.70 percent, whereas mixtures with tire chip inclusion increased by only 18.60 percent. The rate of strength development is illustrated in

figure 16, while the total strength development per testing day is shown in figure 17. Figure 18 shows the comparison between failures of the control and fiber chip composite mixtures.

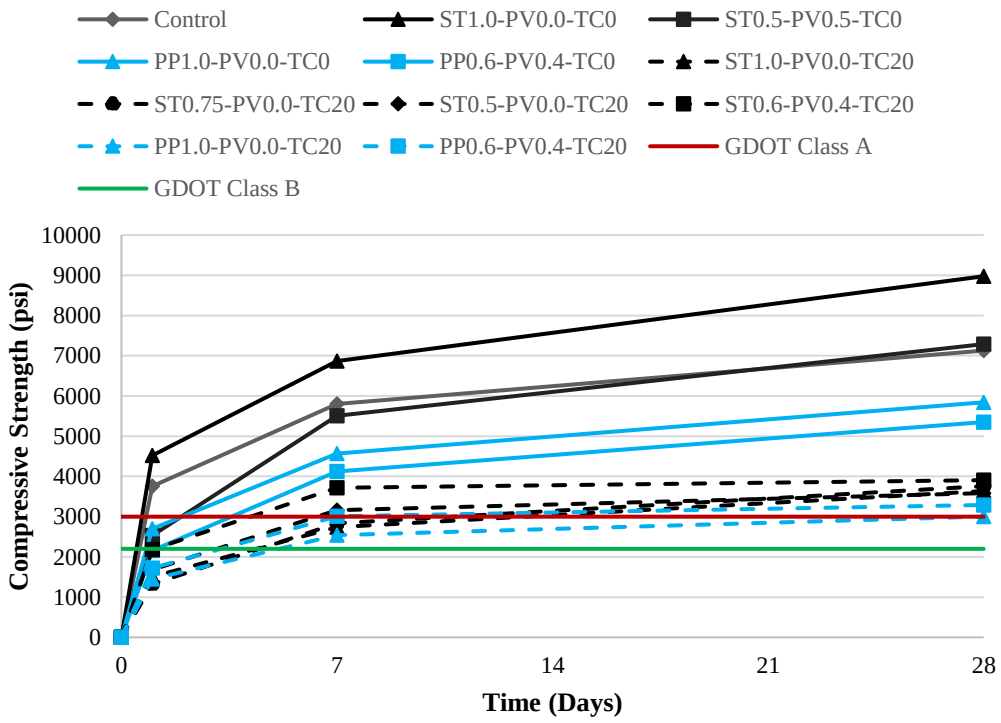

Figure 16. Graph. Average compressive strength of Part I mixtures.

Flexural Strength

The modulus of rupture is a measure of a material's flexural strength, for which there are currently no requirements in GDOT Class A specifications. Because of this, the goal with these mixtures was to create a mixture that performed comparable to or better than the control mixture.

Three prismatic beams with dimensions of 6 inches × 6 inches × 22 inches (152 mm × 152 mm × 559 mm) were formed per mixture and tested at a span of 18 inches under ASTM C78 specifications. Results ranged from 430 psi (3.0 MPa) to 1,058 psi (7.3 MPa) and are shown in table 16. The reduction of MOR strength with tire chip inclusion is listed in table 17.

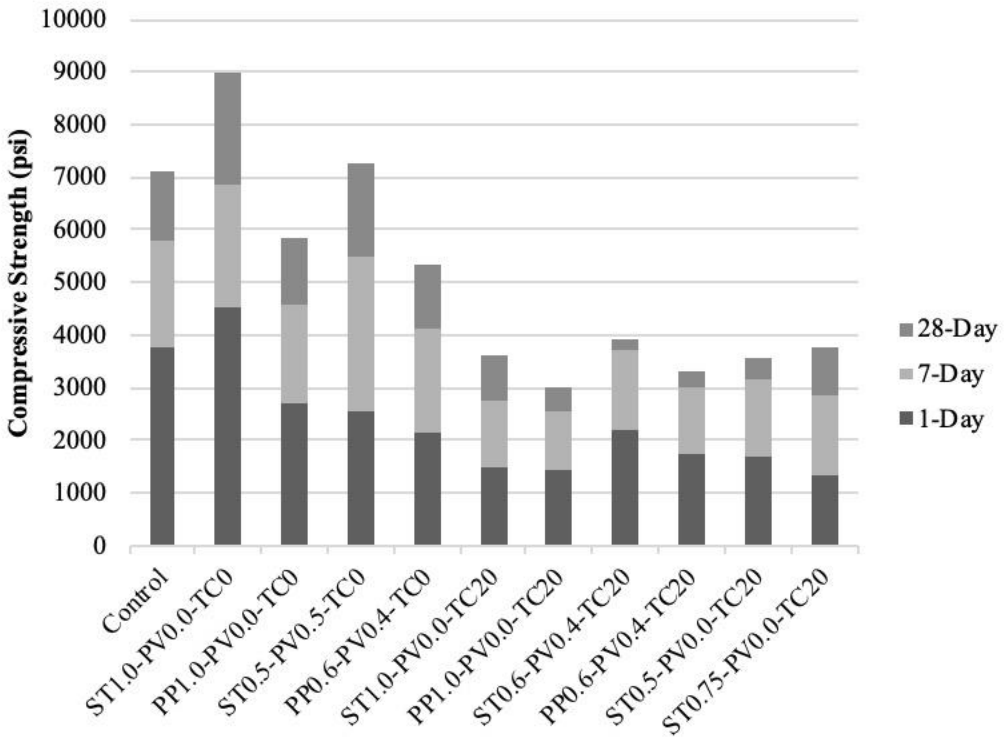

Figure 17. Graph. Total compressive strength gain of Part I mixtures.

Figure 18. Photo. Comparison of compressive cylinders at failure: Control (left), rubberized steel fiber hybrid (right).

Table 16. Average flexural strength of Part I mixtures.

Mixture Description	Average 28-Day MOR (psi)
Control	666
ST1.0-PV0.0-TC0	1058
PP1.0-PV0.0-TC0	430
ST0.5-PV0.5-TC0	883
PP0.6-PV0.4-TC0	532
ST1.0-PV0.0-TC20	782
PP1.0-PV0.0-TC20	520
ST0.6-PV0.4-TC20	769
PP0.6-PV0.4-TC20	536
ST0.5-PV0.0-TC20	681
ST0.75-PV0.0-TC20	649

Table 17. Reduction of MOR strength with tire chip inclusion.

Mixture Description	MOR Strength Reduction, %
ST1.0-PV0.0-TC0 / ST1.0-PV0.0-TC20	26.10
PP1.0-PV0.0-TC0 / PP1.0-PV0.0-TC20	−20.90
ST0.5-PV0.5-TC0 / ST0.6-PV0.4-TC20	12.90
PP0.6-PV0.4-TC0 / PP0.6-PV0.4-TC20	−0.10

It was observed that these rubberized FRC mixtures exhibited significantly increased ductility. While the PVA fibers bridged together the microcracks that developed, the larger steel and PP fibers bridged together the macrocracks. Additionally, the tire chips reduced the overall stiffness and allowed for a more ductile response with each specimen in comparison to the control. The resultant specimens showed clear increase in the displacement at mid-span, although they reached ultimate failure load, and were, thus, held together by fibers until the crack growth and separation in the crack plane was observed. Figure 19 and figure 20 show results from the MOR testing.

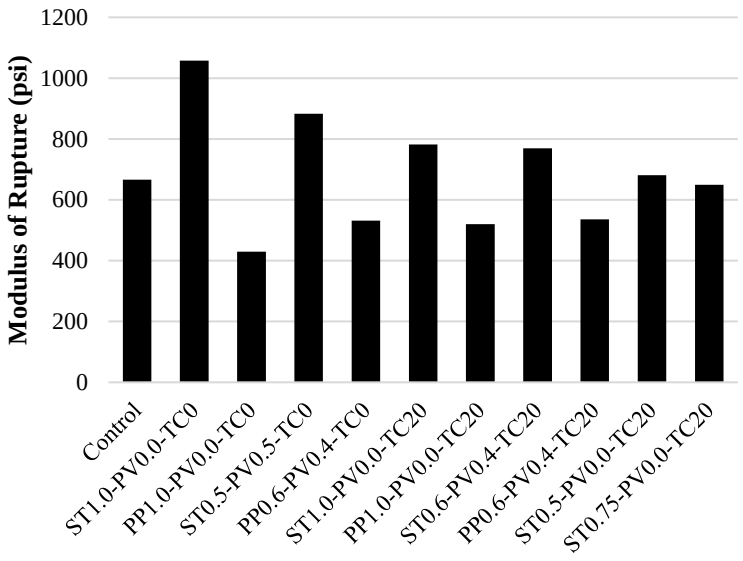

Figure 19. Graph. Average MOR strength of Part I mixtures.

(a) **(b)**

Figure 20. Photos. Isometric comparison of MOR specimens at failure: (a) control, (b) rubberized PP fiber hybrid.

Drop-Hammer Impact Resilience

Compressive strength and flexural strength were heavily considered, although impact resilience became the deciding factor for which mixtures would move to impact evaluation within Part II of this study. Previous research has shown that tire chips have the capability of absorbing impact loads and redistributing the resulting energy to the rest of the structure (Ismail and Hassan 2016). This quality, coupled with the ability of fibers to bridge cracks, was used to develop an optimal concrete mixture that was superior to the control under impact loading.

In accordance with ACI 544.2R, concrete disks, with dimensions of a 6 inch (152 mm) diameter and 2 inch (51 mm) height, were placed in a steel containment apparatus. A 10 lb (5 kg) drop-hammer was then used to repeatedly apply a load on each specimen (about 1 drop every 2 seconds). Photographs comparing the fracture responses between the control and selected mixtures with 20.00 percent tire chip replacement are shown in figure 21. Even just tire chip inclusion alone was sufficient in reducing crack width and kept the specimen in one piece at ultimate failure.

This test was conducted taking points at three stages: initial crack, control failure, and ultimate failure. The initial crack was recorded at first sighting, followed by the second crack or "control failure," which was used as a reference for the performance of fibers and tire chips for energy dissipation before reaching ultimate failure. Ultimate failure was considered the point at which three cracks meet at the center of the specimen. In rare cases, ultimate failure was reached with just two cracks meeting in the center, traversing straight down the middle of the specimen. While the control specimen achieved complete separation at ultimate failure, other mixtures were held together by tire chips and fibers. Results for the drop-hammer impact test can be seen in table 18

and figure 22. There was a 3,525.00 percent incease in the number of drops needed to reach ultimate failure from the control to ST0.75-PV0.0-TC20, failing at 8 drops and 290 drops, respectively.

Figure 21. Photo. Fractured impact disk comparison: Control (top), 20.00 percent tire chip (bottom).

Table 18. Average drop-hammer impact results of Part I mixtures.

Mixture Description	Initial Crack	Control Failure	Ultimate Failure
Control	6	6	8
ST0.0-PV0.0-TC20	13	16	22
ST1.0-PV0.0-TC0	36	69	135
PP1.0-PV0.0-TC0	25	49	121
ST0.5-PV0.5-TC0	56	99	236
PP0.6-PV0.4-TC0	31	65	99
ST1.0-PV0.0-TC20	25	27	85
PP1.0-PV0.0-TC20	42	71	183
ST0.6-PV0.4-TC20	38	63	127
PP0.6-PV0.4-TC20	42	111	237
ST0.5-PV0.0-TC20	25	50	62
ST0.75-PV0.0-TC20	132	220	290

As observed in figure 22, each mixture performed significantly better than the control. The specimen that contained exclusively tire chips, ST0.0-PV0.0-TC20, required twice as many drops to reach ultimate failure compared to the control. However, it was not until fibers were added that the significant improvement in impact resilience could be seen. The effectiveness of tire chip performance in relation to each mixture pair cannot be determined with certainty. While the mixtures containing steel and PVA exhibited a decrease in impact resistance, mixtures containing PP and PVA seemed to significantly benefit from them, although their inclusion does not provide sufficiently workable concrete. These data are highlighted in table 19.

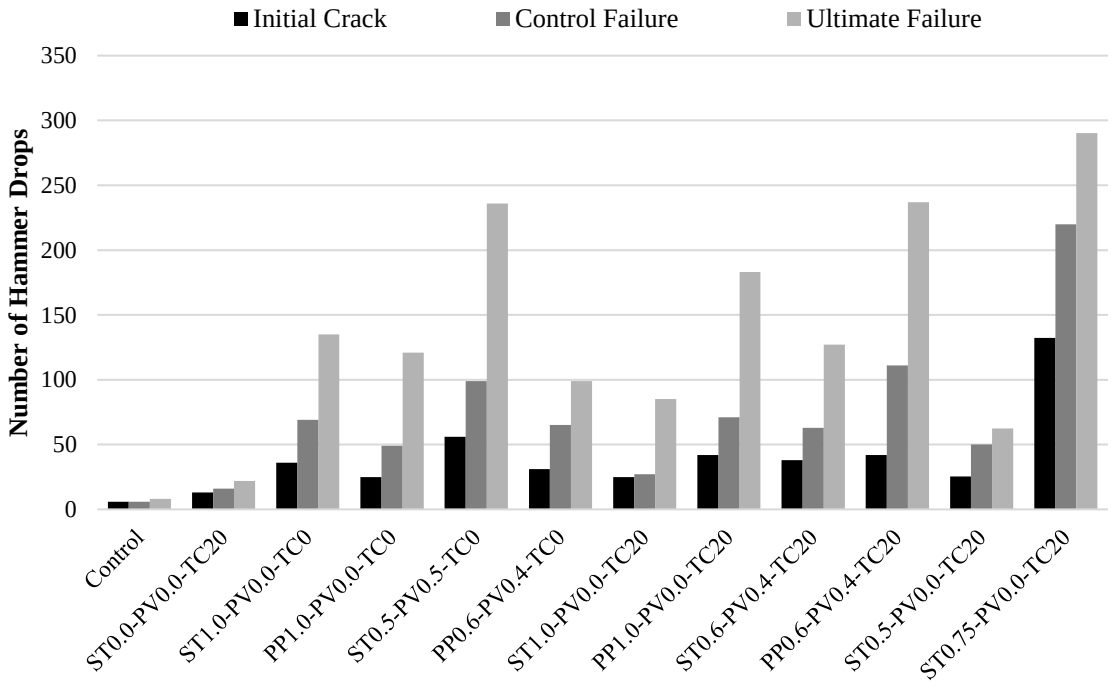

Figure 22. Graph. Average drop-hammer impact results of Part I mixtures.

Table 19. Increase of drop-hammer impact resilience with tire chip inclusion.

Mixture Description	Increase of Impact Resistance, %
ST1.0-PV0.0-TC0 / ST1.0-PV0.0-TC20	−37.70
PP1.0-PV0.0-TC0 / PP1.0-PV0.0-TC20	51.20
ST0.5-PV0.5-TC0 / ST0.6-PV0.4-TC20	−46.20
PP0.6-PV0.4-TC0 / PP0.6-PV0.4-TC20	139.40

Analysis of Steel Fiber Volume Fraction on Mechanical Properties of Concrete

A further analysis was conducted on mixtures specifically containing steel fibers. Based on the data collected, mixtures containing steel fibers clearly exhibited increased performance in compressive strength, flexural strength, and drop-hammer impact resilience. Despite PP and PVA fibers exhibiting promising results, ultimately the workability of the mixtures containing PP and PVA resulted in these mixtures being designated as unfit to continue into Part II of the study.

In the presence of tire chips, the optimum steel fiber volume fraction may differ from normal concrete mixtures. All fiber-reinforced rubberized mixtures containing steel fibers and tire chips have been isolated in figure 23 through figure 26 to illustrate the comparison between varying volume fractions of steel fiber (V_{sf}) in the presence of tire chips.

In terms of compressive strength and the rate of strength development, the three steel fiber and tire chip hybrid mixtures all demonstrated similar results. Based on results shown in figure 23 and figure 24 steel fiber volume fraction has an insignificant effect on compressive strength, ranging from 0.50 to 1.00 percent.

Figure 25 shows that the inclusion of the steel fiber volume fraction has a small effect on MOR, though the correlation is unclear based on the data. As expected, the MOR of STC0.75-PV0.0-

TC20 would fall in between STC1.0-PV0.0-TC20 and STC0.5-PV0.0-TC20. However, STC0.75-PV0.0-TC20 fell even below the control specimen, which was unexpected considering specimens containing steel fibers were the only ones able to exceed the MOR of the control. Regardless of this fact, steel fibers are good at counteracting the diminishing effects on strength resulting from tire chips.

Figure 26 shows the isolated results for the drop-hammer test of specimens ranging from steel fiber volume fractions of 0.50 to 1.00 percent, along with the control and 20.00 percent tire chip mixtures for comparison. Unlike the results from the compression and MOR tests, these outcomes show a possible correlation between steel fiber volume fraction and impact resistance.

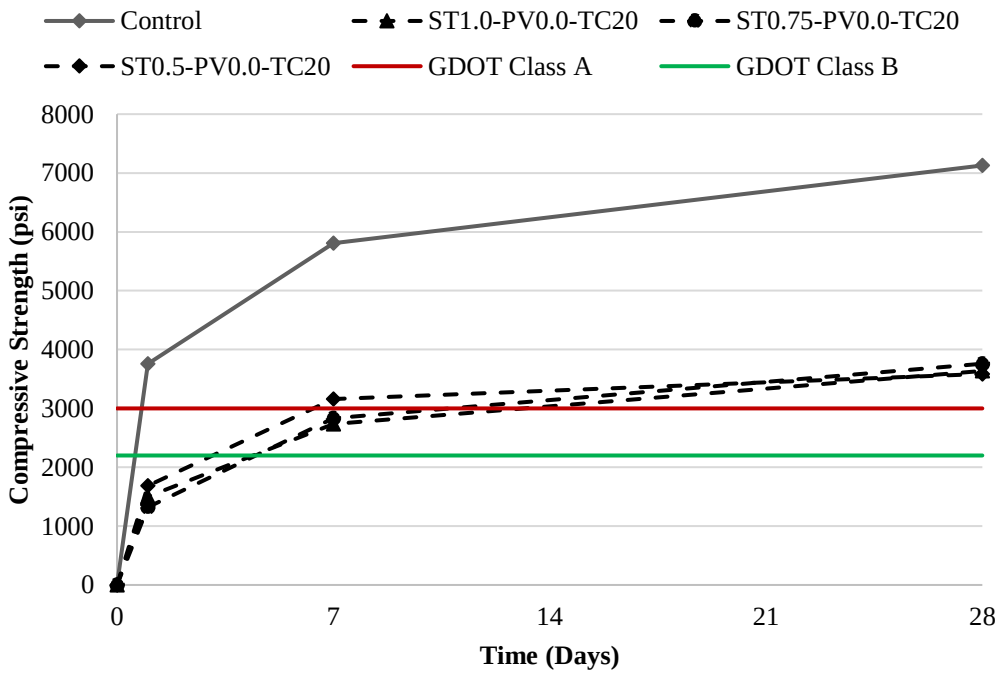

Figure 23. Graph. Average compressive strength observing varying V_{sf}.

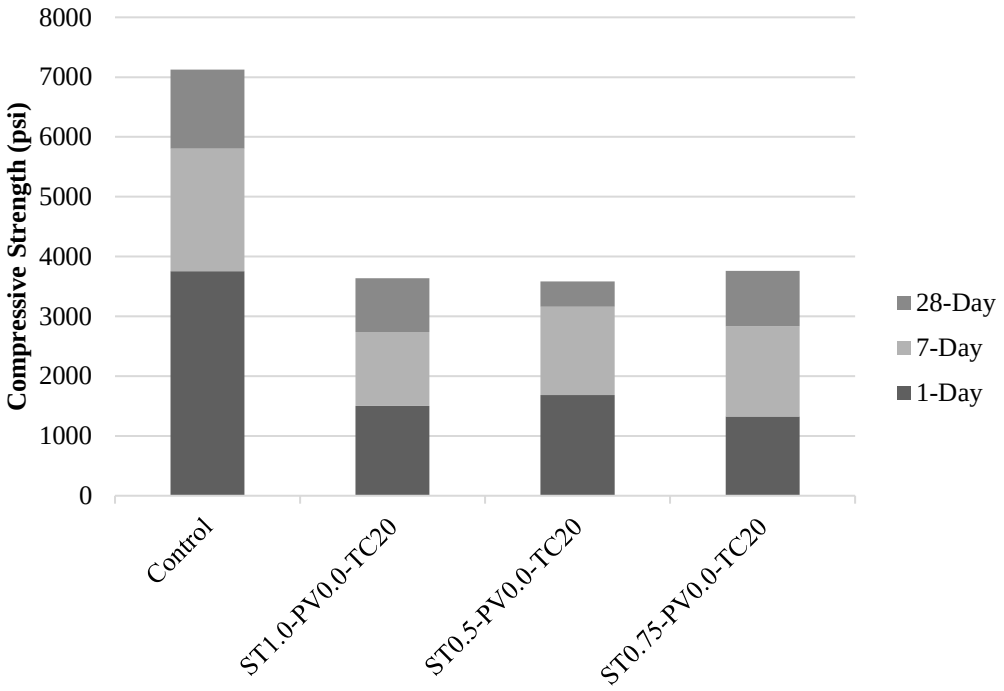

Figure 24. Graph. Total compressive strength gain observing varying V_{sf}.

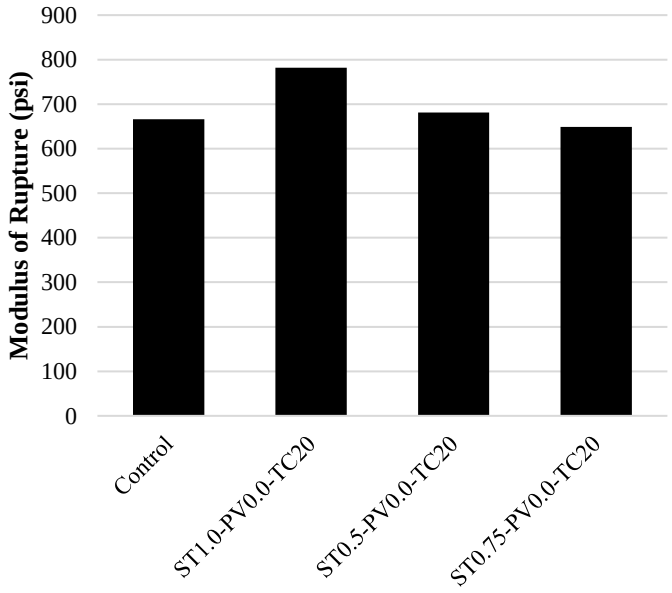

Figure 25. Graph. Average MOR strength observing varying V_{sf}.

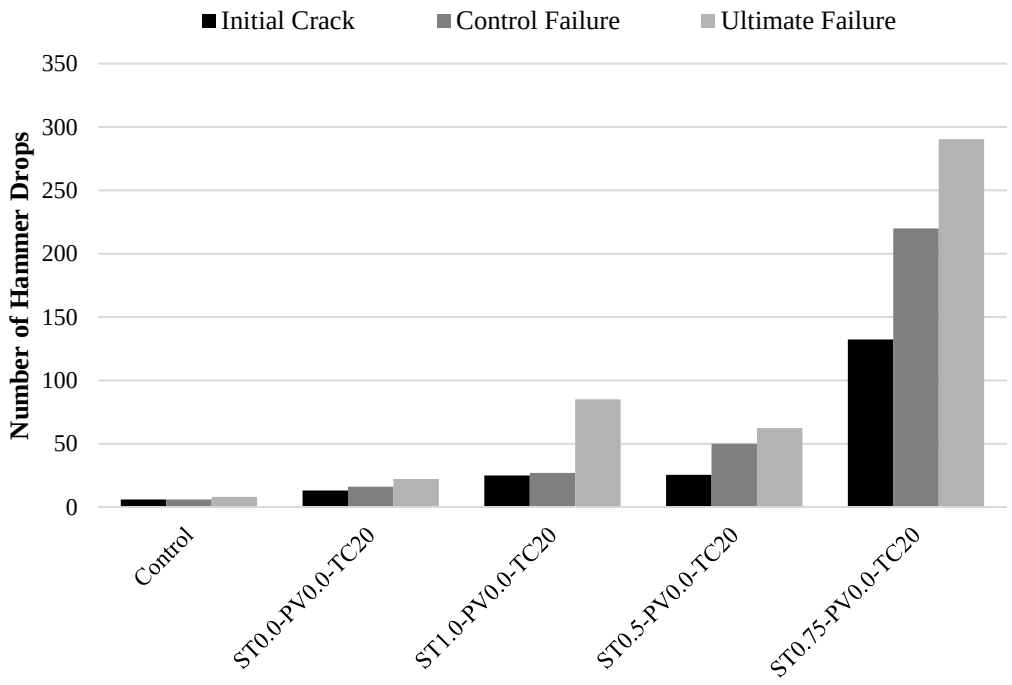

Figure 26. Graph. Average drop-hammer impact results observing varying V_{sf}.

Based on previous research, it was initially expected that the mixture containing 1.00 percent steel would outperform the mixtures with less steel (Masud 2015). However, 0.75 percent steel appears to be the optimum percentage when combined with tire chips. The results from ST0.5-PV0.0-TC20 are reasonable because there are not enough steel fibers to produce adequate reinforcement. Inversely, ST1.0-PV0.0-TC20 appears to contain too much steel, causing the fibers to clump and producing an inadequate distribution and, thus, a poor bond between the steel fibers, concrete, and tire chips in the concrete matrix. Additionally, ST1.0-PV0.0-TC20 was able to redistribute the load after the control failure and resist failure several drops later, unlike ST0.5-PV0.0-TC20 and ST0.75-PV0.0-TC20, which both exhibited constant trends from one failure to another.

The preliminary design of the optimized cementitious composites led the research team to move forward with hybrid mixtures consisting of varying fiber volume fractions of steel fibers and tire chips. Although the tire chips significantly reduced the mechanical strength properties, it was observed that the addition of steel fibers counteracted these negative effects at a greater capacity than PP and PVA fibers. In addition to the increased mechanical performance, the workability of the mixtures containing steel fibers was significantly greater in comparison to that of the PP or PVA mixtures. However, it was unclear whether 0.75 or 1.00 percent was optimal. Flexural strength was greater with 1.00 percent, although 0.75 percent showed significantly improved drop-hammer resilience. As a result, the scaled effects of 0.75 and 1.00 percent steel fiber volume fractions will be studied more in depth in Part II and Part III of this study.

PERFORMANCE EVALUATION OF STATIC BEAM TESTING

Based on results obtained through laboratory evaluation of the fiber-reinforced rubberized concrete, the mixtures shown in table 20 were deemed most optimal moving forward. Because the results from the drop-hammer impact test showed a correlation between steel volume fraction and number of drops to reach ultimate failure, varying volume fractions were observed.

Table 20. Static beam specimen mixture proportions by volume.

Designation	w/c	Cement Content, lb/yd^3	% Steel Fiber (Volume Fraction)	% Tire Chip (Volume Fraction of Coarse Aggregate)	% Coarse Aggregate (Volume Fraction)	% Fine Aggregate (Volume Fraction)
Control	0.42	611	0.00	0.00	100.00	100.00
ST0.0-TC20	0.42	611	0.00	20.00	80.00	100.00
ST0.5-TC20	0.42	611	0.50	20.00	80.00	100.00
ST0.75-TC20	0.42	611	0.75	20.00	80.00	100.00
ST1.0-TC20	0.42	611	1.00	20.00	80.00	100.00

Static Beam Loading Design

After the results from Part I were reviewed, it was deemed that mixtures containing steel fibers and tire chips would be further analyzed in scaled beams of dimensions 7.5 ft length × 0.5 ft width × 0.8 ft height (2286 mm × 152.4 mm × 254 mm) under static loading. In terms of steel reinforcement, rebar cages were initially constructed with two #3 longitudinal bars for the compression steel and two #4 bars for the tension steel. These bars were held together by #2 stirrups spaced every 4.0 inches (102 mm) on center to resist shear failure. The steel bars used in this study possessed a minimum yield strength of 60,000 psi (413.7 MPa) and a Young's modulus of 29,000 ksi (200 GPa). After testing specimens with two #4 tension steel bars, other reinforcing ratios were observed for comparison. The geometry and orientation of the longitudinal bars are included in figure 27 and figure 28. Each beam was tested at a clear span of 73 inches (1,854 mm).

Static load testing was conducted using a 220.0 kip (978.6 kN) capacity hydraulic actuator with the load being distributed by a 6 inch (152 mm) wide steel plate. Specimens were tested at mid-span under an increasing load at a rate of 200 lb (890 N) per second, taking note how the cracks developed over time. A load cell, which was placed at mid-span directly underneath the actuator arm, and a research-grade NDI Optotrak Certus HD motion capture system were used to measure applied load and displacement. The locations of the motion capture sensors are identified in figure 29.

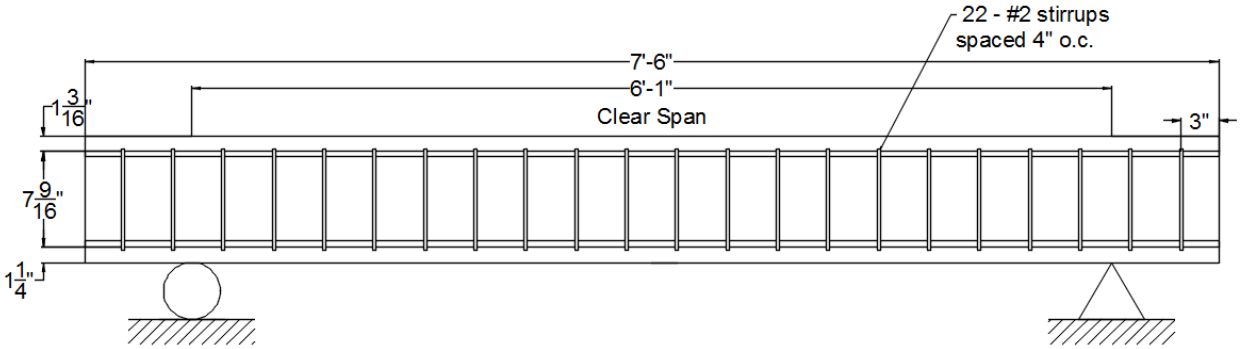

Figure 27. Image. Longitudinal section of reinforced concrete test specimen.

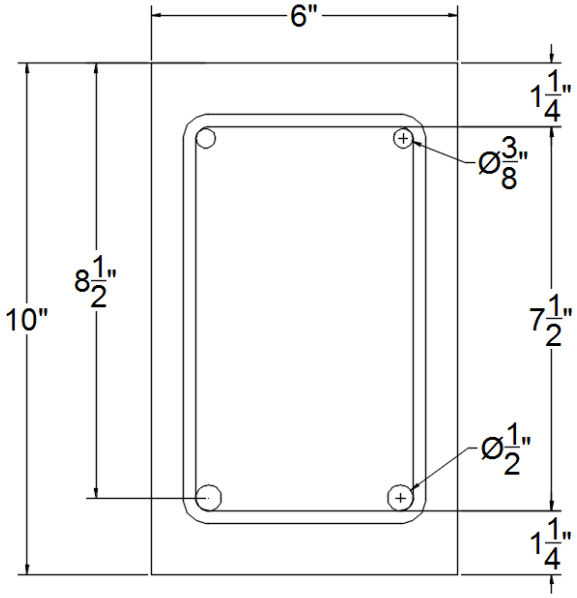

Figure 28. Image. Cross section of reinforced concrete test specimen.

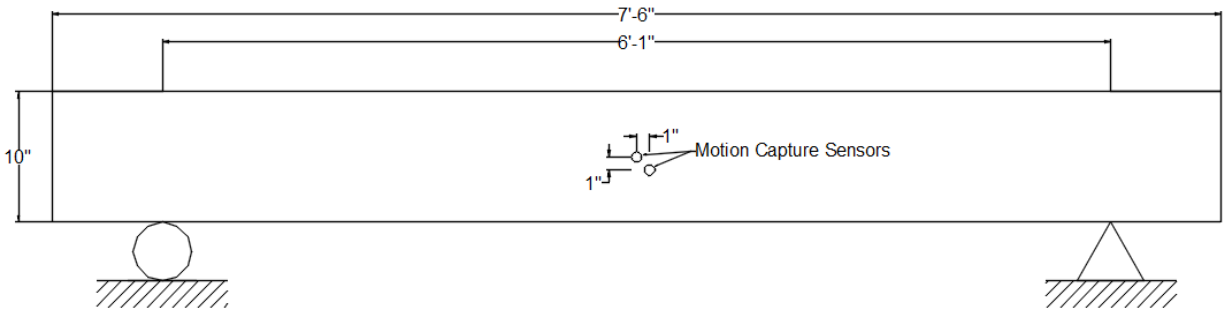

Figure 29. Image. Location of motion capture sensors.

A data acquisition system was used to process the data from the motion capture camera. The frequency was set to 20 Hz to match the rate of the load cell data acquisition. It was imperative to match the frequency to accurately develop load–deflection plots.

Steel Reinforcement Ratio

The fiber-reinforced concrete beams were tested at varying tensile steel reinforcement ratios. The purpose of this was to grasp a better understanding of how reinforcement ratio affects the total energy dissipation of the FRC beams. Specimens were tested with tension steel reinforcement values of 0.20, 0.78, and 1.17 percent. To achieve these reinforcement ratios, specimens comprised two #2, two #4, and three #4 tension steel bars, respectively.

Concrete Mixture Properties

Fresh Concrete Properties Results

Similar to the fiber-reinforced rubberized concrete mixture design investigation, fresh concrete properties were tested on each mixture used to produce static beam specimens. Overall, less variance in properties between mixtures was observed compared to the fiber-reinforced rubberized concrete mixture design investigation due to use of the same type of fiber and tire chip contents within the mixtures. The fresh properties found are summarized in table 21.

Hardened Concrete Properties Results

To produce a more accurate comparison between all Part II mixtures, 4 inch × 8 inch (102 mm × 203 mm) cylinders were created from the same concrete batch used to cast the FRC beams. Because the FRC beams were mixed in two separate batches, three cylinders were produced per batch, resulting in six cylinders total per beam. The compressive strength of all mixtures ranged from 3,502 psi (24.1 MPa) to 5,103 psi (35.2 MPa), which meets GDOT Class A and Class AA

requirements of 3,000 psi (20.7 MPa) and 3,500 psi (24.1 MPa), respectively. A summary of the compressive strength results are listed in table 22 and illustrated in Figure 30.

Table 21. Static beam specimen mixture proportions by volume.

Mixture Description	Slump (in.)	Temperature (F°)	Unit Weight (lb/ft³)	Air Content (%)
Control (ρ = 0.78%)	3.5	86	146.4	5.00
ST0.0-TC20 (ρ = 0.78%)	2.3	86	137.4	4.50
ST0.75-TC20 (ρ = 0.196%)	0.5	63	141.8	4.60
ST1.0-TC20 (ρ = 0.78%)	0.5	87	140.2	2.20
ST0.5-TC20 (ρ = 0.78%)	0.8	60	142.6	3.80
ST0.75-TC20 (ρ = 0.78%)	1.0	68	141.4	4.20
ST0.75-TC20 (ρ = 1.17%)	1.5	64	141.7	4.40
ST1.0-TC20 (ρ = 1.17%)	0.5	62	143.4	3.60

Table 22. Average 28-day compressive strength of FRC cylinders.

Mixture Description	Compressive Strength (psi)
Control (ρ = 0.78%)	5102
ST0.0-TC20 (ρ = 0.78%)	3596
ST0.75-TC20 (ρ = 0.196%)	4003
ST1.0-TC20 (ρ = 0.78%)	3511
ST0.5-TC20 (ρ = 0.78%)	4114
ST0.75-TC20 (ρ = 0.78%)	3878
ST0.75-TC20 (ρ = 1.17%)	4255
ST1.0-TC20 (ρ = 1.17%)	4290

Compressive strength is an important property of FRC beams that combats the potential of crushing/compressive failure occurring prior to tension steel reaching ultimate tensile failure. Experiencing this failure mode would mean that both the reinforcing tensile steel and the steel fibers failed to achieve their maximum energy dissipation potential.

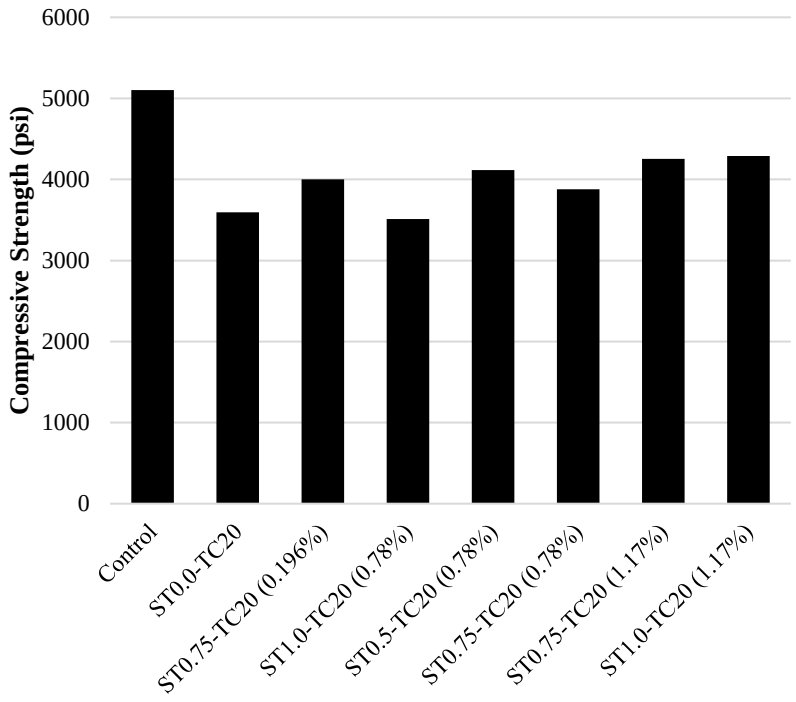

Figure 30. Graph. Average 28-day compressive strength results for static beam specimens.

Static Load Testing Results

The ultimate goal of this test was to determine the toughness, or total energy dissipation capacity, of each FRC beam by integrating the function between load and mid-span deflection over the testing period from initial to final deflection at failure. Eight FRC beams were tested under three-point bending to study the effects of fiber volume fraction, varying reinforcement ratios, and tire chips subjected to static loading conditions. Figure 31 shows the load versus deflection behavior of the static beam specimens.

The control mixture exhibited the lowest toughness at 57.7 kip-in (6,821 KN-mm), while ST0.75-TC20 (1.17 percent) produced the largest static energy dissipation at 120.6 kip-in (13,627 KN-mm), a 109.00 percent increase. All toughness values are tabulated within table 23, in which ρ is calculated by A_s/bd, where A_s is the area of flexural reinforcing steel, b is the beam

width, and d is the depth measured from the top surface of the beam to the centroid of steel. The linear stiffness of each beam was also calculated. This value was taken as the initial slope of the load–deflection curves for each specimen.

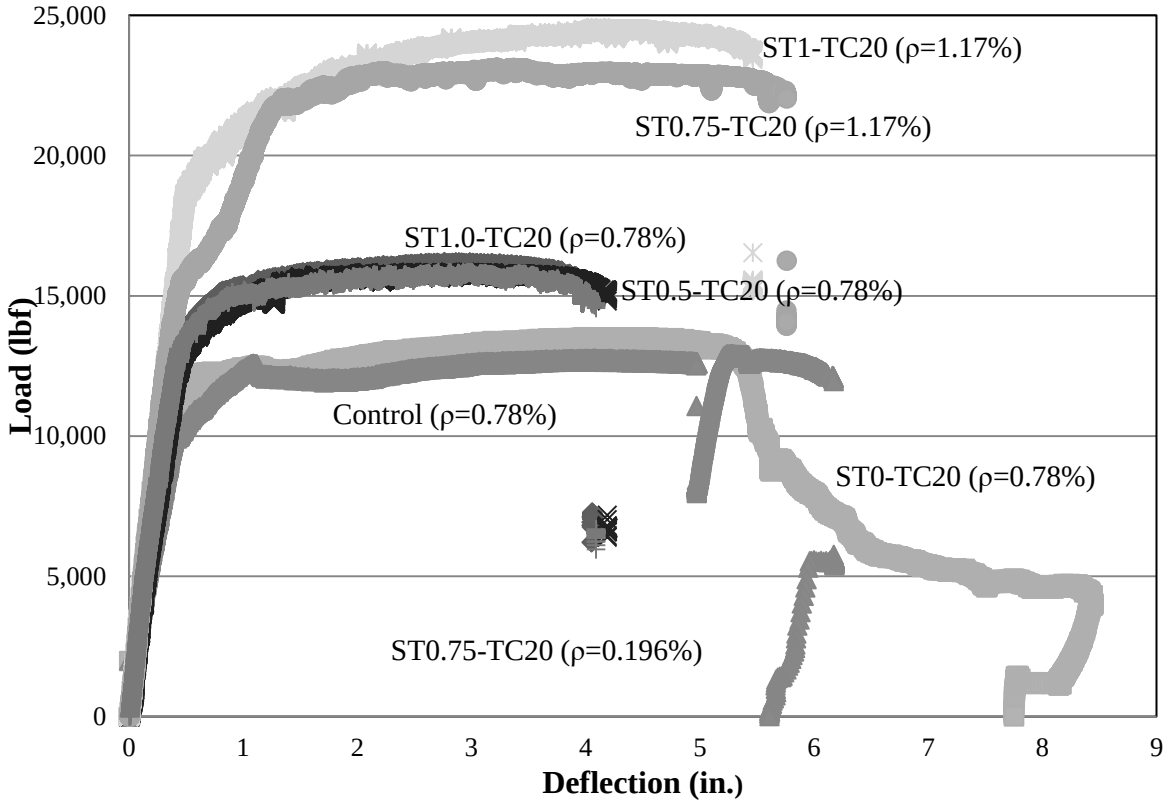

Figure 31. Graph. Load–deflection plot for static beam specimens.

Table 24 lists the failure modes observed for each test specimen, while figure 32 provides visuals of the observed cracking profiles. With the exception of ST0.0-TC20, every specimen failed in tension steel yielding and fracture. Consistent results were observed over the eight rubberized FRD beams tested. Results showed that increasing steel volume fraction led to a slight increase in load capacity, but a slight decrease in deflection, resulting in a similar net static energy dissipation.

Table 23. Total static energy dissipation of FRC beams.

Mixture Description	Toughness (kip-in)	Linear Stiffness (lb/in)
Control (ρ = 0.78%)	57.7	38,159
ST0.0-TC20 (ρ = 0.78%)	64.7	32,349
ST0.75-TC20 (ρ = 0.196%)	27.6	32,937
ST1.0-TC20 (ρ = 0.78%)	59.2	35,087
ST0.5-TC20 (ρ = 0.78%)	60.1	32,700
ST0.75-TC20 (ρ = 0.78%)	58.6	35,784
ST0.75-TC20 (ρ = 1.17%)	120.6	39,876
ST1.0-TC20 (ρ = 1.17%)	119.16	41,527

Table 24. Failure modes of static FRC beams.

Mixture Description	Failure Mode
Control (ρ = 0.78%)	Yielding/Fracture/Shear
ST0.0-TC20 (ρ = 0.78%)	Compression Failure
ST0.75-TC20 (ρ = 0.196%)	Compression and Flexural Failure
ST1.0-TC20 (ρ = 0.78%)	Yielding/Fracture
ST0.5-TC20 (ρ = 0.78%)	Yielding/Fracture
ST0.75-TC20 (ρ = 0.78%)	Yielding/ Fracture
ST0.75-TC20 (ρ = 1.17%)	Yielding/Fracture
ST1.0-TC20 (ρ = 1.17%)	Yielding/Fracture

PERFORMANCE EVALUATION FROM IMPACT BEAM TESTING

The results of the drop-hammer impact tests from the fiber-reinforced rubberized concrete mixtures investigation and the static load tests from Part II led to the optimized mixture design matrix found in table 25. An increase of 3,525.00 percent in performance was observed from mixtures containing steel fiber volume fractions of 1.00 percent. From the results of the static beam tests, it was determined that reinforcement ratios of 0.78 and 1.17 percent are reasonable for specimens without and with fiber reinforcement, respectively.

Control (ρ = 0.78%)

ST0.0-TC20 (ρ = 0.78%)

ST0.75-TC20 (ρ = 0.196%)

ST1.0-TC20 (ρ = 0.78%)

Figure 32. Photos. Failure modes of static beam test specimens.

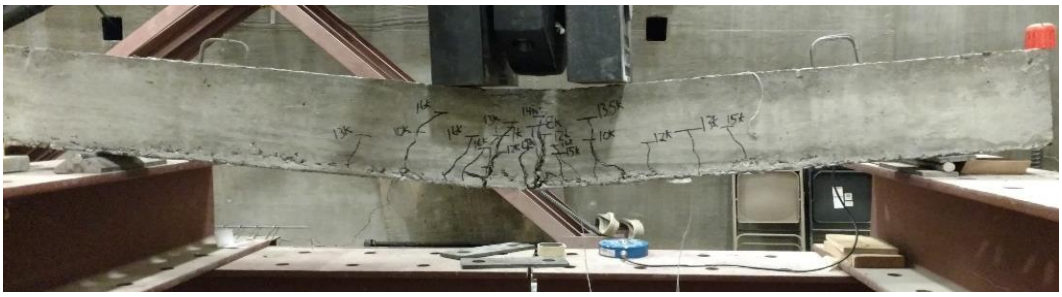

ST0.5-TC20 (ρ = 0.78%)

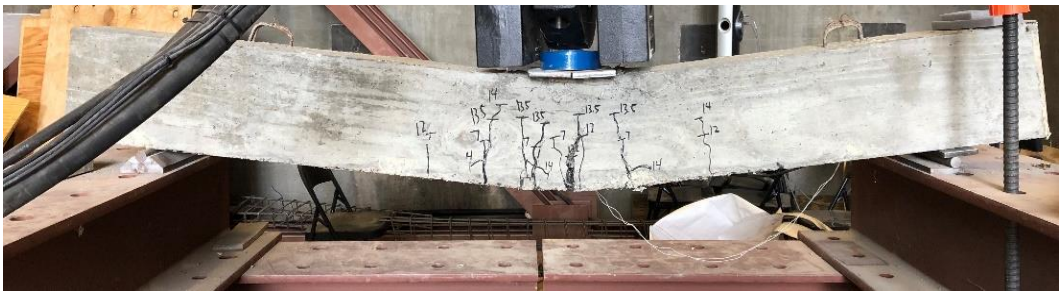

ST0.75-TC20 (ρ = 0.78%)

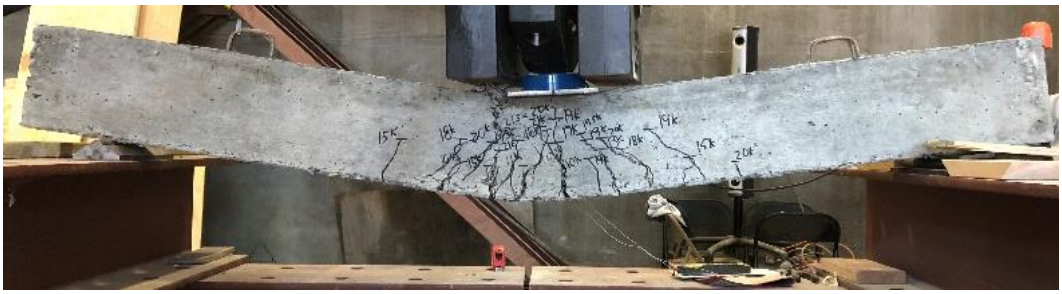

ST0.75-TC20 (ρ = 1.17%)

ST1.0-TC20 (ρ = 1.17%)

Figure 32. (Continued).

Table 25. Impact beam specimens mixture proportions by volume.

Designation	w/c	Cement Content, lb/yd³	% Steel Fiber (Volume Fraction)	% Tire Chip (Volume Fraction of CA)	% Coarse Aggregate (Volume Fraction)	% Fine Aggregate (Volume Fraction)
Control	0.42	611	0.00	0.00	100.00	100.00
ST0.0-TC20	0.42	611	0.00	20.00	80.00	100.00
ST0.75-TC20	0.42	611	0.75	20.00	80.00	100.00
ST1.0-TC20	0.42	611	1.00	20.00	80.00	100.00
ST1.0-TC0	0.42	611	1.00	0.00	100.00	100.00
ST0.75-TC0	0.42	611	0.75	0.00	100.00	100.00

Results from static load testing showed that the control and ST0.0-TC20 mixtures were nearing compressive failure at ρ values of 0.78 percent, while specimens consisting of steel fibers resisted compressive zone failure due to the fibers redistributing load and bridging large cracks. It was observed that specimens with ρ values of 1.17 percent exhibited twice the toughness of the specimens with ρ values of 0.78 percent. From these results, it was determined that had the control and ST0.0-TC20 mixture been designed for ρ = 1.17 percent, the beam would have experienced compression failure long before the tension steel yielded or fractured as a result of low ductility and compressive strength, respectively. From these results, the research team decided that the control and ST0.0-TC20 beams would be designed for ρ = 0.78 percent, while all other beams would be designed for ρ = 1.17 percent.

Impact Beam Testing Design and Procedure

The testing setup is shown in figure 33. The beams used for impact testing utilized the same beam design for static load testing. The beam was simply supported by a pin and roller. Uplift forces were restricted using two ½-inch-thick sheets of insulation between the beam and 2.0 inch × 6.0 inch (60 mm × 152 mm) planks of lumber. Threaded rods, 1.0 inch (25 mm) in diameter,

secured the planks and steel frame, and ultimately were embedded into the concrete strong floor for load transfer.

Figure 33. Photo. Anterior view of impact beam setup.

A 400 lb (181 kg) drop-weight was hung from a release mechanism in the center of a 20.0 ft × 1.0 ft × 1.0 ft (6.1 m × 0.3 m × 0.3 m) cross section vertical sleeve. The drop-weight was held in position by a crane until the time of testing. The drop-weight consisted of multiple components of smaller weights connected together, along with an attached accelerometer, as shown in figure 34. The accelerometer, which possesses a measurement rate of ±5,000 g pk (±160,870 ft/s^2 or 49,000 m/s^2), was set to a sampling rate of 20,000 Hz to capture vibration forces to convert to impact force. This was done as a supplement to a load cell to ensure peak impact force was accurately recorded. A load cell was positioned underneath the pinned support and two ½-inch steel plates. A sampling rate of 10,000 Hz was set for the load cell to balance its limitations with the need to capture the peak impact load. Unlike the accelerometer, the load cell captures the reactionary force of the beam itself, theoretically leading to potentially more valid data.

Finally, deflection at mid-span was recorded using the NDI Optotrak Certus HD motion capture camera used previously in the static testing. As in the static testing, two sensors were glued to the beam and the camera was set to record at 400 Hz per marker to fully measure the displacement–time history.

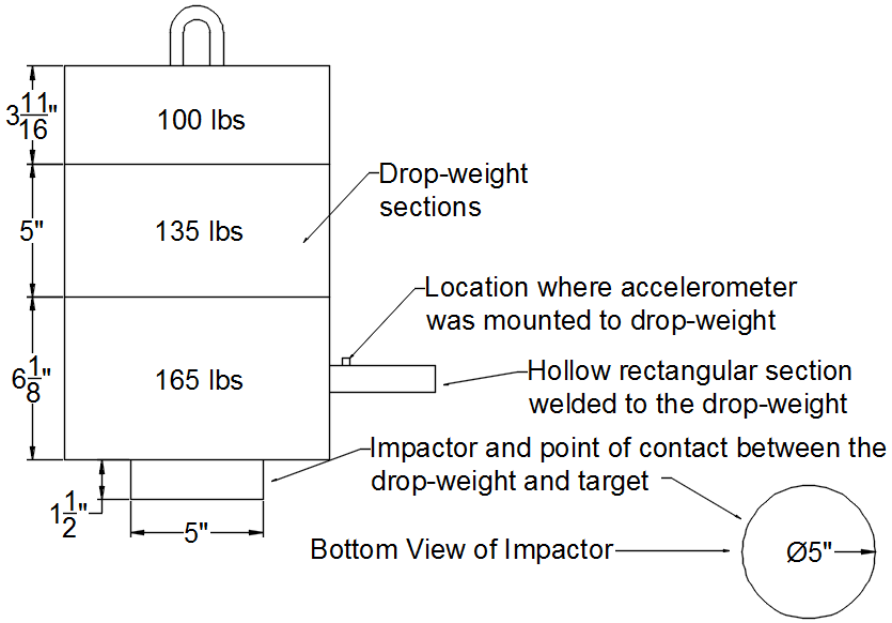

Figure 34. Image. Schematic of drop-weight and accelerometer placement location.

Fresh Concrete Properties

For quality control, fresh concrete properties were tested and reported, as shown in table 26.

Table 26. Fresh concrete properties of impact beam specimens.

Mixture Description	Slump (in.)	Temperature (°F)	Unit Weight (lb/ft³)	Air Content (%)
Control (ρ=1.17%)	4.5	59	143.4	6.10
ST0.0-TC20 (ρ=1.17%)	3.0	58	136.0	5.20
ST0.75-TC20 (ρ=1.17%)	2.0	79	142.0	4.50
ST1.0-TC20 (ρ=1.17%)	2.0	79	144.2	4.20
ST0.75-TC0 (ρ=1.17%)	2.5	81	149.6	4.00
ST1.0-TC20 (ρ=1.17%)	3.0	82	150.4	3.60

Hardened Concrete Properties

Compressive strengths for all impact beam specimens ranged from 3,406 psi (23.5 MPa) (ST0.0-TC20) to 7,601 psi (52.4 MPa) (ST0.75-TC0). Relative to the mixtures consisting of 100.00 percent volume fraction of coarse aggregate, the compressive strengths of mixtures that included tire chips decreased by 46.00, 48.00, and 37.00 percent for ST0.0-TC20, ST0.75-TC20, and ST1.0-TC20, respectively. All mixtures exceeded the minimum requirement of 3,000 psi (20.7 MPa) for GDOT Class A concrete and, with the exception of ST0.0-TC20, exceeded the minimum 3,500 psi (20.4 MPa) for GDOT Class AA Concrete. These compressive strengths are observed in table 27.

Table 27. Average 28-day compressive strength of impact beam cylinders.

Mixture Description	Compressive Strength (psi)
Control (ρ = 0.78%)	6,325
ST0.0-TC20 (ρ = 0.78%)	3,406
ST0.75-TC20 (ρ = 1.17%)	3,926
ST1.0-TC20 (ρ = 1.17%)	4,598
ST0.75-TC0 (ρ = 1.17%)	7,601
ST1.0-TC0 (ρ = 1.17%)	7,329

Impact Load Testing Results and Analysis

Mid-Span Displacement

The deflection at mid-span was compared between specimens to observe the ductility due to impact loading. The motion capture camera used was set to record data at a rate of 400 points per second to capture the displacement history from the initial point of impact until rest. Figure 35 illustrates the displacement–time history of the beam specimens after impact. The letters “A” through “G” denote the locations of the corresponding displacements, further shown in table 28.

To prevent overcrowding of letters within the figure, the lettering is only shown for ST0.0-TC20, as is done in subsequent figures representing displacement–time histories.

The data in table 28 show an increase in displacement at every point in mixtures that included tire chips relative to the corresponding mixtures that did not. The final displacements were taken when the beams reached equilibrium. Because it would not be valid to directly compare displacements between mixtures with steel reinforcement ratios of 0.78 and 1.17 percent, the change in displacement at each point relative to the final displacement was determined per beam and is shown in table 29. Specifically, points "A", "C", and "E" correspond to the first, second, and third impact experienced by the beam.

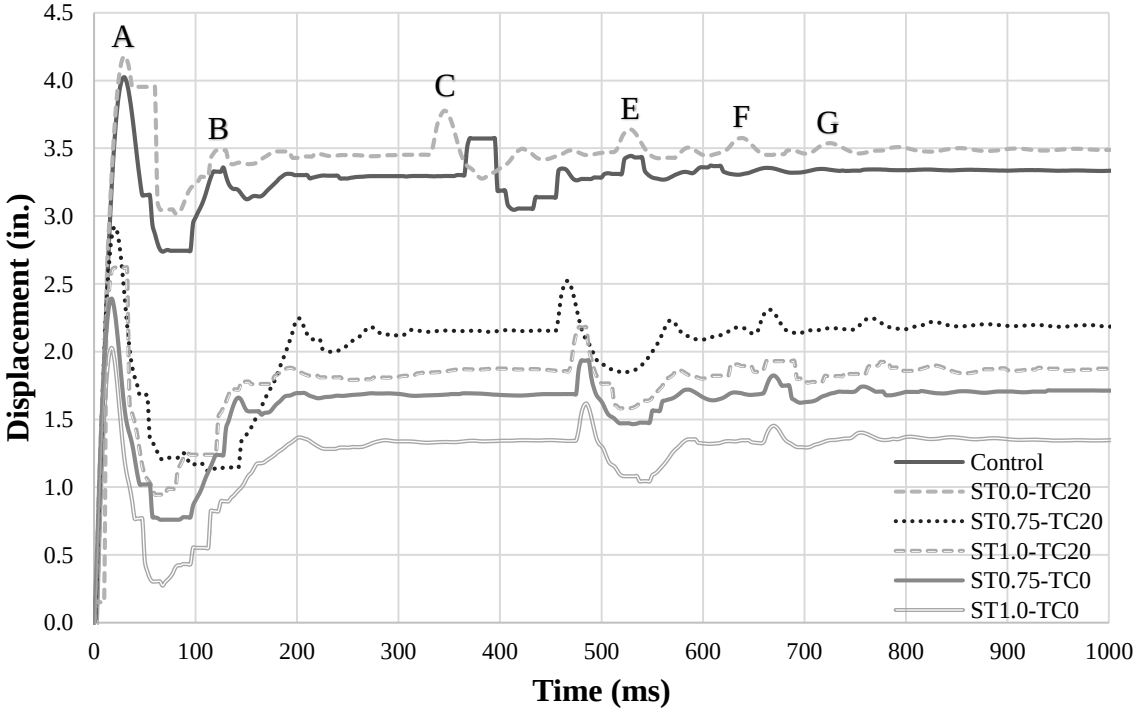

Figure 35. Graph. Displacement–time histories of impact beam specimens.

Table 28. Displacement–time histories of impact beam specimens.

Mixture Description	Displacement (inch)								Duration
	A	B	C	D	E	F	G	Final	Time, ms
Control (ρ = 0.78%)	4.02	3.36	3.57	3.34	3.43	3.37	—	3.34	780
ST0.0-TC20 (ρ = 0.78%)	4.18	3.48	3.78	3.51	3.64	3.57	3.54	3.51	998
ST0.75-TC0 (ρ = 1.17%)	2.39	1.64	1.933	1.717	1.81	1.74	—	1.71	897.5
ST0.75-TC20 (ρ= 1.17%)	2.92	2.24	2.52	2.21	2.3	2.25	—	2.19	985
ST1.0-TC0 (ρ = 1.17%)	2.03	1.37	1.62	1.35	1.45	1.4	—	1.34	950
ST1.0-TC20 (ρ = 1.17%)	2.62	1.88	2.18	1.86	1.93	1.92	1.89	1.87	1,020

Note: — = No data

Impact Forces

The impact forces recorded by the load cell and accelerometer are shown in table 30. From the data, the load cell clearly was unable to register the peak impact forces for all specimens below 1.00 percent steel fiber volume fraction. The accelerometer data correlate to the impact response of the drop-weight, providing an impact force for all beams tested with greater confidence. The load cell missed the peak impact force because of the rebounding effects of the drop-weight impacting the beam and causing the beam to bounce in the air for a short time during which the supports were not in contact with the beam.

Table 29. Change in displacement for impact beam specimens.

Mixture Description	Change in Displacement Relative to Final Displacement, in						
	A	B	C	D	E	F	G
Control (ρ=0.78%)	0.68	0.02	0.23	0.00	0.09	0.03	—
ST0.0-TC20 (ρ=0.78%)	0.67	−0.03	0.27	0.00	0.13	0.06	0.03
ST0.75-TC0 (ρ=1.17%)	0.68	−0.07	0.22	0.01	0.10	0.03	—
ST0.75-TC20 (ρ=1.17%)	0.73	0.05	0.33	0.02	0.11	0.06	0.03
ST1.0-TC0 (ρ=1.17%)	0.69	0.03	0.28	0.01	0.11	0.06	—
ST1.0-TC20 (ρ=1.17%)	0.75	0.01	0.31	−0.01	0.06	0.05	0.02

Note — = No data

Table 30. Comparison of peak impact forces.

Mixture Description	Peak Impact Force from Load Cell, kips	Peak Impact Force Determined from Accelerometer, kips
Control (ρ=0.78%)	12.0	471
ST0.0-TC20 (ρ=0.78%)	15.4	305
ST0.75-TC0 (ρ=1.17%)	73.6	359
ST0.75-TC20 (ρ=1.17%)	36.2	356
ST1.0-TC0 (ρ=1.17%)	383.0	438
ST1.0-TC20 (ρ=1.17%)	311.0	365

Failure Modes of Impact Beams

The failure modes experienced by each beam are shown in table 31, and are further illustrated in Figure 36 and Figure 37. Analysis of the crack propagations from the testing specimens indicates that specimens with 1.00 percent fiber volume fractions were able to successfully prevent shear failure.

Table 31. Failure modes of impact beam specimens.

Mixture Description	Failure Mode
Control (ρ = 0.78%)	Flexural/Crushing/Shear Failure
ST0.0-TC20 (ρ = 0.78%)	Flexural/Crushing/Shear Failure
ST0.75-TC0 (ρ = 1.17%)	Flexural/Crushing/Shear Failure
ST0.75-TC20 (ρ = 1.17%)	Flexural/Crushing/Shear Failure
ST1.0-TC0 (ρ = 1.17%)	No Failure; flexural cracks developed
ST1.0-TC20 (ρ = 1.17%)	No Failure; flexural cracks developed

Both tire chip and steel fiber inclusion produced an increase in energy dissipation capacity of the RC beams subjected to impact forces. Specifically, the primary effect of tire chip inclusion is an increase in displacement and an increase in duration of testing time. It was observed that a steel fiber volume fraction of 1.00 percent was crucial in achieving a global failure response.

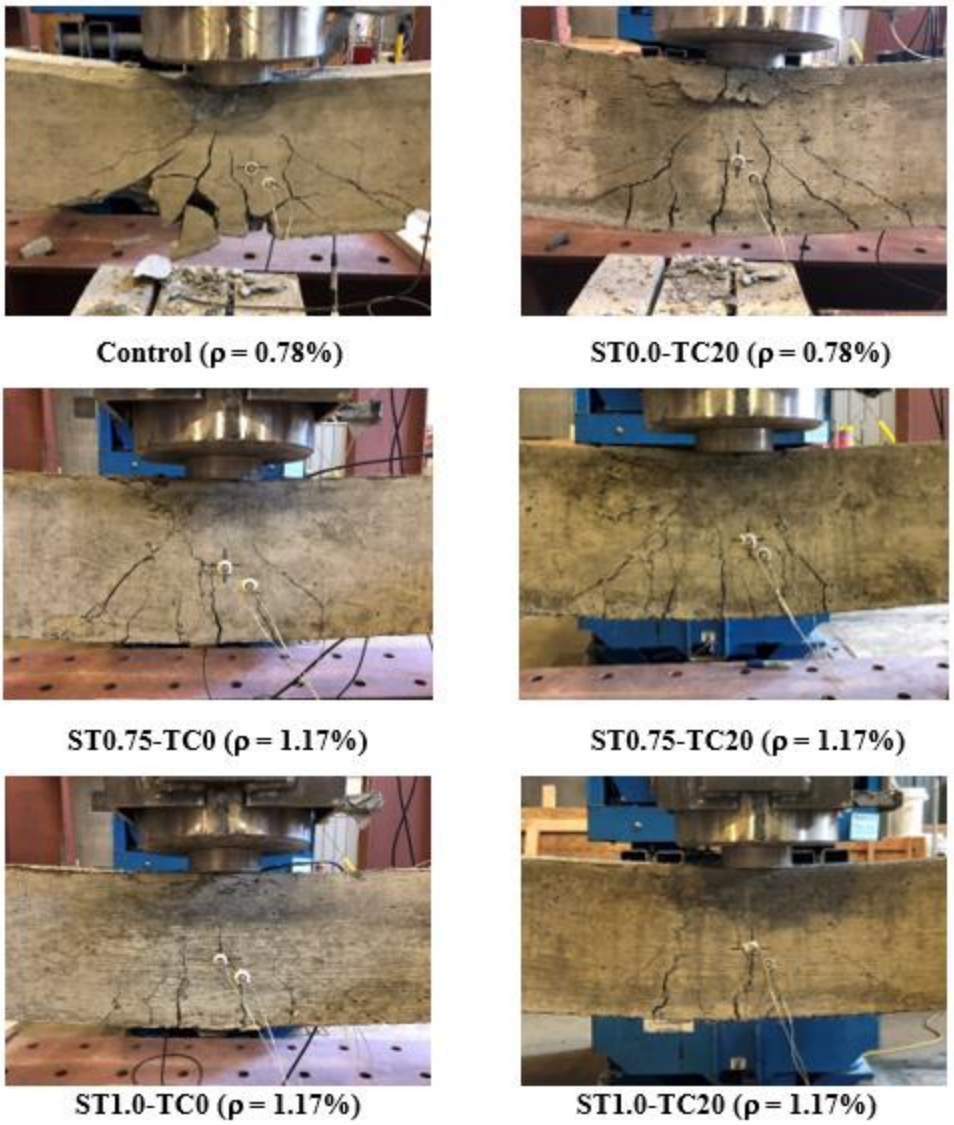

Figure 36. Photos. Anterior view of fractured impact beam specimens.

MIXTURE OPTIMIZATION CONCLUSIONS

Based on the testing discussed within this chapter, the following conclusions were drawn:

- At a 20.00 percent replacement of coarse aggregate by volume, tire chips significantly reduced mechanical properties such as compressive and flexural strength due to reduction in stiffness and greater susceptibility to failure in the cement interfacial transition zone from poor bonding relative to natural coarse aggregate.

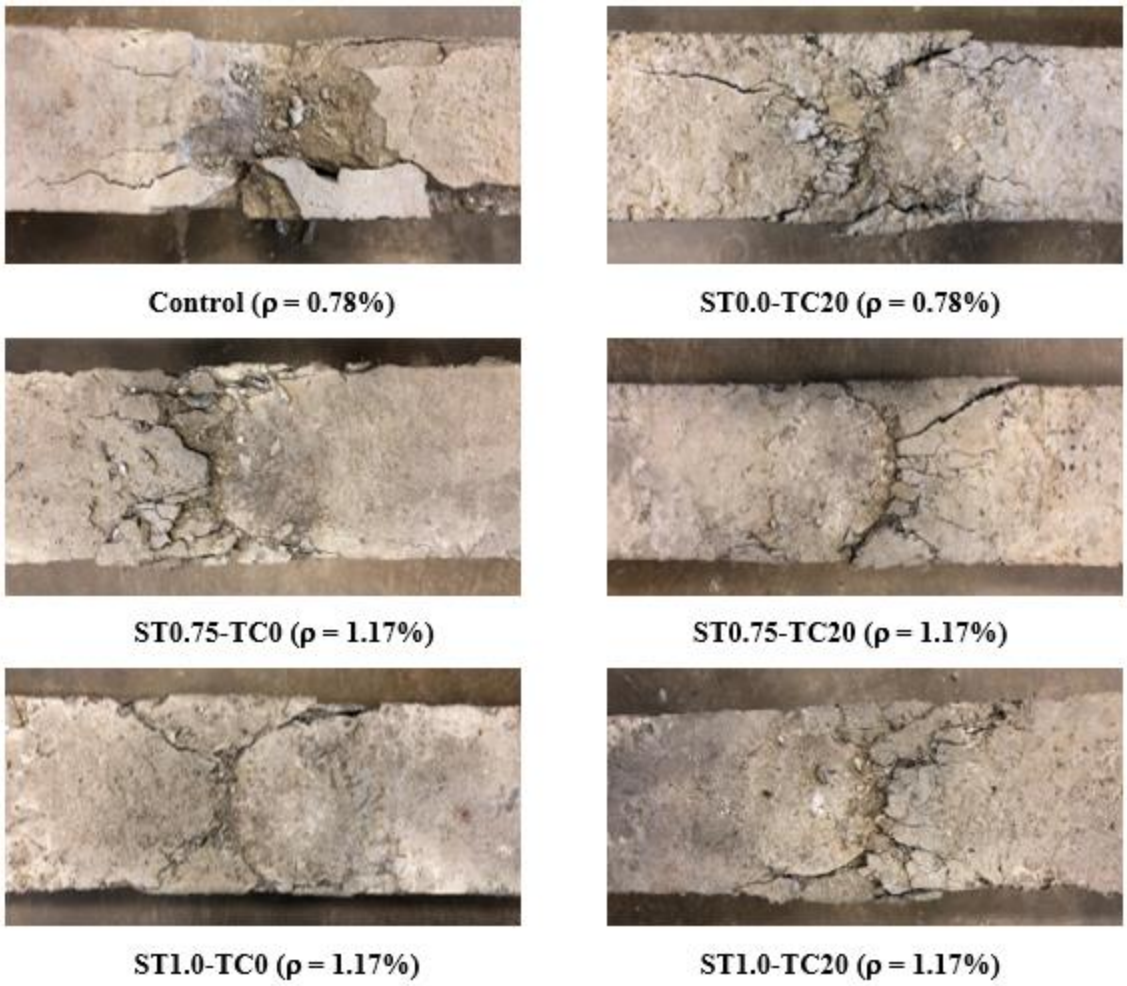

Figure 37. Photos. View of contact surface of fractured impact beam specimens.

- In rubberized mixtures containing fiber reinforcement, steel fibers proved to be the most effective in reversing the adverse effects tire chip inclusion has on mechanical properties, as well as maintaining workability.
- While 0.75 percent steel fiber volume fraction exhibited greater impact resilience than the 1.00 percent specimens with small-scale drop-hammer testing, 1.00 percent performed better than 0.75 percent in large-scale testing. Thus, a 1.00 percent volume fraction will be used moving forward within the project.

- The duration of the displacement–time history in conventional RC beams is increased through the inclusion of tire chips and steel fibers. Greater target rebounding effects are observed due to increased displacement recovery.
- Ultimately, in the next phase of the study a 20.00 percent replacement of coarse aggregate by volume and a 1.00 percent inclusion of steel fiber volume fraction will be used within the large-scale CMB testing, which is discussed in the subsequent chapter.

CHAPTER 4. FINITE ELEMENT MODELING AND LABORATORY-SCALE TESTING OF BARRIER WALL

FINITE ELEMENT MODELING

The finite element analysis performed in this study was divided into three parts: (1) drop-weight impact test on reinforced concrete beam, (2) barrier impact test, and (3) vehicle crash test analysis. The test setups and the modeling features are discussed in the following sections.

DROP-WEIGHT IMPACT TEST ON REINFORCED CONCRETE BEAM MODEL

Geometry

A reinforced concrete beam model of dimensions 8.5 ft length × 0.5 ft width × 10.0 inches height (2,286 mm × 152 mm × 254 mm) was created using ANSYS 18.2 DesignModeler. The geometry of the beam model was taken from the experimental drop-weight testing setup completed during the fiber-reinforced rubberized concrete static and impact testing phase of this investigation. The drop-weight (impactor) for the analysis was created using ANSYS 18.2 DesignModeler. The beam geometry shown in figure 27 and figure 28 was used for analytical investigation of the drop-weight test. The impactor geometry utilized for the drop-weight impact analytical investigation is shown in figure 38.

Boundary Conditions and Test Setup

In the experimental study, the impactor was positioned at the mid-span of the reinforced concrete beam at the height of 20.0 ft (6.1 m). The free-fall velocity of the impactor when it hits the beam was calculated as 35.9 ft/s (10.9 m/s). In the analytical study, the impactor was positioned 0.04 inch (1 mm) above the RC beam and the calculated velocity of 35.9 ft/s (10.9 m/s) was

assigned to it. Fixed boundary conditions were applied to the base of the supports. The analysis (and all the subsequent analyses described in this study) was performed using LS-DYNA version R9.0.1, as shown in figure 39. The reinforced concrete beam and impactor finite element mesh model is shown in figure 40.

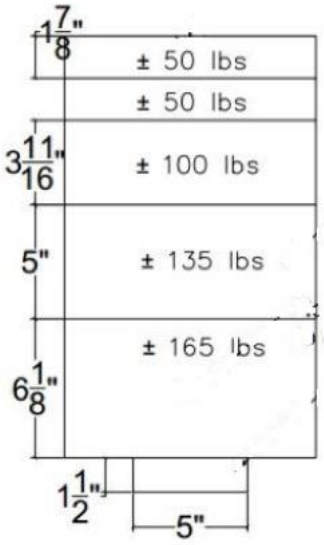

Figure 38. Image. Impactor geometry (for 500 lb drop-weight).

Material

A steel reinforcement with a yield strength of 60,000 psi (413.7 MPa) and a Young's modulus of 29,000 ksi (200 GPa) was used in both the experimental and analytical investigation. For each simulation, either RHT or continuous surface cap model (CSCM) material was used to model concrete for the reinforced concrete beam investigated in the study. The plastic kinematic material model that takes strain rate effects into account was used to model the reinforcement in the beam. The supports and the impactor were assigned elastic material for grade 50 steel. The impactor was modeled as a rigid body member.

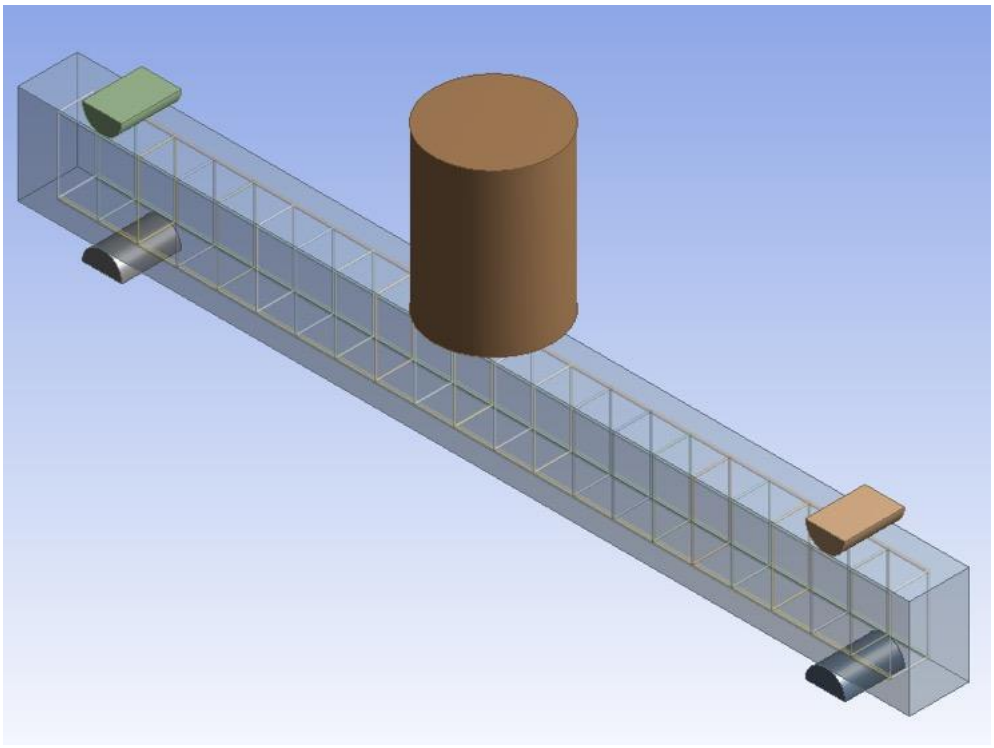

Figure 39. Image. Finite element model of beam impact test.

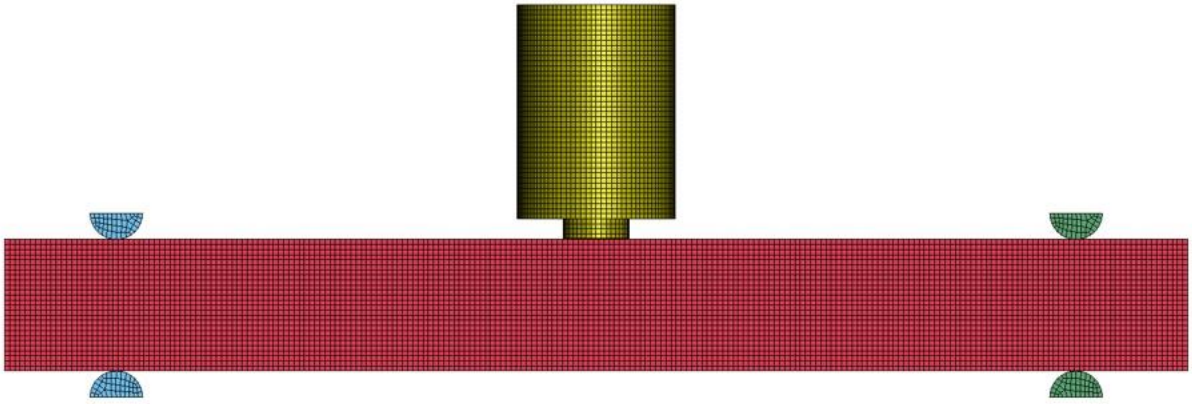

Figure 40. Image. Meshed RC beam and impactor model.

Element Types and Mesh Size

A mesh sizing of 0.4 inch (10 mm) was selected for this analysis. The reinforced concrete beam and the impactor were modeled using eight node solid elements. The rebars were modeled using beam elements.

Contact

The constraint between rebar and concrete was defined using the 'Lagrange in solid' formulation. The contact between the reinforced concrete beam and the impactor was defined using the 'automatic surface to surface' formulation. The contact between the reinforced concrete beam and the supports was defined using the same formulation. The 'Automatic beam to surface' formulation was used to define the contact between the impactor and rebars.

Summary of Findings

The experimental data of the mid-span displacement and peak impact force of the control beam test with the values found in analyses using the CSCM and RHT model are shown in figure 41 and figure 42. In addition, those figures compare the experimental findings from the modified reinforced concrete beam tests to the analysis results using CSCM material. A summary of the predicted peak impact force and peak mid-span displacement for the reinforced concrete beams incorporating steel fiber only (ST1.0-T0) and steel fiber and tire chips (ST1.0-TC20), before and after modification of the RHT concrete model, is presented in figure 43 and figure 44.

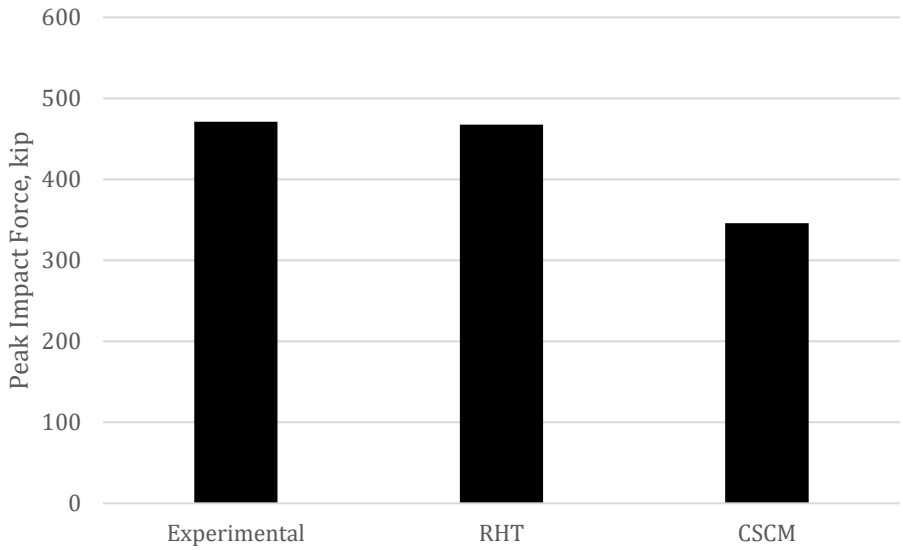

Figure 41. Graph. Comparison of peak impact force prediction using the RHT and CSCM materials for the control beam.

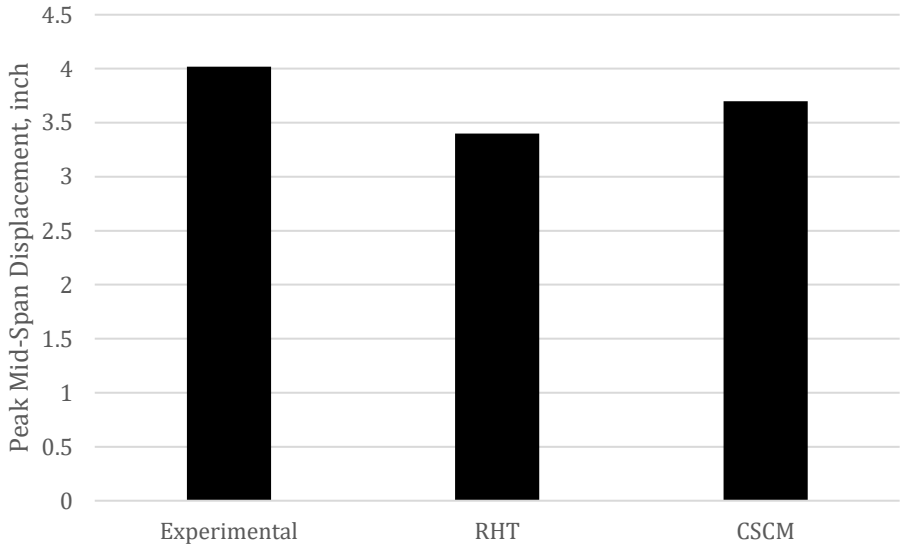

Figure 42. Graph. Comparison of peak mid-span displacement prediction using the RHT and CSCM materials for the control beam.

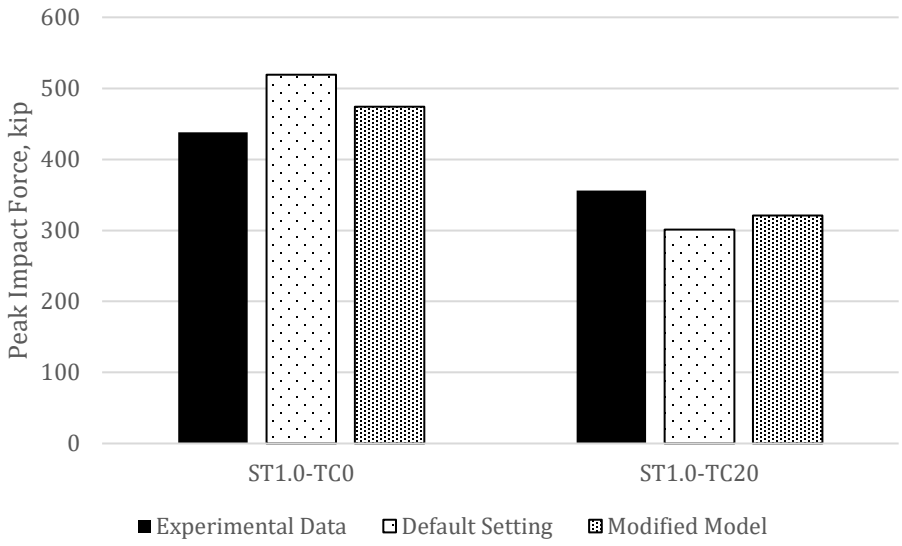

Figure 43. Graph. Summary of peak impact forces using default and modified RHT parameters for the modified RC beams.

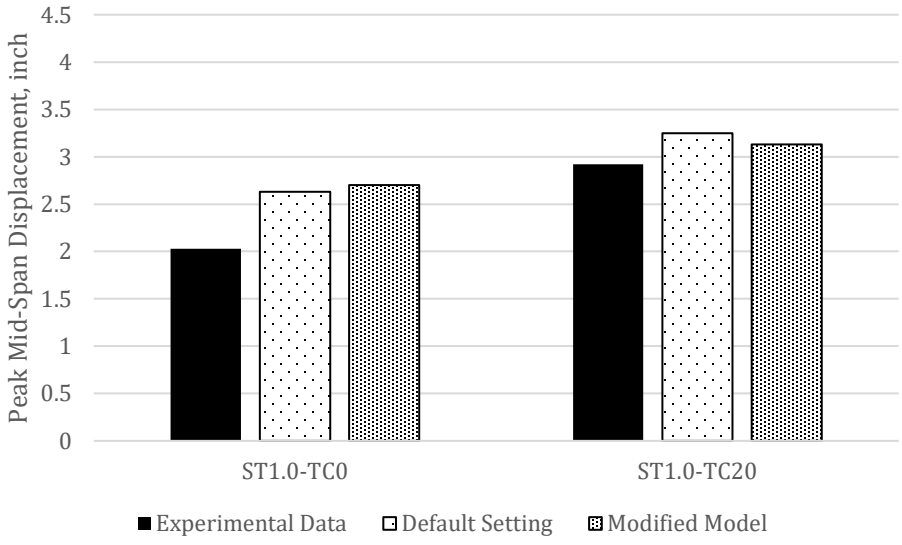

Figure 44. Graph. Summary of peak mid-span displacements using default and modified RHT parameters for the modified RC beams.

In this study, it was assumed that concrete modified with steel fiber and tire chips acts as a homogeneous material. Thus, instead of modeling steel fiber and tire chips in the concrete, the research team attempted to model the changes brought in concrete behavior due to the incorporation of steel fiber and tire chips into the concrete mixture design. Using the RHT material model, the peak and post-peak behaviors of the concrete (in the analytical model/description of concrete) were changed so that the impact force and displacement properties of modified reinforced concrete beams can be predicted. Wang et al. (2017) followed a similar approach to model the behavior of fiber-modified concrete using the RHT material model. In their study, Wang et al. performed experimental tests on concrete with different percentages of fiber replacements. Using the experimental results, modifications were brought into the RHT material model after repeated simulations. For each different volume fraction of fiber in concrete, a different modified model of RHT material was recommended.

The impact test analysis of the control beam showed that using CSCM material results in an impact force different from the experimental data by a large margin (i.e., 26.00 percent less than the experimental value). This discrepancy with the experimental data resulting from analysis with different material models is not unexpected. For example, Brannon and Leelavanichkul (2009) used the RHT material model and CSCM for a numerical simulation of penetration and perforation of high-performance concrete with a steel projectile. In that study, using CSCM material for concrete resulted in a residual velocity of the projectile 12.37 percent higher than the experimental value, whereas RHT material resulted in a residual velocity of the projectile 9.27 percent less than the experimental value.

The beam drop-weight impact study was validated against three experimental beam tests. The RHT material model was found more suitable for modeling steel fibers and tire chips–modified

concrete when compared to the CSCM. For this reason, the RHT material model is recommended for use in modeling the safety barrier crash analysis.

BARRIER IMPACT TEST

Geometry

A cast-in-place concrete median barrier finite element model was developed from the drawings provided by GDOT using ANSYS 18.2 DesignModeler. A steel impactor model of dimensions 4.5 ft long × 4.5 ft wide × 1.0 ft high (1,372 mm × 1,372 mm × 305 mm) was created using ANSYS 18.2 DesignModeler. The length of the barrier was 20.0 ft (6.1 m). The part of the barrier beneath the pavement level is referred to as the *base* in the following sections. For use in the vehicle crash test simulation, the length of the barrier was extended to 75.5 ft (23.0 m).

Boundary Conditions and Test Setup

The bottom face of the base was fixed in its position. The sides of the base were constrained in the transverse direction using a displacement boundary condition, and the two ends of the barrier were constrained in the longitudinal direction using a displacement boundary condition. The objective of this analysis was to evaluate the level of damage sustained by the barrier for a 120~150 kips (534~667 kN) impact force. In conformance with the experimental test setup, the glare screen component of the model was not considered in this analysis. The impactor struck the barrier at a height of 30.0 inches (762 mm) above the pavement level. Figure 45 shows the finite element model for the barrier wall impact test.

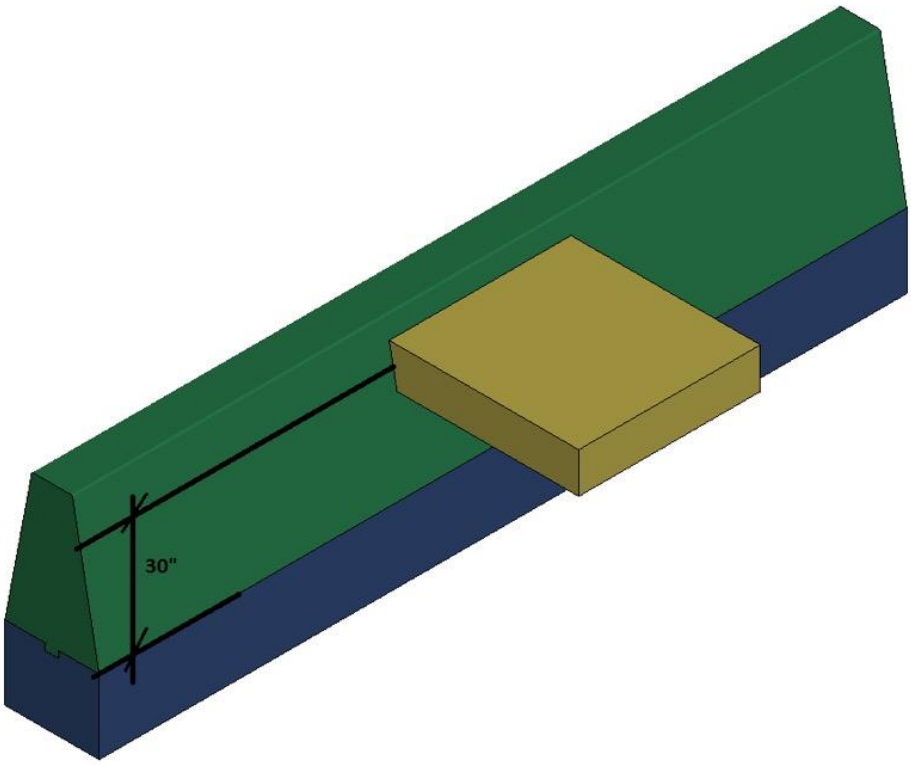

Figure 45. Image. Finite element model showing the barrier impact test.

Material

Similar to the reinforced concrete beam study, the steel reinforcement possessed a yield strength of 60,000 psi (413.7 MPa) and a Young's modulus of 29,000 ksi (200 GPa). The RHT material model was used to model the concrete in the barrier. A plastic kinematic material model was used to model steel reinforcements in the barrier, taking strain rate effects into account. The impactor was assigned elastic material for Grade 50 steel, and it was modeled as a rigid body member. Concrete properties were taken from the control and ST1.0-TC20 mixture results from the fiber-reinforced rubberized concrete mixture investigation earlier in the study.

Element Types and Mesh Size

The mesh sizing selected for this study (figure 46) was 0.8 inch (20 mm). The barrier and the impactor were modeled using eight-node solid elements. The steel reinforcements were modeled using beam elements and are illustrated in figure 47.

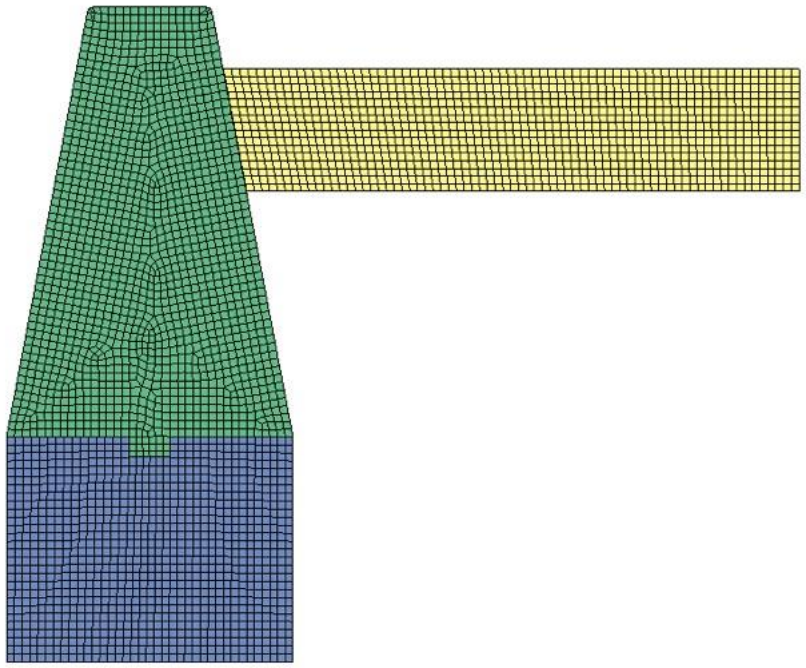

Figure 46. Image. Barrier impact test model showing the mesh size.

Contact

The constraint between reinforcements and concrete was defined using the 'Lagrange in solid' formulation. The contact between the barrier and the impactor was defined using the 'automatic surface to surface' formulation. The contact between the base and the barrier was defined using the 'automatic surface to surface' formulation. The 'automatic nodes to surface' formulation was used to define the contact between the impactor and the rebars. The coefficient of friction between concrete parts was selected as 0.6.

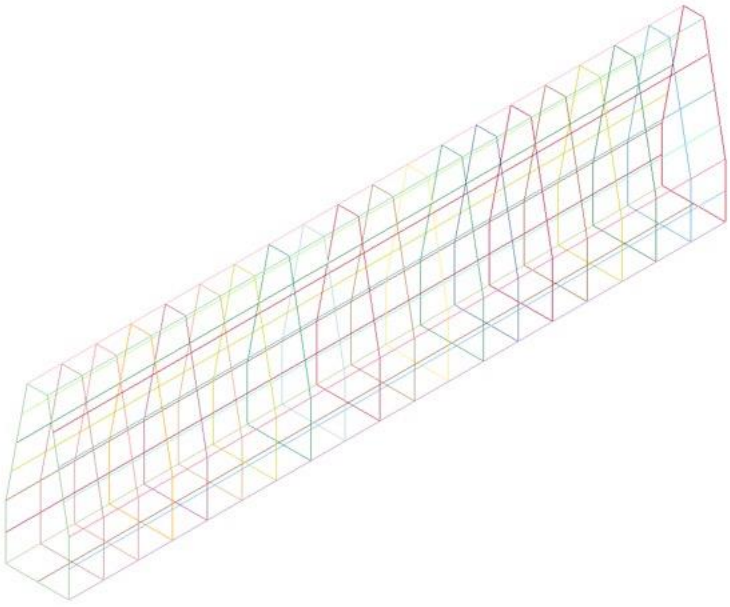

Figure 47. Image. Rebar layout in the barrier and the base.

Summary of Findings

The analysis results including the impact force history, displacement history, axial force, stresses in the reinforcement, and stress distributions in the concrete barrier are presented below. The results indicate the barriers experience minor damage from a solid steel impact, which is anticipated as the single-slope concrete barrier is designed to resist such magnitude of impact.

The aim of the barrier impact analysis was to determine the response of the barrier for an impact force of 150.0 kip (667 kN). After repeated simulations, it was determined that a velocity of 0.2 mph (85 mm/s) of the impactor results in an impact force of 156.0 kip (694 kN). The same velocity of the impactor resulted in an impact force of 137.0 kip (608 kN) for the barrier model analyzed with the ST1.0-TC20 mixture. The time histories of the impact forces for both barriers are presented in figure 48 and figure 49.

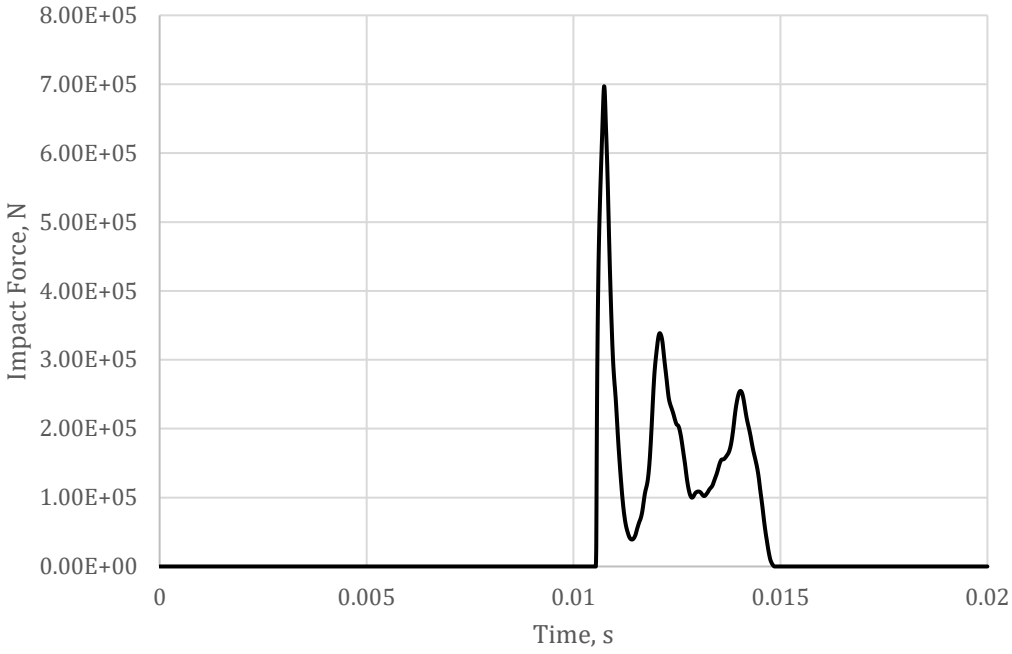

Figure 48. Graph. Impact force–time history of the control barrier.

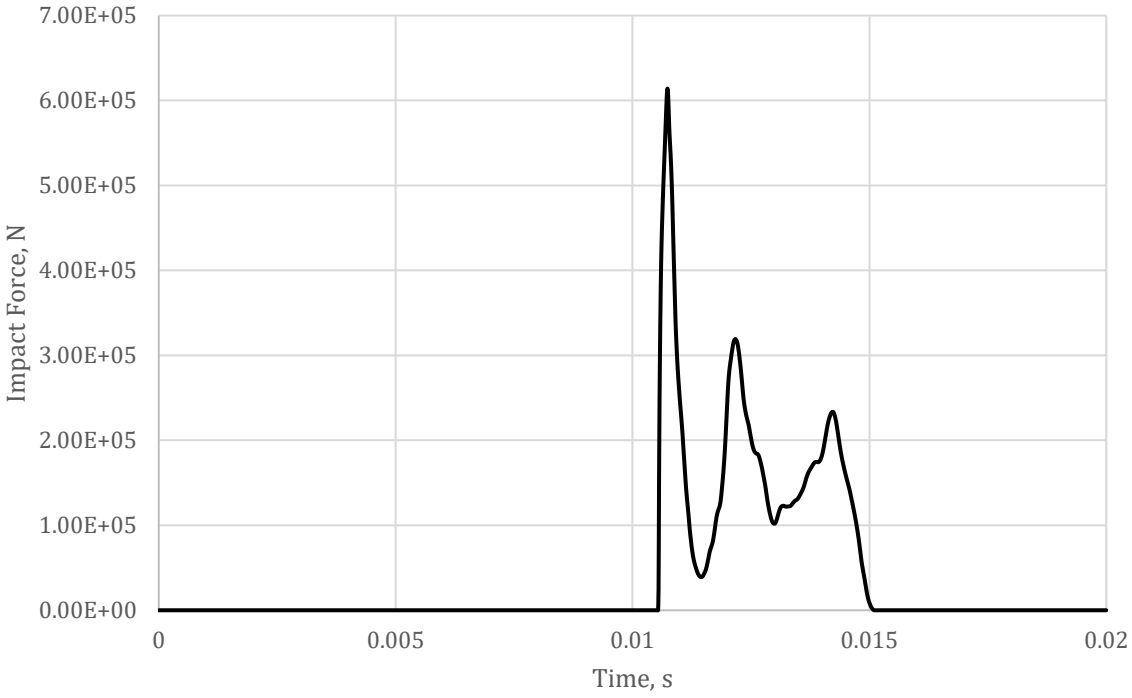

Figure 49. Graph. Impact force–time history of the ST1.0-TC20 barrier.

Figure 50 shows the barrier displacement histories for two cases (control and ST1.0-TC20) at the center of the impacted surface. The peak displacement is 0.005 inch (0.126 mm) and 0.006 inch (0.141 mm) for barriers made with the control and ST1.0-TC20 mixtures, respectively.

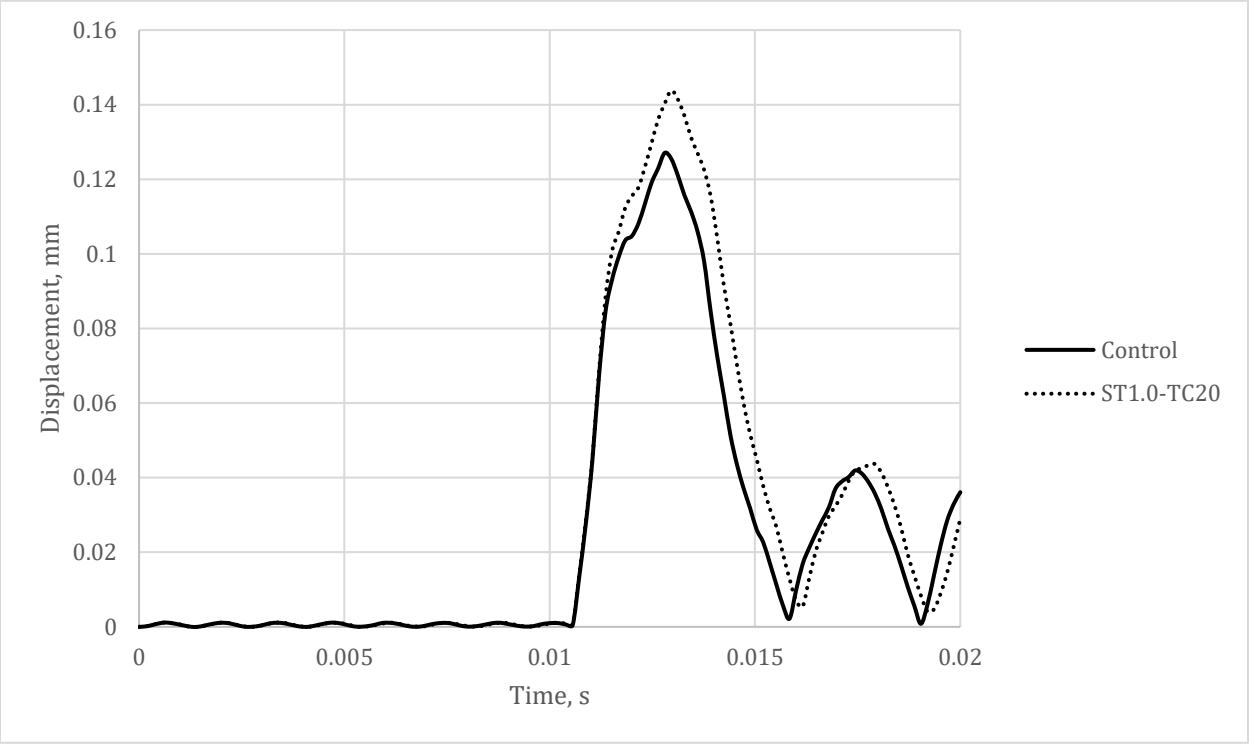

Figure 50. Graph. Displacement–time history at the center of the impacted surface.

An investigation into the axial force distribution was performed in order to predict the peak compressive and tensile stresses of the horizontal bars at the distal and impacted sides of the barrier, as well as the vertical bars of the control barrier at the time of impact (t = 0.0107 s) and after impact. The results of this investigation are presented in figure 51 to figure 53. As shown, the stress in the reinforcements remained within the elastic limit of material. Tensile stress dominated in the horizontal bars at the opposite side of the impact, and compressive stress dominated in the horizontal bars at the impacted side. Vertical bars were in tension at the side of the impact and in compression at the distal side. Vertical bars were subjected to maximum

tension at the horizontal shear key between the barrier and the base. The stress values of the reinforcements of the ST1.0-TC20 barrier also remained within the elastic limit.

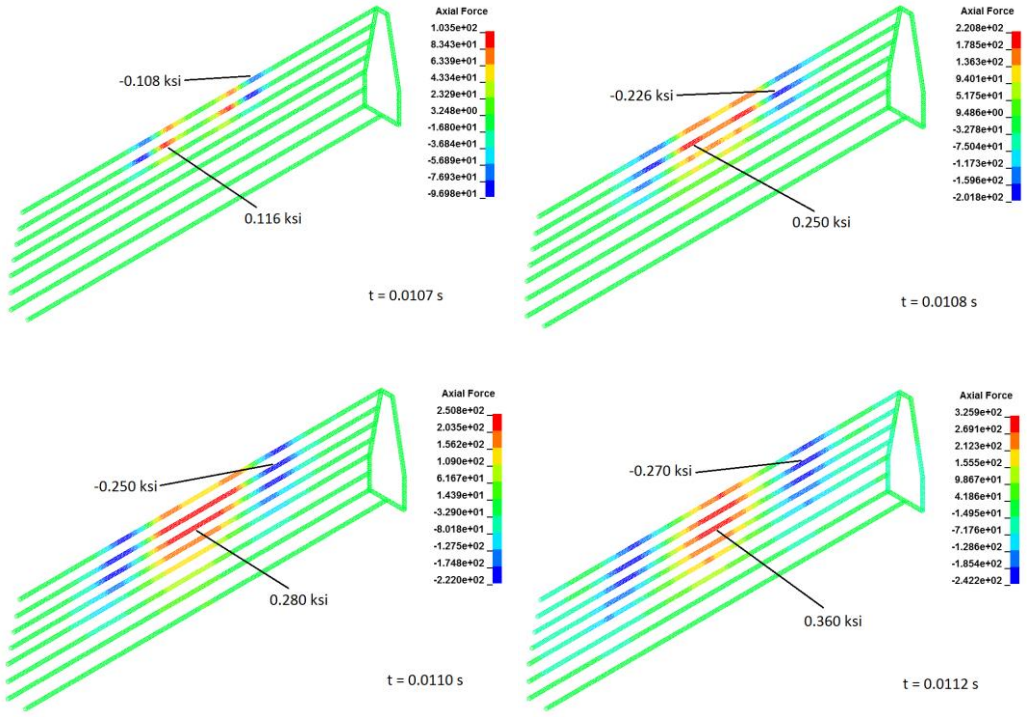

Figure 51. Images. Axial force distribution (unit: N) and compressive and tensile stresses in the horizontal bars at the distal side of the control barrier at various times after impact.

Figure 54 shows the stress distribution in the concrete barrier at the time of impact and immediately (0.0001 s) after impact. The barrier did not undergo significant structural damage because the stress in the materials remained in the elastic range. Table 32 and table 33 provide a summary of the peak stresses, and they are significantly lower than the compressive or tensile strength of the two concrete mixtures.

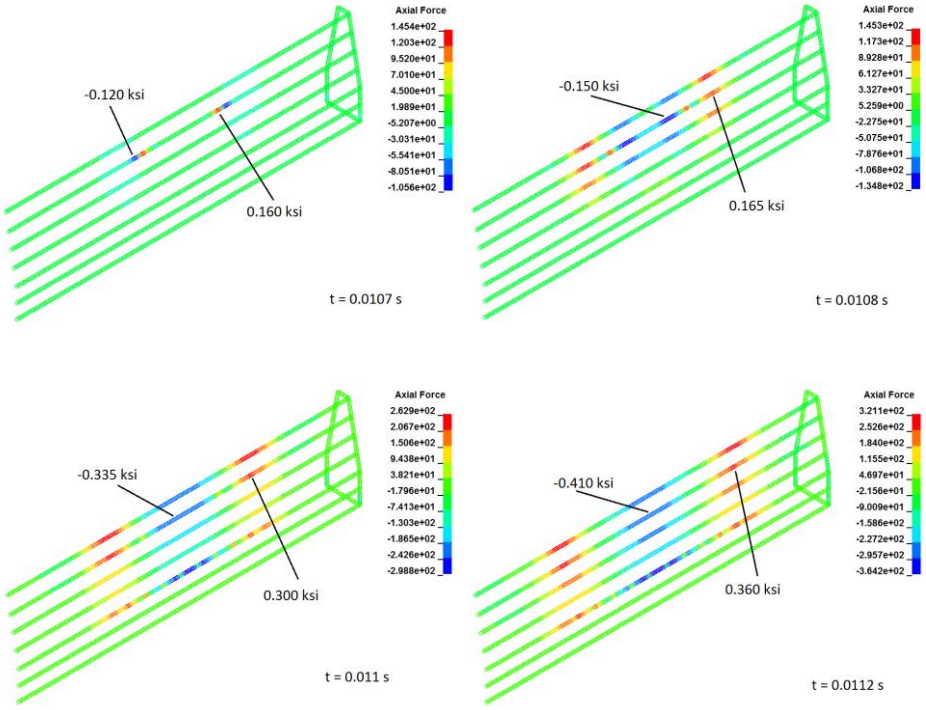

Figure 52. Images. Axial force distribution (unit: N) and compressive and tensile stresses in the horizontal bars at the impacted side of the control barrier at various times after impact.

CRASH TEST ANALYSIS OF PICKUP TRUCK MODEL

Geometry

A 2007 Chevrolet Silverado vehicle finite element model was used for the vehicle crash test simulation investigation. This truck model was developed at the Center for Collision Safety and Analysis (CCSA) laboratory at George Mason University (Mohan et al. 2009). This model is the version 3a coarse model, as specified on the CCSA website, and was released in December 2016. In addition, it conforms to the *AASHTO MASH 2016* requirements for 2270P vehicles.

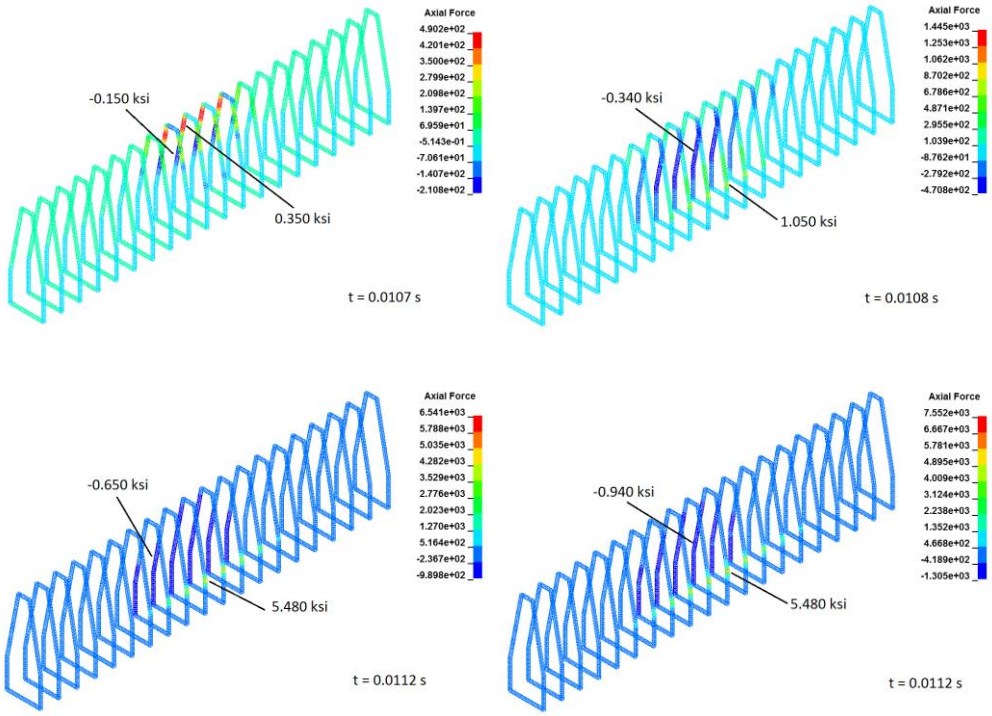

Figure 53. Images. Axial force distribution (unit: N) and compressive and tensile stresses in the vertical bars of the control barrier at various times after impact.

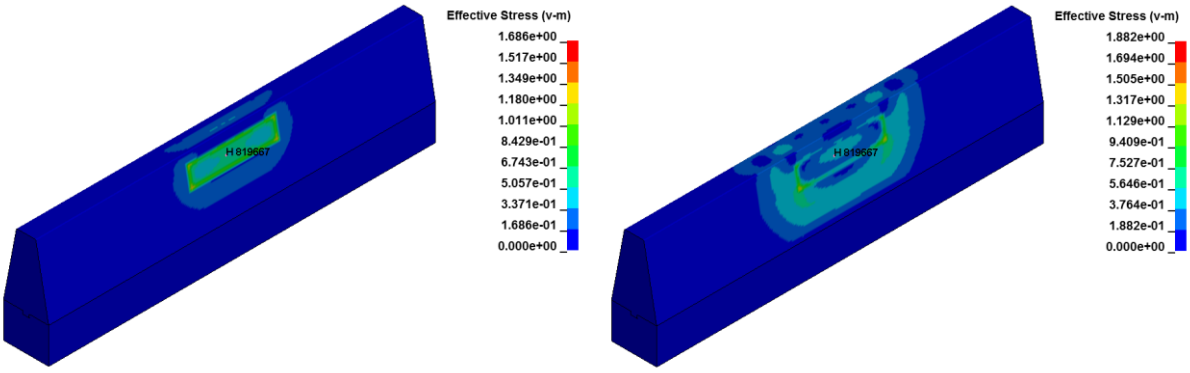

(a) **(b)**

Figure 54. Images. Effective stress distribution in the barrier: (a) at time of impact, (b) immediately after impact (unit: N/mm^2).

Table 32. Summary of peak concrete stresses at time of impact.

Barriers with	Peak Stress (psi), Impact Side		Peak Stress (psi), Distal Side	
	Compressive	Time, s	Compressive	Time, s
Control mixture	243	0.0107	97	0.0107
ST1.0-TC20 mixture	217	0.0107	85	0.0107

Table 33. Summary of peak concrete stresses immediately after impact.

Barriers with	Peak Stress (psi), Impact Side		Peak Stress (psi), Distal Side	
	Compressive	Time, s	Compressive	Time, s
Control mixture	272	0.0108	104	0.0108
ST1.0-TC20 mixture	245	0.0108	97	0.0108

The 2007 Chevrolet Silverado is a 4-door, crew cab, short box pickup truck weighing 5,152 lb (2,337 kg). It has a 4.8L V8 engine and an M30 four-speed automatic transmission. The tire size is P245/70R17. The CCSA website mentions that the finite element model includes structural component details, suspension system details, and a uniform meshing so that it is able to support multi-mode impacts. The vehicle model was meshed at the CCSA laboratory. It has 251,400 elements, 262,061 nodes, and 603 parts. The average mesh size is 0.6–1.0 inch (15–25 mm) with a minimum size of 0.3 inch (7 mm).

Test Setup

The objective of this analysis was to investigate the outcomes of the pickup truck colliding with a cast-in-place concrete median barrier at a speed of 62 mph (100 km/h) at an angle of 25 degrees, as shown in figure 55. The same barrier wall specifications utilized in the earlier laboratory-scale barrier wall testing was used for this analysis. The length of the barrier, the

vehicle model, the speed, and the angle of the collision satisfy the criteria for test level 3-11 as specified in *NCHRP Report 350* and *AASHTO MASH 2016*.

Contact

The contact between the barrier and the truck was defined using the 'automatic surface to surface' formulation. The contact between the steel reinforcement of the barrier and the vehicle was defined using the 'automatic nodes to surface' formulation.

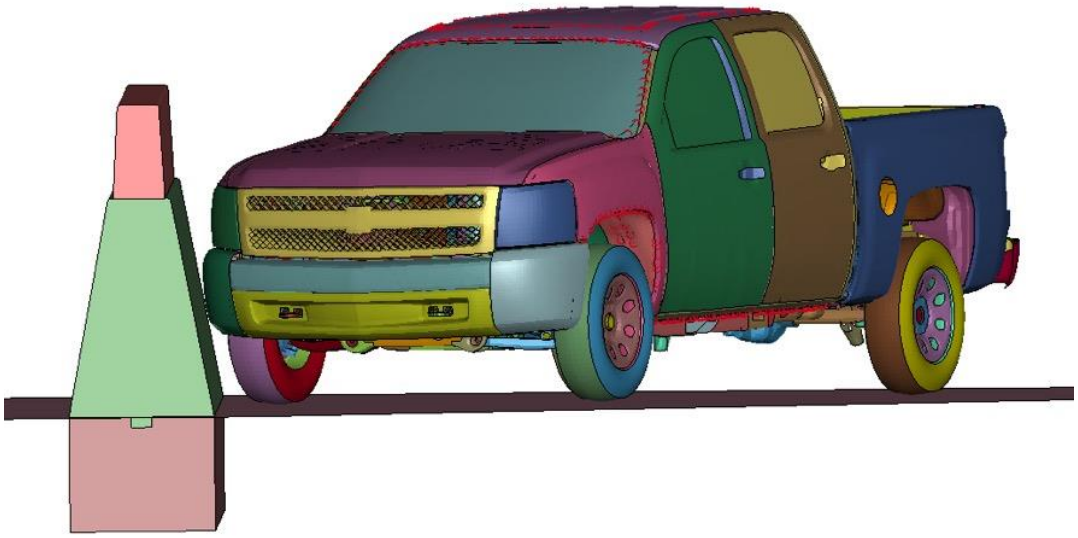

Figure 55. Image. Vehicle model positioned at 25 degrees with respect to the barrier.

Summary of Findings

Results from the crash test analysis of the pickup truck revealed that the concrete barrier is capable of resisting the impact force, and the damage sustained in the barrier is minor, regardless of the concrete material models adopted. The impact force–time histories of ST1.0-TC0 and ST1.0-TC20 revealed significant reduction in impact force when compared to the

impact force–time history of the control barrier (see figure 56). The peak impact force due to the vehicle collision was 168.0 kip (750 kN) in the case of the control barrier. In case of the ST1.0-TC0 barrier, the peak impact force was 44.5 kip (198 kN), which is 73.50 percent lower than the peak impact force produced by the control barrier. In the case of the ST0.75-TC20 barrier, the peak impact force was 41.4 kip (184 kN), which is 75.30 percent lower than the peak impact force generated by the control barrier.

Table 34 provides a summary of peak compressive stresses in the concrete barriers. The magnitude of tensile stress in the concrete barrier was negligible. The effective stress distribution in the concrete barriers at 0.30 s considering different concrete mixtures (i.e., control, ST1.0-TC0, and ST1.0-TC20) is shown in figure 57. Table 35 provides a summary of peak tensile and compressive stresses in the steel reinforcements of the barrier. The shear reinforcements (U.S. #5 bars) on the side of impact at the shear key of the barrier and the base were subjected to peak tensile stress. The shear reinforcements on the distal side were subjected to maximum compressive stress.

A comparison of the post-impact behavior of the vehicle model after collision with the control, ST1.0-TC0, and ST1.0-TC20 barriers was performed and revealed similar behavior between the three barriers. The crash test simulation involving the Chevrolet pickup truck indicated that the vehicle was immediately redirected from the impact and ran parallel to the barrier. Following the initial impact, the back portion of the vehicle collided with the barrier for the second time. The barrier models sustained no significant damage in the pickup truck collision simulations. The resultant velocity of the vehicle after collision with all three barriers decreased by about 6.8 mph (11.0 km/h) from the applied velocity of 62 mph (100 km/h) after the collision.

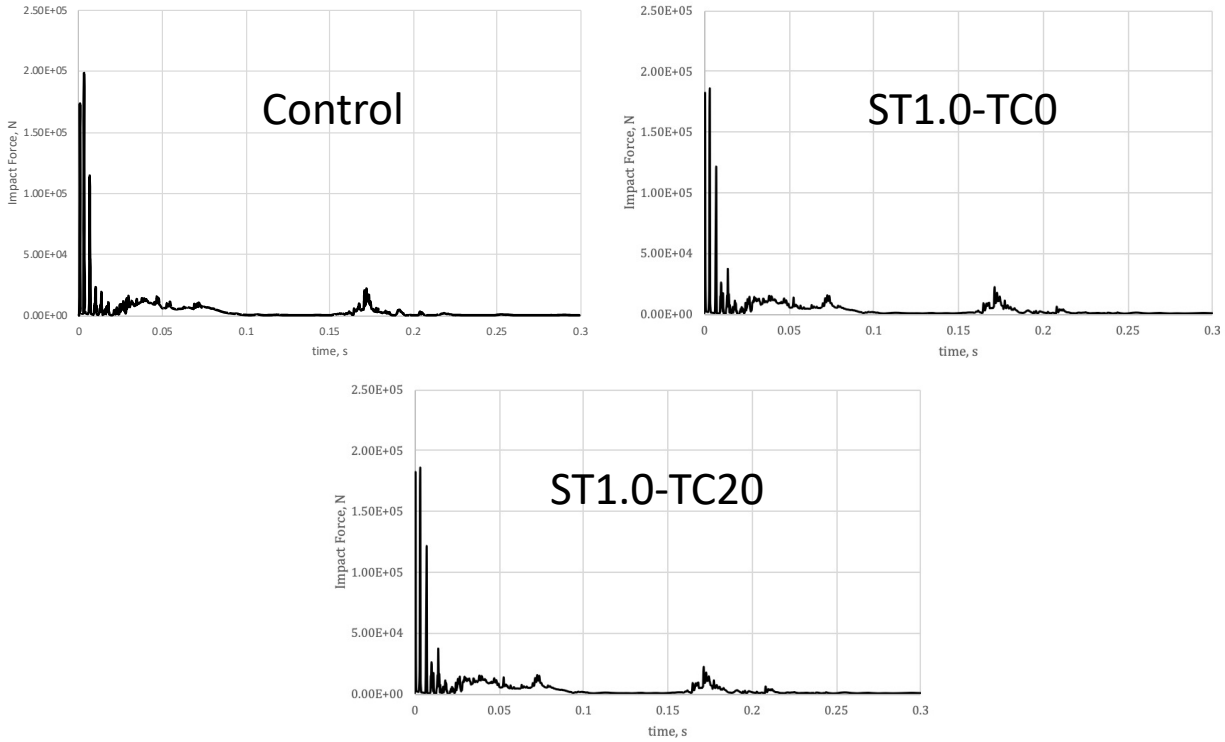

Figure 56. Graphs. Impact force–time history of the barrier wall with different mixtures.

Table 34. Peak stresses in the barriers at different times.

	Concrete Mixture	Time		
		At Impact	0.20 s	0.30 s
Effective Stress (psi)	Control	4,700	9,209	8,876
	ST1.0-TC0	5,134	10,848	10,094
	ST1.0-TC20	3,712	5,583	5,525

Table 35. Peak stresses in the steel reinforcements of the barriers.

Concrete Mixture	Peak Tensile Stress (ksi)	Peak Compressive Stress (ksi)	Time, s
Control	20.88	7.10	0.0275
ST1.0-TC0	23.06	6.82	0.02625
ST1.0-TC20	21.32	7.40	0.02625

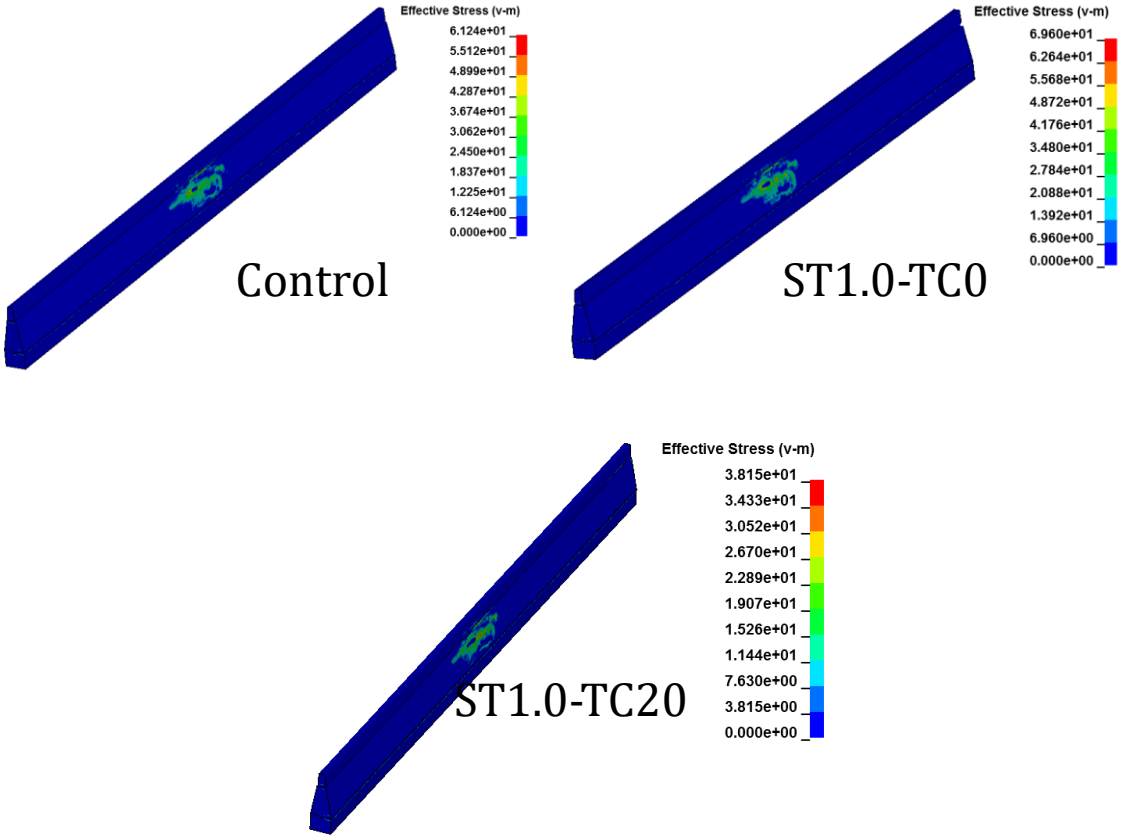

Figure 57. Images. Effective stress distribution of the control barrier at 0.30 s (unit: N/mm^2).

CRASH TEST ANALYSIS OF HEAVY VEHICLE MODEL

Geometry

A Ford 800 single-unit truck (SUT) was used for the heavy vehicle crash test simulation in this study. This truck model was developed by the Federal Highway Administration at the National Crash Analysis Center for modeling heavy vehicle interactions with roadside hardware. The model was later modified by the National Transportation Research Institute in collaboration with Battelle Memorial Institute, Oak Ridge National Laboratory, and the University of Tennessee for improving the roadside hardware impact analysis (NTRCI 2005). The empty weight of the vehicle is 11,051 lb (5,012 kg). A mass of 11,000 lb (5,000 kg) was added to the model for a

total weight of 22,050 lb (10,000 kg). This additional mass was necessary for the truck model to conform to the *AASHTO MASH 2016* requirements for a 10,000S vehicle.

Test Setup

The objective of this analysis was to investigate the outcomes of the SUT colliding with a cast-in-place concrete median barrier at a speed of 56.0 mph (90.1 km/h) at an angle of 15 degrees, as shown in figure 58. The length of the barrier, the vehicle model, the speed, and the angle of the collision satisfy the criterial for test level 4 as specified in *NCHRP Report 350* and *AASHTO MASH 2016*.

Contact

The contact between the barrier and the truck was defined using the 'automatic surface to surface' formulation. The contact between the steel reinforcement of the barrier and the vehicle was defined using the 'automatic nodes to surface' formulation.

Summary of Findings

Simulations were performed for the control, the ST1.0-TC0, and the ST1.0-TC20 barriers. At around 0.10 s, the analysis log file for the control barrier showed failure of the shell elements (of the truck model) in a large number, after which the analysis stopped running. The results for the control barrier simulation were available up to the failure point. The results indicate that the single-slope concrete barrier sustained significant structural damage in the event of a collision with a single-unit truck model. The level of damage sustained was greater in the control barrier, in comparison with the ST1.0-TC0 barrier.

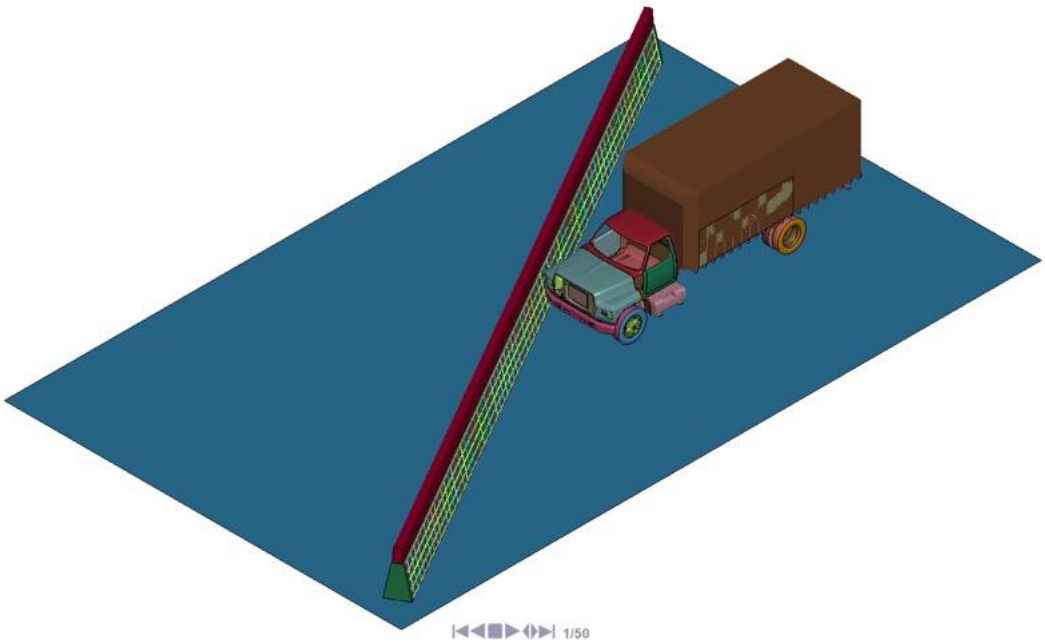

Figure 58. Image. Vehicle model positioned at 15 degrees with respect to the barrier.

Figure 59 shows the impact force–time history of the control, ST1.0-TC0, and ST1-TC20 barriers. Up to 0.06 s, the impact force was similar for the three barriers. In the case of the ST1.0-TC0 barrier, the impact force increased up to 710.0 kip (3158.2 kN). The impact force in the case of the ST1.0-TC20 barrier was almost half that of the ST1.0-TC0 barrier.

At the time of maximum impact force, the maximum compressive stress in the ST1.0-TC0 barrier was 16 ksi (110 MPa). The reinforcement of the glare screen, which is considered a non-structural component, was subjected to maximum tensile and compressive stress at the time of maximum impact force. The maximum tensile and compressive stress was 192 ksi (1,328 MPa) and 165 ksi (1,138 MPa), respectively. Figure 60 presents the stress contour plots of the concrete for the control, ST1.0-TC0, and ST1.0-TC20 barriers without the glare screen. In table 36, the peak stresses for the barriers are summarized, showing that compressive stress in the concrete

was smallest for the ST1.0-TC20 barrier compared to the others. Tensile stress in the reinforcement in the ST1.0-TC20 barrier was the highest of the three barriers.

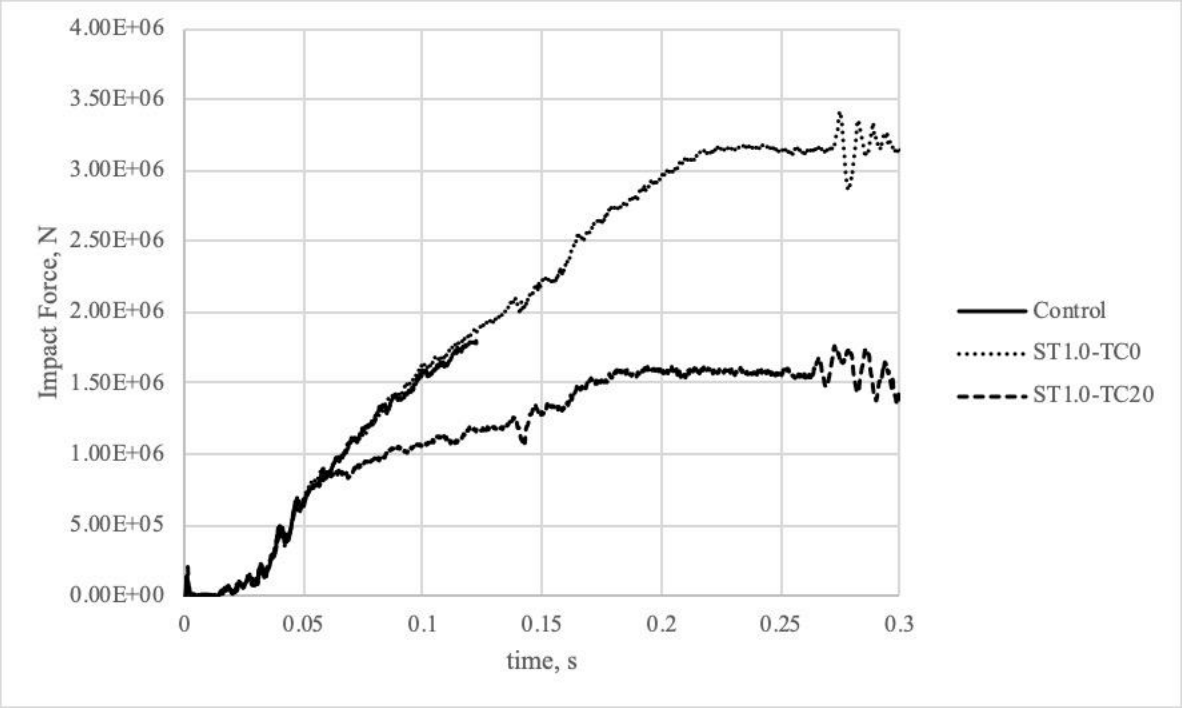

Figure 59. Graph. Impact force–time history of the barriers for single-unit truck simulations.

The displacement histories of the three barrier models at the center of the impacted surface are presented in figure 61. The displacement value, although insignificant, was higher in steel-fiber and tire chips reinforced barrier (ST1.0-TC20) than the other two barriers.

In contrast to the pickup truck model, the post-impact behavior of the Ford 800 was not immediately redirected by the barrier. This performance was anticipated because of the increased total weight of the larger truck (around 4.5 times the weight of the pickup truck), as well as due to the engine being able to reorient to some extent, with respect to the trailer behind. The resultant velocity decreased 30.00 percent within 0.30 s. The barrier sustained significant

structural damage, as the vehicle was not redirected away from the barrier. The analysis log file showed failure in a large number of the shell elements (from the truck model) before the analysis was terminated (t≈0.10 s). On the other hand, the analysis log file for the ST1.0-TC0 and the ST1.0-TC20 barriers showed failure in a large number of solid elements, particularly in the glare screen and the barrier, whereas the number of failed shell elements was reduced. Table 37 provides a summary of the observations from the three-dimensional vehicle crash test analyses.

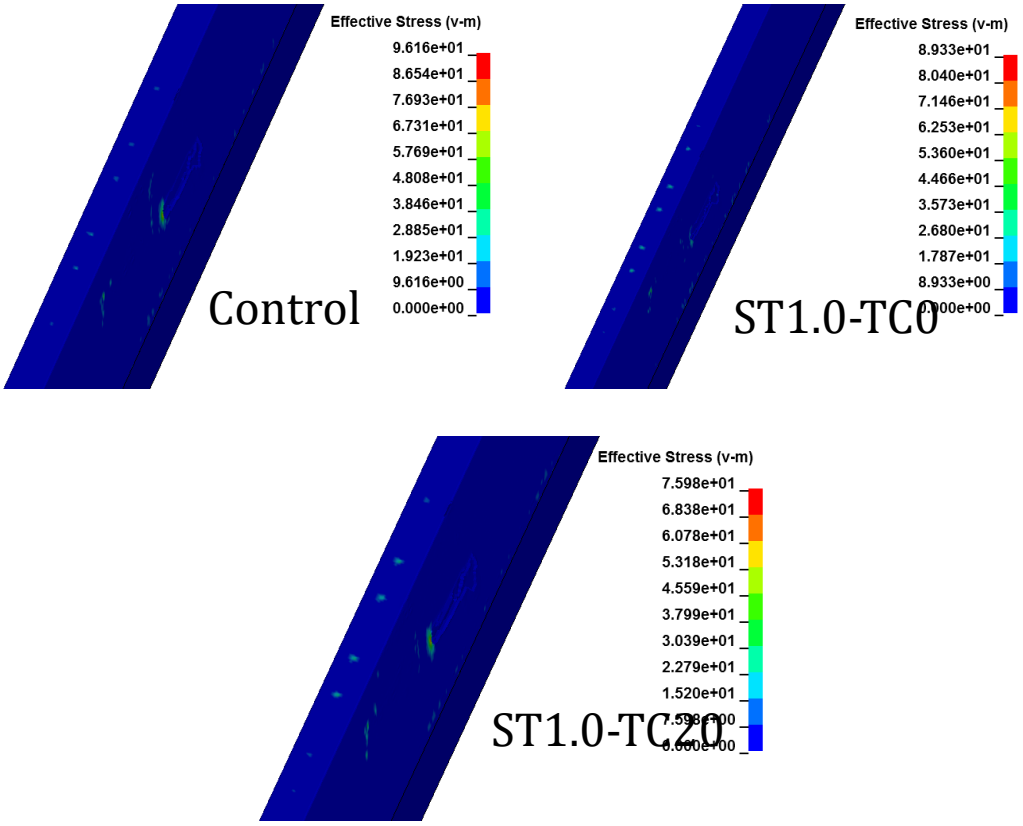

Figure 60. Images. Effective stress distribution in the ST1.0-TC20 barrier (without the glare screen, partial view) at 0.10 s (unit: N/mm^2).

Table 36. Peak compressive and tensile stress in the barriers from truck simulations.

Effective Stress	Mixture			Time, s	Location
	Control	ST1.0-TC0	ST1.0-TC20		
Peak compressive stress in concrete (ksi)	14	13	11	0.10	Barrier
Peak compressive stress in steel reinforcement (ksi)	83	82	84		Barrier
Peak tensile stress in steel reinforcement (ksi)	186	185	190		Shear Reinforcement in the Barrier
Peak compressive stress in concrete (ksi)	—	15	10.9	0.30	Barrier
Peak compressive stress in steel reinforcement (ksi)	—	124	104		Shear Reinforcement in the Barrier
Peak tensile stress in steel reinforcement (ksi)	—	194	265		Shear Reinforcement in the Barrier

Note: — = No data

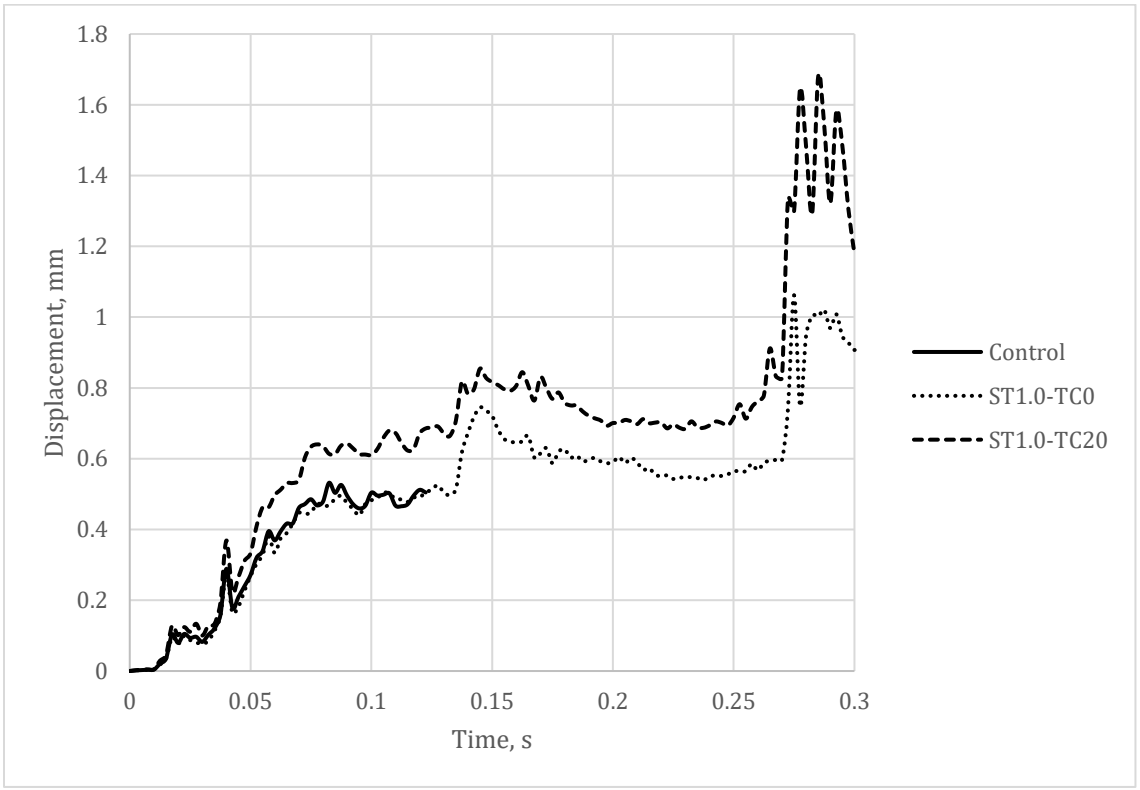

Figure 61. Graph. Displacement at the center of the concrete barriers.

LABORATORY-SCALE BARRIER WALL TESTING

To validate the finite element model developed in this study, testing of two laboratory-scale barrier prototypes with shear keys was conducted under quasi-dynamic impact conditions. This study also allowed for an evaluation of the practicality of producing quality fiber-reinforced rubberized concrete at a ready-mixed concrete scale. The barrier wall was designed for TL-4 conditions. Table 38 provides the design criteria for barriers under TL-4 testing conditions with heights between 36.0 and 42.0 inches (813 to 1,066 mm) tall. H_e is the designated height of the vertical resultant of the transverse load. L_t is the longitudinal distribution of the transverse force. The table was developed by Fossier (2016) based on finite element impact simulations comparing the impact results of a single-unit truck colliding into various barrier heights. Fossier's (2016) study determined that lateral forces increased once the vehicle box structure becomes engaged, and less vehicle roll is experienced as the CMB height is increased.

From table 38, the impact height of 30.0 inches (762.0 mm) was selected for the quasi-dynamic impact testing of a 42.0 inch (1,066 mm) single-slope CMB. Two single-slope barrier configurations, listed in table 39, underwent quasi-dynamic impact testing to evaluate the use of fiber-reinforced rubberized concrete in CMBs. A specimen length of 8.0 ft (2.4 m) was selected due to limitations for controlled laboratory tests. The tests included one GDOT-specified median barrier, the control, and one median barrier produced with fiber-reinforced rubberized concrete, a design with 20.00 percent replacement of the coarse aggregate by volume with recycled rubber tire chips and a 1.00 percent steel fiber addition. The letters "TC" and "ST" refer to tire chips and steel fibers, respectively, following the percentage of volume used in the concrete mixture. The concrete mixture ST1.0-TC20, was selected from scaled-beam testing, and will be compared to the control mixture.

Table 37. Observations from the vehicle crash test analyses.

Event	Observation	
	Analysis with Pickup Truck Model	**Analysis with Single-Unit Truck Model**
Description of Test	Test Level 3; a 5,152 lb (2,337 kg) 2007 Chevrolet Silverado collides with the barrier at a speed of 62 mph (100 km/h) at an angle of 25 degrees	Test Level 4; a 22,050 lb (10,000 kg) Ford 800 single-unit truck collides with the barrier at a speed of 56 mph (90 km/h) at an angle of 15 degrees
Structural Damage in the Barrier	No Structural Damage	Barriers were structurally damaged; Stress results indicated that control barrier sustained greater damages when compared to the modified concrete barriers
Resulting Stress in Concrete	Stress values in the control and the ST1.0-TC0 barriers were higher than the static strength of material; Stress values in the ST1.0-TC20 barrier were higher than the static strength by a small margin	Stress values in the barriers were significantly higher than the static strength of the material
Resulting Stress in Reinforcement	Stress in the reinforcements remained within the elastic limit of material	Stress values in the reinforcements were significantly higher than the static strength of the material
Impact Force Reduction	Impact force in the modified RC barriers reduced significantly when compared to the control barrier result; Peak impact force in the ST1.0-TC0 and ST1.0-TC20 barriers were close	Impact force results were similar for the control and the ST1.0-TC0 barrier; Impact force value changed with percentage of tire chips replacements
Damage in Vehicle	Significant damage	Significant damage; Analysis log file indicated that vehicle sustained greater damage in collision with the control barrier
Vehicle Redirection	Vehicle was redirected instantly	Vehicle was not redirected; Up to 0.30 s vehicle was contained
Velocity Reduction of Vehicle	11% reduction within 0.06 s	30% reduction within 0.30 s

Table 38. *MASH 2016* design criteria for TL-4 barriers (Fossier 2016).

Design Forces and Designations	Barrier Height (in.)			
	36.0	**39.0**	**42.0**	**Tall**
F_t Lateral (kips)	67.2	72.3	79.1	93.3
F_L Long. (kips)	2.6	23.6	26.0	27.5
F_v Vertical (kips)	37.8	3.7	22.0	NA
L_t (ft)	4.0	5.0	5.0	14.0
H_e (in.)	25.1	28.7	30.0	45.5

Note: NA = Not applicable

Table 39. Laboratory test configurations.

Laboratory Test	Barrier Type	Tire Chips	Steel Fibers	Shear Key
Control	One 8 ft long precast barrier	0.00%	0.00%	Yes
ST1.0-TC20	One 8 ft long precast barrier	20.00%	1.00%	Yes

Note: Conversion 1 ft = 0.3 m

Single-Slope Barrier Design

The cast-in-place single-slope barrier has an exposed barrier height of 42.0 inches (1,066 mm) with an embedded base of 22.0 inches (558.8 mm). The slope of the exposed top section of the barrier is 10.8 degrees, designed to allow for vehicles to climb up the wall partially before being redirected upon impact. To be qualified as a *MASH* TL-4 barrier, the compressive strength of the concrete must meet GDOT Class AA (3,500 psi, 24.1 MPa) requirements. A shear key, 2.0 by 4.0 inches (50.8 by 101.6 mm), was implemented into the design to provide extra support and allow for longitudinal continuity. Figure 62 illustrates the most recent GDOT single-sloped barrier design. The inclusion of a shear key required the steel reinforcement to be split into two rebar cages, which were later tied together before placement of the top portion of the barrier. In total, the barrier segments tested included 15 # 4 longitudinal rebar with #5 stirrups spaced every 12.0 inches (305 mm) on-center for reinforcement within the concrete median barrier. The steel

bars used for the study possessed a minimum yield strength of 60,000 psi (413.7 MPa) and a Young's modulus of 29,000 ksi (200 GPa).

Construction of Barrier Walls

Construction of the barrier wall was performed in two segments: placement of the bottom portion of the barrier wall and placement of the top portion of the barrier wall. Placing the barrier wall in two segments created a cold joint, which allowed for the shear key to develop properly prior to the placement of the top section. A similar practice is followed when constructing a barrier in a real-world scenario. Following the specifications provided by GDOT, the bottom portion of the barrier wall was constructed including the 2.0 by 4.0 inch (51 by 102 mm) void for the continuous shear key. After a 1-day minimum duration for a cold joint to form, the top portion of reinforcement was tied to the exposed stirrups from the lower portion and concrete was placed to complete the barrier construction. Figure 63 shows how the phased construction was completed.

Each barrier was instrumented with the same sensors used in the scaled beam testing investigation, with a total of six sensors being placed along the backside of the barrier as shown in figure 64. These sensors were split into five zones to better interpret the displacement that occurred during impact. A data acquisition system was used to process the data from the motion capture camera at a set collection frequency of 100 Hz. Due to the number of sensors used, the marker power was limited to a frequency of 3,000 Hz before sensors were lost. The use of strain gauges, shown in figure 65, along the tensile side of the reinforcement provided information about how the reinforcement performed during the impact. For each barrier, five 0.2 inch (5.0 mm) long strain gauges, a product of Tokyo Measuring Instruments Lab, were used to measure strains on the reinforcing bars. The gauges were glued and waterproofed, using a

cyanoacrylate adhesive and a CT-D25 coating tape, at four different critical locations, with one of the locations having double the number of strain gauges, as shown in figure 65.

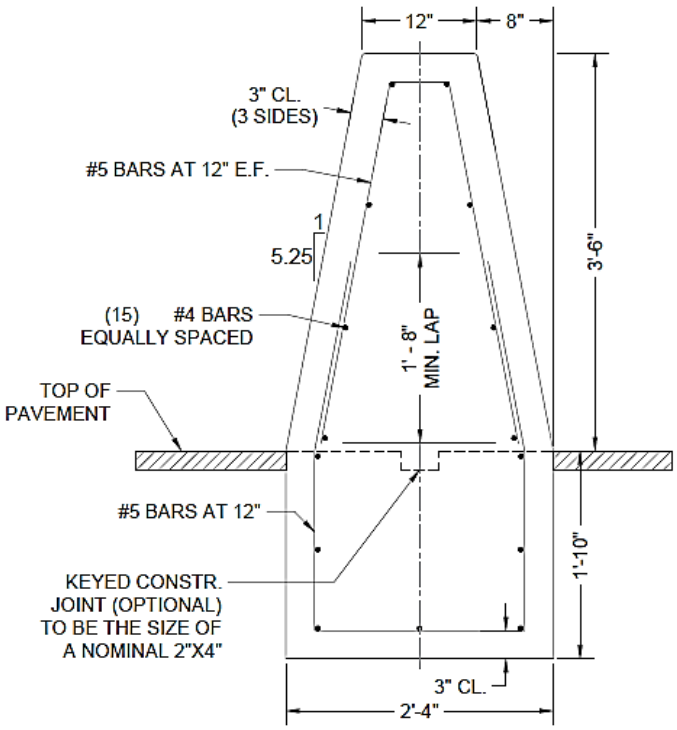

Figure 62. Image. Single-slope concrete barrier (GDOT 2017).

TEST SETUP AND PROCEDURE

A testing configuration for dynamic impact loading conditions was developed. To imitate real-world conditions, a continuous support system was assembled and anchored into the ground to support the barrier for testing. Data collected during the experimental tests include strain gauge readings, displacement measured by a motion capture camera, and the loading and deflection of the actuator upon impact with the barriers.

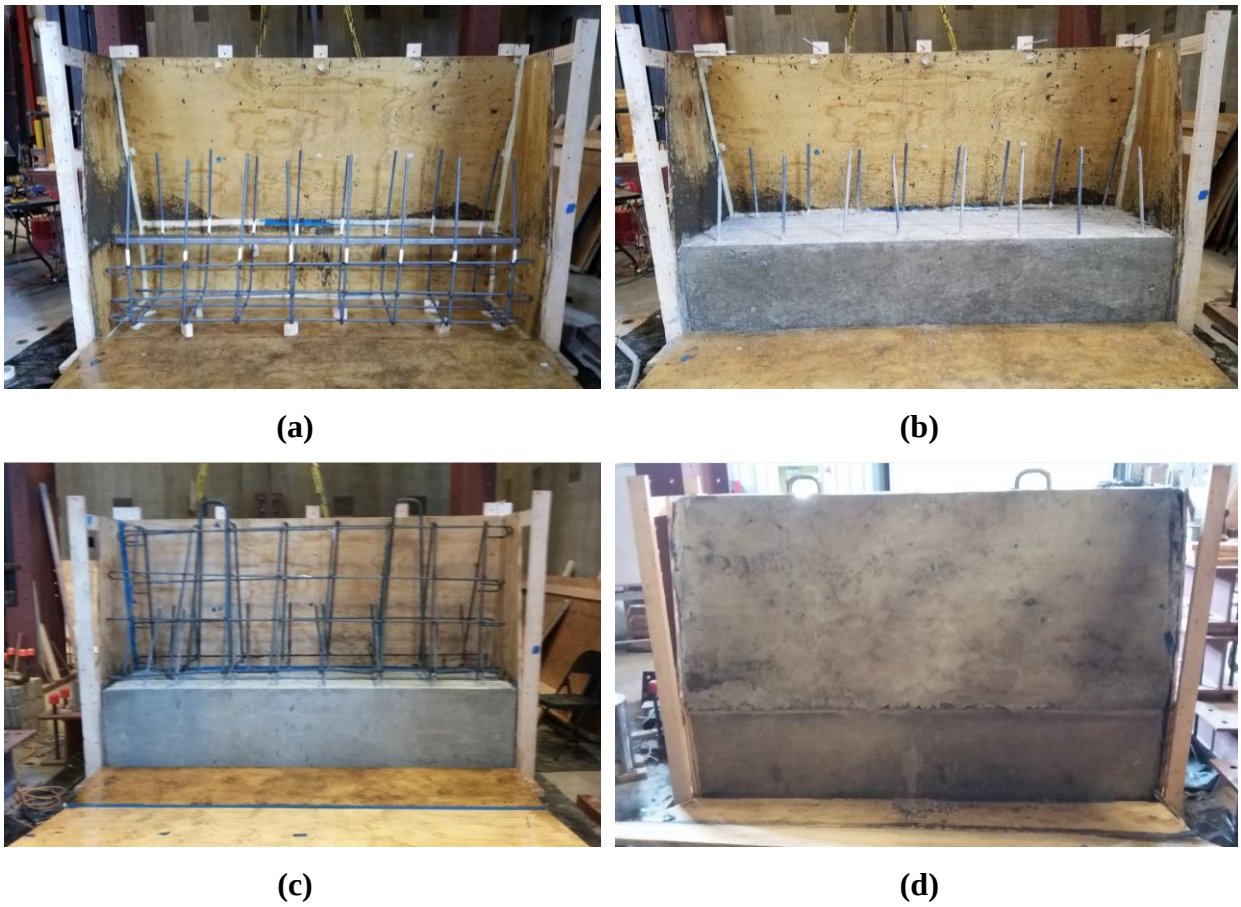

Figure 63. Photos. Phased construction of concrete barrier: (a) bottom reinforcement cage, (b) placement of bottom concrete, (c) top reinforcement cage, (d) completed barrier.

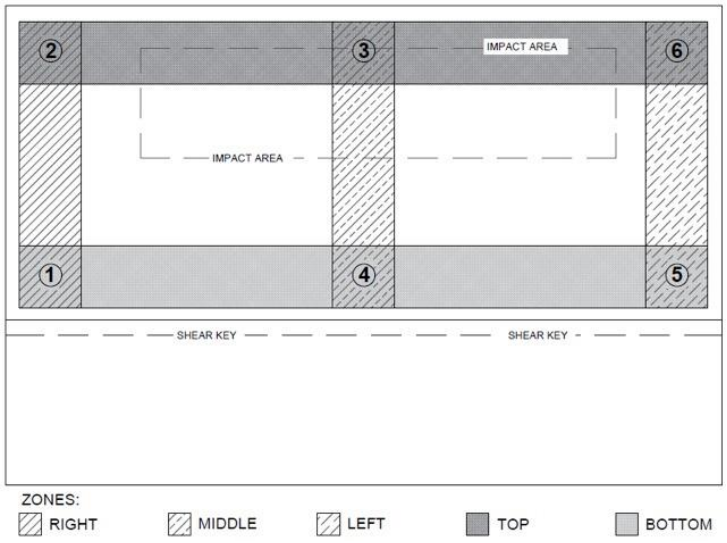

Figure 64. Image. Location of motion capture sensors.

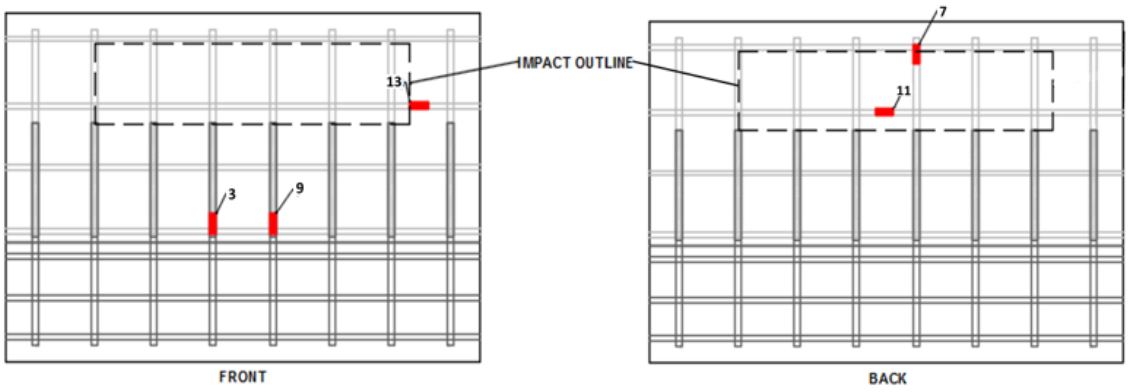

Figure 65. Image. Location of strain gauges.

The response from the ST1.0-TC20 barrier was compared to the GDOT-specified barrier. Data from the load–displacement graphs determine the energy absorption capacity of each barrier. Once the experimental tests were completed and evaluated, the results were then used to validate the finite element model discussed previously in this chapter. This validation allowed for additional full-scale crash simulations in order to understand the three-dimensional impact response and energy absorption capacity of rubberized concrete barrier walls.

Loading Conditions and Application

An MTS Series 201.6 model actuator was used to provide the dynamic impact testing. Ideal for low-frequency testing and simulations, the actuator is fatigue-rated, exhibits low internal friction, and has a compression capacity of 230.0 kips (1,023.1 kN). At full extension, the stroke length of the actuator can reach 20.0 inches (500 mm), providing adequate reach to strike the barrier. The actuator was connected to the high-strength wall to provide dynamic loading conditions. The actuator's length may vary from 107.3 to 143.3 inches (2,724 to 3,651 mm) from the strong wall. This length includes the anchorage of the support I-beam, as shown in figure 66.

Structural Support System

To simulate a cast-in-place testing scenario, W14×132 I-beams were placed along the CMB, providing continuous support to the bottom 22.0 inch (559 mm) section of the barrier, as shown in figure 67. The CMB and the supporting I-beams were anchored onto three additional I-beams that provided the height needed to impact the barrier at the designated vertical impact height, H_e of 30.0 inches (76 mm). The total length of the I-beam support system spanned three connection bearing plates within the strong floor, each spaced 48.0 inches (1,219 mm) on-center.

Load Distribution Beam

A load distribution beam was used to distribute the 150.0 kips (667.2 kN) applied to the barrier wall to mimic real road conditions. AASHTO (1989) specified that the impact dimensions of a load plate should be 13.8 by 27.6 inches (350 by 700 mm) to distribute impact loads for PL-2 (TL 4) barriers. Currently, AASHTO requires a load length of 41.3 inches (1,049 mm) to be applied 27.6 inches (700 mm) above the moment slab attached to a bridge rail.

Figure 66. Photo. Actuator attached to strong wall.

To simulate an impact from a single-unit truck bumper under TL-4 testing conditions, an I-beam with a width of 14.8 inches (375 mm) and a length of 63.8 inches (1,619 mm) was attached to the end of the actuator. Due to the limited connection locations at the end of the actuator, a customized I-beam with stiffeners was attached to the actuator and served as the load distribution beam.

Experimental Setup Design

The experimental setup shown in figure 67 illustrates the laboratory testing configuration, including the actuator and CMB placement. The configuration consisted of anchoring three W14×132 I-beams into the strong floor and placing two additional beams between the anchored beams to provide further support. To prevent the possibility of the barrier overturning due to a large external load, this setup design provided an excessive amount of anchorage opportunities for the support system as a safety precaution. The barrier wall was connected into the two end-anchored I-beams to limit the possibility of the barrier sliding.

Due to constraints from the laboratory design, limitations of the setup included a 1.0 inch (25 mm) height difference between the centerline of the actuator and the impact location of the CMB. The centerline of the impact beam and the barrier were different by 2.0 inches (51 mm), a result of the limited attachment options for the impact beam onto the actuator. However, the length of the barrier was deemed adequate for testing without being affected by the off-centered impact area.

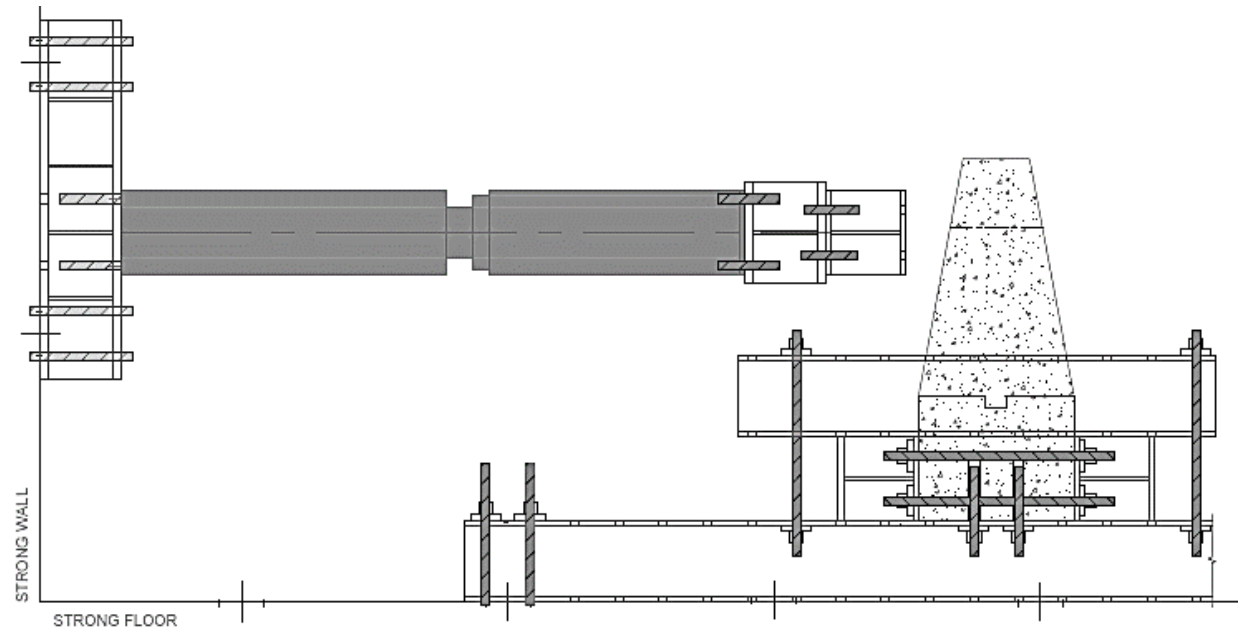

(a)

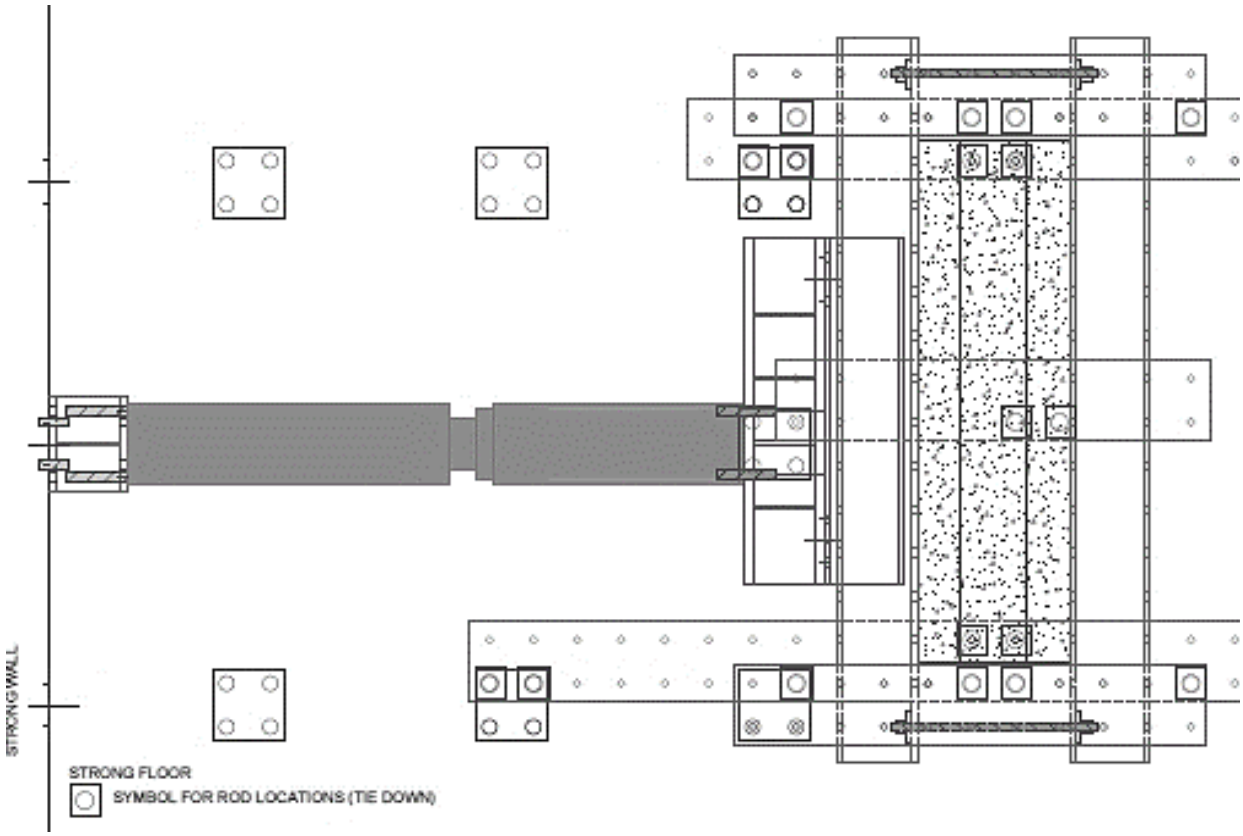

(b)

Figure 67. Images. Experimental setup: (a) elevation view, (b) plan view.

EXPERIMENTAL BARRIER WALL TEST RESULTS

Placement of the concrete barrier walls was performed with the assistance of a local ready-mixed concrete company at the laboratory. Following the phased construction procedure, the barrier was placed in two sections to create a cold joint for the shear key. Blocks of wood were used to elevate the concrete truck to allow the concrete to move with ease down the chute when placing the top portion of the barrier. The barrier consisted of 2.0 cy (1.5 m^3) of concrete for the bottom portion and 2.5 cy (1.9 m^3) of concrete for the top portion; these values also included concrete to conduct the slump test and unit weight test, and produce 15 cylinders for compressive strength testing. Once placed, the barriers were cured using a wet burlap and wrapped in plastic to reduce evaporation, for 28 days.

Fresh Concrete Properties

To ensure compliance to GDOT Class AA concrete standards, outlined above, fresh concrete properties were tested, as reported in table 40. Fresh property testing was conducted for the placements of the bottom and top of the barrier. These mixtures were to follow GDOT-specified allowable limits for Class AA concrete. Slump had an upper limit of 4.0 inches (102 mm) and a lower limit of 2.0 inches (51 mm). Entrained air acceptance limits were to be between 3.50 and 7.00 percent. An ideal range of temperatures, as stated in previous studies, is between 50 and 60°F (10 and 16°C).

Table 40. Fresh properties results for concrete barriers.

Mixture Identification	Slump (in.)	Unit Weight (lb/ft^3)	Temperature (°F)	Air Content (%)
Control – Bottom	2.75	145.0	54.3	2.8
Control – Top	1.75	149.0	61.7	2.6
ST1-TC20 – Bottom	3.25	134.6	61.2	4.3
ST1-TC20 – Top	3.50	130.6	61.5	6

Notes: Conversion: 1 inch = 25.4 mm; 1 lb/ft^3 = 16.02 kg/m^3; (1°F – 32) × 5/9 = −17.22°C

Hardened Concrete Properties

The only hardened concrete property tested for the barrier walls was compressive strength. Comparison of the compressive strengths of the barriers, including the averages, are listed in table 41. Similar to previous studies, the inclusion of tire chips and steel fibers saw a reduction in compressive strength. Both mixtures of the control barrier well exceeded the minimum requirement of 3,500 psi (24.1 MPa) for GDOT Class AA concrete classification. Both mixtures of the ST1-TC20 barrier did not meet the compressive strength requirement, falling below the GDOT Class B compressive strength minimum of 2,200 psi (15.2 MPa).

Table 41. Compressive strength of concrete barriers.

Mixture Identification	Average Compressive Strength (psi)		
	1-Day	7-Day	28-Day
Control – Bottom	1,552	4,880	6,389
Control – Top	1,961	5,106	5,577
Control – Average	1,757	4,993	5,983
ST1-TC20 – Bottom	930	1,817	2,195
ST1-TC20 – Top	467	1,226	1,482
ST1-TC20 – Average	699	1,522	1,839

Note: Conversion: 1 psi = 0.0069 MPa

While the preliminary small-scale batches of the ST1-TC20 mixture had compressive strengths close to the GDOT Class requirement, the large-scale mixture decreased by 15.00 percent. The

higher air content measured during placement of the top section of the barrier lowered the compressive strength compared to the mixture for the bottom section. The suitability of large-scale, ready-mixed concrete level batching of the ST1-TC20 mixture needs further investigation.

Control Barrier Results

Testing of the control barrier consisted of a quasi-dynamic impact at 150.0 kips (667.2 kN) at a ramp rate of 50.0 kips/s (222.0 kN/s), which was held at that force for 0.02 s before the actuator retracted. The actuator was extended out to a distance of less than 1.0 inch (25 mm) from the sloped face of the barrier prior to the start of the test.

No visible damage of the barrier was observed during testing, validating the yield line analysis that was performed prior to experimental testing. Crushing failure at the bottom of the barrier occurred, which was a result of the dowel bars embedded in the concrete to anchor the barrier to the support structure. Due to the dowel bars anchoring the control barrier into the support structure, an increase in loading was observed once the barrier began displacing, pulling the dowel bars out of the concrete.

Figure 68 (a) and (b) illustrate the timed testing of the control barrier from a side view and an aerial view, respectively, over the time of the impact. Displacement of the barrier is shown by the front face of the barrier moving beyond the tie-down bar in figure 68 (a). Figure 68 (b) illustrates the displacement due to rotation of the barrier. The support structure was designed to prevent the CMB from overturning and to prevent sliding due to the large applied force.

Five electrical resistance strain gauges were secured onto the reinforcing bars at critical locations to measure their structural behavior. During the placement of the barrier, two of the strain gauges, CH 3 and CH 11, became unresponsive. CH 3 was located on a bottom vertical rebar on

the impact side of the barrier, at the interface between the two layers. CH 11 was located on the distal side of the barrier on a horizontal rebar. Table 42 includes the recorded maximum strain values observed in the reinforcement during impact.

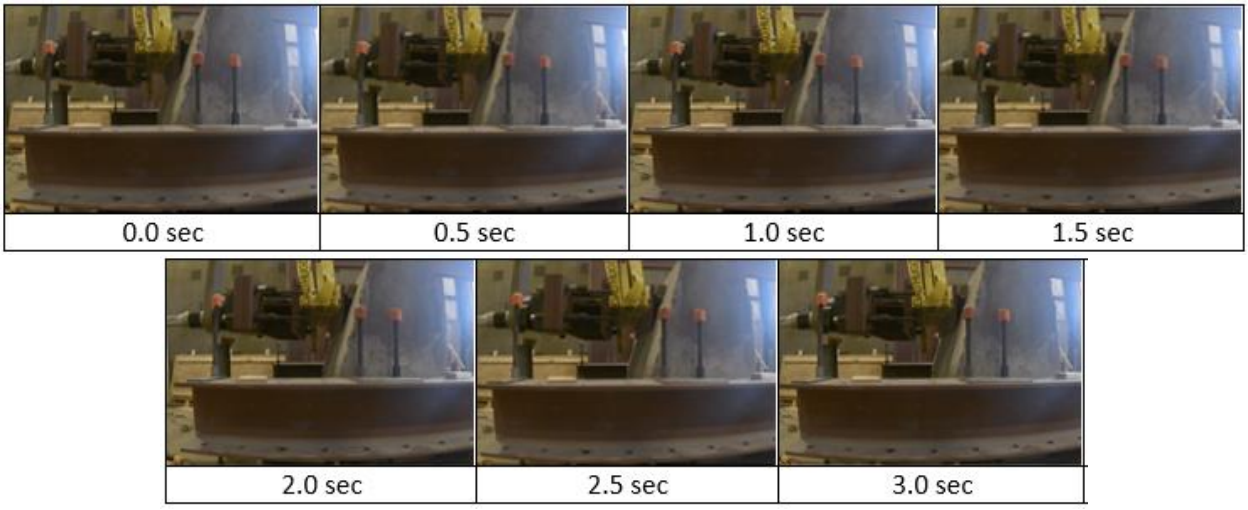

(a)

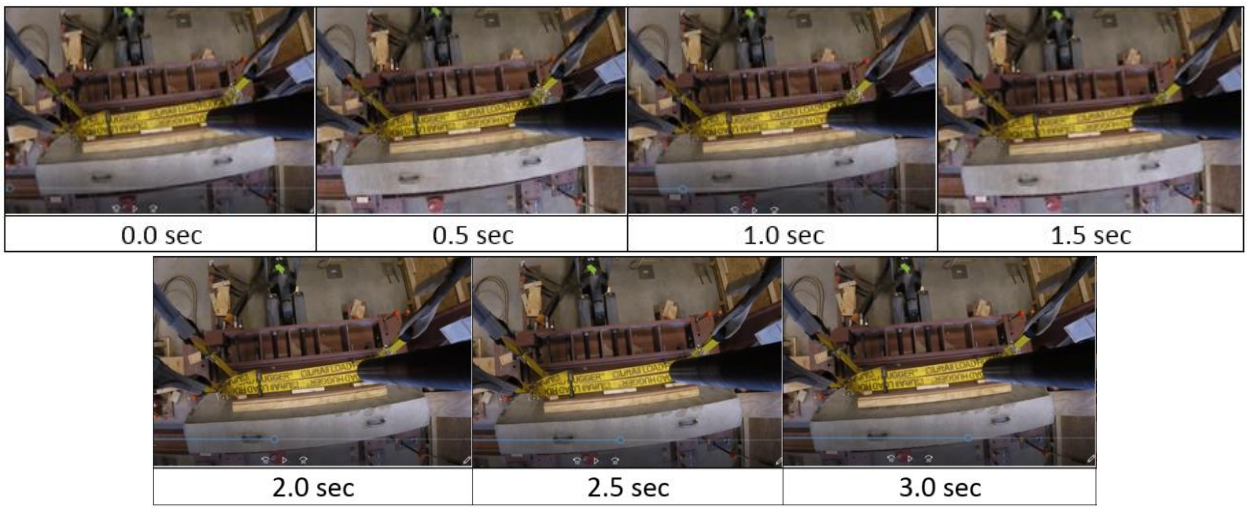

(b)

Figure 68. Photos. Control barrier upon impact: (a) side view, (b) aerial view.

Table 42. Maximum control barrier strain gauge readings (unit: microns).

Location	Vertical Front		Vertical Back	Horizontal Front	Horizontal Back
	CH 3	CH 9	CH 7	CH 13	CH 11
Max. Tension	—	856.24	NA	148.63	—
Max. Compression	—	N/A	−1,687.30	N/A	—

Notes: — = No data; NA = Not available

Upon impact, the largest measured strain, 1,687 με in compression from CH 7, was observed in a vertical rebar on the distal side of the barrier. The distal side of the barrier is in compression upon impact, compared to the front side of the barrier being in tension. As noted in the finite element model evaluation of the barrier wall previously in the investigation, the vertical bars on the impact side of the barrier located at the interface between the top and bottom sections experienced the greatest strain. During the testing of the control barrier, this location included strain gauges CH 3 and CH 9. While CH 3 was unresponsive, CH 9 experienced a maximum strain of 856.2 με. CH 13 was located on a horizontal rebar at the edge of impact on the front side of the barrier, with a maximum strain in tension of 148.6 με. The use of steel reinforcement saw that the majority of the impact load was carried by the vertical reinforcement, resulting in negligible strain in the horizontal rebar. From the data presented in table 42, it can be concluded that the steel reinforcement did not yield, confirming the theoretical model results determined during the finite element modeling developed earlier in the investigation.

Figure 69 illustrates the loading and displacement experienced by the control barrier during impact. Once the actuator reached the programmed load of 150.0 kips (667.2 kN), the control barrier displaced 0.190 inch (0.008 mm). An initial displacement of 0.009 inch (0.228 mm), once the actuator struck the barrier at 150.0 kips (667.2 kN), was determined from a preliminary static structural finite element analysis conducted for each CMB. The control barrier underwent a

larger deflection, as compared to the ST1-TC20 barrier, due to a larger compressive strength, an average of 5,983 psi (41.3 MPa), and a higher Young's modulus of elasticity, 4.4E+06 psi (3.0E+04 MPa). Impact forces have a positive correlation with the stiffness of the barrier, where the higher the stiffness the larger the forces. Since no additional visible damage occurred to the specimen, not including the crushing failure at the base of the structure, the energy from impact was released through deflection.

With the objective of this study being to assess the energy absorption capacity of the CMBs, the energy absorption capacity of each barrier was determined by integrating the function between load and deflection over the testing period. For the control barrier, the area under the curve once the actuator reached and sustained a force of 150.0 kips (667.2 kN) produced an energy absorption capacity of 26.7 kip-in (3,016 kN-mm), a 45.50 percent difference from the ST1-TC20 barrier. The total displacement of the control barrier (found from figure 69) was used to determine the energy absorption capacity. Further comparison between the control and ST1-TC20 barriers' energy absorption capacities and displacement is discussed later in this section.

To measure the displacement of the control barrier, six motion capture sensors were placed along the distal side of the barrier. The sensors were capable of measuring displacement in the X, Y, and Z directions. While movement in the Y-axis was considered negligible, moving left to right, movement in the X-axis was a result of the actuator pushing the barrier backward and rotation. As for quantifying the rotation of the barrier in the XZ-plane, data in the X and Z directions were formulated together to produce the displacement.

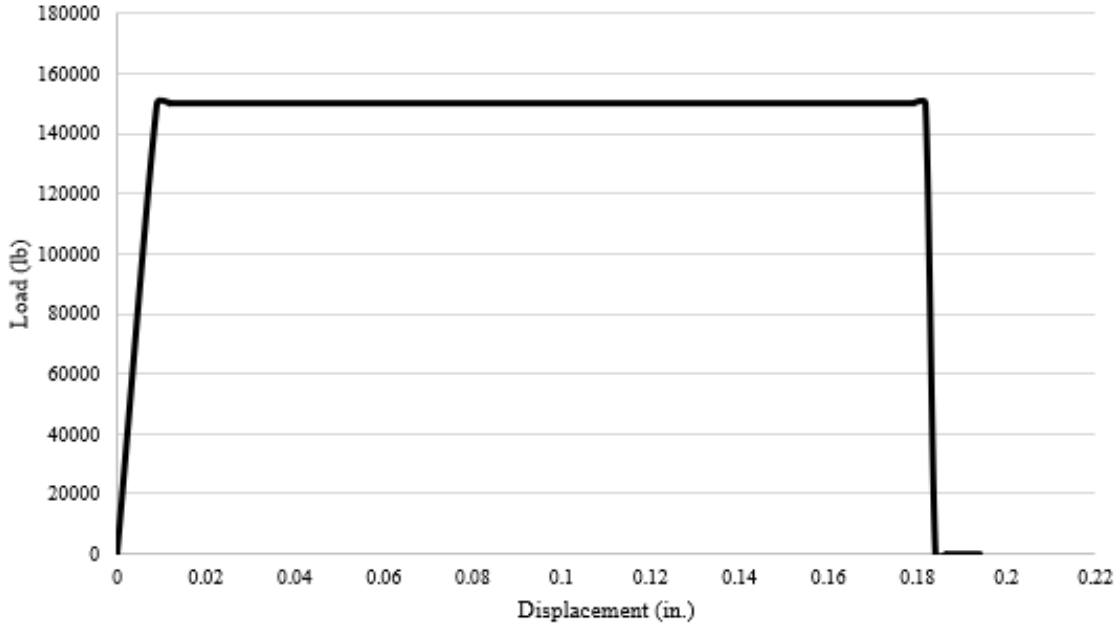

Figure 69. Graph. Load vs. displacement of control barrier.

Changes and Modifications

The performance of the control barrier during impact exhibited little to no engagement of the shear key. In an effort to have the shear key work efficiently, instead of the barrier performing as a solid block of concrete, debonding techniques were used at the interface of the two layers. Simulating a perforated edge, 2.0 inch (51 mm) by 0.8 inch (19 mm) strips of wood spanned the length of the barrier on both sides after the placement of the bottom section. Debonding of the vertical reinforcement at the same location of the wooden strips was another step taken to separate the top portion of the barrier from the bottom. Duct tape and form oil were used to prevent the concrete from bonding to the rebar 2.0 inches (51 mm) below and above the cold joint between the sections. Further modifications to the ST1-TC20 test specimen include the relocation of a strain gauge, CH 13. The results from the control barrier test showed less strain occurred on the horizontal rebar at the edge of the impact along the front side of the barrier, whereas CH 7 on the distal side experienced the largest strain. Figure 70 illustrates the new

location of CH 13 on a distal side vertical rebar next to CH 7. A move such as this will provide more informative details on the structure's behavior during impact.

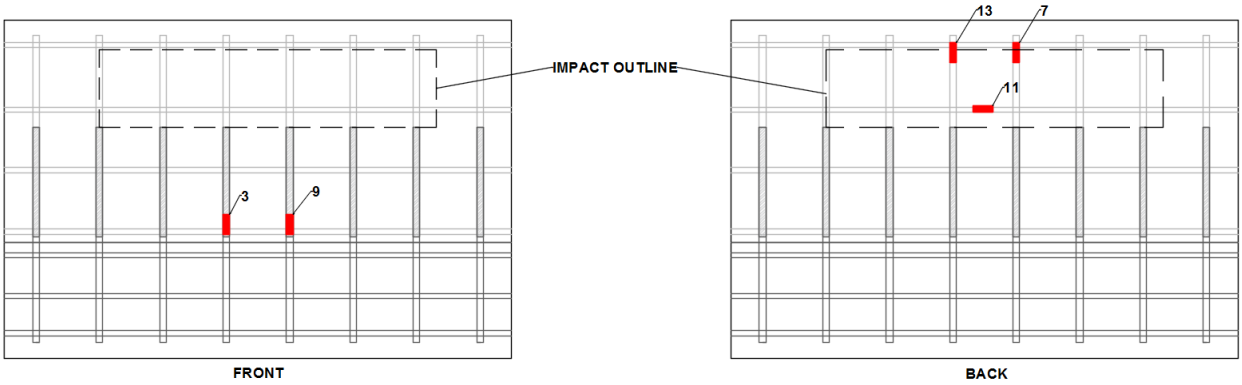

Figure 70. Image. Change in strain gauge location.

ST1-TC20 Barrier Results

Testing of the ST1-TC20 barrier consisted of a quasi-dynamic impact at 150.0 kips (667.2 kN) at a ramp rate of 50 kips/s (222 kN/s), which was held at that force for 0.02 s before the actuator retracted. The debonding efforts instated for this barrier testing had no effect on the barrier's structural integrity, such that no separation of the top and bottom portion of the barrier was observed. Due to the debonding at the interface, the steel reinforcement observed a greater amount of strain compared to the control barrier. No visible damage of the barrier was observed during testing, validating the yield line analysis; however, abrasion occurred on the surface of the barrier upon impact.

Figure 71 (a) and (b) illustrate the timed testing of the control barrier from a side view and an aerial view, respectively. The support system, consisting of multiple steel beams to hold the barrier in place, provided adequate support to reduce any potential of the barrier sliding due to the impact load. No dowel bars were used to anchor the barrier into the support structure during

the testing, as they were deemed inefficient in restraining the barrier. Displacement of the barrier is shown in figure 71 (a) by the front face of the barrier moving closer to the tie-down bar. More displacement, due to rotation from the initial impact, was observed in the ST1-TC20 barrier from the camera views, compared to the control barrier, as shown in figure 71 (b). However, less deflection overall by the impact loading was observed in the ST1-TC20 barrier. From figure 71, the ST1-TC20 barrier performed similarly to the control barrier, even with the lower compressive strength, lack of dowel bars, and the inclusion of debonding methods.

As shown in figure 70, five electrical resistance strain gauges were secured onto the reinforcing bars at critical locations to measure their structural behavior. After placement of the concrete, strain gauge CH 9 became unresponsive, while the other four strain gauges were still functioning. CH 9 was located on a vertical rebar on the front side of the barrier at the shear key. Channels located on the distal side of the barrier measured strain due to compression, whereas the channels on the front side measured tensile strain. Table 43 includes the recorded maximum strain values observed in the reinforcement during impact. Testing of the ST1-TC20 barrier resulted in greater strain within the reinforcement, as compared to the control barrier. The inclusion of steel fibers within the concrete redistributes the load, resulting in increased strain, as determined during the fiber-reinforced rubberized concrete investigation that began this study. From the data, it is concluded that the steel rebar did not yield. A tensile strain of 1,518 με from CH 3, was the largest measured strain from the ST1-TC20 barrier test. CH 3 is located on a vertical rebar on the front side of the barrier at the shear key, which was the same location to experience the largest strain reading in the finite element modeling. Strain readings on the distal side, which was under compression, included a maximum strain of 1,381.1 με from CH 13, 318.3 με from CH 7, and 572.8 με from CH 11.

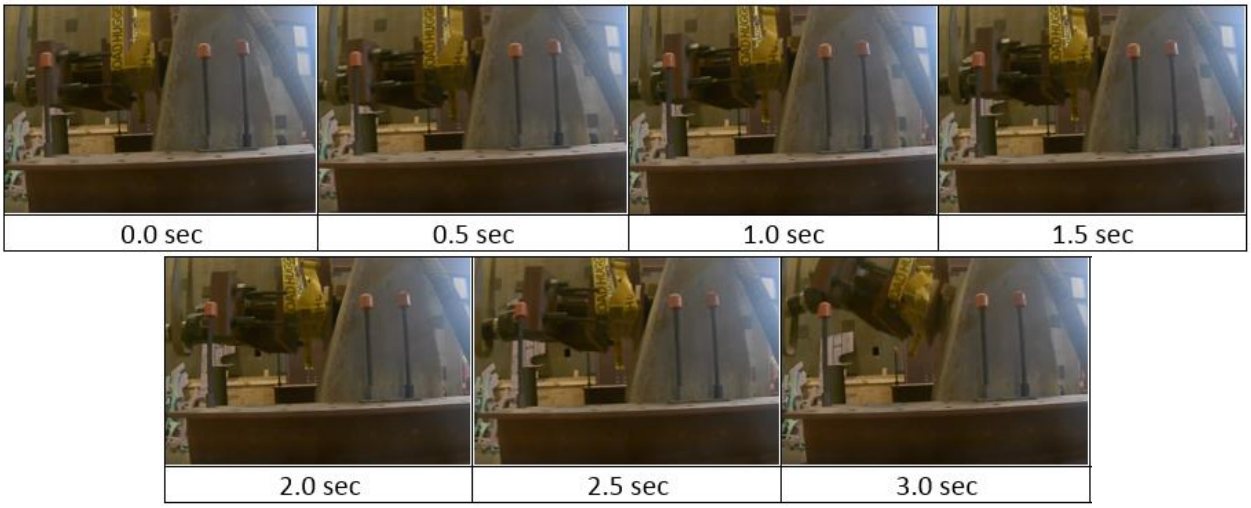

(a)

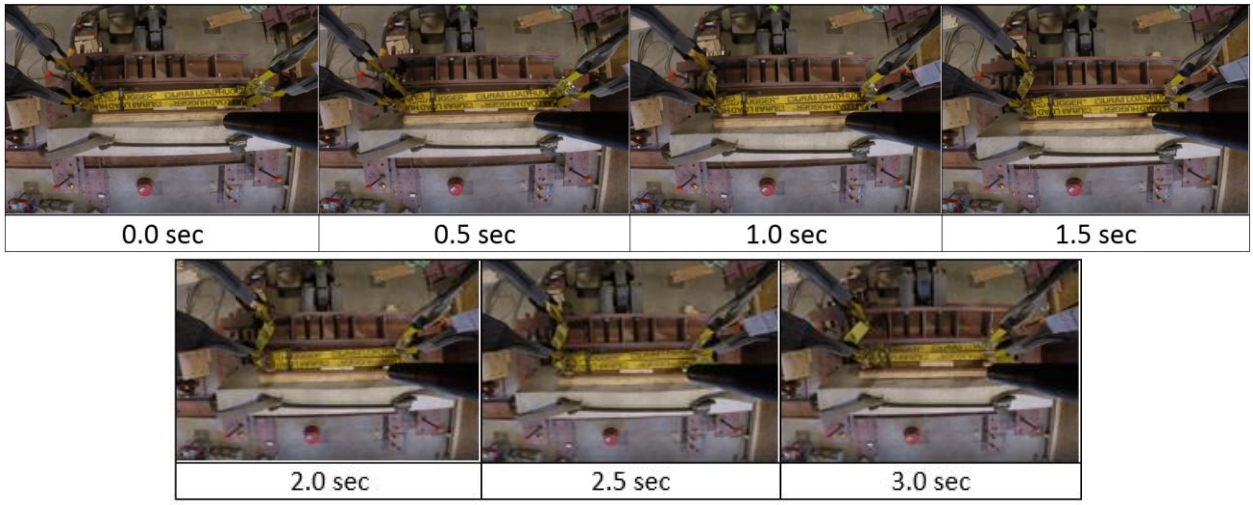

(b)

Figure 71. Photos. ST1-TC20 barrier upon impact: (a) side view, (b) aerial view.

Table 43. Maximum ST1-TC20 barrier strain gauge readings (unit: microns).

Location	Vertical Front		Vertical Back		Horizontal Back
	CH 3	CH 9	CH 7	CH 13	CH 11
Max. Tension	1,518.27	—	NA	NA	NA
Max. Compression	NA	—	−318.33	−1,381.05	−572.80

Note: — = No data

Figure 72 illustrates the loading and displacement experienced by the ST1-TC20 barrier during impact. Once the actuator reached the programmed load of 150.0 kips (667.2 kN), the ST1-TC20

barrier displaced 0.13 inch (0.0052 mm). An initial displacement of 0.0156 inch (0.3960 mm), once the actuator struck the barrier at 150.0 kips (667.2 kN), was determined from a preliminary static structural finite element analysis conducted for each CMB. The ST1-TC20 barrier underwent a lower deflection, compared to the control barrier, due to a lower compressive strength, an average of 1,839 psi (12.7 MPa), and a lower Young's modulus of elasticity, 2.44E+06 psi (1.68E+04 MPa). Similar to the control barrier, no visible damage occurred, resulting in the energy from the impact being released through deflection.

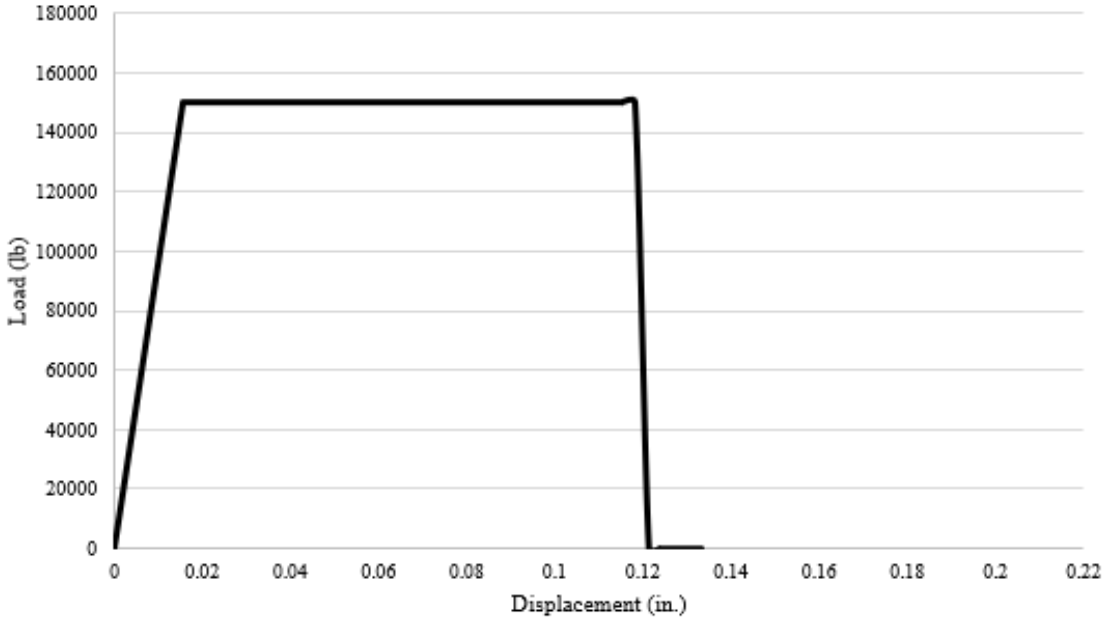

Figure 72. Graph. Load vs. displacement of ST1-TC20.

As for the energy absorption capacity of the ST1-TC20 barrier, the barrier had a capacity of 16.8 kip-in (1,898 kN-mm), a 45.50 percent difference from the control barrier, once the actuator reached and sustained the maximum force of 150.0 kips (667.2 kN). Figure 72 was used to determine the energy absorption capacity. The reduction in the mid-point displacement of the ST1-TC20 barrier is a result of the lower compressive strength and the inclusion of steel fibers.

Unlike the control barrier, which saw a larger deflection, the addition of steel fibers within the ST1-TC20 barrier dissipated the energy from impact over a wider area. An observation made in the fiber-reinforced rubberized concrete mixture investigation earlier in the study shows that the addition of tensile steel reinforcement had a greater impact in increasing the toughness of the FRC beams compared to inclusion of steel fibers. Similar procedures were followed to measure the displacement of the ST1-TC20 barrier using the six motion capture sensors as was conducted when analyzing the control barrier.

SUMMARY OF EXPERIMENTAL BARRIER WALL TEST FINDINGS

In summary, the control barrier met the compressive strength requirement for GDOT Class AA concrete; whereas the ST1-TC20 barrier did not. The reduction in strength for the ST1-TC20 mixture, as well as the lowered Young's modulus, resulted in a greater initial displacement with less total deflection by the impact load compared to the control barrier. Integration of the function between the load and displacement determined each barrier's energy dissipation capacity, which was a 45.50 percent difference in the energy dissipated at the maximum load. Figure 73 illustrates the difference in load versus displacement between the tested barriers. Based on the load–deflection curves, the control barrier was capable of dissipating energy at a 45.50 percent greater capacity due to an increase in compressive strength. The steel fibers within the ST1-TC20 mixture dissipated the impact energy over a wider area, reducing deflection at the mid-point, resulting in a lower dissipation of energy.

The ST1-TC20 barrier had a 53.90 percent greater initial displacement, due to the lower compressive strength and Young's modulus. An increase in ductility was observed in the larger initial displacement of the ST1-TC20 barrier. However, the ultimate deflection of the ST1-TC20

barrier after the maximum impact loading of 150.0 kips (667.2 kN) was 37.50 percent less than the control barrier. The reduction in the mid-point displacement due to the inclusion of steel fibers and tire chips was a result of the steel fibers dissipating the energy over a wider area. The previous fiber-reinforced rubberized concrete beam-scale testing investigation determined that an increase in tensile steel reinforcement allowed the steel fibers to dissipate impact energy at a greater capacity, which was a result of increased deformation at the mid-point.

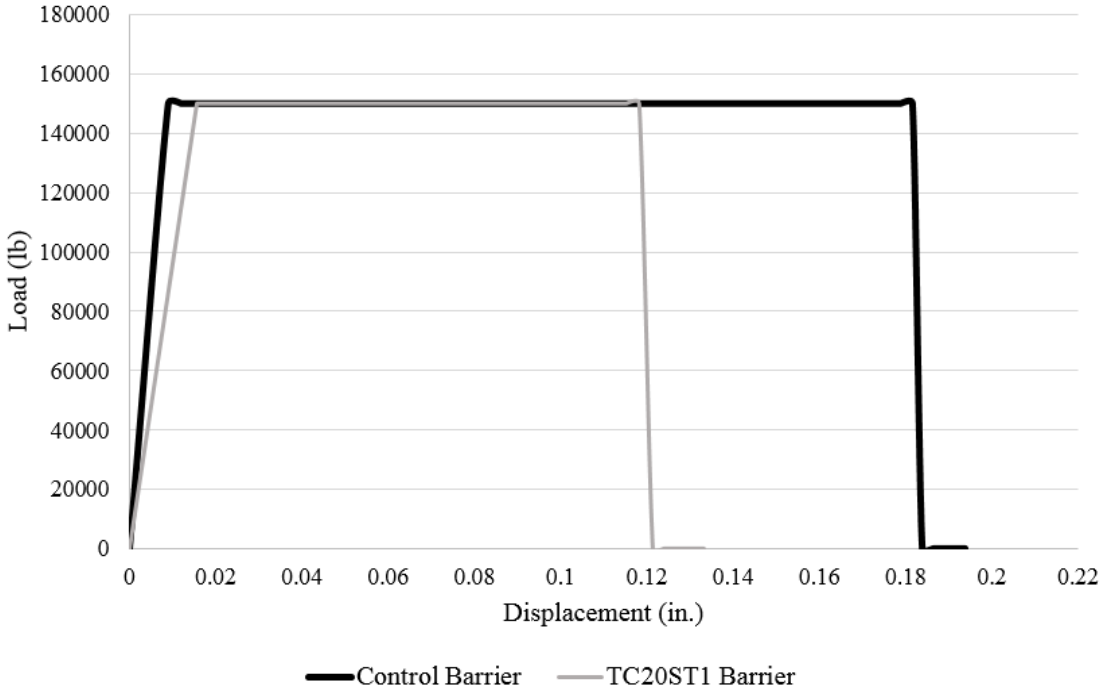

Figure 73. Graph. Summary of load vs. displacement for control and ST1-TC20 barriers.

The use of steel reinforcement saw that the majority of the impact load was carried by the vertical reinforcement, resulting in negligible strain in the horizontal reinforcement. The distal side of the barrier was in compression upon impact, whereas the front side of the barrier was in tension. The control barrier had a larger strain in compression, with 1,687 με on the distal side, which was a 19.90 percent increase from the strain gauge reading on the ST1-TC20 barrier. The

redistribution of the impact energy from the inclusion of steel fibers in the ST1-TC20 barrier produced a tensile strain of 1,518 με on a vertical reinforcement located at the shear key, which was a 55.80 percent increase from the strain gauge reading on the control barrier.

CHAPTER 5. STEEL FIBER–REINFORCED CONCRETE INVESTIGATION

An SFRC investigation was conducted in three parts to assess the viability of reducing the amount of traditional steel reinforcement in concrete members that are subjected to intense loading. Within Part I of the investigation, 13 SFRC mixtures were batched to measure concrete fresh properties, compressive strength, and modulus of rupture. The mixtures comprised SFRC utilizing different steel fiber geometries at fiber concentrations of 0.50, 0.75, and 1.00 percent by total volume. The information learned from Part I was used for scaled beam testing in Part II, which focused on optimization of the steel reinforcement design of SFRC beams. During this investigation, beam tensile and shear reinforcement designs were optimized based on properties of the selected SFRC mixture. Laboratory-scale SFRC beams were created for three-point static testing. The results of this investigation were used to make recommendations for optimized reinforcement design using steel fibers. In Part III, machine learning methods are deployed to develop a highly accurate SFRC strength prediction model.

PART I – SFRC MIXTURE EVALUATION

The main objective of Part I was to determine the effects of aspect ratio and end anchorage on properties of SFRC. To accomplish this, 13 mixtures were designed and tested, which included a control mixture and SFRC mixtures with different fiber geometries at varying fiber volume percentages. Four types of Dramix® steel fibers supplied by the Bekaert Corporation at fiber volume fractions of 0.50, 0.75, and 1.00 percent were used in this study. Fibers varied in geometries, mainly in length and end anchorage. The fiber types and properties used within this study are listed in table 44. The fiber name provides information on the fiber geometry. Within the description “3D/45,” 3D refers to the end anchorage, and 45 refers to the aspect ratio, or the

length of the fiber divided by the diameter. All fibers used within this research were galvanized for improved corrosion resistance. Fibers 3D/80, 4D/65, and 5D/65 are all glued bundles held together by water-soluble glue that breaks apart during the mixing process. The 3D/45 fibers are loose, non-glued fibers. These fibers possess a Youngs' modulus of 29,000 ksi (200 GPa) and 0.80 percent strain at ultimate strength. Figure 74 illustrates the different lengths and end anchorages.

Table 44. Fiber types and properties.

Fiber Name	Length (in.)	Diameter (in.)	Aspect Ratio	Min Dosage (lb/yd^3)	Tensile Strength (ksi)
Dramix® 5D/65	2.4	0.04	65	25	334
Dramix® 4D/65	2.0	0.03	65	34	261
Dramix® 3D/80	2.4	0.03	80	17	178
Dramix® 3D/45	1.4	0.03	45	18	178

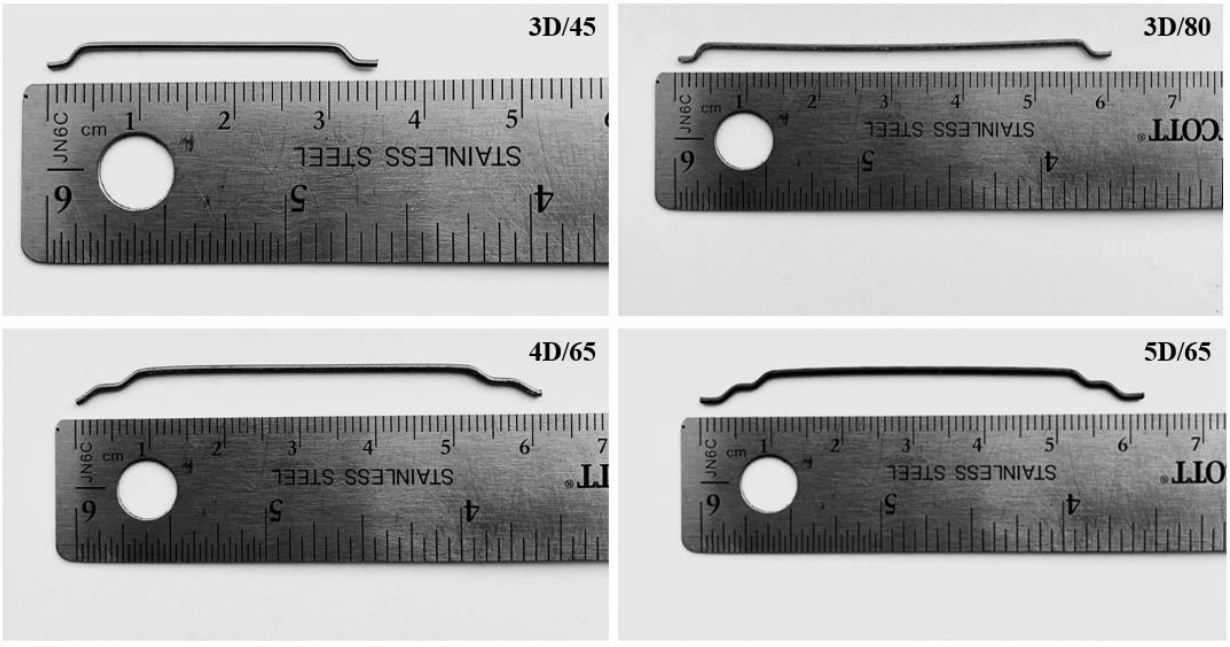

Figure 74. Photos. Fiber types used in SFRC mixtures.

Fresh concrete properties, compressive strength, and MOR were measured and recorded for each mixture. Based on the observed properties, fiber geometries and quantity were selected for use in large-scale SFRC beam testing. For investigative mixtures, the concrete mixture design constituents were held constant, whereby only the fiber amount and geometry changed for each mixture.

Mixture Design Proportioning

Concrete mixtures were designed based on GDOT Class AA concrete. For all mixtures, cement content was maintained at 635 lb/yd^3 (375 kg/m^3) with a constant water-to-cement ratio (w/c) of 0.42. Mixtures were designed for a target slump of 3.0 inches (76 mm) and an air content of 5.00 percent. The concentration of fibers was calculated as a percentage of the total volume of concrete. Dosages of chemical admixtures were determined based on recommendations made by manufacturers. Chemical admixtures HRWRA, VMA, and AEA were utilized to ensure workability of the concrete mixture.

A mixture identification system was developed to display information of each mixture efficiently, for example, 3D/45/0.5. First, the type of end anchorage (i.e., 3D, 4D, or 5D) is shown, followed by the fiber's aspect ratio, then the total fiber volume percentage. As previously stated, the fiber volume content varied from 0.50 to 1.00 percent in 0.25 percent increments. These volume percentages were selected based on current published research. It has been shown that the benefits of steel fibers peak at volume percentages of 1.50 percent; however, concrete mixtures in which the fiber volume surpasses 1.00 percent typically produce unworkable concrete. Table 45 lists the mixture design for the 12 SFRC mixtures tested during the Part I investigation. Each mixture studied in Part I is a variation of the control mixture, allowing for the

hardened property enhancements obtained by the use of fibers to be examined independently and not be influenced by other variables of the concrete mixture.

Table 45. Part I mixture design matrix.

Mix Description	W/C	Cement, (lb/yd^3)	Coarse Aggregate (lb/yd^3)	Fine Aggregate (lb/yd^3)	Steel Fiber (lb/yd^3)
Control	0.42	635	1800	1135	0
3D/45/0.50	0.42	635	1800	1135	66
3D/80/0.50	0.42	635	1800	1135	66
4D/65/0.50	0.42	635	1800	1135	66
5D/65/0.50	0.42	635	1800	1135	66
3D/45/0.75	0.42	635	1800	1135	99
3D/80/0.75	0.42	635	1800	1135	99
4D/65/0.75	0.42	635	1800	1135	99
5D/65/0.75	0.42	635	1800	1135	99
3D/45/1.00	0.42	635	1800	1135	131
3D/80/1.00	0.42	635	1800	1135	131
4D/65/1.00	0.42	635	1800	1135	131
5D/65/1.00	0.42	635	1800	1135	131

SFRC Properties

Fresh Concrete Property Test Results

The fresh concrete properties of slump, air content, temperature, and unit weight are important to consider for concrete production and usage. These properties give insight as to how viable the mixtures are for industry in terms of ease of placement, consolidation, and finishing of the concrete, as well as the long-term durability of the concrete. Based on past research, it is known that the addition of steel fibers into concrete mixtures has a negative impact on the fresh properties of the concrete. These negative impacts include decreased slump, increased air content, and increased unit weight. Based on this information, it becomes even more important to build an understanding of how the fibers used within this study will affect these fresh properties.

Additionally, information collected from these fresh property tests helps to further optimize the dosage of admixtures used within the Part II investigation. Table 46 lists the results collected from the fresh property testing of the Part I mixtures.

Table 46. Fresh concrete property test results of SFRC mixtures.

Mix Description	Slump (in.)	Air Content (%)	Unit Weight (lb/ft^3)	Temperature (°F)
Control	4.5	5.0	148.0	72
3D/45/0.50	4.0	3.0	150.9	73
3D/80/0.50	3.5	3.0	151.2	75
4D/65/0.50	3.0	2.0	150.1	73
5D/65/0.50	3.5	2.5	149.6	64
3D/45/0.75	3.5	2.5	150.0	69
3D/80/0.75	4.0	3.0	151.6	70
4D/65/0.75	4.0	2.5	149.8	73
3D/45/1.00	4.5	3.0	151.0	68
3D/80/1.00	5.0	3.5	152.0	69
4D/65/1.00	5.0	3.2	150.6	72
5D/65/1.00	4.0	3.2	151.2	73

As the literature and ACI 544.4R-18 suggests, slump was tested prior to the addition of steel fibers, as the traditional slump test is not an accurate test method for SFRC mixtures. The workability of the mixtures after the addition of fibers was determined during the placement process, by which a visual inspection was performed observing the ease of placing and finishing the concrete within the specimen molds. The slump values obtained from the testing range from 3.0 to 5.0 inches (76 to 127 mm), most of which fall within the range of the GDOT Class AA standards of 2.0 to 4.0 inches (51 to 102 mm). As the higher volume ratio of fibers leads to a less workable concrete, more HRWRA and VMA was utilized to further the workability of the concrete before addition of the fibers. Overall, the addition of fibers had only a slight negative effect on the workability of the concrete. At higher volume ratios, fiber clumping was evident

despite the increased mixing time. While the control mixture was able to be placed into molds without the use of a vibrating table, the SFRC mixtures required the use of a vibrating table to properly consolidate the concrete into the molds. This was due to the fibers pushing the larger aggregate out in some situations, especially with the longer fibers. At the 1.00 percent fiber volume ratio, it became difficult to finish the surface of the testing specimens, as fibers often stuck out in random directions, being lodged within the aggregate, and had to be pulled out of the mixture.

The air content was fairly consistent for all SFRC mixtures, being slightly lower than the air content of the control mixture. This could be due to the addition of fibers decreasing the amount of entrapped air. The extended mixing time within the drum type mixer also could have played a role in the decreased air content within the concrete. The SFRC mixtures possessed air contents that were 1.50 to 3.00 percent lower in comparison to the 5.00 percent air content of the control mixture. The fiber type had negligible effects on the air content. Air content increased slightly with increasing fiber volume concentration, but by a small margin.

As expected, the unit weight of mixtures containing steel fibers was higher than the control. This is due to the fibers being made of a higher density material than other materials found within the concrete. Despite the increase in unit weight, the highest increase was only 2.70 percent higher than the control unit weight. The unit weights of the SFRC mixtures ranged from 149.6 to 152.0 lb/ft^3 (2,396 to 2,434 kg/m^3), a difference of 1.60 percent. Aside from the initial increase in unit weight, the change of unit weight due to the addition of steel fibers is considered negligible.

Hardened Concrete Property Test Results

Compressive strength and MOR were measured for each of the Part I mixtures. Compressive strength tests were performed at 1, 7, and 28 days of age, while MOR was measured at 28 days of age. The compressive strength and MOR values are the most important properties studied within the Part I investigative mixtures, as these properties are used to further optimize the mixtures and help with beam design for the Part II scaled beam tests.

The compressive strength of the SFRC mixtures increased with increasing fiber content up to 0.75 percent fiber by volume, with a steep decrease in compressive strength for mixtures containing long fibers at the 1.00 percent volume ratio. The increase in compressive strength from the inclusion of steel fibers ranged from 9.80 percent for 3D/80/1.0 to 83.30 percent for 4D/65/0.75. The steep decrease in compressive strength of mixtures containing long fibers at the 1.00 percent fiber volume ratio could be due to fiber clumping between the aggregates, or the end anchorages creating internal cracks as suggested in literature. On average, the SFRC mixtures reached 78.00 percent of their total compressive strength by 7 days of age, with all mixtures surpassing the GDOT Class AA concrete compressive strength requirement of 3,500 psi (24.1 MPa) by 7 days of age. The average compressive strength results are summarized within table 47, while figure 75 shows the development of the compressive strength of the SFRC mixtures for 1, 7, and 28 days of age. Interestingly, the 3D/45 fibers produced the highest compressive strength of the fibers with fiber volume ratios of 0.50 and 1.00 percent, but the lowest compressive strength for the 0.75 percent fiber volume ratio. The trend of these compressive strength results agrees with results reported by Al-Ameeri (2013), with the compressive strength increasing up to 0.75 percent fiber volume fraction and decreasing thereafter. The compressive strength of SFRC appeared to be mostly influenced by fiber length.

As suggested by the literature, the MOR increased with increasing fiber volume ratio. On average, the MOR increased by 39.70, 50.10, and 73.30 percent in comparison to the control for fiber volume ratios of 0.50, 0.75, and 1.00 percent, respectively. In each fiber volume ratio category, the 5D/65 fibers outperformed other fiber geometries, which is due to the five-dimensional end anchorage contributing to the fiber pull-out resistance. At the 1.00 percent fiber volume ratio, the 5D/65 SFRC mixture possessed a MOR strength of 1,360 psi (9.4 MPa), a 105.70 percent increase in comparison to the control mixture. Despite the high MOR measurement of the 5D/65/1.00 mixture, this mixture had a lower compressive strength when compared to the other fiber volume mixtures. The results of the MOR testing are shown in figure 76.

Table 47. Average compressive strength results of Part I investigative mixtures.

Mix Description	Day 1 (psi)	Day 7 (psi)	Day 28 (psi)
Control	1,273	3,895	4,562
3D/45/0.50	1,614	5,259	7,497
3D/80/0.50	1,933	5,572	7,005
4D/65/0.50	1,360	4,001	6,272
5D/65/0.50	1,876	4,725	6,499
3D/45/0.75	2,194	5,369	7,077
3D/80/0.75	2,534	5,961	7,774
4D/65/0.7r5	2,533	6,352	8,360
3D/45/1.00	1,900	6,657	8,226
3D/80/1.00	0,905	4,174	5,010
4D/65/1.00	1,195	4,449	5,393
5D/65/1.00	1,211	5,262	5,845

In an effort to better understand the significance of influence the fibers had on fresh and hardened properties, an analysis of variance (ANOVA) was performed. Comparisons of the observed strengths of the SFRC and control mixtures were made to analyze how interactions

between fiber volume percentage (Vf %), end anchorage (EA), and aspect ratio (AR) influence the compressive strength and MOR. The results of the analysis are summarized in table 48. Overall, the 4D/65 fibers appear to have the greatest statistical significance with changing volume percentage, resulting in p-values of 0.007 and 0.047 ($\leq$0.05) for compressive strength and MOR variations, respectively. While the 3D/45 MOR results showed statistical significance with a p-value of 0.031, compressive strength results showed no significance.

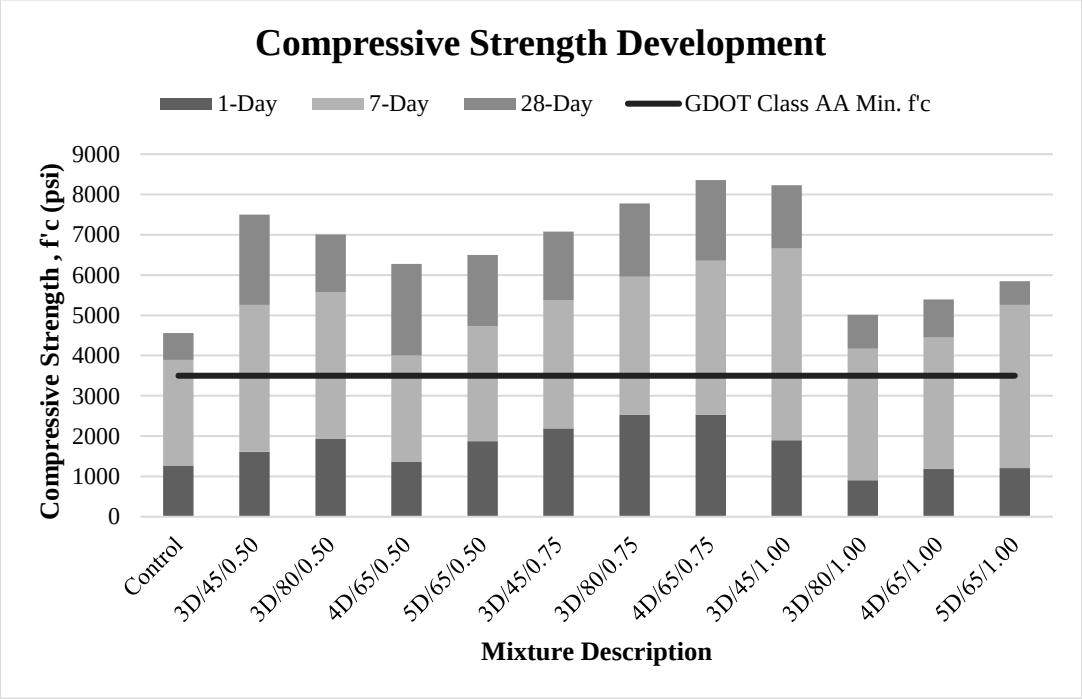

Figure 75. Graph. Compressive strength development of SFRC mixtures.

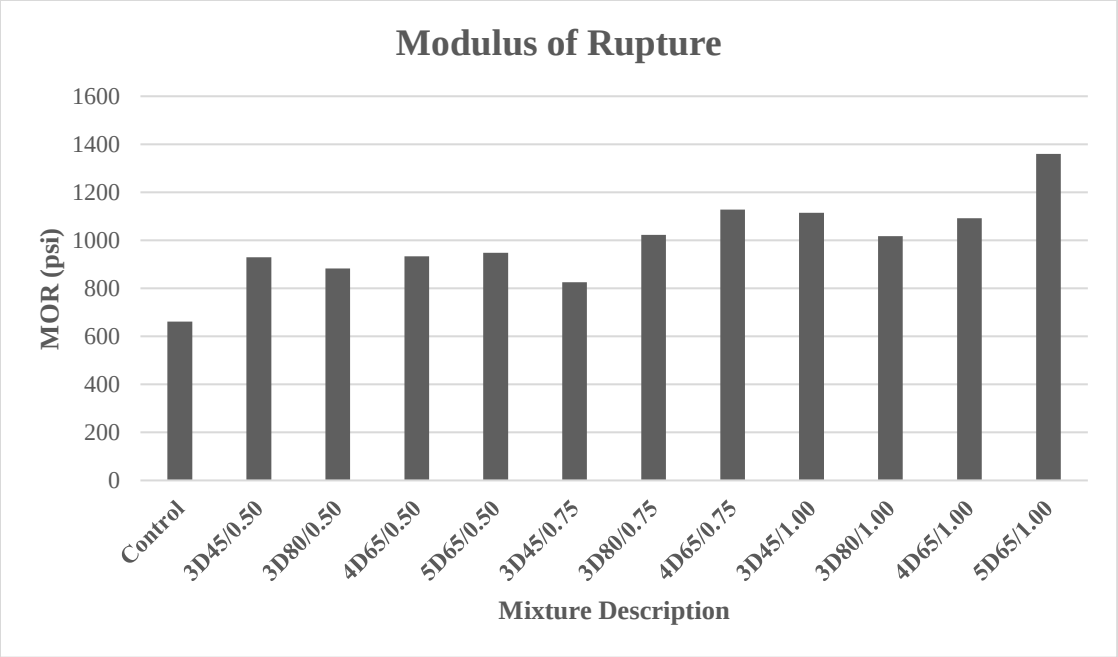

Figure 76. Graph. MOR strength results for SFRC mixtures.

Table 48. ANOVA summary.

Comparison	Source of Variation	Sum of Square	df	Mean Square	F-Value	P-Value
3D/45 Comp. Str.	Vf %	1,351,822	2	675,911	4.35	0.129
3D/45 MOR	Vf %	128,300	2	64,150	14.91	0.005
3D/80 Comp. Str.	Vf %	8,140,721	2	4,070,361	13.84	0.031
3D/80 MOR	Vf %	28,002	2	14,001	2.01	0.215
4D/65 Comp. Str.	Vf %	9,292,880	2	4,646,440	38.71	0.007
4D/65 MOR	Vf %	64,756	2	32,378	5.31	0.047
0.50% Vf Comp. Str.	EA	651,196	2	325,598	0.62	0.549
1.00% Vf MOR	EA, AR	238,028	2	119,014	11.98	0.008

As each MOR result was found to be statistically significant, it can be concluded that the addition of fiber reinforcement increases MOR. Lastly, the influence of the end anchorages and aspect ratios on compressive strength and MOR were analyzed. The 0.50 percent fiber volume compressive strength results were chosen for the ANOVA comparison, as more data were readily available, which provides a stronger statistical model. The 1.00 percent fiber volume MOR

results were chosen based on available data. From the analysis, the end anchorage and aspect ratio had significant influence on MOR values with a p-value of 0.008. However, they were insignificant in increasing compressive strength. The end anchorage primarily aids in increasing fiber pull-out strength, which directly influences MOR.

Based on the results of SFRC mixture investigation, the 4D/65/0.75 SFRC mixture looked promising for use in Part II static beam testing. The 4D/65/0.75 mixture provided the highest compressive strength and enhanced MOR results, and showed the greatest statistical significance with changing fiber volume percentage in comparison to the other mixtures studied. As the majority of currently available research papers focus on SFRC containing 3D steel fibers, there is potential to expand available data on SFRC containing 4D steel fibers. Based on the results of the investigative testing, the 4D/65/0.75 mixture was selected for testing in Part II.

PART II – LABORATORY-SCALE SFRC BEAM TESTING

Part II involved subjecting laboratory-scale SFRC beams to static loading. Laboratory-scale beam testing provided experimental data necessary for the optimization of reinforced concrete member designs. Within this phase, SFRC beams with varying levels of shear reinforcement were made and subjected to static loading utilizing a 220 kip (978.6 kN) hydraulic actuator. A load–deflection curve was developed by performing a three-point bending test on laboratory-scale beams. Toughness, or the total energy required to deform a material, was calculated by summing the area under the load–deflection curve. The flexural toughness parameters were obtained through the three-point static bending test. This information provides insight into the amount of energy that the SFRC material is able to dissipate during deformation.

Beam Configuration

A total of eight beams were used in this testing phase, each measuring 90.0 inches long × 6.0 inches wide × 10.0 inches deep (2286.0 mm × 152.4 mm × 254.0 mm). All beams utilized steel reinforcement with a Young's modulus of 29,000 ksi (200 GPa) and a minimum yield strength of 60,000 psi (413.7 MPa). The reinforcement for the control beam included two #3 longitudinal bars and two #4 longitudinal bars for the compressive and tensile reinforcement, respectively, resulting in a reinforcement ratio of 0.80 percent. These bars were held in place with #2 stirrups spaced at 4.0 inches (102 mm) on center. A preliminary set of laboratory-scale SFRC static beams were tested prior to reinforcement optimization to better understand the load versus deflection results of the SFRC mixtures. Like the fiber-reinforced rubberized concrete mixtures investigation, SFRC beams included a third steel reinforcing bar in the tensile region of the beam to balance the tensile strength with the increased compressive strength of the fibrous concrete. Results of the preliminary static beam tests were considered when determining reinforcement designs for additional SFRC beams. Table 49 summarizes the designs for all eight beams batched within this study phase. Each of the eight beams tested within this study phase varied in either mixture design or reinforcement ratio. Figure 77 illustrates the longitudinal cross sections of the laboratory-scale beams with varying shear reinforcement ratios. Figure 78 illustrates cross sections of laboratory-scale beams with varying tensile reinforcement ratios.

Table 49. Part II beam design summary.

Beam ID	ρ	Concrete Mixture	Shear Reinforcement	Tests
C1	0.80%	Control	#2 Stirrups 4 in o.c.	Flexure
C2	0.80%	Control	#2 Stirrups 4 in o.c.	Flexure
B1	1.21%	3D/45/0.50	#2 Stirrups 4 in o.c.	Flexure
B2	1.21%	3D/80/0.50	#2 Stirrups 4 in o.c.	Flexure
B3	1.21%	4D/65/0.50	#2 Stirrups 4 in o.c.	Flexure
B4	1.21%	5D/65/0.50	#2 Stirrups 4 in o.c.	Flexure
B5	1.21%	4D/65/0.50	#2 Stirrups 8 in o.c.	Flexure
B6	1.03%	4D/65/0.75	#2 Stirrups 4 in o.c.	Flexure
B7	1.03%	4D/65/0.75	#2 Stirrups 8 in o.c.	Flexure

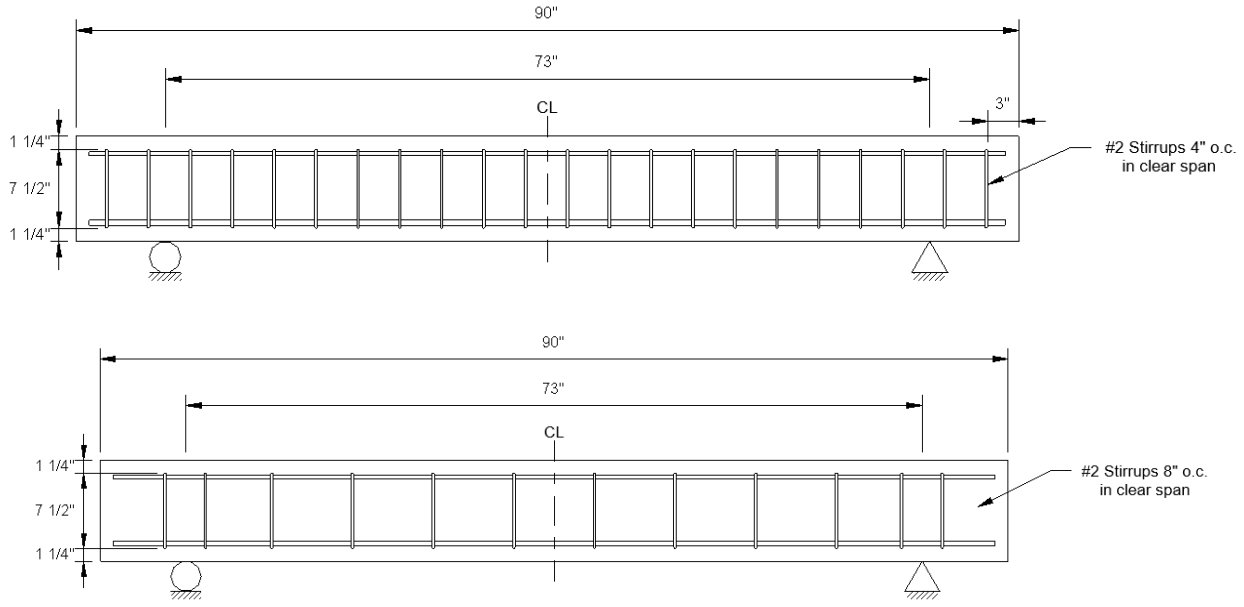

Figure 77. Images. Longitudinal cross sections of laboratory-scale beams.

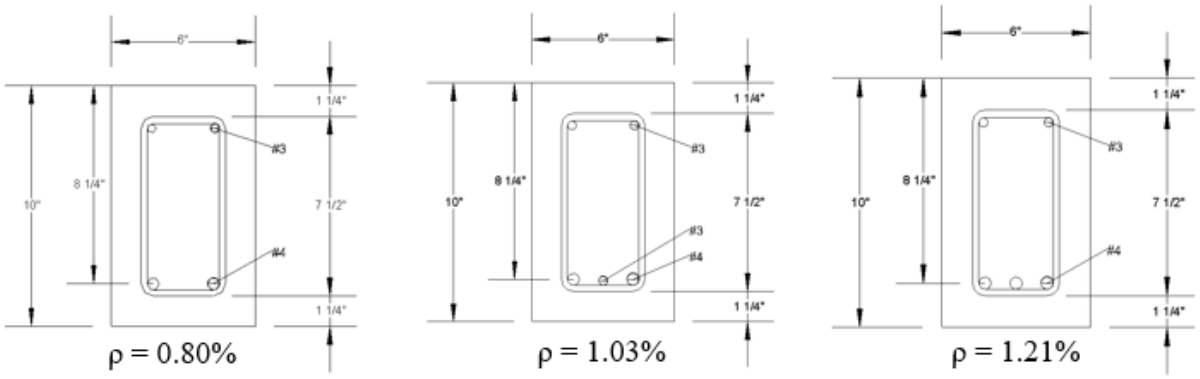

Figure 78. Images. Cross sections of laboratory-scale beam specimens.

Laboratory-Scale Static Beam Testing

Laboratory-scale static beam testing was performed by applying a load at the midspan of the simply supported reinforced concrete beam. From the three-point bending test, the toughness of the FRC beams was measured by integrating the load–deflection curve. This testing allowed for the observation of crack formation over time as the deflection increased. To begin this phase of the study, five beams (one control, and one for each fiber type at a 0.50 percent fiber by volume concentration) were batched for static testing to determine the impact each steel fiber geometry had on SFRC beams' flexural performance when subjected to three-point bending. Results collected from these initial tests were used in conjunction with results from Part I testing for the selection of an SFRC mixture used in the remainder of the study phase. An SFRC mixture was selected, and additional SFRC beams were batched using the selected mixture for static testing. With the selection of a new mixture design for SFRC beams, the tensile reinforcement was balanced with the compressive strength provided by the selected mixture and shear reinforcement was varied as per the beam designs denoted in table 49.

Static Beam Test Configuration

The scaled beams were supported by steel wide flange columns on pin and roller supports to prevent the development of axial forces that could lead to artificial strut action. A pin and roller supported beam system was chosen to allow for movement of the beam at the roller support as mid-span deflection increased. The total unsupported span length was 73.0 inches (1854.2 mm). A 220-kip (978.6-kN) hydraulic actuator was used to apply a load at midspan, where a steel plate measuring 0.5 inch × 14.8 inches × 14.8 inches (13 mm × 375 mm × 375 mm) was used to distribute the load to the beam. The steel plate was used to distribute the load such that a three-point bending test was performed. The hydraulic actuator was set to "deflection controlled," which increased at a fixed rate of 0.005 inch (0.127 mm) per second.

Data Analysis

Static three-point testing was performed to develop a load–deflection curve. This was analyzed by integrating the function between load and mid-span deflection to determine the toughness of the SFRC mixtures. To calculate the toughness, the change in deflection at various points was multiplied by the corresponding load measurement and summarized. Data from preliminary laboratory-scale static beam testing were used for optimization of the steel reinforcement design. Steel reinforcement ratios in conjunction with steel fibers were analyzed for balancing of the design. These results were used to draw conclusions on the energy dissipation capacities of the SFRC mixtures. In addition to static testing, fresh properties and compressive strengths of the optimized mixtures were measured and reported.

SFRC Static Beam Test Results

A preliminary set of laboratory-scale static beams was batched with fiber volume percentages of 0.50 percent. For these preliminary beams, the compressive strengths of six cylinders were measured at 28 days of age. The static beams were subjected to a three-point bending test by applying a load at mid-span using a 220 kip (978.6 kN) hydraulic actuator. The load–deflection curve developed from testing is shown in figure 79; beams are denoted by their beam identification followed by their respective average compressive strength value within the legend in the figure. These beam identification numbers follow those included in 49. From the load–deflection curve, the toughness was calculated by determining the area under the curve. Additionally, the linear stiffness of each mixture was analyzed and the estimated value calculated. Table 50 summarizes the static test results for the beams. The maximum moment, M_u, and corresponding shear force, V_u, are calculated using the maximum load, P_u, recorded by the hydraulic actuator.

The first set of beams were used to observe the influence fiber geometry has on laboratory-scale reinforced concrete beams and included beams C1, and B1 through B4. Figure 80 shows the crack development from static testing of these beams. Within the figure, beams B1 and B2 were pictured at the point of max load, while beams B3 and B4 were pictured at the termination of testing. Regretfully, the research team was unable to procure photographs of beams B1 and B2 at failure. From static testing, flexural and flexural-shear cracks were observed on all beams within this test set. The type of crack was determined by inspecting the inclination of the crack from the bottom of the beam. Flexural cracks propagated straight up from the bottom of the beam. Flexural-shear cracks grew perpendicular to the bottom of the beam, after which they inclined toward the point of loading.

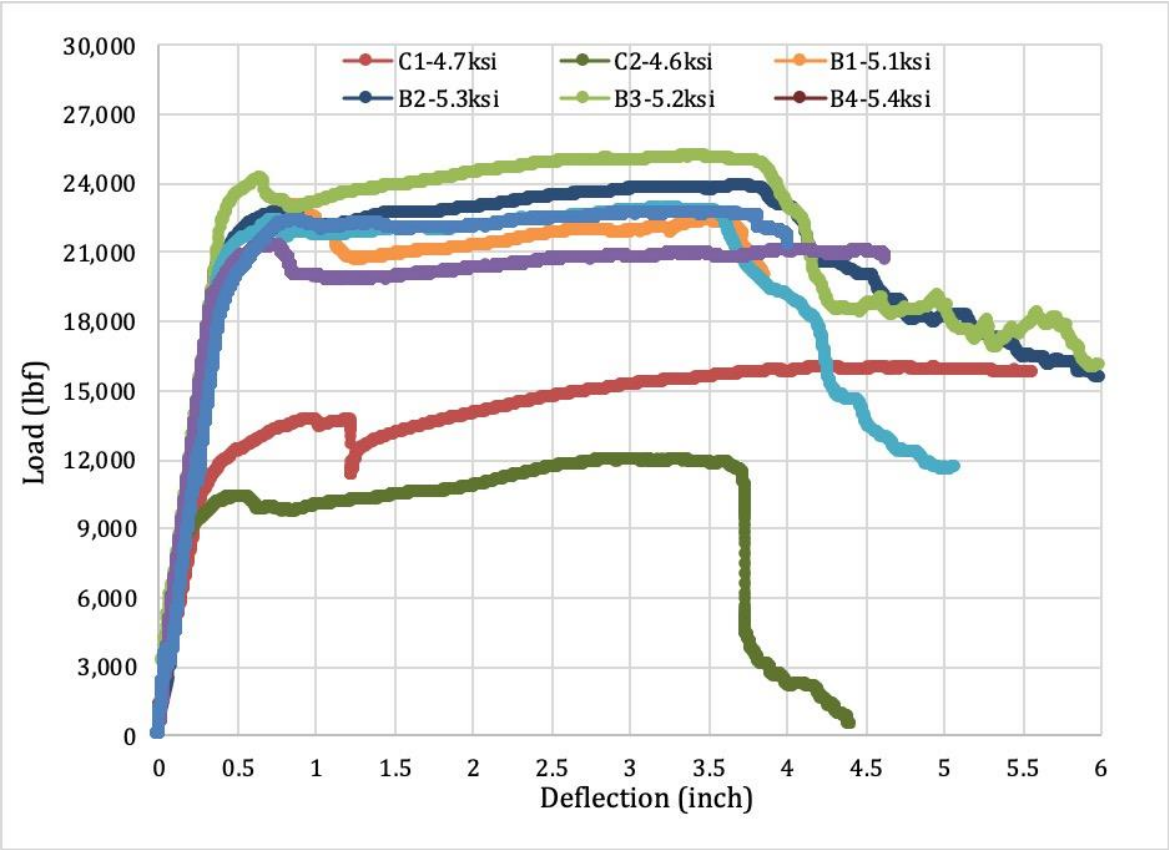

Figure 79. Graph. Part II SFRC beam static testing load vs. deflection results.

Table 50. Beam static test results.

Beam ID	P_u (kip)	M_u (kip-ft)	V_u (kip)	Toughness (kip-in)
C1	16.8	24.3	8.4	79.0
C2	12.0	18.2	6.0	41.2
B1	23.0	34.9	11.5	86.3
B2	23.8	36.3	11.9	145.9
B3	25.2	38.3	12.6	135.9
B4	24.6	37.6	12.3	139.8
B5	22.8	34.8	11.4	98.8
B6	21.6	32.4	10.8	95.7
B7	20.4	34.5	10.2	85.2

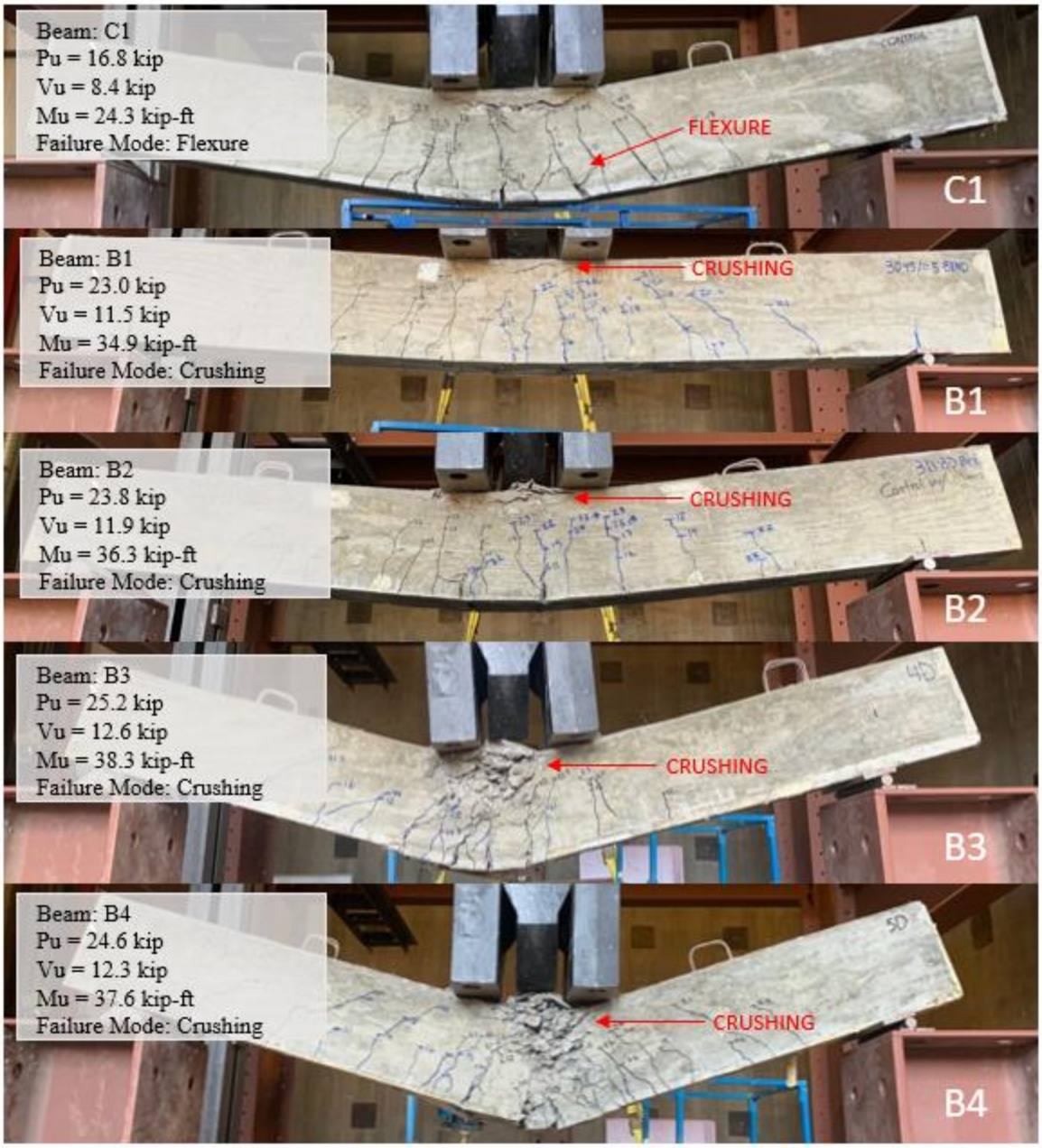

Figure 80. Photos. Crack propogations of C1 and SFRC beams B1 through B4.

The distribution of the flexural cracks showed how well the concrete was able to redistribute internal stresses throughout the material. More flexural cracks showed that the load was more evenly distributed across the tensile face of the beam. From figure 80, all of the SFRC beams experienced similar crack development. In comparison to beam C1, the SFRC beams were more

efficient at distributing the tensile stresses throughout the beam. Beam C1 developed fewer, larger flexural cracks that were very concentrated at the point of loading. All beams experienced crushing of concrete within the compression zone, which resulted in increased deflection before tensile steel could yield. This is undesirable, as this allows for a rapid increase in deflection upon failure, as shown from the load–deflection curves presented within figure 79.

On average, flexural capacity was increased by 51.30 percent when comparing the average results of the preliminary SFRC beams to the C1 beam. The SFRC beams B1 to B4 possessed an additional tensile reinforcing bar to combat the increased compressive capacity obtained from steel fibers, similar to the earlier investigation of the fiber-reinforced rubberized concrete. By analyzing the cross sections of the concrete beam design, it was determined that the additional reinforcement bar increases the flexural capacity by approximately 20.00 percent, resulting in a flexural capacity increase of 31.30 percent from steel fibers. Within the preliminary test set, the highest capacity was obtained by beam B3, withstanding a maximum moment of 38.3 kip-ft (51.8 kN-m) and maximum shear of 12.6 kip (55.9 kN). While beam B4 contains 5D/65 fibers, the observed flexural capacity of 37.6 kip-ft (50.9 kN-m) was only 3.50 percent higher than that of B2 with the 3D/80 fibers. As expected, the use of 3D/45 within beam B1 resulted in the lowest flexural performance enhancement compared to the other fiber types tested, due to the short length of the fibers. Results from static testing closely resembled patterns observed in the SFRC MOR observations. None of the beams within this test set experienced shear cracking.

There was a 91.98 percent increase in toughness from the addition of fibers at 0.50 percent by volume, in comparison to the control beam. Overall, the SFRC mixtures performed similarly to one another, with B2 resulting in the highest toughness value of 145.9 kip-in (16,484 kN-mm), and the highest linear stiffness of 55.6 kip/in (9,737 kN/mm). B2, which utilized the 3D/80/0.5

mixture possessed a higher toughness than B3, due to better redistribution of the post-crack load. The higher observed toughness of B2 can be contributed to possessing the longest fiber of those studied in this research. The additional fiber length allowed for more development length of fibers, and increased the load required for fiber pullout to occur. If only the strain hardening region of the load–deflection curves are considered, beam B3 outperforms all other beams within the test set. The 3D/45/0.5 mixture resulted in the lowest toughness of all the SFRC mixtures, due to the low aspect ratio and short fiber length resulting in a lower post-crack performance.

Based on the findings of the preliminary static beam testing, mixture 4D/65/0.75 was selected for use in the remainder of the Part II static SFRC beam investigation. This mixture was selected based on the impressive static beam results of beam B3, and the hardened property results from Part I testing.

Beams B3 and B5 were batched using the 4D/65/0.5 SFRC mixture with beam B3 containing stirrups at 4 inches on center, like beam C1, while beam B5 featured stirrups at 8 inches on center, like beam C2. By comparing beam B3 with beam B5, it is shown that the increased spacing of the shear stirrups decreased the flexural capacity of the SFRC beams by 9.10 percent, which is much less than the decrease of 25.10 percent between beams C1 and C2. The increased stirrup spacing of beam C2 resulted in a shear failure; however, beam B5 only experienced the development of flexural-shear cracks, and ultimately failed from crushing. From figure 79, it is observed that the onset of crushing failure within the compression zone resulted in beam B5 failing rapidly, while beam B3 was able to continue carrying load through a larger deflection.

With the increased shear stirrup spacing, beam B5 experienced the development of flexural shear cracks at the mid-span of the beam. A reduction in shear reinforcement led to the toughness of

the SFRC beams being reduced by 27.30 percent, dropping from 135.9 kip-in (15,790 kN-mm) to 98.8 kip-in (11,165 kN-mm) for beams B3 and B5, respectively. For comparison, the drop in toughness comparing beams C1 and C2 was 47.80 percent, a drop from 79.0 kip-in (8,928 kN-mm) to 41.2 kip-in (4,655 kN-mm). The change from a shear failure to a flexure-shear failure shows that fibers may be used as a partial replacement for shear reinforcement, however for this particular beam design a higher volume of fiber is required to procure a flexural failure mode for the SFRC beam.

Beams B6 and B7 were batched using the 4D/65/0.75 SFRC mixture, which possessed the highest compressive strength results within Part I testing. Beam B6 contains stirrups at 4 inches on center, while beam B7 contains stirrups at 8 inches on center. This mixture was chosen to combat the early crushing failure observed in beams B3 and B5. In comparison to beams B3 and B5 made with a tensile reinforcement ratio (ρ) of 1.21 percent, beams B6 and B7 feature an optimized tensile reinforcement ratio (ρ) of 1.03 percent. With the decrease in flexural reinforcement, beam B6 resulted in a flexural toughness of 95.7 kip-in (10,813 kN-mm), which is 29.60 percent lower than the flexural toughness of 135.9 kip-in (15,790 kN-mm) observed by beam B3. The increased stirrup spacing within beam B7 led to a decrease in flexural toughness of 10.90 percent of that observed by B6. This is not as significant as the 27.30 percent reduction in toughness observed by comparing beam B3 to B5.

As observed in figure 81, beams B6 and B7 experienced flexural failure, with full yielding of flexural steel reinforcement. With the increased compressive strength and decreased flexural steel ratio, in comparison to preliminary beams, a longer strain hardening region was obtained. Both beams B6 and B7 experienced little crushing of concrete within the compressive zone, allowing for the flexural steel to be fully utilized until yielding occurred. Additionally, the load

drop experienced at initial concrete cracking of beam B7 was less than that experienced by beam B6, which can be attributed to the increased compressive strength of the SFRC mixture. The failure modes of beams B6 and B7 are shown in figure 81.

SFRC Static Beam Summary

Part II testing has shown that fiber reinforcement may be used as a partial replacement for shear reinforcement at fiber volumes of 0.75 percent or greater. The results of this study agree with the findings of the study conducted by Choi et al. (2007), in which a fiber volume ratio of 0.75 percent was used to replace the minimum stirrup requirements set by ACI 318-14. By incorporating steel fibers, the flexural and shear capacity of the reinforced concrete beam was increased, and partial amounts of reinforcing steel were able to be removed from the design without loss of strength.

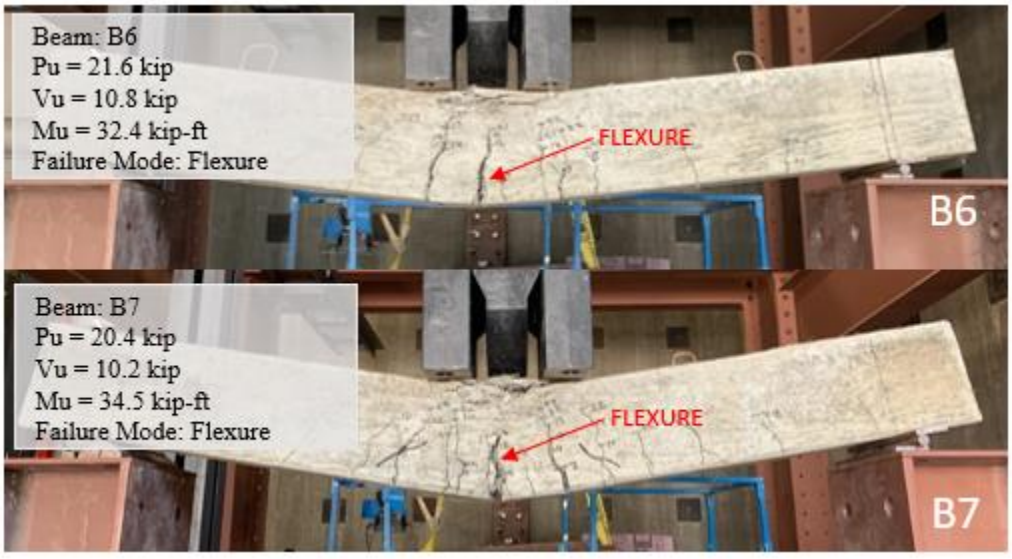

Figure 81. Photos. Comparison of B6 and B7 failure modes.

PART III – SFRC MECHANICAL PROPERTY PREDICTIONS USING MACHINE LEARNING ALGORITHMS

Part III of the SFRC investigation involved the use of machine learning classification and regression tree methods for the prediction of SFRC compressive strength and MOR values based on concrete mixture parameters. These models were developed using a database constructed with data from this experimental study and from previously published literature. The database was split, 80.00 percent for the training data set used for training the model, and the remaining 20.00 percent as the test data set for comparison of the mechanical property predictions. The types of decision tree methods used were random forests, bootstrap aggregation (or "bagging"), and gradient boosting.

Data Acquirement

The data were acquired from various research papers that were published on the mechanical properties of SFRC. By collecting experimental results from various published investigations, an experimental established database for training a prediction model was created. From this literature review, concrete mixture proportions, fiber properties, and measured concrete mechanical property data were collected and categorized. In total, the database included experimental results from 12 published sources—Acikgenc et al. (2013), Al-Ameeri (2013), Alavi Nia et al. (2012), Campione and Letizia Mangiavillano (2008), Guerini et al. (2018), Guler et al. (2019), Kwak et al. (2002), Lee et al. (2019), Marar et al. (2016), Song and Hwang (2004), Soulioti et al. (2011), and Torres and Lantsoght (2019)—and results collected totaling 103 observations. The database constructed is presented in Appendix A and includes the following SFRC mixture properties: cement proportion (cp; lb/ft^3), coarse aggregate proportion

(cap; lb/ft^3), fine aggregate proportion (fap; lb/ft^3), water to cement ratio (w/c), fiber length (fl; inch), fiber aspect ratio (ar), volume of fibers (Vf; %), and reinforcement index ($ri = Vf \times l_f / d_f$).

Decision Tree Models

Three types of decision tree machine learning methods were implemented within this study phase. The methods used were random forests, bootstrap aggregation or "bagging," and gradient boosting. Random forests are an ensemble of individually generated decision trees that each make their own prediction. All of the trees that were developed by this analysis were uncorrelated, meaning that the predictions made from one tree do not influence the predictions made by another tree. Random forests were uncorrelated because when developing decision trees, each node of a tree considers a random sample of *m* predictors of the total set of *p* predictors.

Data Analysis and Model Validation

Machine learning is a powerful statistical method used to develop accurate estimations of SFRC mechanical properties and to measure the correlation between mixture parameters. From the machine learning models, a better understanding of the influence each parameter has on the compressive strength and MOR of SFRC mixtures was developed. These correlations and influences were measured by comparing the accumulated reduction in mean squared error (MSE) each time a variable was selected as a node split for a tree within the forest. This provides important information on how steel fibers interact with the concrete mixture constituents and how mechanical properties may be enhanced. Validation of the models was performed by examining the root-mean-square error (RMSE) and coefficient of determination. Additionally, prediction values obtained by the model were compared with predictions obtained by the

proposed design expressions discussed in literature. As discussed within the literature review, Guler et al. (2019) has reported the expressions shown in table 51 to be accurate SFRC mechanical property prediction expressions. These equations were chosen to be compared against the machine learning models developed within this study for comparison. The mechanical property values measured within Part I of the SFRC investigation were used to measure the accuracy of the models with GDOT-specific concrete mixtures.

Table 51. SFRC mechanical property strength expressions.

Researcher	Compressive Strength	Flexural Strength
Abedel et al.	$f'c = f'c + 5.222RIv$	$f'f = f'f + 5.222RIv$
Guler et al.	$f'c = 0.92f'c - 1.44vf + 14.6RIv$	$f'c = 0.24f'c + 1.12vf + 7.1RIv$
Padmarajaiah	$f'c = f'c + 1.998RIv$	$f'f = f'f + 5.222RIv$

Machine Learning Decision Tree Model Results

To begin the analysis, the random forest method was used to develop decision trees. The decision trees developed with the random forest method for compressive strength and MOR are shown in figure 82. The decision trees help to show the hierarchy of parameter importance in the decision-making process of the models. The top three most important parameters for compressive strength were determined to be water/cement ratio, fiber reinforcement index, and fiber length. The top three most important parameters for MOR were fine aggregate proportion, coarse aggregate proportion, and fiber reinforcement index.

It is widely known that the water/cement ratio has the greatest influence on the compressive strength of concrete. When the water/cement ratio of the mixture is lower than 0.34, then the fiber reinforcement index is the next referenced parameter by the decision trees, showing that fibers have a greater influence on concrete mixtures with low water/cement ratios than those with

high water/cement ratios. The fine aggregate proportion is shown to have the greatest influence on the flexural strength of SFRC according to the developed decision tree model. As the fine aggregate proportion increases, the coarse aggregate proportion will decrease, allowing for the fibers to have a greater impact on the flexural strength.

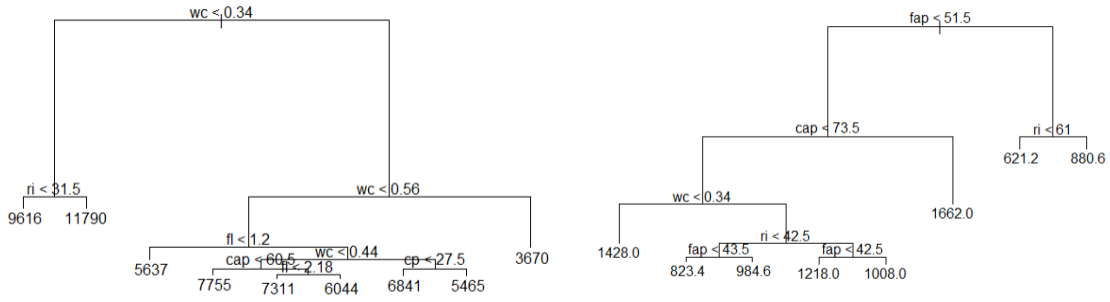

(a) **(b)**

Figure 82. Images. Random forest decision trees for: (a) compressive strength, (b) MOR predictions.

Pruning of the decision trees was performed to increase the performance of the models. By pruning the tree, unnecessary terminal nodes are determined through cross-validation and removed to achieve the optimal level of tree complexity. Pruning of the trees led to a decrease in the MSE of the predictions and a less cluttered decision tree, as shown in figure 83.

To better understand how the mixture parameters of the models influence one another, correlation matrices were plotted to illustrate the interaction of parameters and their influence on the mechanical properties of SFRC. Within figure 84, each parameter is plotted against all other parameters, resulting in a blue marker for a positive correlation, or red for a negative correlation with each other parameter. The size of the correlation circles designates the influence, or change, the parameter has on the other input parameters, with larger circles signifying greater influence.

This is especially useful for visualizing the considerations made by the decision trees and seeing how each parameter affects the compressive strength and MOR of concrete.

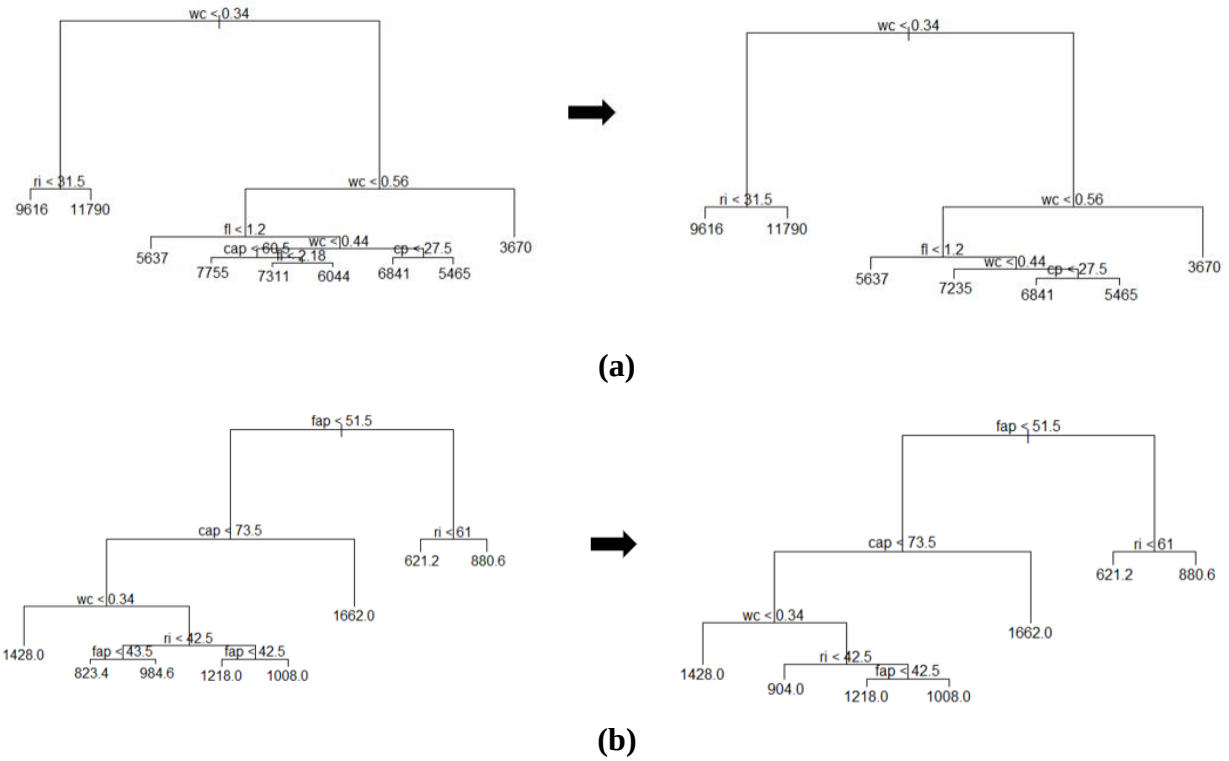

Figure 83. Images. Before and after pruning of random forest decision trees for: (a) compressive strength, (b) MOR predictions.

From the matrices, an increase in coarse aggregate proportion has a positive effect on compressive strength and MOR, while an increase in fine aggregate proportion has an inverse effect. This was due to higher contents of coarse aggregate allowing for the coarse aggregate to interlock within the concrete matrix and carry a great portion of the load. As expected, an increase in water/cement ratio leads to a decrease in compressive strength and MOR. The only fiber property that had an influence on compressive strength was the fiber length, which increased the compressive strength slightly as the length of the fibers increased. This was due to

an increased fiber length allowing for more bridging of microcracks by the fibers. With respect to MOR, an increase in any fiber property leads to an increase in flexural strength.

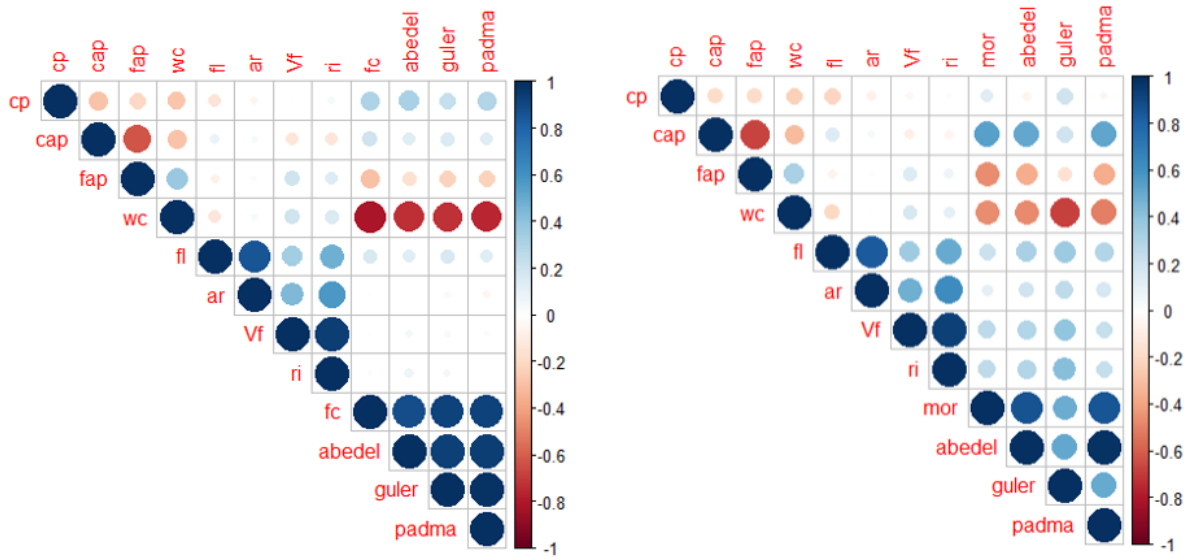

(a) **(b)**

Figure 84. Images. Parameter correlation plots for: (a) compressive strength, (b) MOR.

Using the two most defining parameters shown by the decision trees, a 2D partition was created in which data points were plotted based on the defining parameters of the corresponding mixture. The two most influential parameters for compressive strength are water/cement ratio and fiber reinforcement index. For MOR, the two most influential parameters were coarse aggregate proportion and fiber reinforcement index.

The analysis showed that as the reinforcement index of fibers increases, the compressive strength of the SFRC mixtures increases. Further, the 2D partition showed that the fiber reinforcement index has a greater influence on compressive strength in mixtures with lower water/cement values, as was shown with the decision tree. SFRC mixtures with a water/cement ratio around

0.3 showed a larger variation in the average compressive strength values with increasing fiber reinforcement index compared to concrete mixtures with a water/cement ratio of 0.6. As the water/cement ratio decreases, the strength of the cement paste increases and, thus, the strength of the bonds between the fibers and aggregates increases. This allows for more load to be transferred across internal microcracks as they form, and aids with aggregate interlock.

The researchers examined the influence of the fiber reinforcement index with varying coarse aggregate proportion on MOR of SFRC mixtures and found that as the coarse aggregate proportion decreases, less aggregate interlocking occurs and more load is transferred through the fibers. Essentially, the fibers begin to act as the coarse aggregate within the mixture as they become the largest ingredient within the mixture. The fibers act similarly to reinforcing bars in reinforced concrete beams and add additional tensile capacity to MOR test specimens.

Comparison of Machine Learning Methods and Established Design Expressions

The accuracies of the prediction models were determined by measuring the RMSE and R^2 for the design expressions shown in table 51 in comparison with the machine learning models. Overall, all machine learning methods implemented within this investigation produced strength predictions of mixtures within the SFRC dataset with great accuracy. Compared to design expressions, the machine learning models developed predictions with less RMSE. The gradient boosting machine (GBM) is the most accurate prediction model for SFRC mechanical properties. Table 52 summarizes the RMSE and R^2 results of each prediction method used. The results show that the GBM model was the most accurate of the prediction methods with RMSE and R^2 values of 575 and 0.947, respectively, for compressive strength, and 115 and 0.936, respectively, for MOR.

Table 52. Machine learning model accuracy measurements.

Prediction	Measurement	Prediction Method					
		Random Forest	Bagged	GBM	Abedel et al.	Guler et al.	Padmarajaiah
Compressive Strength	RMSE	787	629	575	970	1341	1070
	R^2	0.926	0.945	0.947	0.864	0.833	0.870
MOR	RMSE	208	172	115	229	866	242
	R^2	0.851	0.927	0.936	0.794	0.305	0.804

Comparisons between the observed and predicted values of all strength prediction methods were considered and revealed that predictions made by the machine learning models were all in close proximity of the line of equality between the predicted and observed test values. There are no outliers amongst the predictions by the machine learning models.

The established SFRC compressive strength expressions found in literature (see table 51) underestimated the strength of the SFRC mixtures. Mixtures with lower compressive strength values tended to be overestimated by the proposed expressions, while mixtures with higher measured compressive strength tended to be underestimated. This is added to the fact that the proposed expressions do not account for other more influential parameters of the concrete mixture, such as the water/cement ratio or aggregate proportioning. Interestingly, it was determined that the proposed expressions overestimated the flexural strength of the SFRC mixtures, with the expression proposed by Abadel et al. (2016) being the least accurate for the testing set. This analysis concludes that the machine learning models more accurately predicted the compressive and flexural strengths of the SFRC mixture testing set. While the researchers who proposed the expressions found them to be accurate for their mixture data as discussed in literature, these expressions do not consider other aspects of the SFRC mixture that influence mechanical properties. The machine learning models are able to take these parameters into

consideration when developing strength predictions by learning how the individual mixture components interact with each other through determining trends in the data.

Validation of Machine Learning Models

Model validation is important for determining whether a model is performing as expected, and it provides insight to potential limitations and uses of the model. From table 52, the GBM model has the lowest number of residual error and the greatest R^2 results in comparison to other models considered. Because of this high accuracy, the GBM model was used moving forward with the investigation. For model validation, strength predictions of Part I SFRC mixtures were developed using the GBM model and proposed strength expressions. Comparisons of the GBM model with the proposed strength expressions was performed to examine the prediction method accuracy. It was important to validate the model with GDOT SFRC mixture data to ensure that the models are reliable predictors for GDOT. Figure 85 and figure 86 display the comparison between the predicted and the observed compressive and flexural strength values of Part I SFRC mixtures, respectively.

As shown in figure 85, the published design expressions underestimated the compressive strength of the Part I mixtures. In general, the GBM model overestimated the compressive strength value while still being more accurate than the design expressions. The difference between the observed values and GBM predicted values ranged from 131 to 1095 psi (0.9 to 7.5 MPa), with the greatest difference occurring with the mixtures containing 1.00 percent fibers by volume. The proposed expressions predict a slight increase in the compressive strength of SFRC mixtures with an increase in fiber volume, which is expected as an increase in fiber

volume increases the reinforcing index, the only fiber parameter used in the expressions proposed by Abadel et al. (2016) and Padamarajaiah (1992).

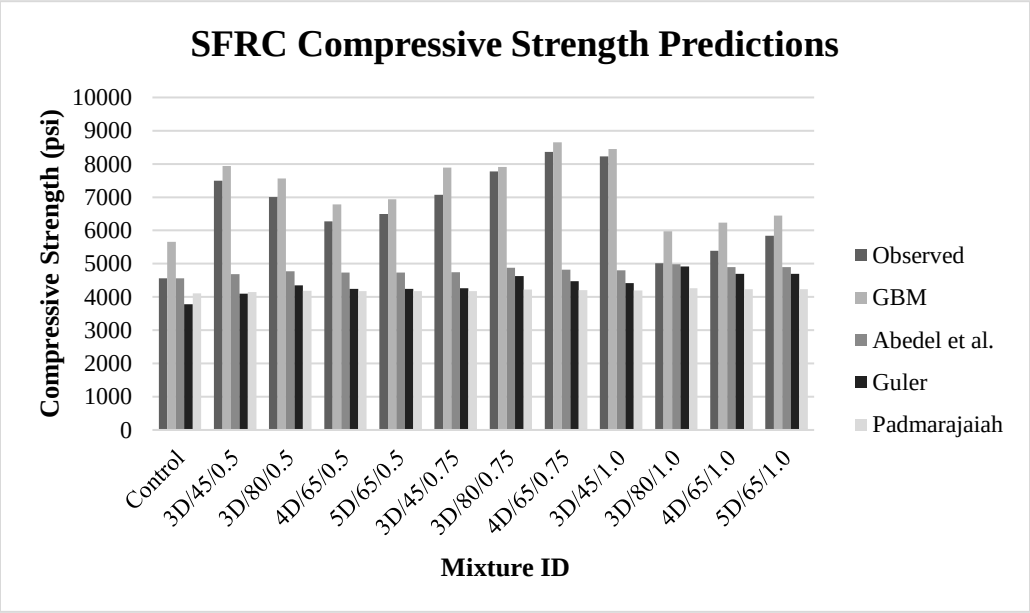

Figure 85. Graph. Comparison of compressive strength prediction models.

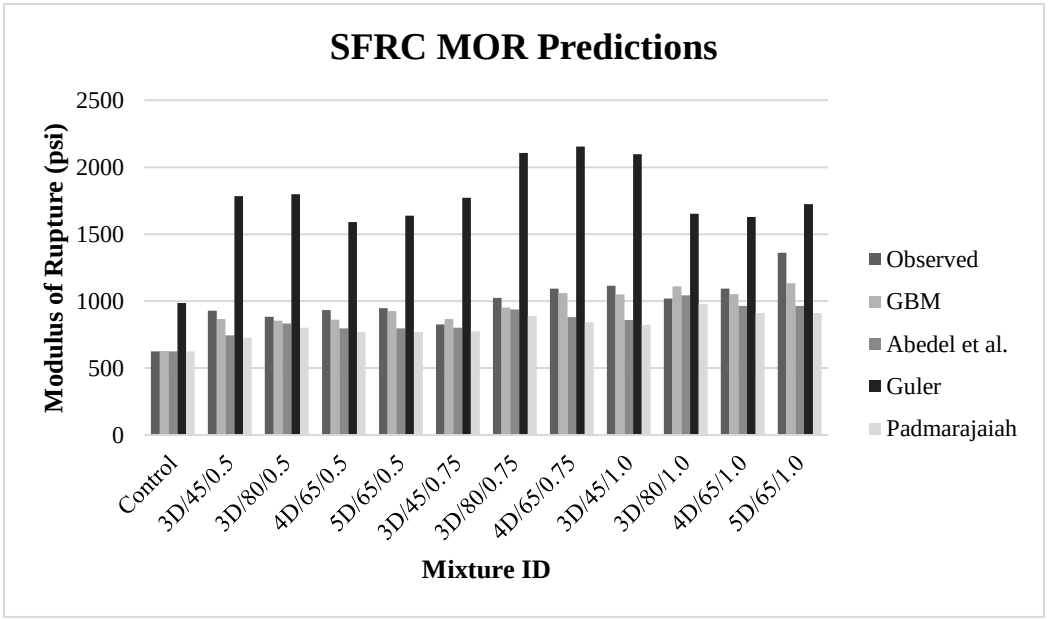

Figure 86. Graph. Comparison of flexural strength prediction models.

Figure 86 illustrates that the majority of the prediction methods are close in accuracy, with the expression proposed by Guler et al. significantly overestimating the flexural strength of the Part I SFRC mixtures. The majority of the predictions agreed with the trends found in MOR experimental data, showing that flexural strength increased with increased fiber volume fraction. The equation proposed by Guler et al. uses the compressive strength of the SFRC mixture within the expression, a potential cause of the increased error. A comparison of the prediction methods was performed by determining the ratio between the measured and predicted values. The results of the comparisons reinforce the accuracy of the GBM model. The GBM model overpredicted Part I compressive strength by 8.60 percent on average, and underpredicted the flexural strengths by 4.00 percent. Expressions proposed by Abedel et al. were the second most accurate prediction method, having underpredicted both the compressive and flexural strengths by 38.40 and 15.30 percent, respectively. These results indicate that the GBM model predicts the compressive and flexural strength of SFRC with far greater accuracy than other proposed expressions. The GBM model is able to consider all aspects of the SFRC mixture when developing a prediction, rather than only considering the base compressive or flexural strength and the fiber reinforcing indexes as the other prediction expressions offer.

Model Deployment

The GBM model is useful for estimating the compressive and flexural strengths of SFRC mixtures without having to perform time-consuming destructive testing. Deployment of the model allows for users to have access to the GBM model without needing to have RStudio to run the model code. The webpage link, https://ugagdotrp1709.shinyapps.io/GDOT-RP-17-09-App/, provides access to the full potential of the GBM model for SFRC strength predictions. The GBM model developed within this study phase is deployed using the shinyapps R package, which

allows for the program to run in the cloud on shared servers operated by RStudio. This deployment method allows for the GBM model to be run from a webpage where users, such as GDOT, may develop SFRC strength predictions and mixture costs based on mixture parameter inputs. Figure 87 shows the shinyapp webpage developed for the GBM model.

Deployment of the machine learning model allows for users to develop predictions of their own SFRC mixtures with reliable accuracy. With this powerful prediction method, one can analyze a variety of concrete mixtures for their suitability for fiber reinforcement. As fiber reinforcement adds upfront costs to the concrete mixture, it is important to ensure that the addition of fibers will enhance the mechanical properties of the mixture enough to justify the increased cost. By first developing strength predictions for potential SFRC mixtures, one is able to conclude if the addition of fibers is beneficial before needing to produce test samples or even ordering the fibers. As this model accounts for all aspects of mixture proportions, it is far more reliable than other proposed SFRC strength expressions, and may be referenced during the mixture design process. It is recommended that if a user designs a mixture using the deployed model, a test mixture should still be performed to both validate the strength prediction and to determine admixture proportioning to counteract the unfavorable fresh properties of the SFRC mixture.

Economic Considerations for SFRC Mixtures

The use of SFRC has many benefits aside from the enhanced mechanical properties. With the use of fiber reinforcement, traditional steel reinforcement may be replaced, which saves both material and labor costs. Additionally, the durability of the concrete element is increased, which may lead to lowered maintenance costs and longer service life. These savings should be

considered when performing an economic analysis on the use of SFRC in comparison to conventional reinforced concrete.

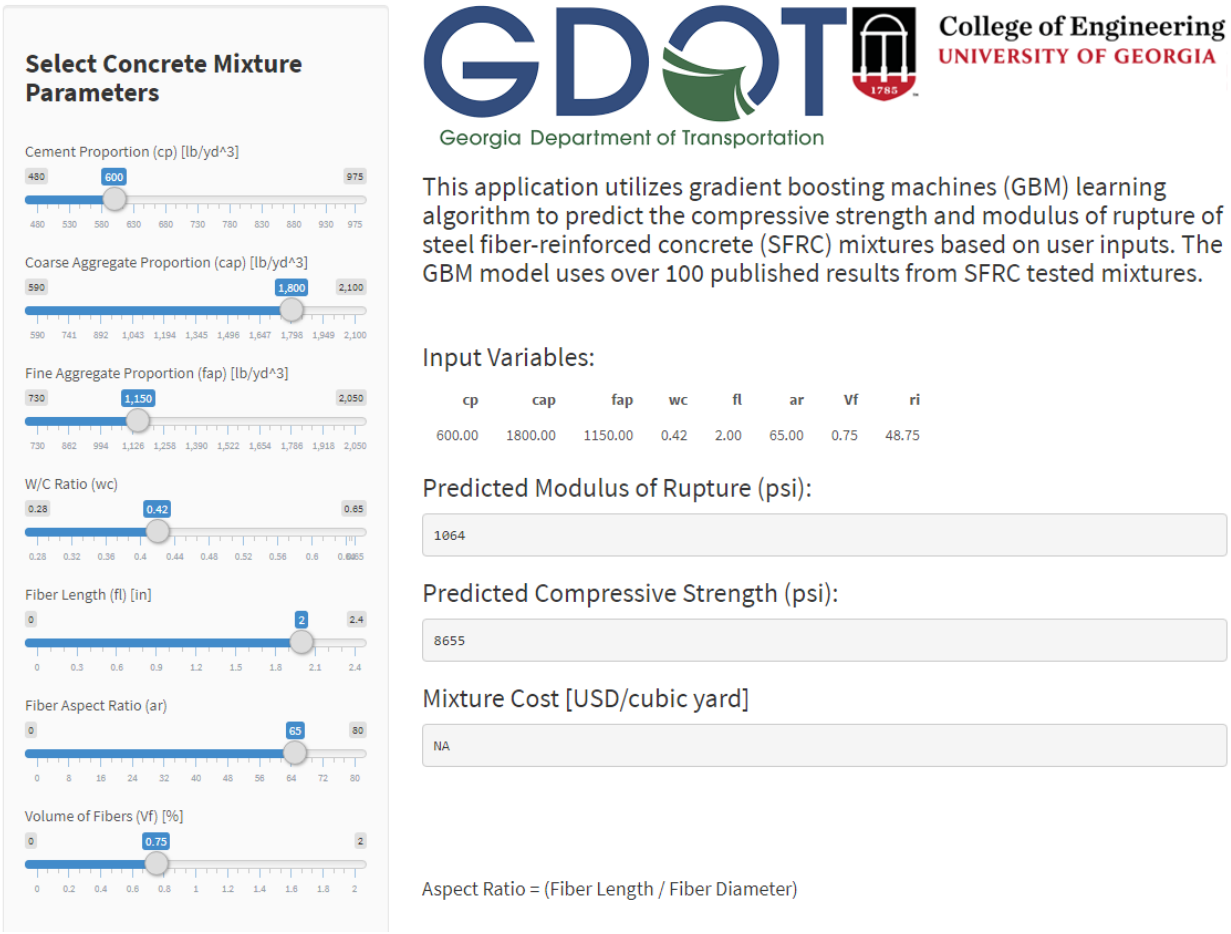

Figure 87. Image. Deployed model webpage (cost inputs excluded).

Economic Analysis

An economic analysis was performed to determine the cost effectiveness of using steel fibers in GDOT standard concrete mixtures. Material costs were collected from suppliers for the purpose of this analysis. The costs of materials are shown as USD ($) / ton (0.91 metric ton). Table 53 summarizes the cost analysis, with the total unit cost for one cubic yard of the concrete mixture

shown. Costs of materials used in this analysis reflect the cost of materials from suppliers within Georgia.

Table 53. Part I SFRC mixture costs per cubic yard.

	Material/Cost								
	Cement	**Coarse Agg.**	**Fine Agg.**	**Water**	**Steel Fibers**	**AEA**	**HRWRA**	**VMA**	**TOTAL**
Mixture	*$140/ton*	*$24/ton*	*$18/ton*	*$0.60/ton*	*Varies**	*$3.50/gal*	*$8/gal*	*$15/gal*	
Control	$44.45	$21.60	$10.22	$0.08	—	$0.08	$2.28	$3.35	**$82.06/cy**
3D/45/0.50	$44.45	$21.60	$10.22	$0.08	$62.42	$0.08	$2.28	$3.35	**$144.47/cy**
3D/80/0.50	$44.45	$21.60	$10.22	$0.08	$57.82	$0.08	$2.28	$3.35	**$139.87/cy**
4D/65/0.50	$44.45	$21.60	$10.22	$0.08	$60.44	$0.08	$2.28	$3.35	**$142.50/cy**
5D/65/0.50	$44.45	$21.60	$10.22	$0.08	$77.53	$0.08	$2.28	$3.35	**$159.58/cy**
3D/45/0.75	$44.45	$21.60	$10.22	$0.08	$93.67	$0.08	$2.28	$3.35	**$175.73/cy**
3D/80/0.75	$44.45	$21.60	$10.22	$0.08	$86.77	$0.08	$2.28	$3.35	**$168.82/cy**
4D/65/0.75	$44.45	$21.60	$10.22	$0.08	$90.71	$0.08	$2.28	$3.35	**$172.77/cy**
3D/45/1.00	$44.45	$21.60	$10.22	$0.08	$124.83	$0.08	$2.28	$3.35	**$206.89/cy**
3D/80/1.00	$44.45	$21.60	$10.22	$0.08	$115.63	$0.08	$2.28	$3.35	**$197.69/cy**
4D/65/1.00	$44.45	$21.60	$10.22	$0.08	$120.89	$0.08	$2.28	$3.35	**$202.94/cy**
5D/65/1.00	$44.45	$21.60	$10.22	$0.08	$155.05	$0.08	$2.28	$3.35	**$237.11/cy**

Notes: *Fiber costs: 3D/45 = $0.95/lb; 3D/80 = $0.88/lb; 4D/65 = $0.92/lb; 5D/65 = $1.18/lb
— = No data

As expected, the addition of steel fibers into the concrete mixture greatly increased the unit cost of the concrete mixture. The costs of fibers differ based on the geometry of the fiber and the fiber coating. The cost of the 3D/45, 3D/80, 4D/65, and 5D/65 are $0.95/lb, $0.88/lb, $0.92/lb, and $1.18/lb, respectively. The 5D/65 is the most expensive fiber per pound, due to the advanced end anchorage and a special galvanized coating that reduces exposed fiber corrosion. On average, there was an increase in unit cost of 78.66, 120.63, and 157.30 percent for fiber volume fractions of 0.50, 0.75, and 1.00 percent, respectively. While the use of steel fibers may increase the unit cost of the concrete mixtures dramatically, the benefits obtained through the use of fibers can outweigh the additional cost if used correctly in the proper application

One method of considering the costs and benefits of fiber reinforcement is by determining the cost per unit increase in concrete strength. To do this, the correlation between the increase in compressive strength and the increase in unit cost of the concrete mixture was determined. Table 54 summarizes the cost per unit (1 psi) increase in compressive strength and MOR of the Part I SFRC mixtures. The cost effectiveness of fibers differed with fiber content. For example, the 3D/45 fiber was the most cost effective for increasing the compressive strength for fiber volumes of 0.50 and 1.00 percent, but was the least effective at a fiber volume of 0.75 percent. Overall, the 3D/45 fiber was determined to be the most cost effective for increasing compressive strength, showing a 1 psi (0.0068 MPa) increase in compressive strength for approximately $0.03, on average. In contrast, the 3D/80 fiber was the least cost effective of the fibers studied, showing a 1 psi (0.0068 MPa) increase in compressive strength for an average of $0.10. Inspecting the change in flexural strength, 4D/65 fibers were the most cost effective for improving the flexural capacity of concrete mixtures, costing an average of $0.23 per unit increase in flexural strength. In contrast, the 3D/45 fibers were the least cost effective for improving flexural capacity, costing $0.36 per unit strength increase, on average.

Table 54. Cost ($USD) per unit increase in strength of fibers studied.

	Cost per Unit Increase in f'c			Cost per Unit Increase in MOR		
Fiber	**Vf = 0.5%**	**Vf = 0.75%**	**/f = 1.0%**	**Vf = 0.5%**	**f = 0.75%**	**Vf = 1.0%**
3D/45	0.021	0.037	0.034	0.233	0.570	0.276
3D/80	0.024	0.027	0.258	0.260	0.240	0.324
4D/65	0.035	0.024	0.146	0.222	0.194	0.280

Cost Savings Potentials with Fiber-Reinforced Concrete

The use of SFRC provides cost benefits in other forms than just increased strength. As discussed within the literature review, fibers can be used as a replacement of traditional steel reinforcement in various applications, most notably, as a replacement for shear stirrups in reinforced concrete beams, or as primary or secondary reinforcing steel in concrete slabs and bridge decks. By replacing traditional reinforcing steel, both material and labor cost savings are obtained. Steel fibers may be added to the concrete mixture at the batch plant, and transported onto the job site for placement. The amount of labor and time required for laying reinforcing bars is reduced, as workers need only to place the SFRC into the forms and finish as normal.

SFRC possesses enhanced shrinkage crack resistance, reduced permeability, and overall greater strength than conventional concrete. The increased strength reduces maintenance costs significantly. Areas that are often prone to deteriorating first, such as control joints and slab corners, are reinforced to withstand more loading. Additionally, joint spacing can be increased, which reduces the number of critical loads and edges and corners that typically control the design of slabs. Slab thickness may be reduced with the use of SFRC, as flexural strength is increased. As observed from Part II SFRC beam testing, SFRC beams possessed far greater flexural strength.

CHAPTER 6. CONCLUSIONS AND RECOMMENDATIONS

This study investigated the performance of recycled tire chip aggregates in conjunction with fiber reinforcement in standard portland cement concrete for the purpose of optimizing impact resilience. Further, a finite element model was developed and validated through laboratory-scale testing for the purposes of performing vehicle crash simulation of a single-slope CMB as an alternative to full-scale crash tests. Finally, an experimental and analytical investigation into SFRC was performed in order to realize the benefits of steel fiber on concrete properties. Ultimately, the following major conclusions were drawn from this study.

CONCLUSIONS

Fiber-Reinforced Rubberized Concrete Investigation

- In rubberized mixtures containing fiber reinforcement, steel fibers proved to be the most effective in terms of reversing the adverse effects tire chips have on mechanical properties, as well as maintaining workability.
- Increasing steel fiber volume fraction in rubberized mixtures improved flexural strength, although it had inconsequential effects on compressive strength.
- Drop-hammer impact resilience decreases as a result of overcrowding within the concrete matrix at a small scale. As a result, 0.75 percent steel volume fraction exhibited greater impact resilience than 1.00 percent.
- When subjected to static load testing, rubberized mixtures without fiber reinforcement showed an increase in ductility compared to the control; however, they were more susceptible to crushing failure at the contact surface.

- Steel fiber inclusion at 0.50, 0.75, and 1.00 percent volume fraction improved the flexural capacity of the fiber-reinforced rubberized concrete beams and decreased deflection compared to the control.
- Because fiber-reinforced concrete beams improve flexural and shear capacity, it is desirable to increase the flexural steel reinforcement ratio by 50.00 percent to maximize the energy dissipation potential of the fiber reinforcement, ultimately increasing toughness.
- In conventional reinforced concrete beams without fiber reinforcement or tire chip inclusion, impact forces were dissipated through a local failure, resulting in what is widely known as scabbing (i.e., ejection of target material on distal side), as well as spalling at the target contact surface. Therefore, the kinetic energy was dissipated through fractures of the beam on a local area rather than beam deformation.
- Steel fiber and tire chip inclusion significantly reduced impact forces as a result of increased ductility and more effective energy distribution at initial impact.
- Increasing steel fiber volume fraction from 0.75 to 1.00 percent slightly reduced deflection; however, it increased resistance to compressive, flexural, and shear failure to ultimately achieve an overall target response (global failure).
- The effectiveness of tire chip inclusion decreased with increasing steel fiber volume fraction. It was observed that more energy was dissipated through the steel fiber–reinforced concrete mixture than with the tire chips at higher volumes of steel. This is attributed to increased compressive strength resulting in shear/flexural capacity increases.

Finite Element Model and Laboratory-Scale Testing of Barrier Walls

- The impact resilience properties of the concrete material models were evaluated by changing the failure and post-failure behavior parameters in the concrete material models. Based on the parameter study conducted, the improved material model enabled the prediction of impact performance of tire chip and steel fiber–modified concrete barriers with reasonable accuracy.
- The finite element analysis indicates that the single-slope concrete median barriers were able to successfully resist impact forces generated from a pickup truck collision and, thus, contain and redirect a lightweight pickup truck without sustaining significant damage to the barriers.
- The effect of enhanced impact resilience and ductility from steel fiber and tire chip–modified barriers is more evident for crash incidents involving heavy truck vehicles. In the heavy truck collision models, the barriers without such enhancement in concrete materials sustained relatively severe to excessive deformations when the post-impact behaviors were compared to those of the light truck vehicle.
- The experimental setup for laboratory testing of CMBs was developed based upon the researchers' intuition due to there being no standardized ASTM.
- The control and ST1-TC20 (1.00 percent steel fiber and 20.00 percent tire chip) barriers produced no visible damage due to the dissipation of energy from impact through deflection.
- The presence of steel fibers increased the area under compression along the distal side of the barrier, seeing a 19.90 percent reduction in the maximum strain reading of the ST1-TC20 barrier compared to the control barrier.

- Overall, the ST1-TC20 performed as well as the control barrier at the impact load of 150.0 kips (667.2 kN), despite a 105.00 percent lower compressive strength.

Steel Fiber–Reinforced Concrete Investigation

- The addition of steel fiber reinforcement into concrete mixtures improved the compressive strength. Compressive strength increased as the volume of fibers increased, up to a fiber volume of 0.75 percent, at which the increase in strength began to diminish.
- SFRC possessed 54.36 percent more flexural strength than conventional concrete mixtures, on average. Flexural strength increased with increasing fiber volume.
- Long fibers were more effective at increasing flexural strength than short fibers, as they have more development length across internal cracks.
- Ultimately, the 4D/65/0.75 mixture resulted in the most desirable hardened property strengths of the Part I mixtures, and was selected for use within the Part II static beam testing.
- Similar to what was observed from MOR results, the inclusion of fibers increased the flexural and shear capacity of reinforced concrete beams by 51.30 percent.
- Steel fibers proved to be a potential partial replacement for shear stirrups within SFRC beams. With an addition of fibers at 0.75 percent by volume, the spacing in shear stirrups was able to be doubled without a noticeable effect on the load capacity.
- The GBM machine learning model is a more accurate predictor of SFRC compressive and flexural strength than published design equations. This is primarily due to the GBM's ability to consider all aspect of the SFRC mixture design when predicting strength, while proposed design equations are more limited.

RECOMMENDATIONS

Based on the findings of this study, the following recommendations are made:

- Fiber-reinforced concrete should be proportioned using the absolute volume method. Steel fibers are to be measured as a volume fraction of the total batch volume.
- As steel fibers reduce the workability of fresh concrete, additional dosages of HRWRA should be included in the mixture. Trial batches should be tested to determine the workability of the designed mixture, and any necessary adjustments made to admixture dosages.
- Fiber reinforcement should be included with rubberized mixtures subjected to strong impact forces. Although rubber particles have the ability to increase the energy dissipation capacity of concrete on their own, mechanical properties are negatively impacted, and fiber reinforcement aids in preventing failure by reducing crack propagation and crushing.
- Steel fibers could be integrated into concrete structures that are subjected to intense loading or impact loading. The increased toughness of SFRC provides better dissipation of energy.
- Fiber reinforcement can be used as a partial replacement of tensile or shear reinforcement; however, designs should be reviewed and approved by a licensed structural engineer.
- Increasing the steel reinforcement ratio should be considered as an effective method of increasing concrete toughness, possibly without significantly increasing cost.

- Crash simulations involving heavy vehicles must be evaluated when the full-scale impact test results become available in order to fully validate the results. A large-scale test must be developed to validate the impact performance of steel fiber–reinforced composites.
- For roadways where high frequency of heavy truck vehicles is expected, concrete barriers modified with steel fibers and/or tire chips may be considered in order to reduce the impact force and damage sustained in barriers as well as vehicles.
- Improvement in large-scale ready-mixed concrete production is recommended for the concrete mixtures incorporating tire chips to ensure GDOT Class AA specifications are satisfied for compressive strength.
- Fire accompanying a vehicle collision should be considered in future studies as it is strongly recommended to assess the structural integrity of such cementitious composites in case of fire.

APPENDIX A: SFRC MIXTURE PARAMETER DATABASE

SFRC Mixture Parameter Database

Reference	Mix ID	Input Parameters									
		cp	cap	fap	w/c	fl	ar	Vf	ri	fc	mor
Acikgenc et al. (2013)	80/60	20	54	54	0.65	2.36	80	0.5	40	3550	544
	80/60	20	54	54	0.65	2.36	80	1	80	3400	725
	80/60	20	54	54	0.65	2.36	80	1.5	120	3300	943
	65/60	20	54	54	0.65	2.36	65	0.5	32.5	3550	1189
	65/60	20	54	54	0.65	2.36	65	1	65	3500	696
	65/60	20	54	54	0.65	2.36	65	1.5	97.5	3500	870
	55/30	20	54	54	0.65	1.18	55	0.5	27.5	3550	943
	55/30	20	54	54	0.65	1.18	55	1	55	3500	624
	55/30	20	54	54	0.65	1.18	55	1.5	82.5	3200	696
	40/30	20	54	54	0.65	1.18	40	0.5	20	3550	798
	40/30	20	54	54	0.65	1.18	40	1	40	3300	609
	40/30	20	54	54	0.65	1.18	40	1.5	60	2800	667
Al-Ameeri (2013)	SF1	35	52	42	0.49	1.18	60	0	0	5133	682
	SF2	35	52	42	0.49	1.18	60	0.5	30	5452	798
	SF3	35	52	42	0.49	1.18	60	0.75	45	6554	1088
	SF4	35	52	42	0.49	1.18	60	1	60	6264	1233
	SF5	35	52	42	0.49	1.18	60	1.25	75	6163	1378
	SF6	35	52	42	0.49	1.18	60	1.5	90	6105	1523
Alavi Nia et al. (2012)	W/C 0.46 St 0.5	24	55	57	0.46	2.36	80	0.5	40	6525	1668
	W/C 0.46 St 1.0	24	54	57	0.46	2.36	80	1	80	6815	537
	W/C 0.36 St 0.5	28	54	57	0.36	2.36	80	0.5	40	8265	725
	W/C 0.36 St 1.0	28	54	56	0.36	2.36	80	1	80	8700	696
Campione, et al. (2008)	1	28	66	53	0.49	1.18	60	1	60	5248	798
	2	28	66	53	0.49	1.18	60	1	60	5049	480
	3	28	66	53	0.49	1.18	60	1	60	5018	783
Guerini et al. (2018)	C45-PC	17	39	27	0.5	0	0	0	0	6212	780
	C45-s1-0.5%	27	62	43	0.5	1.38	65	0.5	33	6753	972
	C45-s1-1.0%	27	62	43	0.5	1.38	65	1	65	6792	811
	C45-s2-0.5%	27	62	43	0.5	2.36	65	0.5	33	6334	863
	C45-s2-1.0%	27	62	43	0.5	2.36	65	1	65	6740	885
	C50-s1-0.5%	27	62	46	0.45	1.38	65	0.5	33	7724	812
	C50-s1-1.0%	27	62	46	0.45	1.38	65	1	65	7050	795
	C50-s2-0.5%	27	62	46	0.45	2.36	65	0.5	33	7570	876
	C50-s2-1.0%	27	62	46	0.45	2.36	65	1	65	6840	929

Guler et al. (2019)	Guler_Control	25	78	44	0.4	0	0	0	0	5970	1335
	H30_0.25	25	78	44	0.4	1.18	40	0.25	10	5535	1575
	H30_0.5	25	78	44	0.4	1.18	40	0.5	20	5748	1724
	H30_0.75	25	78	44	0.4	1.18	40	0.75	30	5996	1847
	H60_0.25	25	78	44	0.4	2.36	67	0.25	17	5900	1614
	H60_0.5	25	78	44	0.4	2.36	67	0.5	34	6007	1876
	H60_0.75	25	78	44	0.4	2.36	67	0.75	50	6360	2053
Kwak et al. (2002)	FHB1-2	30	66	35	0.33	1.97	0	0	0	9077	1293
	FHB2-2	30	66	35	0.33	1.97	62.5	0.5	31	9251	1465
	FHB3-2	30	66	35	0.33	1.97	62.5	0.75	47	9947	1552
	FHB1-3	30	66	35	0.33	1.97	62.5	0	0	9077	—
	FHB2-3	30	66	35	0.33	1.97	62.5	0.5	31	9251	—
	FHB3-3	30	66	35	0.33	1.97	62.5	0.75	47	9947	—
	FHB1-4	30	66	35	0.33	1.97	62.5	0	0	9077	—
	FHB2-4	30	66	35	0.33	1.97	62.5	0.5	31	9251	—
	FHB3-4	30	66	35	0.33	1.97	62.5	0.75	47	9947	—
Kwak et al. (2002)	FNB2-2	19	69	44	0.62	1.97	62.5	0	0	4466	—
	FNB2-3	19	69	44	0.62	1.97	62.5	0.5	31	4466	1124
	FNB2-4	19	69	44	0.62	1.97	62.5	0.75	47	4466	—
Lee et al. (2019)	3D-0.37	18	54	50	0.35	2.36	67	0.37	25	7395	1003
	3D-0.6	18	54	50	0.35	2.36	67	0.6	40	7105	1015
	3D-1.0	18	54	50	0.35	2.36	67	1	67	7540	1266
	4D-0.37	18	54	50	0.35	2.36	67	0.37	25	7395	998
	4D-0.6	18	54	50	0.35	2.36	67	0.6	40	7685	1077
	4D-1.0	18	54	50	0.35	2.36	67	1	67	7685	1119
	5D-0.37	18	54	50	0.35	2.36	67	0.37	25	6960	983
	5D-0.6	18	54	50	0.35	2.36	67	0.6	40	7830	993
	5D-1.0	18	54	50	0.35	2.36	67	1	67	7250	1079
Marar et al. (2016)	C30-Control	28	50	50	0.5	0	0	0	0	5786	--
	C30-65-0.5	28	50	50	0.5	2.36	65	0.5	33	5539	--
	C30-65-1.0	28	50	50	0.5	2.36	65	1	65	6873	--
	C30-65-1.5	28	50	50	0.5	2.36	65	1.5	98	5583	--
	C30-80-0.5	28	50	50	0.5	2.36	80	0.5	40	5873	--
	C30-80-1.0	28	50	50	0.5	2.36	80	1	80	5960	--
	C30-80-1.5	28	50	50	0.5	2.36	80	1.5	120	6322	--
	C50-Control	36	44	46	0.43	0	0	0	0	8048	--
	C50-65-0.5	36	44	46	0.43	2.36	65	0.5	33	7671	--
	C50-65-1.0	36	44	46	0.43	2.36	65	1	65	8019	--
	C50-65-1.5	36	44	46	0.43	2.36	65	1.5	98	8439	--
	C50-80-0.5	36	44	46	0.43	2.36	80	0.5	40	7613	--
	C50-80-1.0	36	44	46	0.43	2.36	80	1	80	7540	--
	C50-80-1.5	36	44	46	0.43	2.36	80	1.5	120	7308	--

Song and Hwang (2004)	Control	30	66	46	0.28	0	0	0	0	12325	928
	0.5	30	66	46	0.28	2.36	64	0.5	32	13195	1189
	1	30	66	46	0.28	2.36	64	1	64	13775	1465
	1.5	30	66	46	0.28	2.36	64	1.5	96	14210	1784
	2	30	66	46	0.28	2.36	64	2	128	13920	2103
Soulioti et al. (2011)	Plain	27	23	76	0.5	0	0	0	0	6757	645
	H0.5	27	23	76	0.5	1.22	41	0.5	21	7308	551
	H1	27	22	75	0.5	1.22	41	1	41	6366	667
	H1.5	27	22	74	0.5	1.22	41	1.5	62	7279	841
Torres and Lantsoght (2019)	Control	36	37	55	0.4	0	0	0	0	2987	418
	M1-0.3	35	35	53	0.45	2.36	80	0.3	24	4785	418
	M2-0.6	35	35	53	0.45	2.36	80	0.6	48	4031	782
	M3-0.9	34	34	51	0.5	2.36	80	0.9	72	4220	870
	M4-1.2	32	32	49	0.55	2.36	80	1.2	96	4394	893

ACKNOWLEDGEMENTS

The University of Georgia acknowledges the financial support for this work provided by the Georgia Department of Transportation. The authors also thank the many GDOT personnel who assisted with this study. A special thanks is offered to Peter Wu, P.E., Bureau Chief with the GDOT Office of Materials and Testing; Jason Waters, GDOT Concrete Branch Chief, GDOT Office of Traffic Operations; Michael Turpeau, Jr., GDOT State Safety Program Supervisor; Carlos Baker, GDOT Road Design Engineer; and Brennan Roney, GDOT Research Manager. In addition, the research team thanks the numerous materials suppliers that supported this study, including Argos USA and Liberty Tire Recycling.

REFERENCES

AASHTO. (1989). Guide Specification for Bridge Railings. American Association of State Highway and Transportation Officials, Washington, DC.

AASHTO. (2016). *Manual for Assessing Safety Hardware, MASH-2.* American Association of State Highway and Transportation Officials, Washington, DC.

Abadel, A., Abbas, H., Almusallam, T., Al-Salloum, Y., and Siddiqui, N. (2016). "Mechanical Properties of Hybrid Fibre-Reinforced Concrete – Analytical Modelling and Experimental Behaviour." *Magazine of Concrete Research,* 68(16), pp. 823–843. doi:10.1680/jmacr.15.00276.

Abdallah, S. (2017). "Effect of Hooked-End Steel Fibres Geometry." *International Journal of Civil, Environmental, Structural, Construction and Architecture Engineering,* 10 pp.

ACI Committee 544. (2009). *ACI 544.2R-09 Measurement of Properties of Fiber Reinofrced Concrete.* American Concrete Institute. Retrieved from http://concrete.org.

ACI Committee 544. (2018). *ACI 544.4R-18 Guide to Design with Fiber-Reinforced Concrete.* American Concrete Institute. Retrieved from http://concrete.org.

Acikgenc, M., Alyamac, K.E., and Ulucan, Z.C. (2013). "Fresh and Hardened Properties of Steel Fiber Reinforced Concrete Produced with Fibers of Different Lengths and Diameters." In *Proceedings of the 2nd International Balkans Conference on Challenges of Civil Engineering,* Tirana, Albania, May 23–25.

Afroughsabet, V. and Ozbakkaloglu, T. (2015). "Mechanical and Durability Properties of High-Strength Concrete Containing Steel and Polypropylene Fibers." *Construction and Building Materials,* 94, pp. 73–82.

Al-Ameeri, A. (2013). "The Effect of Steel Fiber on Some Mechanical Properties of Self Compacting Concrete." *American Journal of Civil Engineering,* 1(3), pp. 102–110. doi:10.11648/j.ajce.20130103.14.

Alavi Nia, A., Hedayatian, M., Nili, M., and Sabet, V.A. (2012). "An Experimental and Numerical Study on How Steel and Polypropylene Fibers Affect the Impact Resistance in Fiber-Reinforced Concrete." *International Journal of Impact Engineering,* 46, pp. 62–73. doi:10.1016/j.ijimpeng.2012.01.009.

Alberta Infrastructure and Transportation. (2007). "H7 Bridges." *Roadside Design Guide.* pp. 1–2.

Amirkhanian, A. and Roesler, J. (2019). *Overview of Fiber-Reinforced Concrete Bridge Decks.* InTrans Project 15-532, National Concrete Pavement Technology Center, Iowa State University, 37 pp.

Atahan, A.O. and Sevim, U.K. (2008). "Testing and Comparison of Concrete Barriers Containing Shredded Waste Tire Chips." *Materials Letters,* 62, pp. 3754–3757.

Balaguru, P. and Ramakrishnan, V. (1988). "Properties of Fiber Reinforced Concrete: Workability, Behavior Under Long-Term Loading, and Air-Void Characteristics." *ACI Materials Journal*, 85(3), pp. 189–196.

Banthia, N. and Sappakittipakorn, M. (2007). "Toughness Enhancement in Steel Fiber Reinforced Concrete Through Fiber Hybridization." *Cement and Concrete Research*, 37(9), pp. 1366–1372.

Baun, M. (1992). "Steel Fiber Reinforced Concrete Bridge Deck Overlays: Experimental Use by Ohio Department of Transportation." In *Transportation Research Record: Journal of the Transportation Research Board*, 1392, TRB, National Research Council, Washington, DC, ISSN: 0361-1981, pp. 73–78.

Beason, W.L., Ross, H.E., Perera, H.S., Campise, W.L., and Bullard, D.L. (1989). "Development of a Single-Slope Concrete Median Barrier." Report No. 9429CDK-1, State Department of Highways and Public Transportation, Austin, TX, 98 pp.

Bekaert (2020). All-Round Concrete Reinforcement Solution. https://www.bekaert.com/en/product-catalog/construction/concrete-reinforcement/all-round-concrete-reinforcement-solution. Accessed January 2020.

Bhutta, A., Farooq, M., Borges, P., and Banthia, N. (2018). "Influence of Fiber Inclination Angle on Bond–Slip Behavior of Different Alkali-Activated Composites Under Dynamic and Quasi-Static Loadings." *Cement and Concrete Research,* 107, pp. 236–246.

Bielenberg, R.W., Faller, R.K., Quinn, T.E., Sicking, D.L., and Reid, J.D. (2014). *Development of a Retrofit, Low-Deflection, Temporary Concrete Barrier System.* Final Report No. TRP-03-295-14, Midwest States Regional Pooled Fund Program, Lincoln, NE, 366 pp.

Bligh, R.P., Abu-Odeh, A.Y., Hamilton, M.E., and Seckinger, N.R. (2004). *Evaluation of Roadside Safety Devices using Finite Element Analysis.* FHWA/TX-04/0-1816-1 Final Report, Texas Department of Transportation, Austin, TX, 66 pp.

Bordelon, A. (2007). *Fracture Behavior of Concrete Materials for Rigid Pavement Systems.* Thesis, University of Illinois at Urbana-Champaign, Urbana, IL, 165 pp.

Brannon, R.M. and Leelavanichkul, S. (2009). *Survey of Four Damage Models for Concrete.* Technical Report, Sandia National Laboratories, U.S. Department of Energy. doi:10.2172/993922.

Bullard, D.L., Bligh, R.P., Menges, W.L., and R.R., Haug. (2010). *Volume 1: Evaluation of Existing Roadside Safety Hardware Using Updated Criteria – Technical Report.* Report No. NCHRP Project 22-14(03), 202 pp.

Campione, G. and Letizia Mangiavillano, M. (2008). “Fibrous Reinforced Concrete Beams in Flexure: Experimental Investigation, Analytical Modelling and Design Considerations.” *Engineering Structures,* 30(11), pp. 2970–2980. doi:10.1016/j.engstruct.2008.04.019.

Choi, K.-K., Park, H.-G., and Wight, J. K. (2007). “Shear Strength of Steel Fiber–Reinforced Concrete Beams without Web Reinforcement.” *ACI Structural Journal,* 104(1), pp 12–21.

Deluce, J. R. and Vecchio, F. J. (2013). “Cracking Behavior of Steel Fiber–Reinforced Concrete Containing Conventional Steel Reinforcement.” *ACI Structural Journal,* 110(4), pp. 481–490.

Dhakal, M., Al-Masud, M., Alam, A., Montes, C., Kupwade-Patil, K., Allouche, E., and Saber, E. (2013). “Design, Fabrication and Testing of a Full-Scale Geopolymer Concrete Median Barrier.” *World of Coal Ash*, Vol. Cement & Concrete V, 15 pp. doi:10.13140/RG.2.1.3003.2487.

Dobrovolny, C.S., Sheikh, N.M., Fossier, P.B., Brauner, K., and Guidry, C. (2015). “Design and Full-Scale Crash Testing of an Anchored Temporary Concrete Barrier and its Transition System for Use on Asphalt Pavement.” Transportation Research Board 94th Annual Meeting, Jan 11-15, Washington, DC, 16 pp.

Dopko, M. (2018). *Fiber Reinforced Concrete: Tailoring Composite Properties with Discrete Fibers.* Thesis, Iowa State University, 177 pp.

Durham, S.A., Chorzepa, M.G., and Stallings, K. (2017). *Investigation of Recycled Tire Chips for Use in GDOT Concrete Used to Construct Barrier Walls and Other Applications.* Final Report No. FHWA-GA-15-14. Georgia Department of Transportation, Atlanta, GA, pp. 116.

El-Salakawy, E., Brière., F., Masmoudi., R., Tighiouart., B., and Benmokrane, B. (2001). *Impact Test on Concrete Bridge Barriers Reinforced with GHRP Composite Bars.* Final Report No. 1220-00-BD03, Ministry of Transportation of Quebec Structural Department, Sherbrooke, Quebec, Canada, 93 pp.

El-Salakawy, E., and Islam, M. (2014). “Repair of GFRP-Reinforced Concrete Bridge Barriers.” ASCE Journal of Bridge Engineering, 19(6): 04014016, pp 1-11.

Elchalakani, M. (2015). “High Strength Rubberized Concrete Containing Silica Fume for the Construction of Sustainable Road Side Barriers.” *Structures,* 1, pp. 20–38.

FHWA. (2013). “Cast-In-Place Concrete Barriers.” Federal Highway Administration, Washington, DC. https://www.dot.nd.gov/divisions/maintenance/guardrail/docs/Guardrail webpage/FHWA Charts.pdf.

Fossier, P., and Longstreet, W. (2016). Bridge Rail Testing Program Confirm Mash Compliance. Research Needs Statements. Transportaton Research Board AFB20 Committeee Mid-Year Meeting.

Fujikake, K., Li, B., and Soeun, S. (2009). "Impact Response of Reinforced Concrete Beam and Its Analytical Evaluation." *Journal of Structural Engineering,* 135(8), pp. 938–950.

GDOT. (2006). *Supplemental Specifications, Section 500-Concrete Structures.* Georgia Department of Transportation. Atlanta. GA.

GDOT. (2017). *Special Detail Concrete Median Barrier Type S-1, S-2 and S-3 and Concrete Glare Screen.* Georgia Department of Transportation. Atlanta, GA.

Grzebieta, R.H., Zou, R., Corben, B., Judd, R., Kulgren, A., Tingval, C., and Powell, C. (2002). "Roadside Crash Barrier Testing." Proceedings of ICRASH, 3rd, Melbourne, Australia, 14 pp.

Guerini, V., Conforti, A., Plizzari, G., and Kawashima, S. (2018). "Influence of Steel and Macro-Synthetic Fibers on Concrete Properties." *Fibers,* 6(3). doi:10.3390/fib6030047.

Guler, S., Yavuz, D., Korkut, F., and Ashour, A. (2019). "Strength Prediction Models for Steel, Synthetic, and Hybrid Fiber Reinforced Concretes." *Structural Concrete,* 20(1), pp. 428–445. doi:10.1002/suco.201800088.

Hammonds, B.R. and Troutbeck, R. (2012). "Crash Test Outcomes for Three Generic Barrier Types." ARRB Conference, 25th, 2012, Perth, Australia, 22 pp.

Highway Research Board Committee on Guardrails and Guide Posts. (1962). "Full-Scale Testing Procedures for Guardrails and Guide Posts." Highway Research Correlation Services Circular 482.

Hirsch, T.J., Post, E.R., and Hayes, G.G. (1972). *Vehicle Crash Test and Evaluation of Median Barriers for Texas Highways.* Report No. 146-4, Texas Highway Department, 126 pp.

Ismail, M.K. and Hassan, A.A. (2016). "Performance of Full-Scale Self-Consolidating Rubberized Concrete Beams in Flexure." *ACI Materials Journal,* 113(1), pp. 1–6.

Itoh, Y., Liu, C., and Kusama, R. (2007). "Dynamic Simulation of Collisions of Heavy High-Speed Trucks with Concrete Barriers." *Chaos, Solitons & Fractals,* 34(4), pp. 1239–1244.

Jeon, S-J., Choi, M-S., and Kim, Y-J. (2008). "Ultimate Strength of Concrete Barrier by the Yield Line Theory." *International Journal of Concrete Structures and Materials,* 2(1), pp. 57–62.

Jewell, J., Rowhani, P., Stoughton, R., and Crozier, W. (1997). *Vehicular Crash Tests of a Slip-formed, Single Slope, Concrete Median Barrier.* Final Report No. FHWA/CA/ESC-98/02. California Department of Transportation. Sacramento, CA, 101 pp.

Kardos, A. and Durham, S. (2015). "Strength, Durability, and Environmental Properties of Concrete Utilizing Recycled Tire Particles for Pavement Applications." *Construction and Building Materials,* 98, pp. 832–845.

Kim, K-M., Briaud, J-L., Bligh, R., and Obu-Odeh, A. (2010). "Full-Scale Impact Test of Four Traffic Barriers on Top of an Instrumented MSE Wall." *Journal of Geotechnical and Geoenvironmental Engineering,* 136(3), pp. 431–438.

Kwak, Y.-K., Eberhard, M.O., Kim, W.-S., and Kim, J. (2002). "Shear Strength of Steel Fiber–Reinforced Concrete Beams without Stirrups." *ACI Structural Journal,* 99(4) pp. 530–538.

Lee, D.H., Han, S.-J., Kim, K.S., and LaFave, J.M. (2017). "Shear Capacity of Steel Fiber–Reinforced Concrete Beams." *Structural Concrete,* 18(2), pp. 278–291. doi:10.1002/suco.201600104.

Lee, J., Zi, G., Lee, I., Jeong, Y., Kim, K., and Kim, W.S. (2017). "Numerical Simulation on Concrete Median Barrier for Reducing Concrete Fragment Under Harsh Impact Loading of a 25-ton Truck." *Journal of Engineering Materials and Technology*, 139(2), 9 pp.

Lee, S.-J., Hong, Y., Eom, A-H, and Won, J-P. (2018). "Effect of Steel Fibers on Fracture Parameters of Cementitious Composites." *Composite Structures.* doi: 10.1016/j.compstruct.2018.08.002.

Lee, S.-J., Yoo, D.-Y., and Moon, D.-Y. (2019). "Effects of Hooked-End Steel Fiber Geometry and Volume Fraction on the Flexural Behavior of Concrete Pedestrian Decks." *Applied Sciences,* 9(6). doi:10.3390/app9061241.

Li, Q.M., Reid, S.R, Wen, H.M., and Telford, A.R. (2005). "Local Impact Effects of Hard Missiles on Concrete Targets." *International Journal of Impact Engineering,* 32, pp. 224–284.

Mak, K.K., Gripne, D.J., and McDevitt, C.F. (1994). "Single-Slope Concrete Bridge Rail." In *Transportation Research Record: Journal of the Transportation Research Board,* 1468, TRB, National Research Council, Washington, DC, pp. 25–33.

Marar, K., Eren, Ö., and Roughani, H. (2016). "The Influence of Amount and Aspect Ratio of Fibers on Shear Behaviour of Steel Fiber Reinforced Concrete." *KSCE Journal of Civil Engineering*, 21(4), pp. 1393–1399. doi:10.1007/s12205-016-0787-2.

Masud, M. (2015). *Multi-Scale Impact Resilient Smart Composites (MIRACs) for Hazard Mitigation*. Thesis, University of Georgia, 141 pp.

McDevitt, C. (2000). "Basics of Concrete Barriers" *Public Roads*, Federal Highway Administration Research and Technology, 63 (5).

Mohan, P., Marzougui, D., Arispe, E., and Story, C. (2009). *Component and Full-Scale Tests of the 2007 Chevrolet Silverado Suspension System.* Federal Highway Administration, U.S. Department of Transportation, Contract No. DTFH61-02-X-00076, 38 pp.

Mongiardini, M., Faller, R.K., Reid, J.D., Meggers, D., El-Aasar, M.G., and Plunkett, J.D. (2013). "Design and Testing of a Concrete Safety Barrier for Use on a Temporary FRP Composite Bridge Deck." *Journal of Bridge Engineering,* 18(11), pp. 1198–1208.

Naaman, A.E. (2003). "Engineered Steel Fibers with Optimal Properties for Reinforcement of Cement Composites." *Journal of Advanced Concrete Technology,* 1, pp. 241–252.

Namy, M., Charron, J-P., and Massicotte, B. (2015). "Structural Behavior of Bridge Decks with Cast-in-Place and Precast Concrete Barriers: Numerical Modeling." *Journal of Bridge Engineering*, 20(12), 11 pp.

Nataraja, N., Dhang, N., and Gupta, A.P. (1999). "Statistical Variations in Impact Resistance of Steel Fiber–Reinforced Concrete Subjected to Drop Weight Test." *Cement and Concrete Research,* 29(7). pp. 989–995.

Noaman, A.T., Bakar, B.H.A., Akil, H.Md., and Alani, A.H. (2017). "Fracture Characteristics of Plain and Steel Fibre Reinforced Rubberized Concrete." *Construction and Building Materials,* 152, pp. 414–423.

NTRCI. (2005). *Methodology for Validation and Documentation of Vehicle Finite Element Crash Models for Roadside Hardware Applications – F800 Single Unit Truck FEM Model for Crash Simulations with LS-DYNA.* National Transportation Research Center, Inc. https://thyme.ornl.gov/FHWA/F800WebPage/description/desc2.html.

Padmarajaiah, S.K. (1992). *Influence of Fibers on the Behavior of High Strength Concrete in Fully/Partially Prestressed Beams: An Experimental and Analytical Study.* Dissertation, Indian Institute of Science, Bangalore, India.

Polivka, K.A., Sicking, D.L., Bielenberg, B.W., Faller, R.K., Rohde, J.R., Reid, J.D, and Coon, B.A. (2006a). *Performance Evaluation of the Permanent New Jersey Safety Shape Barrier – Update to NCHRP 350 Test No. 3-10 (2214NJ-1).* Final Report No. TRP-03-177-06, National Cooperative Highway Research Program, Transportation Research Board, Washington, DC, 65 pp.

Polivka, K.A., Sicking, D.L., Bielenberg, B.W., Faller, R.K., Rohde, J.R., Reid, J.D., and Coon, B.A. (2006b). *Performance Evaluation of the Permanent New Jersey Safety Shape Barrier – Update to NCHRP 350 Test No. 4-12 (2214NJ-2).* Final Report No. TRP-03-178-06, National Cooperative Highway Research Program, Transportation Research Board, Washington, DC, 62 pp.

Rosenbaugh, S.K., Sicking, D.L., and Faller, R.K. (2007). *Development of a TL-5 Vertical Faced Concrete Median Barrier Incorporating Head Ejection Criteria.* Midwest Roadside Safety Facility Research Report No. TRP-03-194-07, Lincoln, NE, 355 pp.

Ross, H.E., Sicking, D.L., Zimmer, R.A., and Michie, J.D. (1993). *Recommended Procedures for the Safety Performance Evaluation of Highway Features.* National Cooperative Highway Research Program Report 350, Transportation Research Board, Washington, DC.

Rowhani, P., Glauz, D., and Stoughton, R.L. (1993). "Vehicle Crash Tests of Concrete Median Barrier Retrofitted with Slipformed Concrete Glare Screen." In *Transportation Research Record: Journal of the Transportation Research Board,* 1419, TRB, National Research Council, Washington, DC, pp. 35–42.

Saatci, S. and Vecchio, J.V. (2009) "Effect of Shear Mechanisms on Impact Behavior of Reinforced Concrete Beams." *ACI Structural Journal,* 106(1), pp. 78–86.

Sheikh, N.M., Bligh, R.P., and Holt, J.M. (2012). "Minimum Rail Height and Design Impact Load for *MASH* TL-4 Longitudinal Barriers." Transportation Research Board 91st Annual Meeting, Jan 22–26, Washington, DC, 16 pp.

Sheikh, N.M., Bligh, R.P., and Menges, W.L. (2008). *Crash Testing and Evaluation of F-Shape Barriers on Slopes.* Final Report No. FHWA/TX-08/0-5210-3, Texas Department of Transportation, Austin, TX, 86 pp.

Sheikh, N.M., Bligh, R.P., Albin, R.B., and Olson, D. (2009). "Application of Precast Concrete Barrier Adjacent to a Steep Roadside Slope." In *Transportation Research Record: Journal of the Transportation Research Board,* 2195, TRB, National Research Council, Washington, DC, pp. 121–169.

Song, P.S. and Hwang, S. (2004). "Mechanical Properties of High-Strength Steel Fiber–Reinforced Concrete." *Construction and Building Materials,* 18(9), pp. 669–673. doi:10.1016/j.conbuildmat.2004.04.027.

Soulioti, D.V., Barkoula, N.M., Paipetis, A., and Matikas, T.E. (2011). "Effects of Fibre Geometry and Volume Fraction on the Flexural Behaviour of Steel-Fibre Reinforced Concrete.' *Strain,* 47(s1), pp. e535–e541. doi:10.1111/j.1475-1305.2009.00652.x.

Stolle, C.J., Reid, J.D., and Faller, R.K. (2014). *Zone of Intrusion for Permanent 9.1-Degree Single-Slope Concrete Barriers.* Final Report No. TRP-03-292-13, Wisconsin Department of Transportation, Madison, WI, 161 pp.

Tate, S. (2019). *Investigation into the Use of Tire Derived Rubber Aggregates and Recycled Steel Wire Fiber for Use in Concrete Subjected to Impact Loading.* Thesis, University of Georgia, Athens, GA.

Torres, J.A. and Lantsoght, E.O.L. (2019). "Influence of Fiber Content on Shear Capacity of Steel Fiber–Reinforced Concrete Beams." *Fibers,* 7(12), 102 pp. doi:10.3390/fib7120102.

Tropynina, E. (2012). *Structural Design Issues on GFRP-Reinforced Concrete Bridge Barriers.* Ryerson University Theses and Dissertations 1710, Toronto, Ontario, Canada, 138 pp.

Ulker, M.B.C., Rahman, M.S., Zhen, R., and Mirmiran, A. (2008). "Traffic Barriers under Vehicular Impact: From Computer Simulation to Design Guidelines." *Computer-Aided Civil and Infrastructure Engineering,* 23(6), pp. 465–488.

Wafa, F. and Ashour, S. (1992). “Mechanical Properties of High-Strength Fiber Reinforced Concrete.” *ACI Materials Journal*, 89(5), pp. 449–455.

Wang, S., Yan, L., Liang, Q., and Xu, M. (2017). “Research on RHT Constitutive Model Parameters of Fiber Reinforced Concrete Based on Experiment and Numerical Simulation.” *Advances in Engineering Research*, 135, pp. 185–192.

Wiebelhaus, M.J., Lechtenberg, K.A., Faller, R.K., Rohde, J.R., Terpsma, R.J., Bielenberg, R.W., Sicking, D.L., and Reid, J.D. (2010). *Development of a Temporary Concrete Barrier to Permanent Concrete Median Barrier Approach Transition.* Final Report No. TRP-03-208-10, Midwest States Regional Pooled Fund Program, Lincoln, NE, 172 pp.

Williams, W.F., Bligh, R.P., and Menges, W.L. (2011). *Mash Test 3-11 of the TxDOT Single Slope Bridge Rail (Type SSTR) on Pan-Formed Bridge Deck.* Final Report No. FHWA/TX-11/9-1002-3, Texas Department of Transportation, Austin, TX, 62 pp.

Yakoub, H. (2011). “Shear Stress Prediction—Steel Fiber–Reinforced Concrete Beams without Stirrups.” *ACI Structural Journal*, 108(3), pp. 304–314.

Yazıcı, Ş., İnan, G., and Tabak, V. (2007). “Effect of Aspect Ratio and Volume Fraction of Steel Fiber on the Mechanical Properties of SFRC.” *Construction and Building Materials*, 21(6), pp. 1250–1253. doi:10.1016/j.conbuildmat.2006.05.025.

Yoo, D.-Y., Kim, S., Park, G.-J., Park, J.-J., and Kim, S.-W. (2017). “Effects of Fiber Shape, Aspect Ratio, and Volume Fraction on Flexural Behavior of Ultra-High-Performance Fiber-Reinforced Cement Composites.” *Composite Structures*, 174, pp. 375–388.

Zollo, R.F. (1997). “Fiber-Reinforced Concrete: An Overview After 30 Years of Development.” *Cement and Concrete Composites*, 19(2), pp. 107–122.

Zou, Y., Tarko, A.P., Chen, E., and Romero, M.A. (2014). “Effectiveness of Cable Barriers, Guardrails, and Concrete Barrier Walls in Reducing the Risk of Injury.” *Journal of Accident Analysis and Prevention*, 72, pp. 55–65. doi. 10.1016/j.aap.2014.06.013.